



**HAL**  
open science

## Microfluidic synthesis of switchable materials

Juan Héctor Gonzalez Estefan

► **To cite this version:**

Juan Héctor Gonzalez Estefan. Microfluidic synthesis of switchable materials. Material chemistry. Université de Bordeaux, 2019. English. NNT : 2019BORD0199 . tel-02984774

**HAL Id: tel-02984774**

**<https://theses.hal.science/tel-02984774>**

Submitted on 1 Nov 2020

**HAL** is a multi-disciplinary open access archive for the deposit and dissemination of scientific research documents, whether they are published or not. The documents may come from teaching and research institutions in France or abroad, or from public or private research centers.

L'archive ouverte pluridisciplinaire **HAL**, est destinée au dépôt et à la diffusion de documents scientifiques de niveau recherche, publiés ou non, émanant des établissements d'enseignement et de recherche français ou étrangers, des laboratoires publics ou privés.

THÈSE PRÉSENTÉE  
POUR OBTENIR LE GRADE DE  
**DOCTEUR DE**  
**L'UNIVERSITÉ DE BORDEAUX**

ÉCOLE DOCTORALE DES SCIENCES CHIMIQUES  
SPÉCIALITÉ : PHYSICO-CHIMIE DE LA MATIÈRE CONDENSÉE

Par Juan Héctor GONZÁLEZ ESTEFAN

**Microfluidic Synthesis of Switchable Materials**

Sous la direction de : Guillaume CHASTANET  
(co-encadrant: Mathieu GONIDEC)

Soutenue le 31 octobre 2019.

Membres du jury :

M. MAGLIONE, Mario	Directeur de Recherche	ICMCB-CNRS	Président
M. PUIGMARTÍ-LUIS, Josep	Professeur	ETH Zürich	Rapporteur
Mme. BLEUZEN, Anne	Professeur	ICMMO Université Paris-Sud	Rapporteur
M. CHASTANET, Guillaume	Chargé de Recherche	ICMCB-CNRS	Examineur
M. GONIDEC, Mathieu	Chargé de Recherche	ICMCB-CNRS	Invité



# Acknowledgements.

First, I would like to thank Dr. Mathieu Gonidec and Dr. Guillaume Chastanet for directing this project and for tutoring me along the last three years.

My work during the PhD was funded by the Mexican Government through the program “Becas al Extranjero” sponsored by the Mexican Council of Science and Technology (CONACyT, program 073096, announcement 291060), for which I am deeply thankful. Moreover, I received additional support from the DAAD for a one-month research stay at the Universität Bayreuth in Germany, and from LabEx Amadeus for a one-week stay at the European Synchrotron Radiation Facility in Grenoble, France.

Additionally, I must thank MPhil. Janette Estefan Garfias, MA. Marie Janette González Estefan and MSc. Tiziana Jäggi, for their emotional and financial support along these doctoral studies.

I would also thank the members of group of research (Molécules et Matériaux Commutables), especially those who actively took part in collaborations with us: Dr. Nathalie Daro, Dr. Mathieu Marchivie, Dr. Patrick Rosa, Dr. Lorenzo Poggini, Dr. Corine Mathonière, MSc. Thi Thiet Vu and MSc. Xing-Hui Qi.

Moreover, this project would not have been possible without the support from the Institut de Chimie de la Matière Condensée de Bordeaux, directed by Dr. Mario Maglione, or without the help from the many researchers and members of the staff of the ICMCB and the Placamat, especially Dr. Philippe Guionneau, Dr. Éric Lebraud and Dr. Samuel Marre.

Many of the side projects developed during this PhD involved mutual help and collaborations with a network of researches, specially Dr. I. A. Ibarra, MSc. D. Alvarado Alvarado, Dr. B. Weber, Dr. N. Shustova Dr. J. A. Real and Dr. J. Valverde Muñoz, Dr. I. Oyarzabal, Dr. A. Valentín and many members of the M3 group at the CRPP in Bordeaux.

Finally, I am very thankful and proud of my alma matter, the Université de Bordeaux and its Doctoral School of Chemical Sciences, for giving me the access to a high-level education, and for letting me share three years with wonderful people from many different continents.



## Table of contents

<b>General introduction.</b>	<b>7</b>
<b>Part 1. Basic concepts of microfluidics and spin crossover.</b>	<b>9</b>
Chapter 1.1 Fundamentals of microfluidic synthesis.	11
1.1.1 The two approaches to carry reactions using microfluidic process.	12
1.1.2 Flow profiles of a liquid flowing along a channel.	13
1.1.3 The droplet as a reactor.	16
1.1.4 Droplet generation.	19
1.1.5 Pressure oscillations.	23
Chapter 1.2. Fundamentals of spin crossover.	25
1.2.1 Definition and origin of spin crossover.	25
1.2.2 Multiple models to understand spin crossover.	27
1.2.3 The Non-interacting model.	28
1.2.4 The reaction enthalpy ( $\Delta H$ ).	30
1.2.5 Reaction entropy ( $\Delta S$ )	31
1.2.6 Interacting models part 1: Basic concepts.	32
1.2.7 Hysteresis and the interaction constant.	35
1.2.8 Finite systems.	39
1.3 Summary	42
1.4 Outline of this work.	43
References to part 1.	44
<b>Part 2. Fundamental aspects in the microfluidic synthesis of materials.</b>	<b>47</b>
Chapter 2.1 Theoretical framework: The two approaches of synthesis in droplet microfluidics.	49
2.1.1 The <i>generation</i> → <i>combination</i> approach.	49
2.1.2 The <i>combination</i> → <i>generation</i> approach.	54
2.1.3 Comments on the <i>combination</i> → <i>generation</i> and <i>generation</i> → <i>combination</i> approaches.	56
Chapter 2.2 The microfluidic devices developed for the synthesis of switchable materials.	58

2.2.1 First attempts.	58
2.2.2 Preliminary experiments without reactants: Determination of the adequate flow rates.	60
2.2.3 Second experimental approach: <i>Combination</i> → <i>generation</i> .	61
2.2.4. Summary and conclusions to developed microfluidic devices for the synthesis of switchable materials.	66
Chapter 2.3. In situ fine-tuning of microfluidic chips by swelling and its application to droplet microfluidics.	68
2.3.1 General approach	69
2.3.2 Swelling in PDMS walls	70
2.3.3 Kinetics.	78
2.3.4 Modulation of the droplet size.	84
2.3.5 Reliability- related experiments.	87
2.3.6 Summary and conclusions about the use of swelling to modulate the critical dimensions of PDMS chips and the size of droplets produced by them.	95
2.4 Perspectives of Part 2.	97
References to part 2.	100

## **Part 3. Microfluidics applied to the synthesis of switchable materials. 103**

Chapter 3.1. Synthesis of Hofmann [Fe(pz)Pt(CN) <sub>4</sub> ] 3D network	105
3.1.1 What is known on the [Fe(pz)Pt(CN) <sub>4</sub> ] compound.	105
3.1.2 Strategy followed.	107
3.1.3 Preliminary tests.	109
3.1.4 The first approach for the synthesis of [Fe(pz)Pt(CN) <sub>4</sub> ]: <i>Generation</i> → <i>combination</i> .	110
3.1.5 The second approach for the synthesis of [Fe(pz)Pt(CN) <sub>4</sub> ]: <i>Combination</i> → <i>generation</i> .	114
3.1.5.a. The design of a starting sequence to avoid backflow and the formation of oil-bridges at the beginning of the operation of the chips.	114
3.1.5.b. The performance of the Blue Chip.	116
3.1.5.c. The performance of the Red Chip.	119
3.1.5.d. The design of a finishing sequence to avoid diffusion of reactants and the formation of precipitates in the chip at the end of its operation.	122
3.1.5.e. Cleaning the microfluidics-synthesized sample (first successful experiment).	124
3.1.6. Properties of the synthesized compounds.	124
3.1.6.a Synthesis of a bulk-synthesized reference sample (first reference material).	124
3.1.6.b. Characterization of the products.	125
3.1.6.c. Magnetic characterization of the products.	127

3.1.6.d. Morphological characterization of the products (first successful experiment).	129
3.1.6.e. Comparison of results with the literature.	131
3.1.7. Reproducibility and performance.	132
3.1.7.a. Reaction conditions and performance.	133
3.1.7.b. Synthesis of a reference sample.	135
3.1.7.c. Cleaning of the samples.	136
3.1.7.d. Morphological characterization of the products (second successful experiment).	137
3.1.8. Conclusions and discussion.	140
Chapter 3.2. Improvements of devices based on the <i>combination</i> → <i>generation</i> approach	147
3.2.1. Improvement of the device.	147
3.2.2. The use of swelling to modulate the droplet diameter in an operating device.	153
3.3 Conclusions to part 3	156
References to part 3	158
<b>General conclusions.</b>	<b>161</b>
<b>Appendix</b>	<b>165</b>



## General introduction.

Spin crossover is a phenomenon that gives some coordination compounds with transition metal ions a switchable behavior. There, the electronic configuration in the  $3d$  orbitals changes upon the exposure of the material towards stimuli, like light irradiation or changes in the temperature or pressure. This phenomenon is known since the second half of the twentieth century and its use in many applications has been envisioned, for example, as sensors (of temperature,<sup>1</sup> pressure<sup>2</sup> and gases<sup>3</sup>), as contrast agents in nuclear magnetic imaging,<sup>4</sup> as thermochromic pigments and as a medium to store information.<sup>5</sup>

Although their switching behavior is interesting from a scientific point of view, spin crossover materials are not used for any industrial application nowadays. There are many reasons for this, starting by the fact that other materials competing for the same niches of applications have great performances. Yet, spin crossover materials are very promising since they allow us to have two sets of properties in the same material (color, density, magnetic susceptibility and so on). In many ways, this switchable essence of spin crossover materials is a resource waiting to be exploited: On one side, we can choose the state of the system at will, and on the other, we can read the response of the material to quantify the magnitude of a stimulus.<sup>6</sup>

One of the greatest challenges to give spin crossover an industrial application is the fact that some microscopic features of these materials (like the particle size or the presence of crystal defects or dopants) affect their behavior. Since we do not have access to particles of infinite size, to perfect crystals or to substances that are completely pure, these features blur our knowledge about these materials. In fact, a same material synthesized by two groups can have different properties, even if the typical characterization procedures indicate that both samples are equivalent. So, there is a degree of irreproducibility in the synthesis of spin crossover materials (even in the ones that only require mixing two aqueous solutions).

We believe that the origin of this irreproducibility is related with the unpredictability of the motion of fluids inside the flasks and beakers where these materials are conventionally synthesized. In other words, the reaction conditions (in terms of how the reactants are mixed) influence the microscopic features of the product, which later affect its behavior. If we could mix the reactants reproducibly, we would obtain materials with the same microscopic features and therefore, the same behavior as well. Moreover, the better we could control the reaction environment, the easier it would be to engineer it and to produce materials with predictable microscopic features.

To reach this goal, we propose the use of microfluidics. Here, small amounts of fluids are manipulated using microscopic channels with dimensions between tens and hundreds of micrometers. The flow in such channels tends to be laminar, predictable and controllable in space and time to the scale of micrometers and milliseconds. This way, microfluidics gives us the possibility of mixing solutions with reactants and of carrying reactions with a degree of control unreachable by the conventional methodologies.

Nevertheless, this is not an easy task. Consider that the products we target are solids, which means that they can sediment and clog the channel or affect the flows inside it in unpredictable ways. Most devices reported in the literature can perform very well carrying out reactions that produce soluble or nanoparticulate products and have never been used for the synthesis of solids in form of larger particles. Therefore, we cannot work directly with every device found in literature. To avoid clogging, we focus our efforts towards droplet microfluidics. There, a stream of droplets (usually made of water)

are carried along a channel and are separated from each other by flow of an immiscible fluid (mineral oil or a fluorinated oil). Since each of these droplets acts as a microreactor, manipulating them allows us to influence the reaction environment where the product is precipitating.

Droplet microfluidics gives us additional benefits in the long term. For instance, we could add different reactants sequentially to the same droplet, either to quench the reaction and obtain nanoparticles, or to synthesize core-shell and core-multi-shell particles. And just as any technology, it has drawbacks. Especially, droplet microfluidics tends to involve the use of surfactants to stabilize the droplets. Since the presence of surfactants could influence the behavior of spin crossover materials, we cannot use them, and therefore our flexibility when selecting the right geometry to work with becomes more restricted.

In this thesis, we present our work during the last three years trying to develop the technology to synthesize spin crossover solids in chip-based droplet microfluidic systems. Part 1 describes the current state of the art of droplet-based microfluidics and spin crossover and presents an outline of this thesis. Part 2 presents our work from the narrative of microfluidics and describes our experiments that did not involve the use of reactants. Finally, part 3 describes our experience when our devices are used with reactive flows.

## References.

- 1 C.-M. Jureschi, J. Linares, A. Boulmaali, P. Dahoo, A. Rotaru and Y. Garcia, *Sensors*, 2016, **16**, 187.
- 2 D. Gao, Y. Liu, B. Miao, C. Wei, J.-G. Ma, P. Cheng and G.-M. Yang, *Inorg. Chem.*, 2018, **57**, 12475–12479.
- 3 C. Bartual-Murgui, A. Akou, C. Thibault, G. Molnár, C. Vieu, L. Salmon and A. Bousseksou, *J. Mater. Chem. C*, 2015, **3**, 1277–1285.
- 4 I.-R. Jeon, J. G. Park, C. R. Haney and T. D. Harris, *Chem. Sci.*, 2014, **5**, 2461–2465.
- 5 A. Holovchenko, J. Dugay, M. Giménez-Marqués, R. Torres-Cavanillas, E. Coronado and H. S. J. van der Zant, *Adv. Mater.*, 2016, **28**, 7228–7233.
- 6 P. Gütllich, H. A. Goodwin and Y. Garcia, *Spin Crossover in Transition Metal Compounds I*, Springer, 2004.

# Part 1. Basic concepts of microfluidics and spin crossover.

## *Introduction.*

At first glance, microfluidics and spin crossover seem like very distant fields. On one side, microfluidics is the “*science and technology of systems that process or manipulate small ( $10^{-9}$  to  $10^{-18}$  litres) amounts of fluids, using channels with dimensions of tens to hundreds of micrometres.*”<sup>1</sup>

Microfluidics is applied in many different fields (especially in biology and chemistry) and has many branches. One of them is droplet microfluidics, where microscopic channels carry a stream of droplets made of a liquid that are carried by and separated from each other by another fluid. ***Chip-based droplet microfluidics let us engineer the production and manipulation of microscopic droplets and to control the flows inside of them in a very accurate and reproducible way. These droplets can be used as microreactors to carry reactions where the reaction environment is exceptionally well-controlled.***

On the other side, spin crossover is phenomenon that occurs in some transition metal ions, which can be described at different levels of complexity. Basically, materials exhibiting spin crossover have a switching behavior, characterized by a change in the electronic configuration of the electrons in their  $3d$  orbitals. ***Spin crossover is a process that involves low amounts of energy and in some compounds, it occurs in a cooperative way. The behavior of such systems is very sensitive to macroscopic features of the material, especially to the particle size. Since these features depend on the method of synthesis, the reaction conditions of spin crossover materials can affect their properties.***

Spin crossover is approached by a scientific field named molecular magnetism, which aims to “*design molecular systems that exhibit predictable magnetic properties.*”<sup>2</sup> Following such goal, in this PhD project, we explore the use of microfluidics in the synthesis of switchable molecular materials for the first time. We believe that the high degree of control offered by droplet microfluidics is a great platform to engineer the reaction environment where the synthesis of spin crossover materials is performed. This way, it enables the synthesis of solid switchable materials in a reproducible and controlled way, and therefore the product should display reproducible and predictable properties. To fully understand the strategy we developed to achieve this ambitious goal, this first part presents the basics concepts of both microfluidics and spin crossover phenomenon.

In chapter 1, we explain the main aspects about chip-based droplet microfluidics. Here, we want to introduce the reader into the non-intuitive behavior of liquids flowing through microscopic channels. We write about the specific case when microfluidics is used to generate a stream of droplets of water that are carried by a flow of oil. We describe the behavior of the flows inside the navigating droplets, as well as some methods to influence these flows. Finally, we describe how these droplets are produced and give a general introduction to the pressure oscillations in these systems.

In chapter 2, we describe the main aspects about spin crossover. Here we want to show the reader the switching behavior of spin crossover materials, as well as the main models to understand the phenomena underneath. We explain spin crossover from the scope of the ligand field theory, and we invite the reader to see spin crossover from a diversity of logical frames. We briefly describe some models that grow in complexity and we finally explain why nanoparticles of spin crossover materials display a different behavior from the micrometric particles

## Chapter 1.1 Fundamentals of microfluidic synthesis.

Turbulence is quite present in our everyday life. From the soft chaotic movement of the smoke coming from an incense, to the catastrophic hurricanes and tornados, and in the invisible forces that shake the airplane as we fasten our seatbelts and try to relax. A precise definition of turbulence can be complicated but in general, a flow is turbulent when it moves in unpredictable ways.<sup>3</sup> In fact, chemists are so habituated to this unpredictability (in the motion inside beakers and test tubes, in the magnetically stirred Schlenk tubes and sonication baths) that it is invisible to our overindulged (mis)conception of the physical world. We do not think about turbulence in our everyday life anymore. So, what if we could eliminate this turbulence and see if the chemical universe that we claim to understand really behaves according to the notions we developed neglecting such unpredictable movements? The interest for carrying reactions in microfluidic systems originates from a general tendency of fluids: When they flow through narrow channels, they do it without any turbulence. This is the laminar flow shown in figure 1.1.

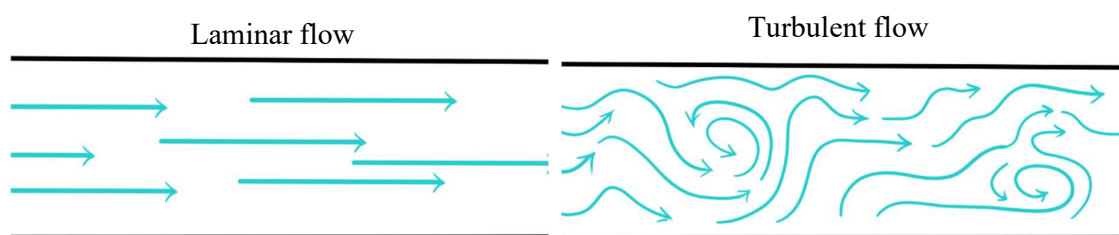


**Figure 1.1.** Laminar and turbulent flows.

The statement that flows in narrow channels are laminar is clearly not a universal law (or at least, not a rule that can be applied to all fluids with the same rigor); nevertheless, there is a simple parameter that vaguely predicts whether a flow will occur in a laminar or in a turbulent way, i.e. the Reynolds number (eq. 1.1). This non-dimensional number describes the ratio of the inertial over the viscous forces that act on the fluid inside the channel (or pipe, tube, etc.). Whenever the Reynolds number is lower than a threshold (which some authors claim to be close to 2300 for practical applications),<sup>4</sup> a laminar flow is to be expected. Otherwise, a turbulent flow is predicted:

$$\text{Re} = \frac{\rho u L}{\mu} = \frac{u L}{\nu} \quad (1.1)$$

Here,  $\rho$  is the density of the fluid,  $u$  is its linear speed and  $L$  is the hydraulic diameter of the channel, while  $\mu$  and  $\nu$  are the dynamic and kinematic viscosities, respectively.

### 1.1.1 The two approaches to carry reactions using microfluidic process.

So far, there are strictly only two approaches to carry reactions in chip-based microfluidics systems: *Continuous* or *segmented* flow microfluidics.

Exploiting the laminar prevalence in the flows across microscopic channels, the *continuous-flow* approach in microfluidic synthesis is based on controlling the reaction conditions in a specific region of the system (called the reaction-diffusion environment or RD environment).<sup>5,6</sup> To generate an RD environment, two (or more) flows of solutions with reactants are set to run side by side along the same channel. Additionally, flows of pure solvent can be set to run parallel to the reactants along the space between the side walls of the channel and the flows of reactants, as shown in figure 1.2. Here, the reactants enter in contact with each other only through lateral diffusion. Many features in these areas can be influenced by external factors (like the temperature or the selected flow rates), which can be modulated and engineered.

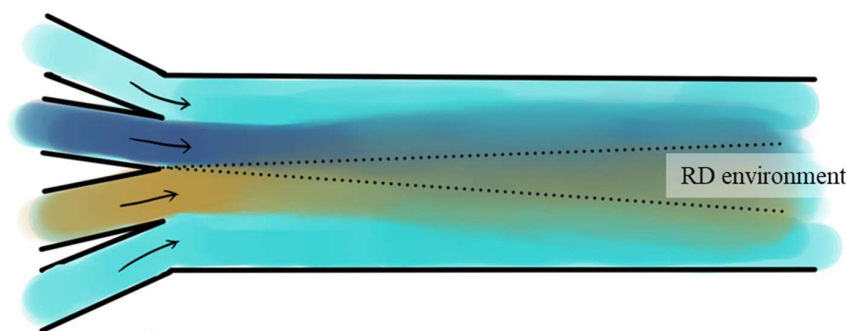


**Figure. 1.2.** Continuous flow device developed by Puigmarti-Luis *et al.* to perform the synthesis of TTF-Au composite under controlled reaction-diffusion conditions.<sup>6</sup> The clear blue color represents the pure solvent, while the deep blue and yellow colors represent the solutions with reactants.

For example, using a continuous flow device like the one on figure 1.2, Puigmarti-Luis *et al.* synthesized a TTF-Au composite.<sup>6</sup> They showed that a change in the ratio of the flow rates of the solution of pure solvent with respect to the flow rates of the solutions with reactants induced changes in the structural features of the obtained product.

In fact, the impact that continuous flow microfluidics can have on a reaction depends on the reaction itself: On whether the mixing speed of reactants can have an impact on the features of the reaction product. Clearly, in some reactions this effect is null. Nevertheless, at the present day, already enough examples exist to justify the interest in using these methods. Especially, since it allows the synthesis of solids, where the shape of the particles is rationally chosen, and because it permits obtaining metastable products.

The second approach, called *segmented flow microfluidics*, is mainly based on carrying out the reactions inside microscopic droplets of water that are separated from each other and carried by a flow of oil, as shown in figure 1.3. Let us clarify two aspects of the nomenclature in this thesis. First, in all the following figures, water will be represented in light blue and

second, here “oil” only means a liquid that is not miscible with water (like silicon oil, mineral oil or fluorinated hydrocarbons), and along this text, the term “oil” will be used to express low-viscosity mineral oil unless expressed otherwise.

In many aspects, segmented flow microfluidics is the opposite to continuous flow synthesis. First, even if here the fluids are contained inside narrow channels (below 200  $\mu\text{m}$  wide), and they are used in operating conditions under which the Reynolds number predicts nothing but a laminar flow, a set of secondary fluxes appears inside each droplet carried along the channel (explained in section 1.1.3).<sup>7-17</sup> These fluxes can help to accelerate the mixing of reactants, leading to relatively fast mixing rates. Additionally, the surface area-to-volume ratio (which is inversely proportional to the droplet diameter) is remarkably high in microscopic droplets, especially when compared with the conventional reactors in chemistry laboratories, like Erlenmeyer flasks, test tubes or beakers. This is relevant, first because high surface-to-volume ratios facilitate the heat transfer between the droplet and its surroundings; but more importantly, because the flows inside the droplets allow a fast mixing, as well as a quick mass and heat transfer in the droplet.<sup>18,19</sup>

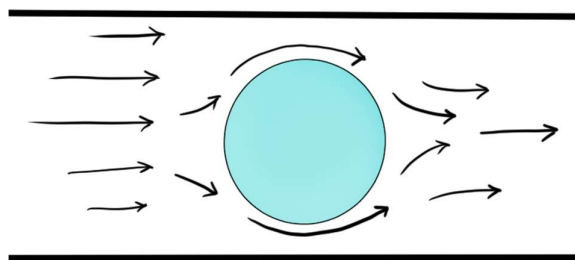


**Figure 1.3.** Archetypical segmented flow microfluidic configuration comprising a channel through which oil separates and carries droplets of water.

Additionally, if two solutions are located at each hemisphere of the droplet, the interface area-to-volume ratio between them is very high as well, facilitating their mixing through diffusion. Many phenomena appearing in segmented flow microfluidics contradict intuitive thinking. To understand them, it is mandatory to explain some fundamental concepts of fluid dynamics of incompressible flows.

### *1.1.2 Flow profiles of a liquid flowing along a channel.*

There are attractive interactions between the walls of a channel and the molecules of a liquid flowing along it that depend on the nature of both materials (dipole moments, polarizabilities, etc.). Since the molecules that form the walls of the channel have a fixed position (contrary to the molecules of the liquid flowing along the channel), there is a difference in the linear speed between them and the molecules of the fluid. These attractive interactions hinder the advance of the molecules of the fluid next to the walls of the channel. The closer to the channel’s wall, the higher this hindrance, so molecules further away from the walls are progressively less affected by this. This leads to different linear flow speeds of the fluid across the channel, which

start from a minimum next to the boundaries of the channel and find a maximum in the center of it (figure 1.4). In other words, the interaction between the molecules of the fluid phase and the walls of the channel, combined with the interaction between the molecules themselves leads to the existence of a gradient of flow velocities across the channels. This flow profile is modelled as a parabola because in a circular channel, a laminar flow is parabolic in its nature.<sup>4</sup> Here, it will be presented exclusively as a conceptual element to understand further phenomena.

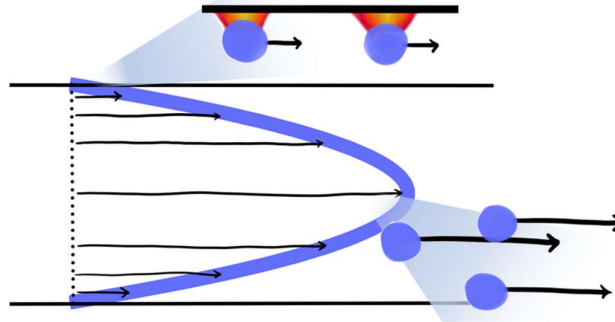


**Figure 1.4.** Parabolic flow profile (purple) of oil in a channel. On the upper side, a zoom of the molecules next to the wall. On the lower-right side, a zoom of the fast molecules without interaction with the walls of the channel. The linear flow speed at each point is qualitatively represented with the length of the arrows.

It should be noted, that the linear flow speeds in microfluidics (in the order of centimeters per second) are negligible with respect to the speed of sound in oil or water (above one thousand meters per second).<sup>20</sup> Since the compression waves in these fluids are so much faster than their linear flow speed, they should be treated as incompressible fluids. Due to the conservation of mass (which here implies also a volume conservation due to the incompressibility of the fluids), the flow that crosses a rigid and unbranched channel is constant and independent from its size, the pressure in it or its pressure gradient. In other words, if an imaginary plane is placed across the channel (occupying its whole cross-section), the integral of the linear flow speed of the fluid across the plane should be equal to the flow of fluid entering the channel.

In branched channels, the initial flow is divided into each of its branches. Here, the addition of the flow of all branches remains constant and equal to the flow of fluid entering the initial channel. The exact flow entering each branch depends on their corresponding fluidic resistance and can be calculated according to the electronic-hydraulic analogy. This means that the same equations used to calculate voltage and current in electronics can be applied in microfluidics by replacing voltage by pressure (P), charge by volume (V); and obviously, current by flow rate (Q). Just like in electronics there are power sources with constant voltage, and power sources with constant current, in microfluidics there are pumps of constant flow and pumps of constant pressure. For example, suppose the case where a pump of constant flow is used to introduce a flow Q into the branched system shown in figure 1.5.

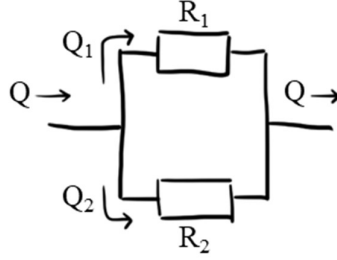


**Figure 1.5.** Branched system to illustrate the electronic-hydraulic analogy.  $Q$  is the total flow,  $Q_1$  and  $Q_2$  are the flows passing through each branch, while  $R_1$  and  $R_2$  are their corresponding hydraulic resistances.

Here, an initial flow is divided into two channels that have a different fluidic resistance (which here will be equivalent to the presence of a resistor in electronics) and finally both channels meet towards the outlet of the chip. To calculate the flow in each of the branches, first we need to consider that the electronic-hydraulic analogy transforms the Ohm's law ( $U = RI$ ) into the following:

$$P = RQ \quad (1.2)$$

Here  $P$  is the pressure drop over the system,  $R$  is the fluidic resistance and  $Q$  is the flow.

Now consider that using the same analogy, the resistance in parallel systems such as the one presented in figure 1.5 is equal to:

$$\frac{1}{R} = \frac{1}{R_1} + \frac{1}{R_2} \quad (1.3)$$

Where  $R_1$  and  $R_2$  are the numeric values of the fluidic resistances along channels 1 and 2 respectively. Combining these equations, we deduce that the pressure drop in the system equals:

$$P = \frac{R_1 R_2}{R_1 + R_2} Q \quad (1.4)$$

From the electronic-hydraulic analogy, we easily deduce that the pressure difference on both branches is the same, so applying equation 1.2 on each branch, we obtain:

$$Q_1 = \frac{P}{R_1} = \frac{R_2}{R_1 + R_2} Q \quad (1.5)$$

$$Q_2 = \frac{P}{R_2} = \frac{R_1}{R_1 + R_2} Q \quad (1.6)$$

The flow resistance here mentioned is a very important concept in microfluidics because, given a certain flow rate, it allows the calculation of the pressure difference between a given point inside of a chip and its surroundings, the pressure difference between the entrance and exit of the fluids in a channel, or even the pressure difference between two arbitrary points inside the chip. In a straight channel, the pressure difference between two points can be calculated according to different models, which differ in precision and computational costs.

Commonly, the equation used to calculate the hydraulic resistance in microfluidics in rectangular channels with a laminar flow is the following:<sup>21</sup>

$$\frac{P}{Q} = \frac{12\mu L}{wh^3 \left[ 1 - 0.63 \frac{h}{w} \tanh\left(1.57 \frac{w}{h}\right) \right]} \quad (1.7)$$

Here,  $h$  and  $w$  are the height and the width of the channel. Note that these parameters are not exchangeable, in contradiction with common sense. Instead, this equation only applies to channels where the width is larger than the height. If the channels height is larger than its width, these terms should be exchanged, and both values are set to be equal in a square channel. Whenever the importance of a precise value of the hydraulic resistance compensates the computational cost, more precise models can be found in the literature.<sup>22</sup>

The phenomena here described have important consequences in microfluidics. For instance, the flow profile of oil flowing across a channel carrying a stream of droplets will influence some external parameter of the droplets, like their speed and their distance to the walls,<sup>23</sup> but it will also influence the internal parameter, i.e. their internal fluxes. Moreover, the maximum pressure that a chip fabricated by the PDMS-on-PDMS method can take is around 4 atm, so the design of microfluidic chips is restrained by their fluidic resistance and the operating conditions they are expected to work under.

### *1.1.3 The droplet as a reactor.*

Droplets in segmented flow microfluidic synthesis are generally made of aqueous solutions carried by and separated from each other by oil. Water and oil can, however, be changed by any pair of solvents that are not miscible and are compatible with the material of the chip. The speed at which the droplet moves along the channel depends on its size and the dimensions of the droplet.

The speed of the droplet depends on the drag force that oil exerts on the droplet, accelerating it from  $v_{droplet} = 0$  to its equilibrium speed. Under the conditions usually used in microfluidics (when  $10^{-4} < Re < 0.2$ ), this drag force can be approximated according to the Stokes drag:<sup>23</sup>

$$F_{Drag} = 3\pi\mu a v_t \quad (1.8)$$

Here,  $\mu$  is the viscosity of the oil,  $a$  is the diameter of the droplet and  $v_t$  is the relative velocity of the oil with respect to the droplet.

In all cases, the speed of the droplet cannot be faster than the average linear flow speed of the carrier oil in the region of the channel it occupies, as shown in figure 1.6. In an analogous way, the speed at which a sailing ship navigates depends on the speed of the wind and the size of the sail but cannot be faster than the average linear speed of the wind that drags it forward.

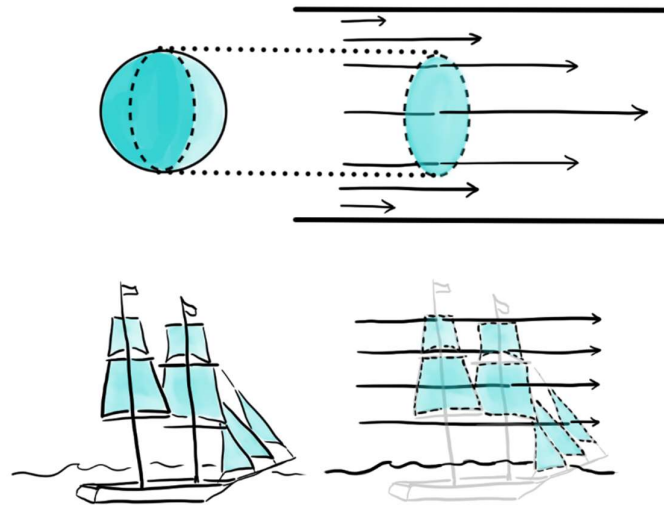


**Figure 1.6.** Drag force that the flow of oil acts on the droplets of water in a microfluidic device compared with the drag force that the wind acts on the sails of a ship.

At the beginning of section 1.1.2, it was explained that next to the walls of the chip, the molecular interactions between the wall and the oil lead to a reduction in its linear flow speed. In an analogous way, the molecules in the interface between the droplet of water and the carrying oil have attractive interactions. Therefore, any difference in linear flow velocities between both sides of this interface leads to additional currents on both of its sides (i.e. inside and between the droplets).

These fluxes form patterns that depend on different factors, which many groups have analyzed using theoretical and experimental approaches. A detailed description of the internal flow of droplets in microfluidics can be found in literature.<sup>7-16</sup> In general, if gravity is neglected and the droplets are arranged in a single stream moving along the center of a straight channel without contact with each other, then the flux patterns inside the droplet will have the same planes of symmetry as the channel that carries them. For example, if droplets move in the  $x$  direction along the center of a channel that has a plane of symmetry (the  $x$ - $z$  plane), the fluxes inside them are symmetrical with respect to the same plane. Figure 1.7 shows such a case. It must be considered that the actual magnitude and direction of the currents inside such a droplet depend on the difference in the linear speeds between the droplet and the oil around it.

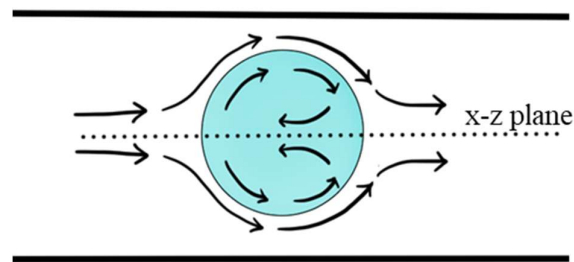


**Figure 1.7.** ‘Symmetry problem’ of the mixing in a droplet traveling in the center of a straight channel, highlighting the  $x$ - $z$  symmetry plane.

The presence of a x-z plane of symmetry in the channel is especially problematic for chemical synthesis in droplet microfluidics. For the reaction to occur inside a droplet containing two solutions of reactants on each side of the x-z plane, as shown in figure 1.7, it is necessary that the reactants enter in contact either by mixing or through the diffusion of the chemical species across the droplet. Nevertheless, if the fluxes inside the droplet contain a x-z plane of symmetry, the fluxes across this plane are forbidden by symmetry, and this means that the only way the reactants can cross the mirror plane and enter in contact is through diffusion. Since this is a major concern in droplet microfluidics, it will be named here as *the symmetry problem*.

To solve the symmetry problem different approaches have been proposed. Here is a summary of the most important ones:

- Channel asymmetry: Introduction of curvatures or obstacles in the channel that eliminate its x-z mirror plane.<sup>24</sup> Figure 1.8A.
- Perpendicular droplet generation: The use of a T-junction where oil follows a straight path and the liquid containing the reactants intercepts it laterally, distributing all reactants on both sides of the mirror plane.<sup>25,26</sup> Figure 1.8B.
- Chaotic mixing through obstacles: Building an obstacle that breaks the x-y mirror plane and induces a set of asymmetrical fluxes inside the droplet.<sup>27</sup> Figure 1.8C.
- Out-of-center droplets: Generating droplets that do not move along the center of the channel (which breaks the x-y plane of symmetry).<sup>15</sup> Figure 1.8D.
- Droplet merging: instead of combining the reactants before the droplet generation, generating two independent droplets, each one with a solution of reactants, and merging them leads to a quick mixing of both. A deeper discussion of this subject can be found in part 2 of this manuscript.

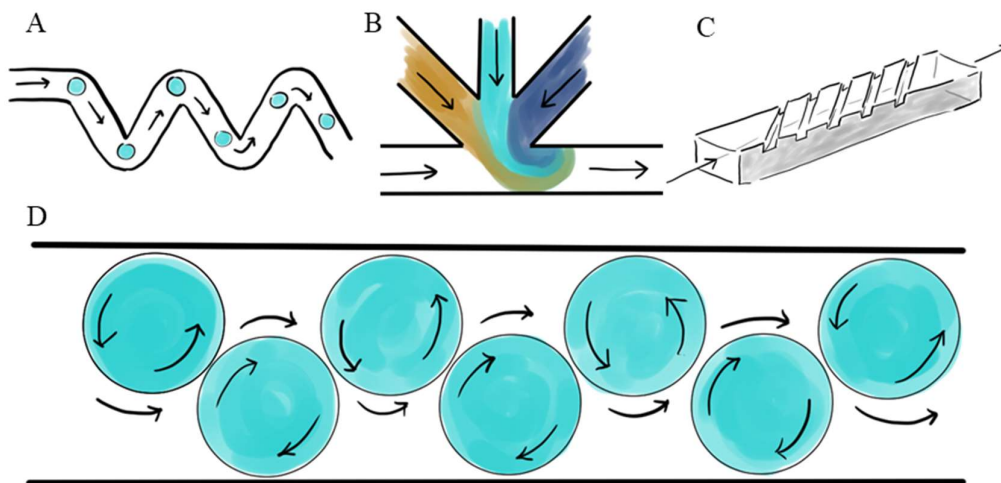


**Figure 1.8.** The most important methods to solve the symmetry problem in microfluidics.

Finally, it is worth mentioning that the internal fluxes in droplets are highly reproducible. This means that microfluidics can be particularly attractive in carrying reactions that are very sensitive to the mixing conditions. Moreover, as our understating of the factor

governing the internal fluxes inside droplets grows, so does our capability to predict and engineer them. This is particularly interesting in the synthesis of switchable materials because their properties depend on the shape and size of their particles, as well as on the presence of defects in the crystals (see chapter 2 of this part). Such features are difficult to control, engineer or even reproduce with conventional methods, so microfluidics could have great applications in that field.

### 1.1.4 Droplet generation.

The methods used to generate droplets in microfluidic systems are commonly divided into two categories: *Passive* and *active*. The difference between them relies on the absence or presence of an external input of energy for the generation of the droplets. If the droplets are generated only through the forces that put the fluids in motion (syringe pumps, pressure regulators, etc.) they are said to be *passive*. If additional energy inputs are used (electric, mechanical or laser pulses, centrifugal force, changes in temperature, etc.), they are called *active* methods.<sup>28</sup>

Adjusting the properties of the flows of liquids (like the surface tension, viscosity or flow rates) tends to be considered as an active method.<sup>28</sup> Nevertheless, this claim could be questioned since no additional energy input is used here. Literature about active droplet generation methods is easy to find<sup>28</sup> and here, only the passive methods will be presented.

The two most frequently used geometries to generate droplets in microfluidics are T-junctions and flow-focusing configurations as shown in figure 1.9. Other configurations like co-flow and K-junctions can be found in literature,<sup>28</sup> but they are rarely used in chip microfluidics. Typically, in T-junctions, a straight flow of mineral oil is intercepted perpendicularly by a flow of water; while in flow-focusing junctions, a straight flow of water is intercepted laterally by two flows of oil. The nomenclature of the droplet generators used here is presented in figure 1.9. Both junctions will comprise one water-inlet, one or two oil-inlet and one exit channel.

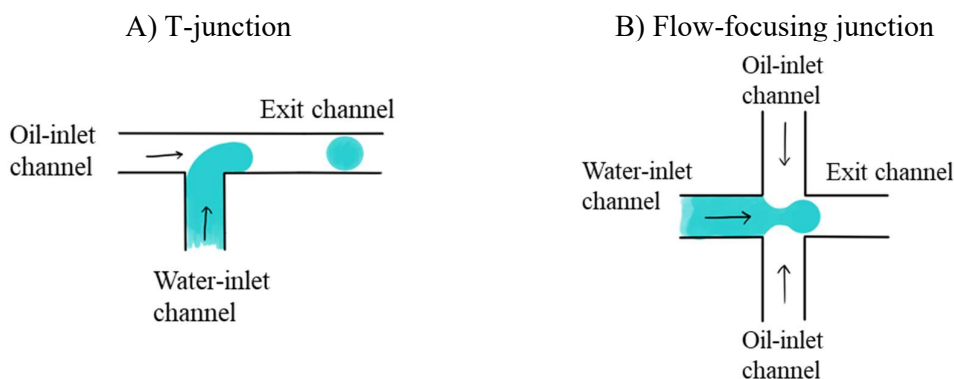


**Figure 1.9.** Geometry of T- (A) and flow-focusing (B) junctions.

In both configurations there are different mechanisms under which the droplets can be generated. So far, 5 mechanisms for the generation of droplets in microfluidic devices have been evidenced,<sup>28</sup> but only three will be discussed here: Squeezing, dripping and jetting (shown in figure 1.10 for a T-junction and in figure 1.11 for a flow-focusing junction).

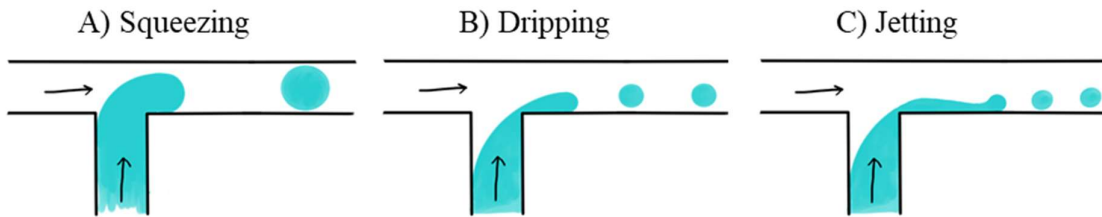


**Figure 1.10.** Droplet generation in the squeezing (A), dripping (B) and jetting (C) regimes in a T-junction.

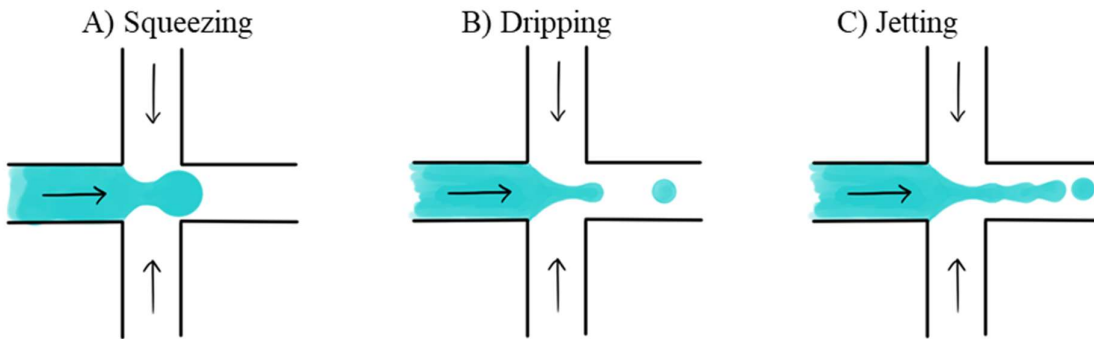


**Figure 1.11.** Droplet generation in the squeezing (A), dripping (B) and jetting (C) regimes in a flow-focusing junction.

In a T-junction, the squeezing mechanism (also called “geometric mechanism”) starts with the water advancing inside the oil-inlet channel. Since water occupies a portion of the transversal area of the channel, the space through which oil can flow is reduced. Since the flow resistance depends on the geometry of the channel carrying the fluid (see section 1.1.2), the partial occupation of the space in the channel by the incoming water leads to an increase in the fluidic resistance, and therefore, in the pressure as well. At some point, the water occupies the whole transversal area of the channel. Exactly here, the accumulated pressure detaches the portion of water that already entered the oil-inlet channel. After detachment of the droplet, the pressure is suddenly reduced because oil can again flow across the whole cross-section area of the exit channel.<sup>29-31</sup> This increase and sudden fall in pressure is a source of pressure and flow oscillations in the chip as shown in figure 1.12.

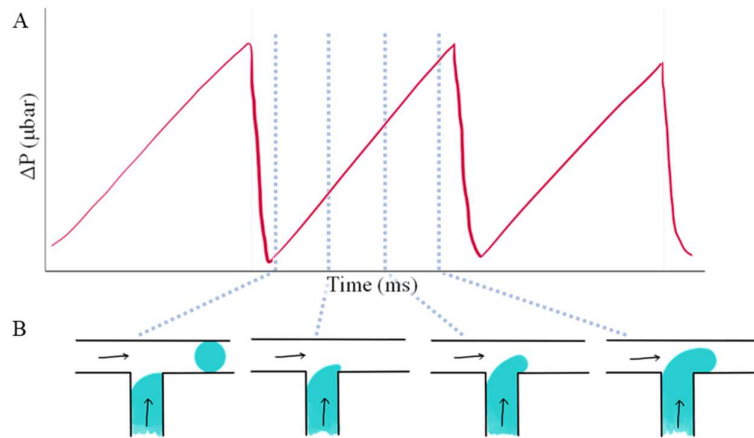


**Figure 1.12.** Pressure oscillations due to the formation of droplets (A), and state of the junction at different moments of the formation of droplets through a squeezing mechanism (B).

Flow-focusing configurations can also operate through the squeezing mechanism as depicted in figure 1.11. Since in this mechanism the droplet is detached when it completely occupies the cross-section of the channel, its dimensions depend mainly on the dimensions of the channels. This is the reason why it is also named *geometrical mechanism*. In the face of a change in flow rates of oil or its viscosity, the dimensions of the droplets marginally change.<sup>32</sup> This fact leads to serious difficulties in the modulation of the dimensions of droplets generated via this mechanism, as is discussed in part 2.

The dripping mechanism appears when the flow of oil is increased to a critical point where the drag force generated by the oil over the water entering the oil-inlet channel is high enough to detach it before it completely occupies the whole channel cross-section. In other words, while in the squeezing mechanism the droplet of water is detached when it covers the whole cross-section area of the exit channel; in the dripping mechanisms the droplet of water is detached before, as shown in figure 1.10B.

The dimensions of the droplets generated in the dripping mechanism depend on the ease to detach the droplets from its originating flow. In other words, as the droplet is formed, the breaking moment depends on the balance between two forces. On one side, the force that the oil exerts on the droplet as it grows (occupying the transversal area of the exit channel) and, on the other side, the surface tension that opposes the break of the front of water. The first of these forces depends on the drag force that the oil exerts on the water. The second one, on the interfacial tension between water and oil. So, it is intuitive that the droplet size should depend on the ratio of both forces.

There are different equations to predict the droplet size generated under this mechanism at different computational costs,<sup>32–34</sup> but the easiest equation that can predict the change in the diameter (D) of the droplet is to correlate it with the inverse of the capillary number of the continuous phase:<sup>35</sup>

$$D \approx a + b \frac{1}{Ca} \quad (1.9)$$

Here,  $a$  and  $b$  are empirical parameters and  $Ca$  is the capillary number of the continuous phase, which is a dimensionless number related with the coefficient between the viscous force and the interfacial tension between water and oil:

$$Ca = \frac{\mu u}{\gamma} \quad (1.10)$$

where,  $\mu$  is the dynamic shear viscosity,  $u$  is its linear flow speed of the continuous phase (its average across the channel) and  $\gamma$  is the interfacial tension between oil and water.

Some intuitive conclusions can be easily taken from this model:

- The increase in the interfacial tension ( $\gamma$ ) results in the expansion of the droplet diameter ( $dD/d\gamma > 0$ ). Reducing the interfacial tension (for example by adding surfactants to the oil) results in smaller droplets.
- Increasing the linear flow speed of oil ( $u$ ) results in a decrease in the droplet diameter, for example by increasing the flow rate of oil ( $dD/du < 0$ ).
- The use of more viscous oils (increase in  $\eta$ ) results in smaller droplets ( $dD/d\eta < 0$ ).

According to Shui *et al.*<sup>36</sup> and Zhu *et al.*,<sup>37</sup> the capillary number is even useful to predict the mechanism of generation of droplets. Inspecting the behavior of a microfluidic system in a T-junction<sup>36</sup> and co-flow configuration<sup>37</sup> at different flow rates, both research groups found clear boundaries dividing the regimes where droplets are formed *via* a squeezing, a dripping or a jetting mechanism. For example, as an approximation, Zhu *et al.*<sup>37</sup> explain that when the capillary number of the continuous phase is below 0.1, a squeezing mechanism is expected. At values of  $Ca$  of the continuous phase between 0.1 and a 0.35, a dripping mechanism is predicted.

The pressure oscillations generated through the dripping mechanism should be smaller than those formed through squeezing because, contrary to the case of squeezing, the droplet here never occupies the whole cross-section area of the channel. Nevertheless, since the cross-section area of the channel is partially occupied by water as the droplets are formed, the fluidic resistance of the oil flowing in the channel is cyclically changed as well. Therefore, pressure oscillations are still present in this case.

The third mechanism presented here is jetting. This mechanism appears at high linear flow speeds of mineral oil, when the drag force of oil causes a strong elongation in the front of water (forming a jet), and multiple breaking points appear, as shown in figure 1.10C. For microfluidic synthesis of solids, this mechanism is to be avoided because: (i) since multiple breaking points are formed, the size of the droplets are highly dispersed; (ii) because of the chaotic nature of the formation of droplets, its average diameter is difficult to modulate; (iii) finally, if two solutions of reactants encounter inside a jet (and the reaction product is a solid), there are high chances that the precipitate will form an aggregate large enough to clog the channel.

Clearly, the dripping mechanisms is the most convenient to generate droplets for chemical reactions due to the ease to modulate the droplet dimensions and its low size

dispersity. Even so, the proper generation of droplets requires special attention in the experimental settings to ensure minimal perturbations in the flow.

### 1.1.5 Pressure oscillations.

Under ideal conditions, the only source of oscillations in the pressure and flow in a droplet microfluidics system comes from the droplet generation (explained previously). Nevertheless, there are additional sources of pressure oscillations that can affect the generation frequency of droplets and therefore contribute to the dispersion in the droplet sizes. The first one is clearly the acoustic pollution present in all chemistry laboratories (coming from extractors, people walking by or talking, and so on). Further on, displacement pumps always have pulsations, even if it is not explicitly explained by the producer. This is because the movement of the pistons in syringe pumps is generated by the rotation of electric motors, as exemplified in figure 1.13.

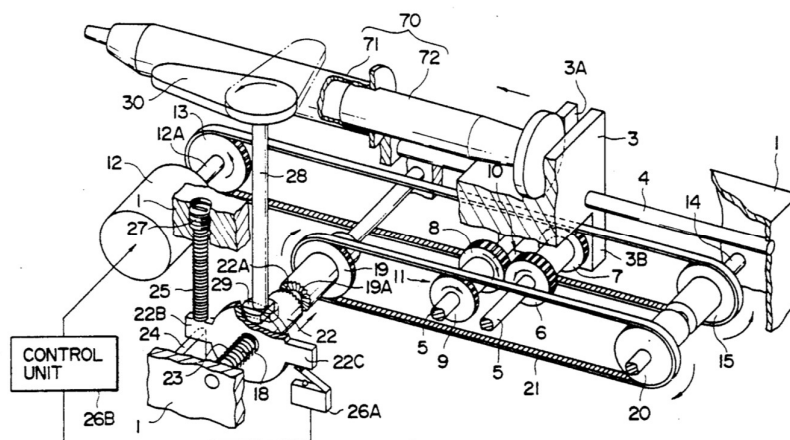


**Figure 1.13.** Example of the functioning of a syringe pump as presented in the patent US 5,176,646A.<sup>38</sup> The stepper motor (number 12) is attached to the control unit. As the motor rotates, it puts a set of pieces into motion, which translates into the movement of the piston of the syringe.

The motors chosen for these applications are usually stepper motors because they allow a very precise movement compared with DC motors or continuous rotation servo-motors. For instance, a conventional DC motor comprising 2 magnets and 3 electromagnets, would lead to 6 pulsations in the torque per revolution (or a pulsation every 60 degrees). This pulsation of rotation of the motor is translated into a pulsation of the piston in the syringe, and finally it results in a pulsation in the flow of the corresponding liquid inside the microfluidic chip. The precise magnitude of this pulsation will depend on the gearbox used by the pump and the syringe size (or more precisely, its internal cross-section area). Nevertheless, it is obvious that the smaller the pulsations in the rotation of the motor, the smaller the pulsations in the flow inside the chip. In this sense, stepper motors (as the one shown in figure 1.14) are unchallenged.

For example, accurate stepper motors in the market, like the motor 42BYGHM809 of JiangSu WanTai Motor co.,Ltd<sup>39</sup> can make 400 steps per turn, and it can be controlled with a AMIS-30543 driver (fabricated by ON semiconductor)<sup>40</sup> that allows an accuracy of 128 pseudo-steps per step. These two parts ensembled together could be used to reach 51 200 pseudo-steps per turn. This is equivalent to a pulsation every 0.00703125 degrees (8500 times smaller than with a conventional DC motor).



*Figure 1.14. Conventional stepper motor.*

Whenever a displacement pump is used, it must be considered that the pulsations involve a sudden movement of the piston of the syringe. The amount of matter released in each pulsation is proportional to the cross-section area of the syringe. This means that flow pulsations are stronger in wider syringes. Some pumps have additional mechanisms to dampen the pulsations, like the use of flexible shaft couplers. In those devices, small pulsations of high frequency pulsations are easier to dampen than those with low frequencies and big volumes. In fact, these mechanisms can only dampen pulsations above a critical frequency. This is the reason why producers of syringe pumps specify a set of minimum flow rates to ensure a “pulsation free” flow, and why these minimum flow rates depend on the syringe diameter.<sup>41</sup>

Nowadays, pumps that generate flows with a constant pressure can be found in the market. In such devices, the flow rates are those that correspond to the pressure set on the system. Fortunately, these devices can be coupled with a flow sensor to adjust the pressure automatically and maintain a constant flow. The pressure oscillations using these systems do not share the same origin as those present in displacement pumps, and they might gain more importance in microfluidics as they become more accessible in terms of price, space and infrastructure requirements.

## Chapter 1.2. Fundamentals of spin crossover.

### 1.2.1 Definition and origin of spin crossover.

What is spin crossover and when it was first discovered are two questions that tend to be overlooked in the spin crossover community. The IUPAC gold book defines spin crossover the following way:<sup>42</sup>

*A type of molecular magnetism that is the result of electronic instability [...] caused by external constraints (temperature, pressure, or electromagnetic radiation), which induce structural changes at molecular and lattice levels.*

As an archetypical example, the  $[\text{Fe}(\text{2-pic})_3]\text{Cl}_2 \cdot \text{EtOH}$  compound is usually taken.<sup>42</sup> Between low temperatures (90 K) and high temperatures (298 K), the geometry of the octahedral coordination sphere of this compound strongly differs.<sup>43</sup> Figure 1.15 shows the geometry of the  $[\text{Fe}(\text{2-pic})_3]^{2+}$  ion in low- and in high-temperature states as well as the electronic configuration of their 3d orbitals.

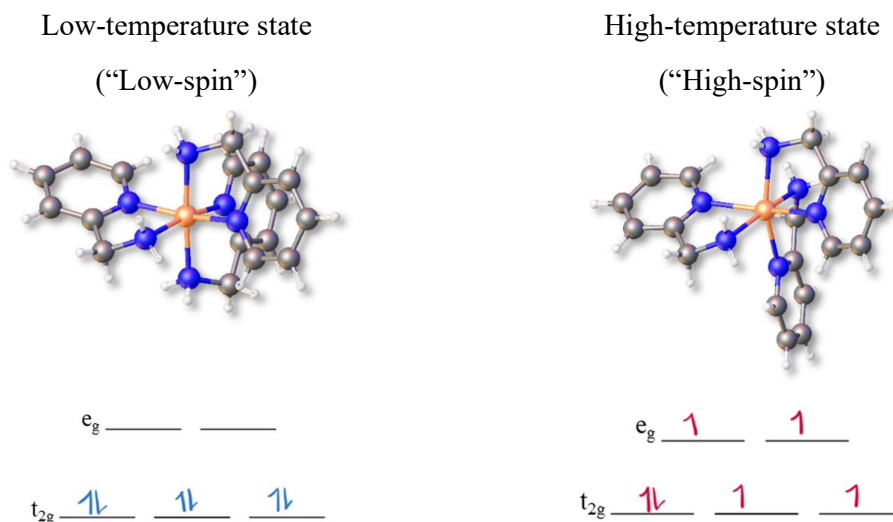


**Figure 1.15.** Comparison of the geometry and the electronic configuration of a typical Fe(II) spin crossover compound ( $[\text{Fe}(\text{2-pic})_3]\text{Cl}_2 \cdot \text{EtOH}$ ).<sup>43</sup>

When the geometry of both ions is compared, the coordination sphere of the Fe(II) in the high-temperature state is considerably more distorted and with longer Fe-N bond lengths. These geometrical changes are explained in the frame of ligand field theory (remember that in octahedral geometry, 3d ions have their orbitals split in  $t_{2g}$  and  $e_g$  levels): The  $e_g$  orbitals, partially occupied in the high-temperature state, have a more antibonding nature than the  $t_{2g}$  orbitals, leading to an increase in the bond lengths and the volume of the coordination sphere.

According to some authors,<sup>44-47</sup> the study of spin crossover started with the work of Cambi *et al.*,<sup>48</sup> where the magnetic susceptibility of some Fe(III) compounds did not obey the Curie Weiss rule. When Cambi *et al.* in 1934,<sup>48</sup> published the article, ligand field theory was not developed yet, and therefore, they tried to explain their results in terms of the previous models, i.e. by a change in the polar moments in the analyzed compounds. This explanation lacked an appropriate model. Indeed, crystal field theory had just been formulated in the early 1930's by Hans Bethe<sup>49</sup> and John van Vleck,<sup>50</sup> and ligand field theory would only be proposed in the 1950's by Griffith and Orgel<sup>51-53</sup> (two decades after Cambi *et al.* reported their results). The reason why their compounds did not obey the Curie Weiss model is because they undergo a change in their electronic configuration (since the ligand field strength around the Fe(III) ions was close to the critical value that decides whether the most stable configuration is the low-spin or the high-spin one).

The first time that spin crossover was identified as such, was in the work of R. C. Stoufer *et al.* in 1961.<sup>54</sup> There, according to the models of Orgel, Co(II) compounds could only exist in two states (there, called *spin free* and *spin paired*, that nowadays are named *high-spin* and *low-spin* states correspondingly). Nevertheless, many compounds containing Co(II) ions display magnetic moments that do not correspond to the predicted ones. Instead, their magnetic moments belong to a range of values between the two predicted ones for each state. According to Stoufer *et al.*, this apparent contradiction could be explained by the presence of both states in each sample. This way, the experimental value of the magnetic moment corresponds to the molar fraction of each state, multiplied by their corresponding magnetic moments. Motivated by the possibility that each molecule could be brought from one state to another reversibly, Stoufer *et al.* measured the magnetic susceptibility of bis-(2,6-pyridindialdihydrazone)-cobalt(II) iodide at different temperatures, showing a thermal dependence of the magnetic moment. This way, they determined the fraction of each state at different temperatures to obtain the equilibrium constant. When plotting the logarithm of the equilibrium constant as a function of  $T^{-1}$ , they obtained a straight line from which the conversion enthalpy and entropy could be determined. This was the first time that such an approach was applied, and surprisingly, this way of understanding the nature of spin crossover prevails until the present day. Figure 1.16 shows a curve of the high-spin fraction made from the data of Stoufer *et al.*<sup>54</sup>

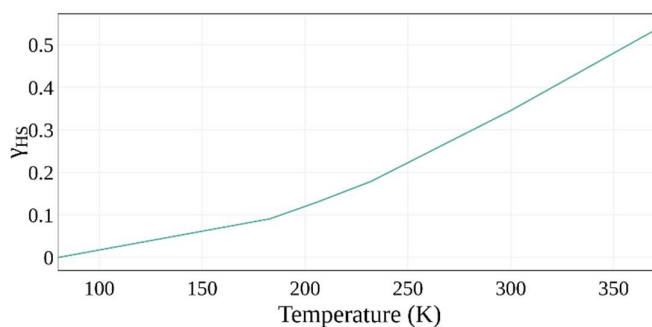


**Figure 1.16.** High-spin fraction of bis-(2,6-pyridindialdihydrazone)-cobalt(II) iodide at different temperatures built from the data of Stoufer *et al.*<sup>54</sup>

Although the definition of spin-crossover given by IUPAC suits the purposes of this thesis, it can (and eventually will) be improved. First, note that the occurrence of spin crossover obeys general thermodynamic laws, and can only happen if the Gibbs free energy permits it (since the Gibbs free energy predicts the spontaneous changes of systems when they are subjected to constant pressure and are immersed in a bath of constant temperature). Because of this, spin crossover could be triggered by any external constraint that affects the Gibbs free energy, and not only by “[...] *temperature, pressure, or electromagnetic radiation* [...]” as expressed in the definition from IUPAC. Additionally, other phenomena can easily be miscategorized as spin crossover under the definition given by IUPAC (like charge-transfer or valence tautomerism).

### *1.2.2 Multiple models to understand spin crossover.*

It is easy to understand the driving force underneath spin crossover from the perspective of the ligand field theory: When the energetic difference between the  $t_{2g}$  and  $e_g$  levels is small (weak ligand field), electrons will fill all the  $d$  orbitals before pairing; and when the difference is big, they will pair before populating all the  $d$  orbitals. So, if the energetic difference is neither too strong nor too weak, both cases can coexist, and the change from one to another can be triggered by external stimuli. How exactly this principle unveils into a macroscopic behavior is, nevertheless, a very complex phenomenon that can be described at different levels of depth, and from different points of view.

In other words, the ligand field theory is very useful when we want to understand spin crossover at the electronic and atomic levels. However, the switching behavior of spin crossover materials (observed using magnetic, optical or structural characterizations) depends on phenomena occurring at larger scales as well. This is especially important in the solid phase, where molecules are held in a crystalline network, with given symmetry elements, intermolecular interactions, domain effects and microcrystalline properties.<sup>55</sup>

According to Scott E. Page, the best way to make sense of such complex phenomena is to use the *many-model thinking* approach.<sup>56</sup> This means that we build our understanding of a phenomenon from a diversity of logical frames, where each one focusses on specific aspects of it. In our case, depending on which features we attempt to understand or predict, we should use the models that can give us useful information at an accessible computational cost. This way, our global understanding of spin crossover emerges as the intertwining of many models. Some of them describe it at the electronic level; some, at the microcrystalline; and others, beyond.

The idea of a universal (or unified) model to describe spin crossover systems can be very seducing; nevertheless, this is impossible nowadays. Why? Because the models that describe spin-crossover at the electronic level are very difficult to apply at the macroscopic level.

For instance, a well-known computational method called “self-consistent field” (also known as SCF, Hartree-Fock or HF) can be used to calculate the wave function of a system.<sup>57</sup> This method ignores some features of the wave-particle duality of electrons, but its relatively low computational cost makes it an attractive choice for calculations in quantum chemistry. This method has a scalability factor of 4, which means that the computational cost to calculate the energy of a system is proportional to  $N^4$ , where  $N$  is the number of electrons and nuclei of such system.<sup>57</sup> So, even if SCF can be used to calculate the free Gibbs energy of the spin change of a single molecule, the computational cost of calculating the hundreds of thousands of molecules in a nanoparticle would increase the computational cost at least  $10^{20}$  times.

As an example, if a given computer required 1 millisecond (which would be remarkably fast) to calculate the optimal geometry, the energy and vibration frequencies of a molecule that displays spin crossover, the time required to calculate the same variables for a nanoparticle would be around  $10^{17}$  seconds (which is comparable to the age of our universe). To reduce the computational cost, methods based on the electron density (and not the wave function) can be employed, because they have a scalability factor of 3.<sup>57</sup> These methods are called DFT (the acronym for “Density Functional Theory”) and can predict the spin crossover temperatures of individual molecules with an acceptable degree of accuracy.<sup>58</sup> Assuming the same calculation time of 1 millisecond for a single molecule, the description of a whole nanoparticle using DFT would require only  $10^{12}$  seconds, which is an impressive reduction in time but still represents more than 30 000 years.

This means that, to describe the spin crossover phenomenon, some simplifications must be done and therefore, some phenomena must be neglected. In other words, since the switching behavior of spin crossover materials is influenced by phenomena happening at different scales, we require different models to describe it at each scale.

### *1.2.3 The Non-interacting model.*

Phenomenological models have been developed first, based on thermodynamic considerations. The simplest model consists in ignoring the interactions between the spin crossover units (we will discuss what is behind the term *interactions* later). Here, each molecule is conceived as being isolated from the others, and all its properties are independent of its neighbors. All these molecules are contained inside a thermal bath at constant temperature and pressure, and are separated from each other by diathermal walls, as shown in figure 1.17. Finally, the walls that contain each spin crossover unit do not allow any magnetic interaction between them. For this reason, the emergence of ferro-, and antiferromagnetic interactions are neglected.

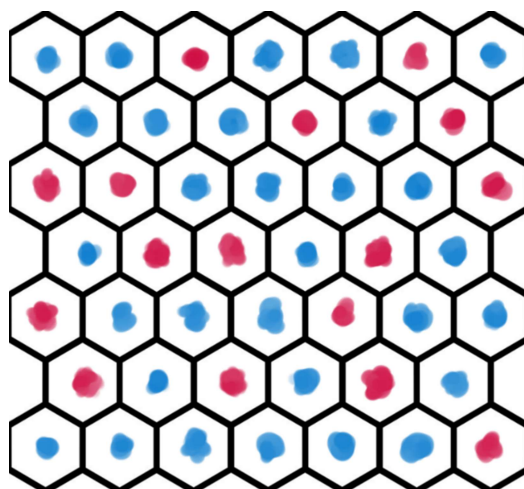


**Figure 1.17.** Lattice of spin crossover units in a non-interacting model, where the blue stains represent molecules in low-spin state, and the red ones, molecules in the high-spin state. The fraction of molecules in high-spin state is 0.35.

In this model, each molecule responds individually to the changes of its surroundings and, although they might not always all be in the same state (since some of them are in the high-spin state while others are in the low-spin one), all of them have the **same probability** of being in each state. This means that if we know the probability for a molecule to be in the high-spin state, we automatically know the fraction of molecules in the high-spin state of the sample and *vice versa*. In non-interacting systems, this probability is related to the Gibbs free energy ( $\Delta G$ ). The reaction is expressed with the low-spin (LS) state as the reactant and the high-spin state (HS) as the product (even if it could be stated inversely with the same authority).



Conventional chemical reactions reach an equilibrium when the amount of reactants and products corresponds to their equilibrium constant  $K_{eq}$ .<sup>59</sup>

$$K_{eq} = \frac{n_{HS}}{n_{LS}} = \frac{\gamma_{HS}}{\gamma_{LS}} = e^{-\frac{\Delta G}{RT}} \quad (1.12)$$

In a non-interacting system at constant pressure and temperature, the Gibbs free energy relates to the reaction enthalpy ( $\Delta H$ ) and entropy ( $\Delta S$ ).<sup>59</sup>

$$\Delta G = \Delta H - T\Delta S \quad (1.13)$$

From equation 1.12, the following equation is obtained.

$$K_{eq} + 1 = \frac{\gamma_{HS}}{\gamma_{LS}} + \frac{\gamma_{LS}}{\gamma_{LS}} = \frac{1}{\gamma_{LS}} \quad (1.14)$$

$$\gamma_{HS} = \frac{K_{eq}}{K_{eq} + 1} \quad (1.15)$$

Using these tools, we can explore the behavior of the system with a minimal amount of information measured experimentally. For instance, when the fraction of molecules in the high-

spin state is equal to the fraction in the low-spin state,  $K_{eq} = 1$ . Because of this,  $\Delta G$  is equal to zero, at an equilibrium temperature  $T_{1/2}$  (eq. 1.17).

$$K_{eq} = 1 = e^0 = e^{-\frac{\Delta G}{RT_{1/2}}} \quad (1.16)$$

$$T_{1/2} = \frac{\Delta H}{\Delta S} \quad (1.17)$$

From an experimental curve, we can extract  $\Delta H$  and  $\Delta S$  by correlating the results to the following linear model:

$$\ln(K_{eq}) = -\frac{\Delta G}{RT} = -\frac{\Delta H - T\Delta S}{RT} \quad (1.18)$$

$$-RT \ln\left(\frac{\gamma_{HS}}{\gamma_{LS}}\right) = \Delta G = \Delta H - T\Delta S \quad (1.19)$$

$$-R \ln\left(\frac{\gamma_{HS}}{1 - \gamma_{HS}}\right) = \Delta H \left(\frac{1}{T}\right) - \Delta S \quad (1.20)$$

When the left-hand side of equation 1.20 is plotted as a function of  $T^{-1}$ , if the resulting plot is a straight line, its slope should be equal to  $\Delta H$  and its intercept, to  $-\Delta S$ . Since  $\Delta H$  and  $\Delta S$  give us different information about the spin crossover process, we can use them to develop some intuitive understanding of spin crossover materials.

#### 1.2.4 The reaction enthalpy ( $\Delta H$ ).

The reaction enthalpy ( $\Delta H$ ) is related with changes in the internal energy and volume between the HS and LS states (remember that the distance and energy of the metal-ligand bonds are different in each state). Enthalpy favors the LS state, and  $\Delta H$  differs across the different spin crossover materials. In general terms,  $\Delta H$  has a value close to 16 kJ/mol (so the reaction going from LS to HS is endothermic and is favored by temperature).<sup>58</sup>

To put the energetics of the spin change in perspective, the  $\Delta H$  of this process is compared with the energy of other phenomena in figure 1.18. The magnitude of the spin crossover enthalpy is close to the energy associated with intermolecular forces of small molecules. The spin crossover process is a phenomenon of relatively low energy and therefore, spin crossover materials are sensitive towards external inputs. We can (and we will) use the non-interacting model to see how the temperature affects the Gibbs free energy, but since the spin crossover molecules are very sensitive to their environment, the non-interacting model can only be applied to a few systems, where the change in spin-state of a molecule does not involve a change in the way it interacts mechanically with its surroundings.

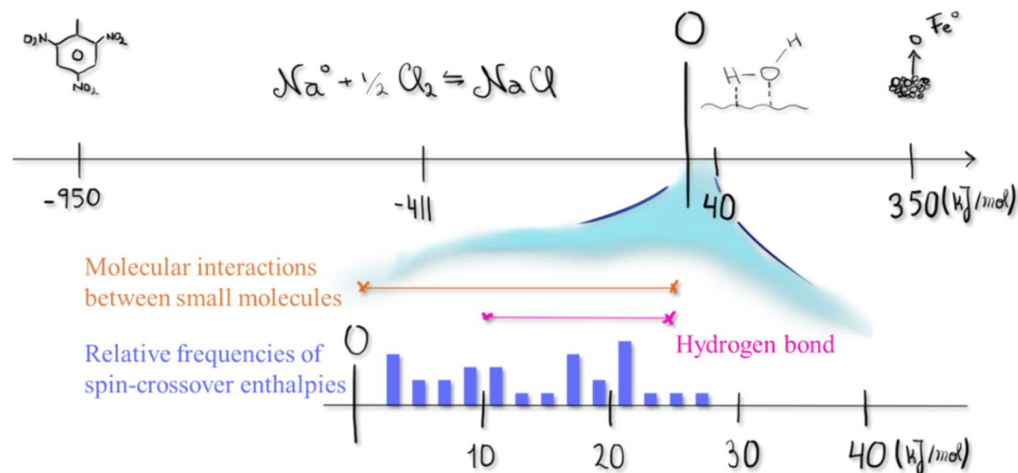


**Figure 1.18.** Comparison of the heats of reaction of different processes: detonation heat of TNT,<sup>60</sup> formation enthalpy of NaCl,<sup>60</sup> vaporization enthalpy of water<sup>61</sup> and iron<sup>62</sup> and typical energies for intermolecular interactions,<sup>63</sup> compared with a histogram of the reaction enthalpies of LS to HS changes in Fe(II) and Fe(III) compounds.<sup>58</sup>

### 1.2.5 Reaction entropy ( $\Delta S$ )

The effect of temperature on the Gibbs free energy in this model can be taken from equation 1.13. Here, it changes linearly with  $T$ , and the rate of this change is equal to  $-\Delta S$ . The entropy in the system is more abstract than the enthalpy. It is a common misconception to assume that the entropy is related to the degree of disorder of the system. This is an oversimplification because “disorder”, *per se*, only exist as an abstraction and it is impossible to assign it a numerical value.<sup>64–66</sup> Instead, entropy relates with the amount of ways it is possible to distribute matter and energy, and yet obtain the same overall thermodynamic result. In other words, even if we know the variables that describe the state of a system (like its temperature, pressure, volume, etc.), this does not tell us anything about the precise location of each atom, each electron or the energy they have. We call *microstate* to each way to arrange the same amount of mass and energy resulting in the same state. The entropy is related to the number of possible microstates of a system (or simply  $W$ ), as shown in the equation 1.21. In the following equation  $R/n$  is the universal gas constant divided by the number of particles. This equation can be found with the Boltzmann constant ( $k_B$ ) instead of  $R/n$ , but here it is convenient to express the equation this way to express the entropy in molar units (J/mol.K).

$$S = \frac{R}{n} \ln W \quad (1.21)$$

In a single spin crossover molecule,  $\Delta S$  is related with the change of the electronic configuration and how the vibration, rotation and translation modes of the molecule and the network become more (or less) accessible after the spin change, and it contributes to the spin crossover temperature as much as  $\Delta H$  itself. Indeed, since bond-lengths are different between the low-spin and the high-spin states, the vibrational modes of the coordination sphere (and consequently the whole molecule as well as the whole network) change upon spin crossover.

Since the HS state has longer bond-lengths than the LS state, its vibrational modes are more accessible and can be populated more easily, i.e. bonds can vibrate more. Due to this, the HS state has a larger entropy than the LS and  $\Delta S$  is positive, which means that the  $T\Delta S$  term of equation 1.13 favors the HS state. Note that according to equation 1.17, the spin-state conversion can only occur if  $\Delta H$  and  $\Delta S$  are of the same sign (otherwise the conversion temperature would be negative, which is impossible to reach). Remember that  $\Delta H$  is positive as well.

In solids, the entropy of the system has an additional contribution due to the diversity of ways to arrange the HS and LS molecules spatially ( $S_{Mix}$ ). Remember that entropy is related to the number of possible microstates of a system. For instance, in a solid with 100% molecules in LS (or HS) state, there is only one way to arrange them in the lattice, so  $W$  is equal to 1 and  $S_{Mix}$  is equal to zero. For all the other cases, the number of ways to arrange the HS and LS molecules in the lattice is given by the statistic combination as:

$$W = \binom{n}{n_{HS}} = \frac{n!}{n_{HS}! n_{LS}!} \quad (1.22)$$

Factorial numbers require high computation costs to be calculated, so in these cases, the Stirling's approximation is used and finally:

$$\ln W \approx (n \ln n - n) - (n_{HS} \ln n_{HS} - n_{HS}) - (n_{LS} \ln n_{LS} - n_{LS}) \quad (1.23)$$

$$\ln W \approx n \ln n - n_{HS} \ln n_{HS} - n_{LS} \ln n_{LS} \quad (1.24)$$

Where  $n$  is the total number of molecules, while  $n_{HS}$  and  $n_{LS}$  are the total number of molecules in HS and LS state correspondingly. Incorporating this equation into equation 1.24, we can easily find that  $S_{Mix}$  (molar) has the following value:

$$S_{Mix} \approx -R(\gamma_{HS} \ln \gamma_{HS} + \gamma_{LS} \ln \gamma_{LS}) \quad (1.25)$$

### 1.2.6 Interacting models part 1: Basic concepts.

Additionally to the temperature stimulus that drives the spin crossover, pressure can affect the spin state of spin crossover molecules as well, normally favoring the LS state. This can be modelled with different degrees of accuracy<sup>67</sup> but, for the purpose of this text, it is enough to clarify that the origin of this resides in the fact that molecules in LS state are smaller than those in HS. This effect of pressure is important to understand the influence of elastic interaction between spin crossover molecules inside a crystal lattice.

In a crystal, molecules are stacked into a lattice, related through symmetry elements, and organized according to weak intermolecular interactions (like hydrogen bonding,  $\pi$ -stacking, dipolar interactions and so on). All the structural changes that occur during the spin crossover, especially the anisotropic volume change, will impact the overall organization of the molecules. The molecules are thus interacting mechanically. In that sense, the non-interacting model ignores that real solids display some degree of *cooperativity*. Here, cooperative means that due to mechanical or elastic interactions between spin crossover units,

the system stops behaving as a collection of individual molecules placed together. Instead, they have a collective behavior influencing the overall spin crossover features.

In the non-interacting model, we used the term “molecule” to represent each coordination unit capable of displaying a spin-crossover conversion. While the non-interacting model can hold for molecule-based materials, that is rarely the case for coordination polymers. Coordination polymers (independently on whether they extend periodically in 1, 2 or 3 dimensions) tend to present some degree of cooperativity. For this reason, in this section the term “molecule” will be replaced by the term “spin crossover unit”. Each spin crossover unit communicates mechanically with its neighbors through inter- and intramolecular interactions. Figure 1.19 shows such an interacting lattice (analogous to the one in figure 1.17), where spin crossover units are mechanically connected to their neighbors by interactions represented as springs.

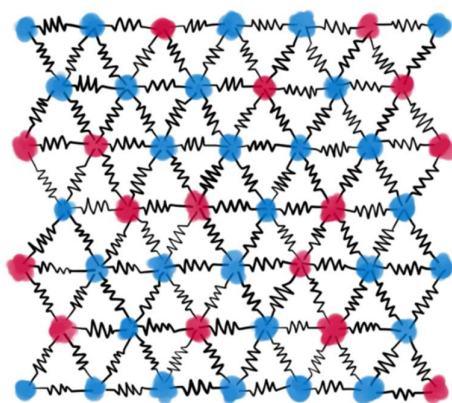


**Figure 1.19.** Lattice of spin crossover units in an interacting model, where the blue dots represent molecules in the low-spin state, and the red ones, molecules in the high-spin state. The fraction of molecules in the high-spin state is 0.35.

In this lattice, the temperature is constant over all the particle but, even if the particle is in mechanical equilibrium with its surroundings, the effective pressure felt by each spin crossover unit is not: The total pressure felt by each spin crossover unit depends on the state of the other spin crossover units in the particle. In other words, the state of the spin crossover units in the particle affects the switching behavior of any given unit inside such particle. An easy way to understand this is to ignore the short distance interactions between the spin crossover units and focus only on how the overall lattice exerts pressure on a given unit. For instance, in figure 1.20 a spin-crossover unit in the HS state is immersed in a LS environment. This LS environment, of lower volume than the reference HS state, exerts a compressive force on the HS unit at the center of the image. This pressure increases the probability that the HS unit at the center mutates into LS state. In an analogous way, a unit in the LS state surrounded by a HS environment would experience some pull (negative pressure) from the bigger HS lattice, favoring its conversion into HS. This kind of interactions are called ferro-elastic interactions because they resemble the ferro-magnetic interactions that favor the alignment of magnetic

moments. Here, instead of having many atoms having a magnetic moment in the same direction, we have many spin crossover units having the same spin state.

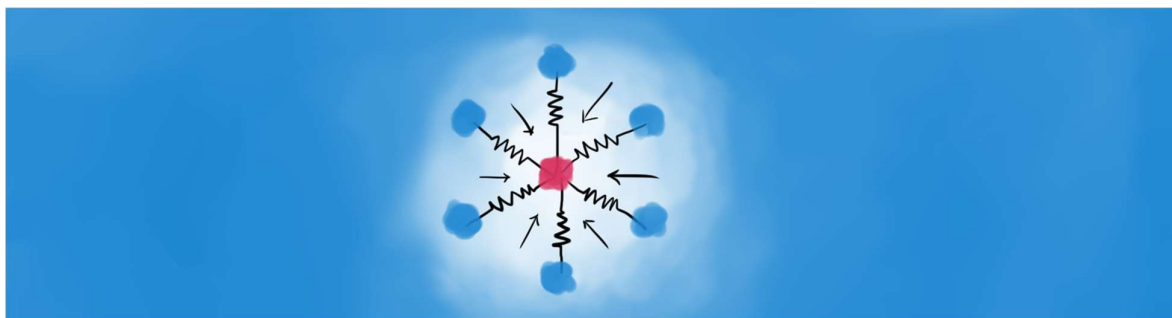


**Figure 1.20.** Spin crossover unit in HS state immersed in a LS environment.

If we consider another case where a HS spin crossover unit is immersed in a mixed environment of units in HS and LS states (as in figure 1.21), the molar volume would remain between the one of a pure HS and the one of a pure LS state. This means, that the pressure applied by the lattice favors HS units to switch into LS in a similar magnitude as it favors LS units to change into HS. In these cases of spin-state diversity, pressure experienced by each spin crossover unit depends specially on the state of its first neighbors, leading to a competition of elastic interactions. This results in antiferro-elastic interactions because they resemble the antiferromagnetic interactions (where the magnetic moments of nearby atoms arrange in opposite directions).

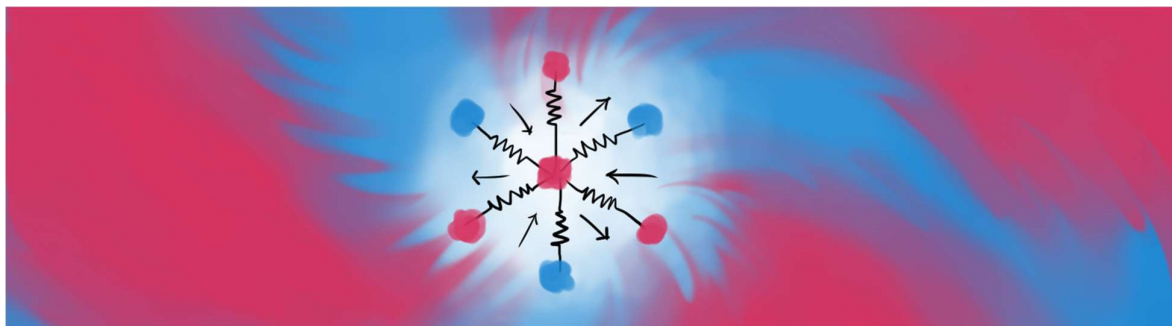


**Figure 1.21.** Spin crossover unit in HS state immersed in a mixed HS-LS environment

As the consequence of these interactions, the behavior of cooperative materials is not described as a simple collection of spin crossover units behaving independently. Instead, the interaction between such units becomes a major factor of its switching behavior. Moreover, elastic competition may give place to the appearance of mixed spin phases with periodic arrangements made of units in HS and LS states,<sup>68,69</sup> as shown in figure 1.22. On the left side of figure 1.22  $\gamma_{HS} = 1/2$ . We see that, instead of forming domains of HS and LS states, the network has a periodic arrangement of spin crossover units in HS and LS states. Here the supercell (highlighted in blue) contains two spin crossover units (one in HS and another one in LS). There are interesting cases where a single material presents so many of these stable

intermediate mixed states that the system seems to produce an infinity of them as the spin transition occurs (like in the concept of “Devil’s Staircase” reported by Trzop *et al.*<sup>70</sup>).

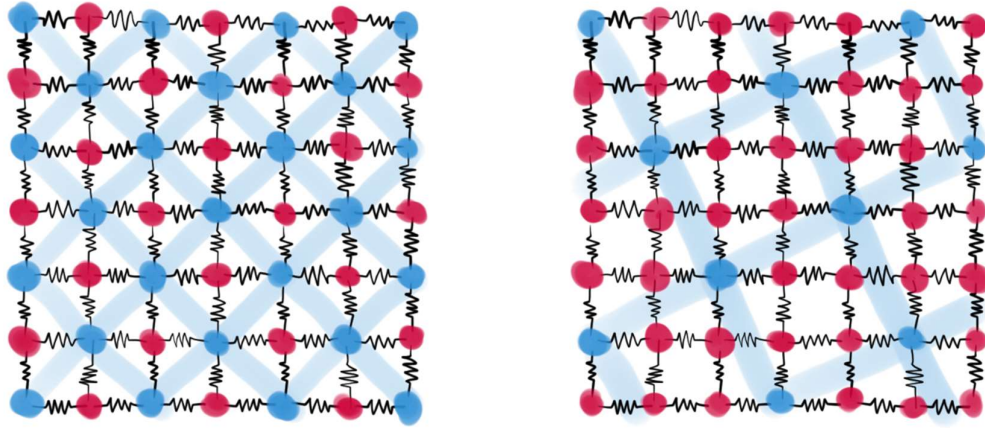


**Figure 1.22.** Mixed HS-LS lattice arrangements with  $\gamma_{HS} = 1/2$  (left) and  $\gamma_{HS} = 4/5$  (right).

### 1.2.7 Hysteresis and the interaction constant.

The interactions between the spin crossover units can be described thermodynamically according to different models (keep in mind that the same equations can be deduced using different strategies). For the purpose of this text, only one model is selected from the literature and it is shown in a simplified way.<sup>71</sup> To describe the immediate environment around each spin crossover unit, an interaction term is added to the expression of the Gibbs free energy, assuming this interaction term is the same for each direction of the crystal. To do so, the Gibbs free energy can be expressed as a function of the HS fraction as a Taylor series.

$$G = b_0 + b_1\gamma_{HS} + b_2\gamma_{HS}^2 + \dots + b_m\gamma_{HS}^m \quad (1.26)$$

To analyze the ideal case where the HS units are diluted in a LS environment,  $\gamma_{HS}$  must tend towards zero to obtain:

$$b_0 = G_{HS \text{ dilution}} \quad (1.27)$$

Here  $G_{HS \text{ dilution}}$  is the Gibbs free energy of the material when the HS units are infinitely diluted. This term can be obtained from the non-interacting model:

$$G_{HS \text{ dilution}} = \gamma_{HS}G_{HS} + \gamma_{LS}G_{LS} - TS_{Mix} \quad (1.28)$$

For convenience, only the first three terms of equation 1.26 are included to obtain equation 1.32:

$$G = G_{HS \text{ dilution}} + \gamma_{HS}\Delta\left(\frac{\partial G}{\partial \gamma_{HS}}\right)_{\gamma_{HS}=0} + \frac{\gamma_{HS}^2}{2}\Delta\left(\frac{\partial^2 G}{\partial \gamma_{HS}^2}\right)_{\gamma_{HS}=0} \quad (1.29)$$

The derivatives in this equation can be substituted by constants, and thus G can be expressed in the following way:

$$G = G_{HS \text{ dilution}} + \gamma_{HS}\Delta_{\text{energy shift}} + \gamma_{HS}^2\Gamma^* \quad (1.30)$$

Here  $\Delta_{energy\ shift}$  is called *energy shift constant* and is usually expressed with the Greek letter  $\Delta$ . Meanwhile,  $\Gamma^*$  is called *interaction constant*.<sup>71</sup> At this point, it is valid to question if the energy shift or the interaction constant have an intuitive meaning. To answer this, the reader must remember that equation 1.30 is deduced after expanding the Gibbs free energy into a Taylor series, and therefore it does not have a mechanistic origin. Of course, after combining this model with other ones, it is possible to associate these constants to other parameters of the materials.<sup>71</sup> Nevertheless, it does not mean that they have an intuitive or mechanistic meaning *per se*. Usually, this equation is expressed in a more simplified way as follows:

$$G = G_{HSdilution} + \gamma_{HS}\gamma_{LS}\Gamma \quad (1.31)$$

Here,  $\Gamma$  is also named *interaction constant*. Although these equations are similar, equation 1.31 is only valid in the specific case when  $\Delta_{energy\ shift} = -\Gamma^*$ . In this case care must be taken in giving the interaction constant an intuitive meaning. As explained in the literature:<sup>71</sup>

*“Originally Drickamer et al. used for the interaction term the symmetric form  $\gamma_{HS}(1 - \gamma_{HS})$  and spoke of an interaction between HS and LS molecules. With the same right we can speak of an interaction only between LS molecules expressing  $\gamma_{HS}$  by the LS fraction  $\gamma_{HS} = 1 - \gamma_{LS}$ . All cases become equivalent after readjusting the linear term.”*

This model is only legitimized by its mathematical simplicity and by the fact that experimental data can be fitted to it. Sometimes these equations describe the behavior of the material accurately (and sometimes they do not) but as stated before, a universal model to make such predictions is unreachable. What is important about these models is that they can predict a phenomenon that the previous models could not: Hysteresis (figure 1.23 B).

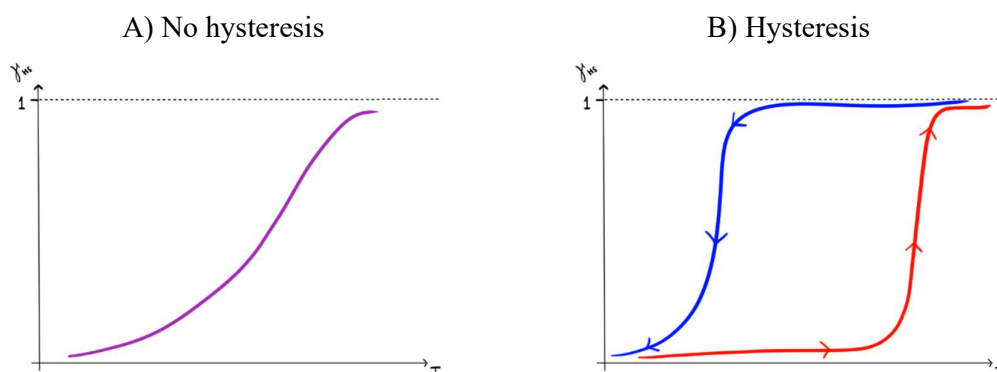


**Figure 1.23.** Typical plots of the HS fraction as a function of the temperature in spin-crossover compounds without hysteresis (left) and with hysteresis (right).

In the field of spin crossover, hysteresis means that the curve representing the high-spin fraction when the sample is warmed up does not have the same path as the equivalent curve when the sample is cooled down. Although the non-interacting model can describe the behavior of some materials by the right fit of their experimental properties, it cannot explain the

occurrence of hysteresis. Instead, equation 1.31 can easily predict hysteresis. First, we substitute  $G_{HSdilution}$  by the expression given by equation 1.28 and evaluate  $S_{Mix}$  according to equation 1.25:

$$G = \gamma_{HS}G_{HS} + \gamma_{LS}G_{LS} - TS_{Mix} + \gamma_{HS}\gamma_{LS}\Gamma \quad (1.32)$$

$$G = \gamma_{HS}G_{HS} + \gamma_{LS}G_{LS} + RT(\gamma_{HS} \ln \gamma_{HS} + \gamma_{LS} \ln \gamma_{LS}) + \gamma_{HS}\gamma_{LS}\Gamma \quad (1.33)$$

Now, considering that  $\gamma_{HS} + \gamma_{LS} = 1$  and that the equilibrium is reached when  $\frac{\partial G}{\partial \gamma_{HS}} = 0$ , equation 1.33 can be differentiated and equated to zero to obtain the following equilibrium condition:

$$0 = \Delta G + \Gamma(1 - 2\gamma_{HS}) - RT \ln \frac{1 - \gamma_{HS}}{\gamma_{HS}} \quad (1.34)$$

It should be remarked that in the non-interacting model, the HS fraction is a function of the temperature, i.e.  $\gamma_{HS} = f(T)$ , as seen in figure 1.23A. In that case, the function  $\gamma_{HS} = f(T)$  was bijective (there is only one value of  $\gamma_{HS}$  at each temperature, and only one equilibrium temperature for each value of  $\gamma_{HS}$ ). This means that we can describe the switching behavior with the inverse function  $T = f^{-1}(\gamma_{HS})$ : Instead of trying to find what is the HS fraction at a given equilibrium temperature; we could try to find the equilibrium temperature for a given HS fraction.

In the interacting model, the function  $T = f^{-1}(\gamma_{HS})$  is not necessarily bijective. In other words, a single equilibrium temperature can be associated with multiple values of  $\gamma_{HS}$ . This can be seen when we solve equation 1.34 to obtain the equilibrium temperature:

$$T = f^{-1}(\gamma_{HS}) = \frac{\Delta H + \Gamma(1 - 2\gamma_{HS})}{\Delta S - R \ln \frac{\gamma_{HS}}{1 - \gamma_{HS}}} \quad (1.35)$$

It is interesting to note that according to equation 1.35, when  $\gamma_{HS} = 0.5$ , cooperativity plays no role in the calculation of the equilibrium temperature and the expression of  $T_{1/2}$  is the same as the one obtained in the non-interacting model.

$$T_{1/2} = \frac{\Delta H}{\Delta S} \quad (1.36)$$

Figure 1.24 is obtained when the function  $T = f^{-1}(\gamma_{HS})$  is plotted at different values of  $\Gamma$  ranging from 0 to  $4RT_{1/2}$ . We can see that the function  $T(\gamma_{HS})$  is bijective in some cases (for example, when  $\Gamma = 0$  or when  $\Gamma = RT_{1/2}$ ), and it is not bijective in others cases (for instance, when  $\Gamma = 3RT_{1/2}$  or when  $\Gamma = 4RT_{1/2}$ ). According to this model, hysteresis occurs when the function  $T = f^{-1}(\gamma_{HS})$  is not bijective.

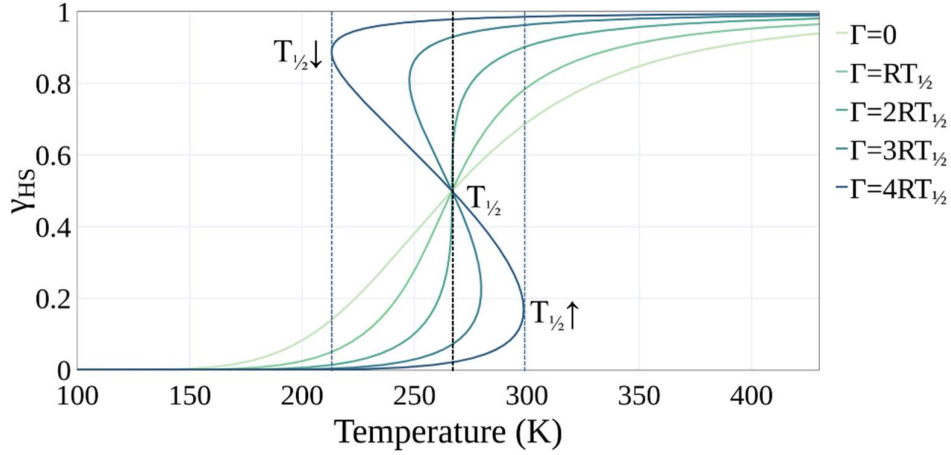


**Figure 1.24.** Plot of  $T^{-1}(\gamma_{HS})$  in an interacting model with different values of  $\Gamma$ , using typical values of  $\Delta H$  (16 kJ/mol) and  $\Delta S$  (60 J/mol.K). All the lines curves have the same value of  $T_{1/2}$ , but the phenomenological values  $T_{1/2}\uparrow$  and  $T_{1/2}\downarrow$  are different.

With the tools we have, we can calculate the critical value of  $\Gamma$  above which hysteresis occurs. In the plot of figure 1.24, this is represented as the first time a curve runs vertically when  $T = T_{1/2}$ . In an equivalent way, this critical point appears when the function  $T = f^{-1}(\gamma_{HS})$  runs horizontally when  $\gamma_{HS} = 0.5$ , i.e. it has a slope equal to zero. When the function  $T = f^{-1}(\gamma_{HS})$  is differentiated with respect to  $\gamma_{HS}$  we obtain the following:

$$\frac{dT}{d\gamma_{HS}} = \frac{R[\Delta H + \Gamma(1 - 2\gamma_{HS})]}{\left(\Delta S - R \ln \frac{\gamma_{HS}}{1 - \gamma_{HS}}\right)^2} \frac{1}{\gamma_{HS}(1 - \gamma_{HS})} - \frac{2\Gamma}{\Delta S - R \ln \frac{\gamma_{HS}}{1 - \gamma_{HS}}} \quad (1.37)$$

After evaluating the derivative of the equilibrium temperature when  $\gamma_{HS} = \frac{1}{2}$  we obtain the next equation:

$$\left(\frac{dT}{d\gamma_{HS}}\right)_{\gamma=\frac{1}{2}} = \frac{4R\Delta H}{\Delta S^2} - \frac{2\Gamma}{\Delta S} \quad (1.38)$$

And finally:

$$0 = \frac{4R\Delta H}{\Delta S^2} - \frac{2\Gamma}{\Delta S} \quad (1.39)$$

From here we can easily see that the critical value  $\Gamma_C$  of  $\Gamma$  appears when it is  $\Gamma_C = 2RT_{1/2}$ . If the material displays a value of  $\Gamma$  higher than  $\Gamma_C$ , it shows hysteresis; if it displays a lower value, it does not show hysteresis.

Let us mention that from the experimental point of view,  $T_{1/2}$  is not accessible when hysteresis curves are recorded. As shown in figure 1.24, for high  $\Gamma$  values,  $T_{1/2}$  is not in the middle of the hysteresis curve but somewhere between the HS to LS and the LS to HS curves. Therefore, when hysteresis is discussed, the switching temperatures in warming and cooling modes,  $T_{1/2}\downarrow$  and  $T_{1/2}\uparrow$ , respectively, are used. Formally, they are not critical parameters as  $T_{1/2}$  is but are very useful to discuss and compare compounds.

### 1.2.8 Finite systems.

One of the most important applications that has been envisioned for spin crossover materials is their incorporation as active components in micro- and nanodevices (for example, in molecular films for electronics).<sup>72-74</sup> Clearly, for such applications, the dimensions of the spin crossover materials would be in the micro- to nanoscale. As already mentioned, the spin crossover phenomenon is very sensitive to environmental factors, and therefore size reduction could therefore strongly influence the spin crossover features. This means that, before spin crossover materials can be incorporated into micro- and nanodevices, their behavior in such scales must be analyzed.

With these ideas in mind, many groups have synthesized nanoparticles of spin crossover materials using various synthetic approaches,<sup>73</sup> mainly using soft or hard templating agents (mainly applied to  $[\text{Fe}(\text{pz})\text{Pt}(\text{CN})_4]$  or Fe-triazole compounds). As a general trend, in all the spin crossover compounds studied so far, particles of spin crossover display the following features as the particle size is reduced (figure 1.25):

- Smaller hysteresis range.
- Smoother curves.
- Residual HS fraction at low temperatures.
- Lower transition temperatures.

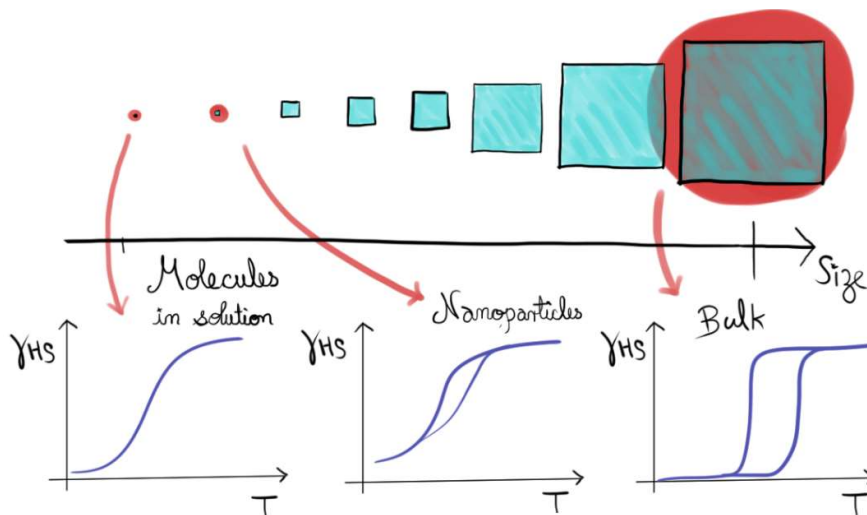


**Figure 1.25.** Nanoparticle behavior as an intermediate between the cooperative behavior in bulk and the one of isolated molecules in solution.

The first aspect to explain is the progressive reduction of the hysteresis as the particles become smaller. In this sense, a single molecule in solution can be understood as an ultra-small nanoparticle containing only one spin crossover unit. So, it is intuitive that the smaller a particle is, the more its behavior would resemble the one of non-interacting molecules, as shown in figure 1.25. Considering that molecules in solution do not interact mechanically

with each other; the smaller a particle is, the less cooperativity it will present. Because the hysteresis and the abruptness of the transition are a consequence of cooperativity, smaller particles have less hysteresis and smoother spin crossover features.

Exactly how this loss of cooperativity occurs might be related with the fact that ferro-elastic interactions act at a long range. Reducing the size of a particle might reduce the correlation length of such ferro-elastic interactions, consequently reducing the cooperativity parameter. Different groups have analyzed the effect of the particle size of spin crossover materials on their switching behavior theoretically, trying to explain the trends observed experimentally. Kawamoto *et al.*<sup>75</sup> as well as Stoleriu L. *et al.*<sup>76</sup> used Monte Carlo simulations and noticed that below a critical size, the hysteresis range of these materials shrinks. Nevertheless, they did not explain the reduction in the value of  $T_{1/2} \downarrow$  or the remaining HS fraction at low temperatures.

To explain the remaining HS fraction at low temperatures, Volatron *et al.*<sup>77</sup> proposed that iron ions of the spin crossover units on the surface of a particle have a different ligand field strength than the ones in the bulk because of two reasons: First, the ligands coordinated to these ions might be displaced by solvent molecules; and second, in case they are coordinated to the metallic ion they would be able to move more freely than the ligands in the bulk, therefore having a different  $C_p$ ,  $\Delta H$  and  $\Delta S$  (figure 1.26). With this in mind, Muraoka *et al.*<sup>78</sup> did 2-dimensional Monte Carlo simulations where the spin crossover units on the edges are locked in the HS state. Their model predicted a reduction of the hysteresis range as the previous ones and gave an origin to the remaining HS fraction at low temperatures (at least the locked shell), and more importantly, it explained the reduction in the transition temperatures in smaller particles.

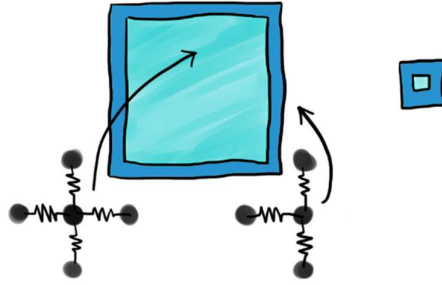


**Figure 1.26.** Surface contribution to the overall switching behavior of spin crossover particles.

Two years later, Gautier *et al.*<sup>79</sup> proposed an additional term in the calculation of the Gibbs free energy to account for the surface energy and the mechanical constraints that such a surface exerts on the core of the particle (equation 1.40).

$$G = \gamma_{HS}G_{HS} + (1 - \gamma_{HS})G_{LS} - T(S_{mix}^b + S_{mix}^s) + S[\sigma_{HS}\gamma_{HS}^s + \sigma_{LS}(1 - \gamma_{HS}^s)] + \Gamma\gamma_{HS}(1 - \gamma_{HS}) \quad (1.40)$$

Here,  $S_{mix}^b$  and  $S_{mix}^s$  are the mixing entropies of the bulk and the surface of the particle respectively,  $S$  is the particle surface, while  $\sigma_{HS}$  and  $\sigma_{LS}$  are supposed to be the interface tension between the particle and its surroundings in the HS and LS state correspondingly. This model predicts the reduction of the hysteresis, lower transition temperatures and the presence of a remaining HS fraction at low temperature.

This very short overview of the effects of size reduction on the spin crossover features gives an idea on how sensitive such materials are to downsizing and highlights the need for reliable methodologies to obtain such nanoparticles.

## 1.3 Summary

In this part, we explained the main aspects about chip-based droplet microfluidics and spin crossover:

- The energy underneath the switchable behavior of spin crossover materials is very low. In some materials, this means that the mechanical work produced after the change of spin-state of a spin crossover unit is enough to influence others in the same particle.
- The cooperative nature of some spin crossover materials makes their behavior susceptible to some microscopic features of the materials, especially their particle size.
- Chips for droplet microfluidics can be conceived as miniaturized factories where a stream of droplets are produced and manipulated in a controlled and reproducible way. These droplets can be filled with the reactants needed to synthesize materials, allowing an exceptional degree of control over the reaction conditions.
- By controlling the production of droplets as well as their size and internal currents, microfluidics has the potential to synthesize spin crossover materials with controlled and reproducible macroscopic features, having a predictable switching behavior.

We must note that many approaches to synthesize spin crossover materials have been explored in the literature<sup>73</sup> and that the control on the particle size distribution, composition, phase, morphology and switching features remains a challenge. In this PhD project, we explore the use of microfluidics in the synthesis of switchable molecular materials for the first time. We believe that the high degree of control offered by droplet microfluidics offers a great platform to engineer the reaction environment where the synthesis of spin crossover materials is performed. This way, it would be possible to synthesize switchable materials exhibiting predictable features.

## 1.4 Outline of this work.

In part 2, we will present the technology we adapted and developed in order to synthesize solid materials in chip-based droplet microfluidics. Chapter 2.1 describes the state of the two possible approaches for the synthesis in droplet microfluidics: Either the solutions of reactants are spread into pairs of droplets and their contents are combined once these droplets merge (*generation*→*combination* approach), or the reactants are combined in a channel that leads to a nozzle where the droplets are produced containing all the reactants *ab initio* (*combination*→*generation* approach).

In chapter 2.2 we present the devices we designed for the microfluidic synthesis of spin-crossover materials. Our devices are based on both approaches, and we start by presenting our devices based on the *generation*→*combination* approach, and later we describe the ones based on the *combination*→*generation* approach.

Later in that part, chapter 2.3 describes a new method we developed to modulate the size of the produced droplets *in situ*. This method is based on the swelling that PDMS displays when it is exposed to a swelling agent (here toluene).

The developments presented in part 2 will be applied to the synthesis of spin crossover materials, as detailed in part 3. This part will then report the strategy followed to make our devices work in real synthetic conditions. Chapter 3.1 will present the synthesis of  $[\text{Fe}(\text{pz})\text{Pt}(\text{CN})_4]$  compound using the different approaches presented in part 1, as well as the different modifications made on the chips to improve the synthetic conditions. Chapter 3.2 will close this manuscript by presenting some preliminary works as perspectives, in terms of compounds (diversifying the reactants and products) and of process (application of the swelling approach).

We improve the performance of our devices further and manage to perform reaction even more difficult, i.e. the synthesis of the Prussian Blue Analogs,  $\text{Rb}_x\text{Mn}[\text{Fe}(\text{CN})_6]_{(2+x)/3} \cdot z\text{H}_2\text{O}$ . Finally, we successfully apply the method to use PDMS swelling to for the modulation of the size of droplets (developed by us and presented in part 2) in an operating device synthesizing  $\text{Rb}_x\text{Mn}[\text{Fe}(\text{CN})_6]_{(2+x)/3} \cdot z\text{H}_2\text{O}$ . We think this method could be of importance to modulate in situ the size of the micro-reactors and consequently affect the features of the synthesized materials.

## References to part 1.

- 1 G. M. Whitesides, *Nature*, 2006, **442**, 368–73.
- 2 O. Kahn, *Molecular magnetism*, VCH, 1993.
- 3 M. Lesieur, *Turbulence in Fluids: Stochastic and Numerical Modelling*, Springer Netherlands, 2012.
- 4 J. Spurk and N. Aksel, *Fluid Mechanics*, Springer Berlin Heidelberg, 2008.
- 5 M. Rubio-Martinez, I. Imaz, N. Domingo, A. Abrishamkar, T. S. Mayor, R. M. Rossi, C. Carbonell, A. J. deMello, D. B. Amabilino, D. Maspoch and J. Puigmartí-Luis, *Adv. Mater.*, 2016, **28**, 8150–8155.
- 6 J. Puigmartí-Luis, D. Schaffhauser, B. R. Burg and P. S. Dittrich, *Adv. Mater.*, 2010, **22**, 2255–2259.
- 7 S. Zhao, A. Riaud, G. Luo, Y. Jin and Y. Cheng, *Chem. Eng. Sci.*, 2015, **131**, 118–128.
- 8 M. Faustini, J. Kim, G.-Y. Jeong, J. Y. Kim, H. R. Moon, W.-S. Ahn and D.-P. Kim, *J. Am. Chem. Soc.*, 2013, **135**, 14619–14626.
- 9 C. N. Baroud, F. Gallaire and R. Danga, *Lab Chip*, 2010, **10**, 2032–2045.
- 10 M. R. Duxenneuner, P. Fischer, E. J. Windhab and J. J. Cooper-White, *Microfluid. Nanofluidics*, 2014, **16**, 743–755.
- 11 H. Kinoshita, S. Kaneda, T. Fujii and M. Oshima, *Lab Chip*, 2007, **7**, 338–346.
- 12 E. Mohammadi, A. King and R. Narayanaswamy, *20th Australas. Fluid Mech. Conf.*
- 13 S. R. Hodges, O. E. Jensen and J. M. Rallison, *J. Fluid Mech.*, 2004, **501**, 279–301.
- 14 L. Jiang, Y. Zeng, H. Zhou, J. Y. Qu and S. Yao, *Biomicrofluidics*, 2012, **6**, 1–12.
- 15 C. M. Leong, Y. Gai and S. K. Y. Tang, *Phys. Fluids*, 2016, **28**, 112001.
- 16 R. Lindken, M. Rossi, S. Große and J. Westerweel, *Lab Chip*, 2009, **9**, 2551–2567.
- 17 S. Ma, J. M. Sherwood, W. T. S. Huck and S. Balabani, *Lab Chip*, 2014, **14**, 3611–3620.
- 18 J. M. Köhler, S. Li and A. Knauer, *Chem. Eng. Technol.*, 2013, **36**, 887–899.
- 19 M. Gonidec and J. Puigmartí-Luis, *Crystals*, 2018, **9**, 12.
- 20 M. Greenspan and C. E. Tschiegg, *J. Res. Natl. Bur. Stand. (1934)*, 2012, **59**, 249.
- 21 M. Bahrami, M. M. Yovanovich and J. R. Culham, *J. Fluids Eng.*, 2006, **128**, 1036–1044.
- 22 M. J. Fuerstman, A. Lai, M. E. Thurlow, S. S. Shevkoplyas, H. A. Stone and G. M. Whitesides, *Lab Chip*, 2007, **7**, 1479–1489.
- 23 J. Zhang, S. Yan, D. Yuan, G. Alici, N.-T. Nguyen, M. Ebrahimi Warkiani and W. Li, *Lab Chip*, 2016, **16**, 10–34.
- 24 L. Jiang, Y. Zeng, H. Zhou, J. Y. Qu and S. Yao, *Biomicrofluidics*, 2012, **6**, 12810.
- 25 H. Song, J. D. Tice and R. F. Ismagilov, *Angew. Chemie Int. Ed.*, 2003, **42**, 768–772.
- 26 I. Shestopalov, J. D. Tice and R. F. Ismagilov, *Lab Chip*, 2004, **4**, 316–321.
- 27 M. A. Ianovska, P. P. M. F. A. Mulder and E. Verpoorte, *RSC Adv.*, 2017, **7**, 9090–9099.
- 28 P. Zhu and L. Wang, *Lab Chip*, 2017, **17**, 34–75.

- 29 V. Van Steijn, C. R. Kleijn and M. T. Kreutzer, *Phys. Rev. Lett.*, 2009, **103**, 1–4.
- 30 P. A. Romero and A. R. Abate, *Lab Chip*, 2012, **12**, 5130–5132.
- 31 A. R. Abate, P. Mary, V. Van Steijn and D. A. Weitz, *Lab Chip*, 2012, **12**, 1516–1521.
- 32 P. Garstecki, M. J. Fuerstman, H. A. Stone and G. M. Whitesides, *Lab Chip*, 2006, **6**, 437–446.
- 33 V. Van Steijn, C. R. Kleijn and M. T. Kreutzer, *Lab Chip*, 2010, **10**, 2513–2518.
- 34 X. Chen, T. Glawdel, N. Cui and C. L. Ren, *Microfluid. Nanofluidics*, 2015, **18**, 1341–1353.
- 35 C. A. Stan, S. K. Y. Tang and G. M. Whitesides, *Anal. Chem.*, 2009, **81**, 2399–2402.
- 36 L. Shui, A. Van Den Berg and J. C. T. Eijkel, *J. Appl. Phys.*, 2009, **106**, 1–8.
- 37 P. Zhu, T. Kong, Z. Kang, X. Tian and L. Wang, *Sci. Rep.*, 2015, **5**, 11102.
- 38 United States of America, 5176646, 1993.
- 39 JiangSu WanTai Motor co.,Ltd, <http://www.wantmotor.com/>.
- 40 ON Semiconductor, <https://www.onsemi.com/>.
- 41 CETONI GmbH, <https://www.cetoni.com/>.
- 42 A. D. McNaught, A. Wilkinson, I. U. of Pure, A. Chemistry and R. S. of Chemistry (Great Britain), *IUPAC Compendium of Chemical Terminology*, International Union of Pure and Applied Chemistry.
- 43 M. Mikami, M. Konno and Y. Saito, *Acta Crystallogr. Sect. B*, 1980, **36**, 275–287.
- 44 P. Gütllich, Y. Garcia and H. A. Goodwin, *Chem. Soc. Rev.*, 2000, **29**, 419–427.
- 45 P. Gütllich, A. B. Gaspar and Y. Garcia, *Beilstein J. Org. Chem.*, 2013, **9**, 342–391.
- 46 F. Renz, *J. Phys. Conf. Ser.*, 2010, **217**, 012022.
- 47 A. Bousseksou, G. Molnár, L. Salmon and W. Nicolazzi, *Chem. Soc. Rev.*, 2011, **40**, 3313–3335.
- 48 L. Cambi and L. Szegö, *Berichte der Dtsch. Chem. Gesellschaft (A B Ser.)*, 1931, **64**, 2591–2598.
- 49 H. Bethe, *Ann. Phys.*, 1929, **395**, 133–208.
- 50 J. H. Van Vleck, *Phys. Rev.*, 1932, **41**, 208–215.
- 51 L. E. Orgel, *J. Chem. Phys.*, 1955, **23**, 1819–1823.
- 52 J. S. Griffith and L. E. Orgel, *Q. Rev. Chem. Soc.*, 1957, **11**, 381–393.
- 53 J. S. Griffith, *The Theory of Transition-Metal Ions*, Cambridge University Press, 1971.
- 54 R. C. Stoufer, D. H. Busch and W. B. Hadley, *J. Am. Chem. Soc.*, 1961, **83**, 3732–3734.
- 55 P. Guionneau, *Dalt. Trans.*, 2014, **43**, 382–393.
- 56 S. E. Page, *The Model Thinker: What You Need to Know to Make Data Work for You*, Basic Books, 2018.
- 57 C. J. Cramer, *Essentials of Computational Chemistry: Theories and Models*, Wiley, 2005.
- 58 K. P. Kepp, *Inorg. Chem.*, 2016, **55**, 2717–2727.
- 59 P. Atkins, P. W. Atkins and J. de Paula, *Atkins' Physical Chemistry*, OUP Oxford, 2014.
- 60 A. Thompson and B. N. Taylor, *Guide for the Use of the International System of Units (SI)*, National Institute of Standards and Technology, 2008.

- 61 W. M. Haynes, *CRC Handbook of Chemistry and Physics*, CRC Press, 2016.
- 62 J. A. Dean and N. A. Lange, *Lange's Handbook of Chemistry*, McGraw-Hill, 15th edn., 1999.
- 63 A. Stone, *The Theory of Intermolecular Forces*, OUP Oxford, 2013.
- 64 P. G. Wright, *Contemp. Phys.*, 1970, **11**, 581–588.
- 65 F. L. Lambert, *J. Chem. Educ.*, 2002, **79**, 187.
- 66 F. L. Lambert, *J. Chem. Educ.*, 2002, **79**, 1241.
- 67 C. P. Slichter and H. G. Drickamer, *J. Chem. Phys.*, 2004, **56**, 2142–2160.
- 68 F. L. Liu, D. Li, L. J. Su and J. Tao, *Dalt. Trans.*, 2018, **47**, 1407–1411.
- 69 M. Paez-Espejo, M. Sy and K. Boukheddaden, *J. Am. Chem. Soc.*, 2016, **138**, 3202–3210.
- 70 E. Trzop, D. Zhang, L. Piñeiro-Lopez, F. J. Valverde-Muñoz, M. Carmen Muñoz, L. Palatinus, L. Guerin, H. Cailleau, J. A. Real and E. Collet, *Angew. Chemie Int. Ed.*, 2016, **55**, 8675–8679.
- 71 H. Spiering, K. Boukheddaden, J. Linares and F. Varret, *Phys. Rev. B - Condens. Matter Mater. Phys.*, 2004, **70**, 1–15.
- 72 L. Poggini, M. Gonidec, J. H. González-Estefan, G. Pecastaings, B. Gobaut and P. Rosa, *Adv. Electron. Mater.*, 2018, **4**, 1–8.
- 73 L. Salmon and L. Catala, *Comptes Rendus Chim.*, 2018, **21**, 1230–1269.
- 74 J.-F. Létard, P. Guionneau and L. Goux-Capes, *Towards Spin Crossover Applications BT - Spin Crossover in Transition Metal Compounds III*, Springer Berlin Heidelberg, Berlin, Heidelberg, 2004.
- 75 T. Kawamoto and S. Abe, *Chem. Commun.*, 2005, **1**, 3933–3935.
- 76 L. Stoleriu, P. Chakraborty, A. Hauser, A. Stancu and C. Enachescu, *Phys. Rev. B - Condens. Matter Mater. Phys.*, 2011, **84**, 1–9.
- 77 F. Volatron, L. Catala, E. Rivière, A. Gloter, O. Stéphan and T. Mallah, *Inorg. Chem.*, 2008, **47**, 6584–6586.
- 78 A. Muraoka, K. Boukheddaden, J. Linares and F. Varret, *Phys. Rev. B - Condens. Matter Mater. Phys.*, 2011, **84**, 1–7.
- 79 G. Félix, W. Nicolazzi, M. Mikolasek, G. Molnár and A. Bousseksou, *Phys. Chem. Chem. Phys.*, 2014, **16**, 7358–7367.

## Part 2. Fundamental aspects in the microfluidic synthesis of materials.

### *Introduction.*

When a material is synthesized using a new method, this act becomes a part of two stories. On one side, the features of the material can be affected by the new method, enriching our knowledge about the material. On the other side, every time a synthetic method is used on a new material, we increase our understanding about the reach, limitations and requirements of the method. A single event, two narratives.

The microfluidic synthesis of switchable materials can be understood along two different lines as well. ***One of these narratives is about how microfluidics affects the features of switchable materials.*** In part 1, we began by highlighting the turbulent flows present in most of the synthetic settings for synthesis in the laboratory (beakers, test tubes and Schlenk flasks that are manually or magnetically stirred). Later, we contrasted the unpredictability of such flows, against the high degree of control and reproducibility in the manipulations of fluids offered by microfluidics. As presented in chapter 1.2, the spin crossover phenomenon is attractive in terms of implementation into electronic devices, requiring the study of chemical routes to promote reliable size reduction. From this perspective, we proposed the use of microfluidic for the synthesis of such materials. Moreover, other groups have already synthesized spin crossover nanomaterials using reverse microemulsions which affords an element of comparison in our exploration.<sup>1</sup> Our progress in this direction will not be addressed in this part but in part 3. Nevertheless, we must remember that the work presented here is aligned with the general goal of exploring the use of microfluidics for the synthesis of switchable molecular materials.

***The second narrative is about how our knowledge about microfluidics increased as we attempted to use it in the synthesis of switchable materials.*** We must clarify that this new knowledge does not necessarily come from the fact that these materials are switchable. It comes from many features of the reactants, the reaction and the product: How the reactants influence the density, viscosity and surface tension of their corresponding solutions; the reaction kinetics; and the solubility, and rates of nucleation and growth of the product. ***In this part, we describe and discuss the PhD project from the narrative of chip-based droplet microfluidics without any reaction.***

In chapter 1, we explained that microfluidic synthesis can be divided into two branches that share commonalities (like the fact that the reaction occurs in controlled and reproducible ways inside of very thin and narrow channels) but provide very different reaction environments. The first branch consists in combining the reactants in a continuous way, allowing the slow mixing of the reactants through diffusion as they flow along the same channel in a laminar way. The second one involves the segmentation of the reaction into small droplets or plugs, to exploit the vortices that appear inside such droplets or plugs to mix the reactants very quickly.

Both branches have shown to be very attractive to perform synthesis and we chose to apply segmented (droplet) microfluidics in the synthesis of switchable molecular materials. We have four main reasons for that. First, the currents inside and between droplets can be used to modulate the mixing of the reactants, which can influence some features of the resulting particles. Second, confining the reaction inside droplets can help in avoiding the unintentional sedimentation of the solid products in the channels of the chip, therefore reducing the risk of clogging. Third, devices based on segmented flow microfluidics can be conceived as small factories, where microscopic reactors are fabricated and manipulated in a modular way, as if they were in an assembly line. Such a modular approach permits the addition of sequential synthetic operations (like addition of multiple reactants, quenching the reaction or washing the products) and offers many parameters that affect the features of the product (like the morphology and size of the resulting particles). Finally, the fourth reason is that some of the present and future goals of the group are related with multi-component materials (for example, with spin crossover particles grafted with gold nanoparticles<sup>2</sup>), and although this would be very challenge to achieve, we believe that droplet microfluidics might be used for the synthesis of core-shell architectures using sequential devices-

It is worth mentioning that the microfluidic approaches we developed are free of surfactants. This is intentional, and is based on the premises that even minute amount of surfactants might affect some features of the product (like their crystallinity or their surface tension), which would influence their switching behavior.

In chapter 2.1, we present the basis of droplet generation and in chapter 2.2, we detail the different devices we designed for the synthesis of spin crossover materials, and we show their model performance in producing and manipulating droplets of water carried by mineral oil (avoiding the use of surfactants). We only focus here on their behavior using water with food colorant. The results of the synthetic experiments using solutions with reactants are discussed in chapter 3.1.

Chapter 2.3 explores a way to modulate the droplet size, assuming that, as for microemulsions, the size of the reactor influences the size of the obtained particles. To do so, we developed a technique to change the critical dimensions of PDMS chips using swelling. This technique will be applied and discussed in chapter 3.2.

## Chapter 2.1 Theoretical framework: The two approaches of synthesis in droplet microfluidics.

Chemical synthesis in segmented flow microfluidic devices can be divided into two approaches, both having advantages and disadvantages. In the first one, here named *generation*→*combination*, two droplets with solutions of reactants are generated almost at the same time and, in order to combine them for the reaction to occur, they are forced to collide and merge. In the second approach, *combination*→*generation*, the droplets are formed after the two flows with reactants encounter in the same channel, therefore generating a stream of droplets containing all the reactants *ab initio*. Figure 2.1 compares both approaches.

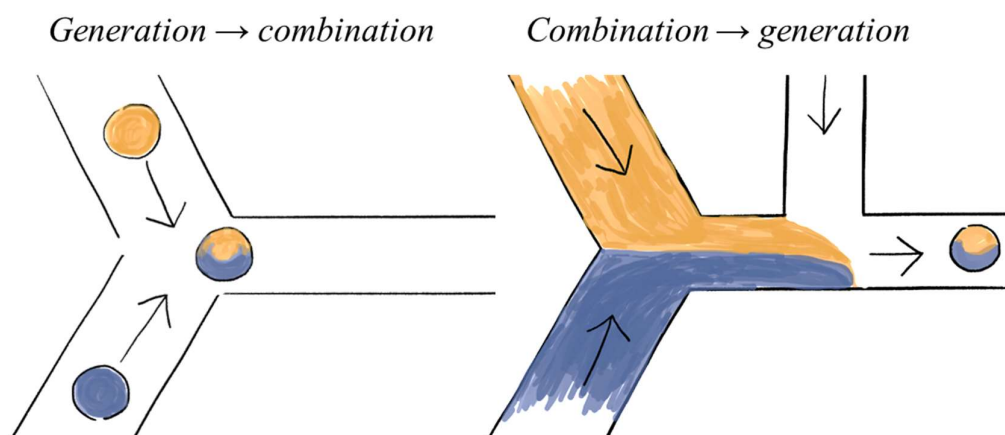


**Figure 2.1.** Comparison of the *generation*→*combination* (left) and the *combination*→*generation* (right) approaches.

In this project we explore both approaches for the synthesis of switchable molecular materials, and in this part we will describe the performance of both approaches when they are operated only with water. Along this chapter, we describe some general aspects about the use of each approach in microfluidic synthesis, so the reader can become familiar with key advantages and disadvantages of each one.

### 2.1.1 The *generation*→*combination* approach.

In the first approach, *generation*→*combination*, two small droplets merge into one droplet which volume is the sum of the volumes of the two original ones. Here, three aspects of this approach will be presented: First, that the merging of droplets induces a mixing process between the contents of both initial droplets; second, the advantages of this approach with respect to clogging in the device; and third, the technical aspects related to the merging efficiency. Finally, this approach is illustrated with experiments from the literature.

The *generation*→ *combination* approach involves an inherent mixing process. To understand this, it must first be considered that the surface area of the droplet that results from the merging is smaller than the addition of the areas of both originating droplets. To illustrate this, let us see what happens when two identical droplets of water merge (assuming they have the same surface tension, volume, etc.). First the radius of the final droplet,  $r_{final}$ , is calculated, considering that the initial and final droplets are spherical:

$$V_{final} = 2V_{initial} \quad (2.1)$$

$$\frac{4}{3}\pi r_{final}^3 = 2 * \frac{4}{3}\pi r_{initial}^3 \quad (2.2)$$

$$r_{final} = 2^{1/3} r_{initial} \quad (2.3)$$

Here,  $V_{final}$  is the volume of the resulting droplet after the merging of the two droplets with volume  $V_{initial}$ , and radius  $r_{initial}$ . Now that the radius  $r_{final}$  is given by equation (2.3), the surface areas,  $A$ , of the initial and final droplets can be calculated:

$$A_{initial} = 4\pi r_{initial}^2 \quad (2.4)$$

$$A_{final} = 4\pi r_{final}^2 = 4\pi 2^{2/3} r_{initial}^2 = 2^{2/3} A_{initial} \quad (2.5)$$

$$A_{final} < 2A_{initial} \quad (2.6)$$

Since the total area of the two initial droplets is  $2A_{initial}$ , which according to equation (2.6) is smaller than the surface area of the final droplet  $A_{final}$ , it is clear that the merging of two droplets leads to a reduction in the total surface area. This reduction in the total interface between water and oil (from  $2A_{initial}$  to  $A_{final}$ ) is translated into different forms of energy that are released after the merging and that constitute the driving force for the fusion of the droplets. In the simple case where both droplets have the same composition and properties (like surface tension, viscosity and density) the total change in energy,  $\Delta E$ , can be easily calculated the following way:

$$\Delta E = \gamma(A_{final} - 2A_{initial}) = \gamma A_{initial} \left(2^{2/3} - 2\right) = \gamma A_{final} \left(1 - 2^{1/3}\right) \quad (2.7)$$

$$\Delta E < 0 \quad (2.8)$$

Where,  $\gamma$  is the interfacial tension between water and oil. Note that, because energy is released,  $\Delta E$  in equation (2.7) should have a negative value. Additionally, even if according to equation (2.7) the energy of the merging increases with the square of the radius of the initial droplets, the volume of the droplet (i.e. the volume that needs to be put in motion when mixing) scales to the cube of the radius. So, if we want to calculate the energy density associated to this mechanism, we should divide  $\Delta E$  by the volume of the final droplet:

$$\frac{\Delta E}{V_{final}} = \frac{\gamma A_{final} \left(1 - 2^{1/3}\right)}{V_{final}} = \frac{\gamma}{r_{final}} 3 \left(1 - 2^{1/3}\right) = -0.780 \frac{\gamma}{r_{final}} \quad (2.9)$$

From equation (2.9), it is evident that the energy density available for the mixing process caused by the merging of two droplets increases with  $\gamma$ , while it decreases with  $r_{initial}$ . This means that mixing is more energetic in small droplets and in cases with higher interfacial tension.

For example, let us imagine that our microfluidic system releases pairs of droplets of water carried by mineral oil (where the interfacial tension would be close to  $\sim 50$  mN/m)<sup>3</sup>. If the droplets merge and form a droplet of 20  $\mu\text{m}$  in radius (or 40  $\mu\text{m}$  in diameter), the energy density released by such a merging would be close to 1950 J/m<sup>3</sup>.

It is interesting to know if this energy density is useful. Here, we must know that the kinetic energy generated by the merging will be converted to different types of energy until it is eventually converted into heat. So, the maximum kinetic energy will appear just after the merging. Hypothetically, if just after the merging 100% of the released energy is translated into kinetic energy ( $\Delta E = \frac{1}{2}mv^2$ ), the droplet of our example would be accelerated to 1.97 m/s.

Likewise, if this energy were completely converted into rotational energy ( $\Delta E = \frac{1}{2}I\omega^2$ , where  $I = \frac{2}{5}mr^2$  because we assume the droplet to be spherical), we can calculate a maximal angular frequency according to the following equation:

$$\omega = 2\pi f = \frac{\sqrt{\frac{5}{\rho} \frac{\Delta E}{V_{final}}}}{r_{final}} \quad (2.10)$$

Here,  $f$  is the rotational frequency, and  $\rho$  is the density of water. In our hypothetical case, the resulting droplet would rotate at 24.8 kHz or 1 490 000 rpm.

Clearly, there is a big uncertainty in the values we used for these calculations and they do not pretend to give accurate results. They only show the magnitudes of energy density released in the process of merging. For instance, in the example just mentioned, the released energy would be enough to make the droplet rotate at 1 490 000 rpm, which is about 150 times faster than a conventional high speed mechanical stirrer.<sup>4</sup> In other words, if only 1% of the energy released from the merging is translated into a mixing motion, this microfluidic system would outmatch the high-speed mechanical stirrers available in the market. This means that in optimal conditions, the energy released by the merging of droplets has a great potential in its use to mix reactants inside droplets.

The *generation*  $\rightarrow$  *combination* approach is quite convenient when the product of the reaction is a solid because of its resistance towards clogging.<sup>5</sup> Basically, clogging occurs when a solid occupies the whole cross-section area of a channel, impeding the passage of fluids across it. Many phenomena can lead to clogging (foreign objects entering the chip, fabrication mistakes, and so on), but here only the sedimentation of the product will be considered. Clogging through this mechanism does not occur in a single step. Instead, it is the outcome of a sequence of stages that cascade after a portion of solid sticks to the walls of the channel. In general terms, once the solid reaction products make contact with the walls, clogging occurs if two conditions are met: First, the flows of both solutions of reactants enter in contact with this

solid so that crystals can grow epitaxially on it (either because of failures in the design of the geometry of the chip, or because of disturbances of the flows caused by the sediment itself); and second, the interaction forces between the solid and the walls are stronger than the drag force that the fluids act on the deposited solids as they grow.

When working in the *generation*→*combination* approach, the reactants enter in contact due to the merging of the droplets (and not before). This means that the reactants enter in contact when they are already contained inside droplets, which means that there is always a layer of oil that physically separates its contents from the walls of the channel. For this reason, if sediment is formed as a product (or by-product) of the reaction, it is formed away from the channel boundaries and can thus hardly stick to the walls. The mechanism just described can therefore not be triggered.

In the face of a brief acute perturbation originating from acoustic pollution, the performance of chips based on this approach is briefly impoverished in the sense that the chance of merging the pairs of droplets will be temporarily reduced. Nevertheless, such ephemeral anomalies do not compromise the later functioning of the chip because they do not lead to the formation of sediments stuck to the walls. This means that the performance of the chip should be preserved even if acoustic pollution causes short-term perturbations of the system.

Even if these devices have great advantages regarding the mixing of reactants and the resistance to clogging, some technical aspects about the merging of droplets must be considered because merging microscopic droplets in a regular way is not an easy task. First, for droplets to merge they must be in contact. This means that the droplets must be generated with the same frequency (even if both solutions with reactants might have different densities, viscosities and surface tensions) and the geometry of the device must guide the droplets close enough to each other, so that they can collide. In other words, devices based on the *generation*→*combination* approach require the precise control of two streams of droplets in time and space. For instance, in chapter 1.1, three mechanisms for droplet generation were presented. Jetting is one of them. Droplets generated through this mechanism usually have a relatively high dispersity in size due to the chaotic nature of its formation.<sup>6</sup> Because of this, it would be impossible to use this kind of devices when droplets are formed through a jetting mechanism.

Second, for two colliding droplets to merge, even if energetically favorable (equation 2.8), they must overcome an activation energy associated with the displacement of oil between the droplets, as well as the rearrangement of the molecules of oil and water constituting the interface. This energy input can have an active origin when additional forces, other than the ones related with the pumping of fluids, are applied. For example, droplets can be electrically charged in opposite ways, so that when they collide, the coulombic force facilitates the merging.<sup>7</sup> This input can also be passive. In such cases, the geometry of the device itself promotes the collision of droplets with enough momentum to merge them. We illustrate those two types of devices by discussing two examples of strategies that have been developed to solve this issue.

The first one was reported by L.-H. Hung *et al.* when working in the group of A. P. Lee in 2005, and was applied to the synthesis of nanoparticles of CdS.<sup>8</sup> In this study, the nozzle of

the chip comprises the equivalent of two conventional T-junctions facing each other, where a straight flow of oil is intercepted perpendicularly by two flows of aqueous solutions coming from both sides of the main channel, as shown in figure 2.2. Here, the droplets are formed almost at the same time because of a push-pull effect.

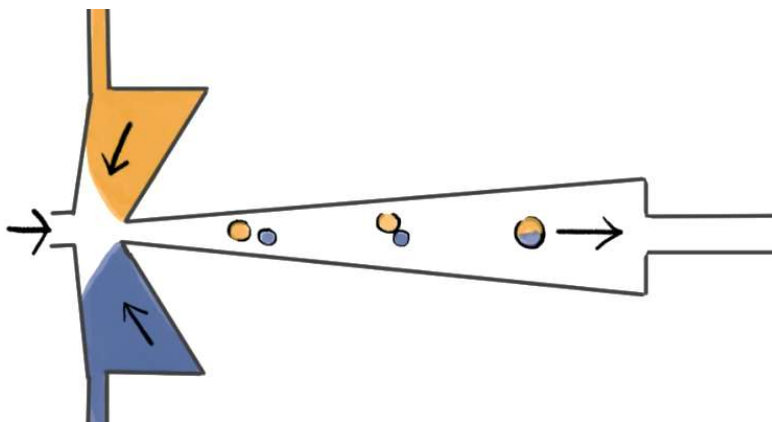


**Figure 2.2.** Geometry of the chip used by L.-H. Hung *et al.*<sup>8</sup> to synthesize nanoparticles of CdS. The triangular “wings” at each site of the droplet generators prevent backflow and help to stabilize the flows of reactants.

To merge the droplets, the exit channel becomes wider, which generates a gradient in the linear flow speed of oil that results in the collision of the droplets. Indeed, as stated in chapter 1.1, due to the conservation laws, the integral of the linear flow speed across any cross-section area of the channel is constant, and therefore, linear flow speeds are reduced in wider channels. As the linear flow speed of oil is slowed down, its drag force on the droplets is reduced as well, slowing down the droplets as they progress along the channel. The linear speed of the droplets here depends on their positions. In pairs of droplets, where one droplet is ahead of the other, the widening of the channel favors their collision simply because the droplet ahead travels slower than the droplet behind. The authors report that efficient droplet coalescence is observed only when the flow rates of oil and water are within a specific range. Comparing the obtained compound with another sample prepared by bulk reaction, the authors identified a reduction in the particle size and an improvement in the particle size distribution.

The second example consists in two articles by L. Frenz *et al.* working with J. C. Baret (during his post-doc in Strasbourg under the direction of A. D. Griffiths). In the first one, a dual nozzle was developed to produce droplet pairs (figure 2.3 a);<sup>9</sup> and in the second one, droplet pairs generated with this dual nozzle were merged using alternating electric fields (figure 2.3 b).<sup>5</sup> By merging these droplets, they carried out the reaction to produce nanoparticles of Fe<sub>3</sub>O<sub>4</sub>.

(a) Dual nozzle to generate pairs of droplets      (b) Merger based on an alternatic electric field

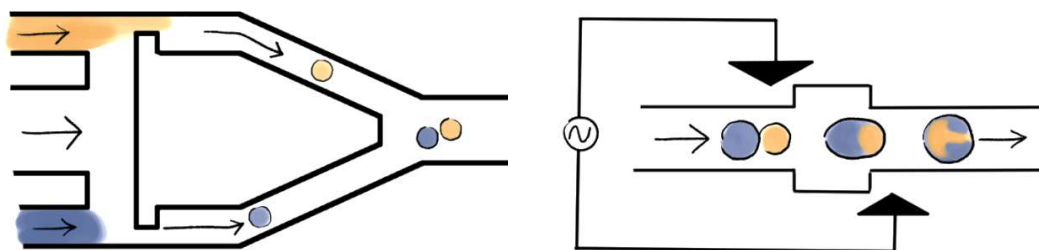


**Figure 2.3.** Devices proposed by Frenz *et al.*:<sup>5,9</sup> (a) Dual nozzle to generate pairs of droplets; (b) apparatus to merge the droplets (merger) based on alternative electric fields.

The dual nozzle proposed by Frenz *et al.* is more complex than the one from Hung *et al.* Basically, a flow of oil is divided in two symmetric branches. Each branch comprises a T-junction where a straight flow of an aqueous solution of reactants is intercepted perpendicularly by a flow of fluorinated oil. The exit channels of both T-junctions meet again shortly after the droplets are generated. Here, droplets are formed almost at the same time because of the oscillations in pressure that occur when the droplets are formed.<sup>9</sup> To promote the merging of the droplet pairs, they use a AC electric field that affects the molecules of surfactant, destabilize the interface, and brings the droplets closer. Without an applied electric field, the author show the absence of merging.<sup>5</sup> Moreover, the authors identify a downsizing effect of microfluidics: When the same reaction is carried in bulk synthesis the average diameter is  $9\pm 3$  nm, while the diameter of the particles obtained using microfluidics is  $4\pm 1$  nm.

The two examples presented in this approach are very similar. Both of them work efficiently only within a specific range of flow rates of oil and water. The main technical difference between them is that the second device has an additional feature: Due to the distance between both junctions, an acute perturbation can hardly cause an undesired mixing of both solutions.

### 2.1.2 The combination→ generation approach.

In the second method, here named *combination*→ *generation*, two flows with reactants encounter in the same channel, and afterwards reach a droplet generator, like a T-junction or a flow-focusing junction. This leads to a stream of droplets containing all the reactants *ab initio*.

In comparison with the *generation*→ *combination* approach (chapter 2.1.1), the energy input originating from the merging of droplets is obviously inexistent here (because these systems are not based on merging droplets to combine the reactants). Therefore, to achieve an efficient mixing of reactants in droplets generated through this approach, other mechanisms for mixing must be employed (like the ones presented in part 1.1)

In the *combination*→*generation* approach, the solutions with reactants are temporarily contained inside the same channel before the droplets are generated. If a solid is formed at this point, the sediment can easily touch the walls. As explained, this can unleash a sequence of cascading stages that could culminate in the clogging of the channel. To avoid the reaction from happening here, an additional flow of solvent is frequently added between the two flows of solutions (the buffer layer, as shown in figure 2.4).

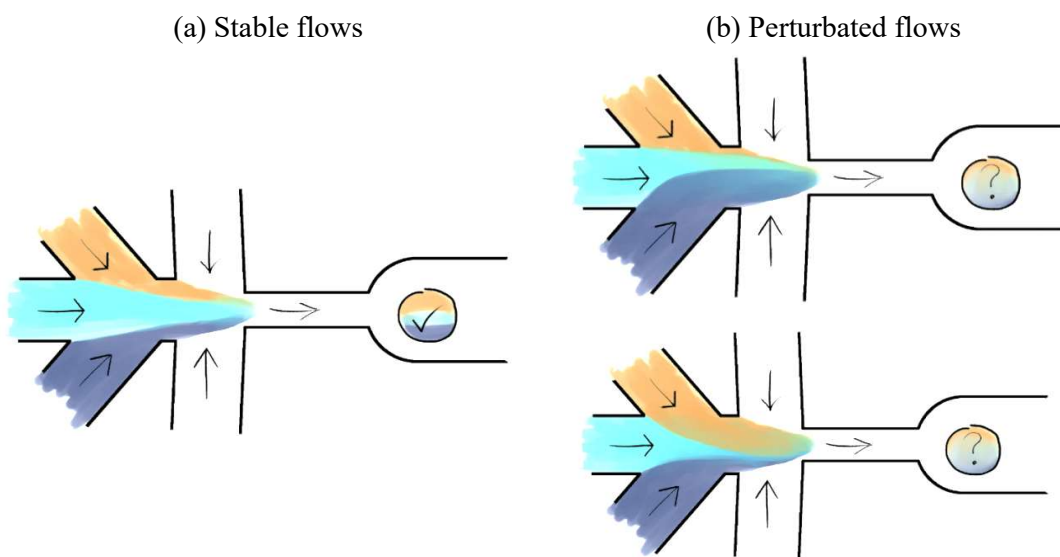


**Figure 2.4.** Comparison between the behavior of a flow focusing device to carry chemical reactions based on the *combination*→*generation* approach when (a) the flows are stable, and (b) the flows are perturbed.

The efficiency of the buffer depends on the diffusion speed of the reactants and on the stability of the flows. In the face of an acute perturbation capable of impoverishing the performance on the buffer layer, devices based on this approach might easily clog. Because of this, an ephemeral anomaly can compromise the later functioning of the chip. These devices have an additional disadvantage over the ones based on the *generation*→*combination* approach when the system is subjected to constant perturbations. While in the *generation*→*combination* approach those perturbations lead to droplets formed with time lags that are too large to allow droplet to merge, in the *combination*→*generation* approach such perturbations result in instant differences between the flow rates of each reactants, resulting in droplets with uneven amounts of reactants. Therefore, in perturbed flows, the amounts of reactants contained in each droplet are, to some extent, unknown (see Figure 2.4).

Even if these devices have some disadvantages regarding the stability to acute perturbations and frequently require additional mechanisms to mix the reactants inside of the droplets, the technical aspects regarding the generation of droplets are much simpler than those in the *generation*→*combination* approach. This is because here it is not necessary to control the stream of droplets in time and space precisely after their formation.

An interesting example of this approach is the study from H. Song *et al.*<sup>10</sup> on mixing in microfluidic systems and its later use in the synthesis of quantum dots of CdS and core-shell structures of CdSe on CdS by I. Shestopalov *et al.*,<sup>11</sup> from the group of F. Ismagilov. There, the authors propose a system where reactants are combined in a channel that intercepts a straight flow of oil perpendicularly. As explained in chapter 1.1, introducing a stream of droplets with reactants laterally on a straight flow of mineral oil solves the *symmetry problem* in the mixing of reactants. Additionally, a lateral injection is used in a second step to add the reactants required to build the shell around the core particles. To improve the mixing furthermore, a zigzagged channel was incorporated just after the T-junction as shown in figure 2.5.

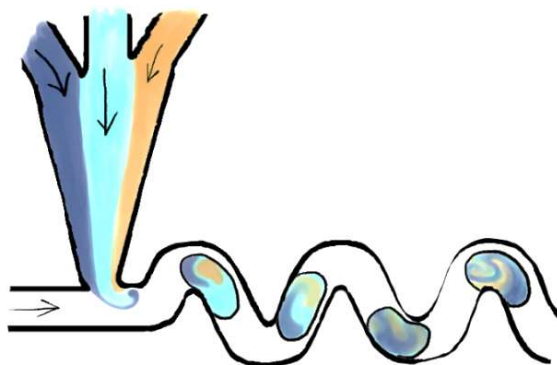


**Figure 2.5.** Geometry of the droplet generator and mixer used by H. Song *et al.*<sup>10</sup> and I. Shestopalov *et al.*<sup>11</sup> Here it should be noted that the contents inside the droplet mix as the droplet moves along the channel.

### 2.1.3 Comments on the combination→ generation and generation→ combination approaches.

The *combination*→ *generation* and the *generation*→ *combination* approaches might seem similar at first glance: The formation of a stable and homogenous stream of droplets containing the reactants to carry a reaction is the goal of both; and their functioning shares some critical processes, like the generation of droplets (contrary to the continuous flow approach). But even if in both approaches a set of fluxes appear inside the droplets because of the difference in the linear speed of the droplet and the linear flow speed of the oil advancing around it; droplets that result from the merging of two former droplets (like the ones obtained from the *generation*→ *combination* approach) do not require any additional means to solve the *symmetry problem* because the merging process itself solves it. In the *combination*→ *generation* approach, the *symmetry problem* remains unsolved unless additional measures are taken. Moreover, in this approach the flows with reactants are dangerously close to each other as they share the same channel just before the droplets are formed. If a layer of pure solvent is not introduced between these flows (as in the article of Shestopalov *et al.* just explained),<sup>11</sup> the reactants would enter in contact before the droplets are formed. This means that the proper functioning of this kind of devices depends on whether the buffer layer can stop the reactants to enter in contact. The severity of a failure on this feature depends, of course, on the nature of

the reaction involved. If the product is soluble in the solutions or if the reaction is carried under low concentrations, no major complications arise. On the other hand, if the solutions of reactants have a high concentration and the product is solid, precipitation can occur prior to the generation of the droplet. If such precipitates stick to the walls of the channel, they can affect the performance of the device in a very negative way: First, they can generate perturbations in the direction of the flow; and secondly, since the precipitate is in contact with both solutions of reactants, further precipitation can occur, leading to the clogging of the channel.

This approach has, on the other hand, some advantages. The proper functioning in devices based on the *combination*→*generation* approach does not rely on the magnitude of the oscillations of the pressure in the system. For this reason, the size of the droplets does not affect the way these devices work. Moreover, since a single stream of droplets is generated here, the constraints in the flow rates that can be used are not related with the synchronization of the generation of droplets at all. For these reasons, the devices based on the *combination*→*generation* approach can work efficiently within a larger range of capillary numbers and flow rates, and can even tolerate changes in the droplet generation mechanism. In table 2.1 the advantages and disadvantages of each approach are compared.

	<i>Generation</i> → <i>combination</i>	<i>Combination</i> → <i>generation</i>
<b>Advantages</b>	No clogging in junctions. Resistant to acute perturbation. Asymmetrical mixing.	Easy to develop. Independent of Ca and the pressure oscillations.
<b>Disadvantages</b>	Difficult to achieve. Might require active methods to merge the droplets.	Potential clogging. Vulnerable to acute perturbation. Requires additional mixing methods to overcome the <i>symmetry problem</i> .

**Table 2.1.** Comparison between the *combination*→*generation* and *generation*→*combination* approaches.

## Chapter 2.2 The microfluidic devices developed for the synthesis of switchable materials.

### 2.2.1 First attempts.

The first attempt to carry the synthesis reaction of  $\text{Fe}(\text{Pz})\text{Pt}(\text{CN})_4$  using microfluidics was based on the *generation*→*combination* approach using the dual nozzles proposed by Frenz *et al.*<sup>9</sup> because of two reasons: The resilience to clogging in this kind of systems and the mixing that results from the merging of droplets. Two drastic features differentiate our approach from theirs. The first one is that we do not merge the droplets using active methods, and the second one is that we do not use any surfactants.

As explained before, the operation of this device consists in the production of pairs of droplets in the dual nozzle, that encounter in the exit channel, where they merge. Here, we refer to this chip as the *Purple Chip*, and its blueprint is shown in figure 2.6.

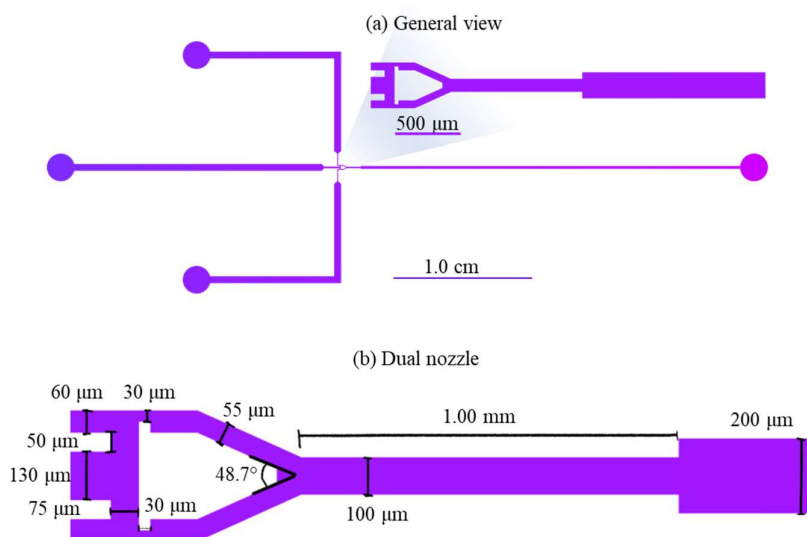


**Figure 2.6.** Blueprint of the first chip we worked with (*Purple Chip*). (a) Overview of the device, and (b) close-up of the dual nozzle, inspired by the work of Frenz *et al.*<sup>5,9</sup>

A problem we found frequently is that, if suddenly the flow rate of oil is increased or the flow rate of water is decreased, instead of exiting the device through the exit channel, oil flowed back through the channels carrying water as shown in figure 2.7. This phenomenon has major repercussions in how the microfluidic systems are piloted (i.e. in how the flow rates can be adjusted to start, end or modulate an experiment).

To understand this phenomenon, it must be considered that, for oil to flow through the exit channel towards the outlet of the chip, it must overcome the viscous forces that hinder its movement (i.e. the hydraulic resistance). Because the exit channel is longer and thinner than

the channels transporting water or oil, sometimes the force that the oil requires to flow through the exit channel is comparable with the force that is required to push the flows of water back. Just like a channel can change its geometry after an increase of pressure and store some volume of fluid, this change in geometry serves to store the volume of water flowing backwards until an equilibrium pressure is achieved.

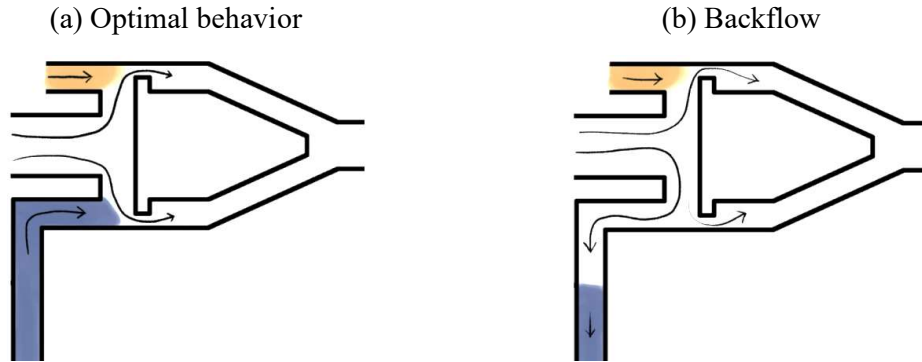


**Figure 2.7.** Comparison between the optimal behavior of the Purple Chip (a) and its performance when backflow occurs on the blue solution (b). Droplets are not shown for clarity.

Another common problem when using this chip laid in the presence of solid objects carried by the flow, that entered the chip during its manufacture or the presence of dust particles coming from the fluids themselves. To avoid the presence of such bodies in the active part of the chip (i.e. in the nozzle), a filter was placed after the inlet of each channel, consisting in a set of cylindrical columns (300 columns of 100  $\mu\text{m}$  in diameter) close to each other (30  $\mu\text{m}$  distance) as shown in figure 2.8. This measure effectively solved this problem.

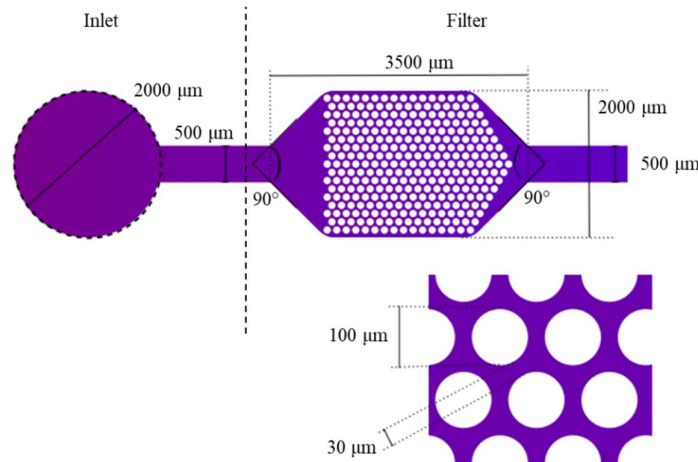


**Figure 2.8.** Blueprints of the filters used in the Purple Chip. In the upper image, the geometry of the filter is presented. In the lower one, the texture of the filter is shown. This texture is used in all the later filters.

The biggest drawback of this filter relies in the impoverishment of the performance of the chip after strong backflows: if oil flows backwards in the channels designed to carry either water or solutions with reactants and the whole filter is wet with oil, oil sticks to the columns

of the filter. Figure 2.9 corresponds to a picture where backflow resulted in the formation of such oil-bridges. When water or solutions with reactants flow again through their corresponding channels, the oil stuck to the columns forms a set of bridges across them. These bridges are difficult to wash away and, when a continuous set of oil-bridges is formed across the filter in the lateral direction, water cannot flow anymore without acting some force on them. For water (or solutions) to flow across the filters now, it must displace the oil from those bridges until it forms a percolation path. The force that water acts on the oil-bridges implies the formation of a difference in pressure at both sides of the filter. This pressure drops back to zero just after a small amount of water passes through. Since the bridges are formed by a liquid, they can easily be rebuilt after the pressure difference at both sides of the filter disappears. This process, where water percolates across the filter by breaking oil-bridges, that are rebuilt as soon as a small volume of water passes through, is cyclical. In fact, it continues until enough oil is washed away and oil-bridges cannot be rebuilt.

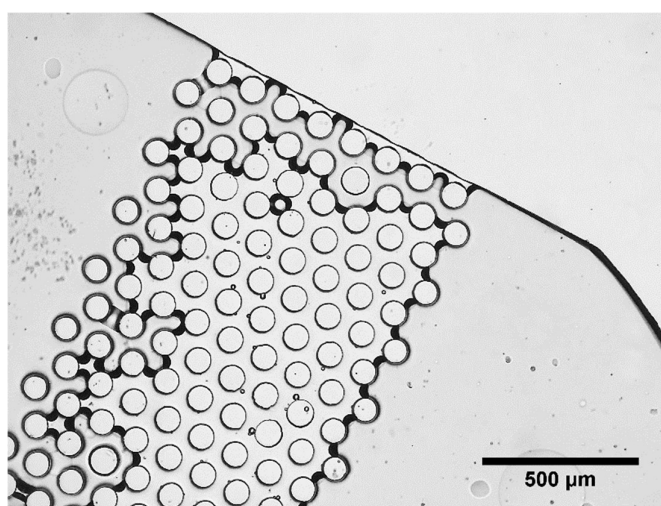


**Figure 2.9** Formation of oil-bridges in the filter of a microfluidic chip with a percolation path across the filter. Although this picture was taken in a later point of the project, it clearly shows the formation of such oil-bridges and how the liquid phase forms a percolation path across them.

### *2.2.2 Preliminary experiments without reactants: Determination of the adequate flow rates.*

Before carrying the reaction, it was necessary to identify the regimes of flow rates under which this device can operate successfully, i.e. pairs are formed in droplets, and they merge. To do so, the *Purple Chip* was prepared using soft-lithography, targeting a height of 65 μm (see the appendix); and was operated using water with food colorant instead of solutions with reactants. The flow rates of water and oil were scanned to analyze the performance of the system at each point. Since the flow rates of both water solutions are preferred to be equal, the operating conditions of this system can only be modulated through changes in the flow rates of water and oil. Since there are only two parameters to vary (the flow rates of water and the flow rate of oil), each operating condition can be related to a point in a bi-dimensional space. The

performance of the chip was analyzed at different points in this space to generate a map (like those of a phase diagram), as shown in figure 2.10.

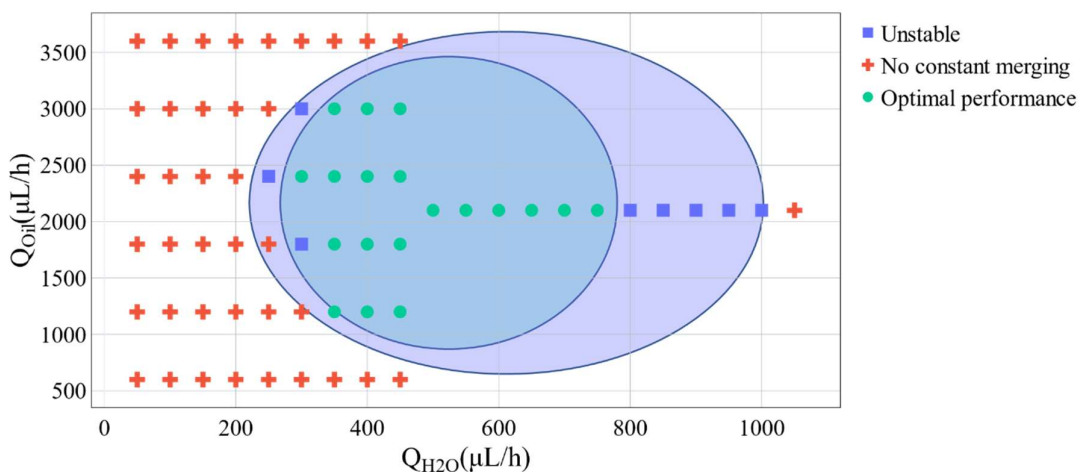


**Figure 2.10.** Flow rates and performance of the chip based on the generation→ combination approach (Purple Chip), with 65  $\mu\text{m}$  in height. Three regimes are identified: No constant merging (only a few pairs of droplets merge, while the vast majority do not), unstable merging (many droplets merge but pairs of droplets are frequently produced but do not merge) and optimal performance (practically every pair of droplets merges).

From these experiments, it was observed that there is a regime of flow rates that allows the proper functioning of this nozzle without any external energy input to merge the droplets. This means that, even if the active methods proposed by Frenz *et al.*<sup>5,9</sup> could ease the coalescence of pairs of droplets generated by this dual nozzle, they are not strictly necessary to produce and merge droplet pairs. Additionally, we found that this regime was surrounded by areas in the “phase diagram” where the operation of the chip did not lead to an efficient merging of the droplets.

The center of the region of stability identified in this set of experiments was selected as the first set of flow rates to attempt to synthesize  $[\text{Fe}(\text{pz})\text{Pt}(\text{CN})_4]$ :  $Q_{\text{oil}} = 2100 \mu\text{L/h}$  and  $Q_{\text{H}_2\text{O}} = 600 \mu\text{L/h}$ . The *generation*→ *combination* approach in our experiments led to an inefficient merging of droplets when the solutions with food colorants were substituted by reactants even if additional elements were incorporated in the design of the chips to favor the merging of droplet pairs, and therefore it was dismissed (see chapter 3.1). For this reason, we changed our strategy towards devices based on the *combination*→ *generation* approach.

### 2.2.3 Second experimental approach: *Combination*→ *generation*.

Here, instead of generating and merging pairs of droplets with solutions of reactants, there is only a single stream of droplets containing all the reactants *ab initio*. As explained before, the proper functioning of these devices does not depend on the pressure oscillations, so they can work efficiently within a larger range of flow rates and capillary numbers than the devices based on the *generation*→ *combination* approach. Our first device based on this approach is shown in figure 2.11, here named *Blue Chip*. Here, a straight flow of water is intercepted

laterally by two perpendicular flows of solutions with reactants from each side. The three flows are contained in the same channel until two flows of oil intercept them laterally from each side in a flow-focusing junction. In this point, the combined flow of reactants and water is split into a single stream of droplets.

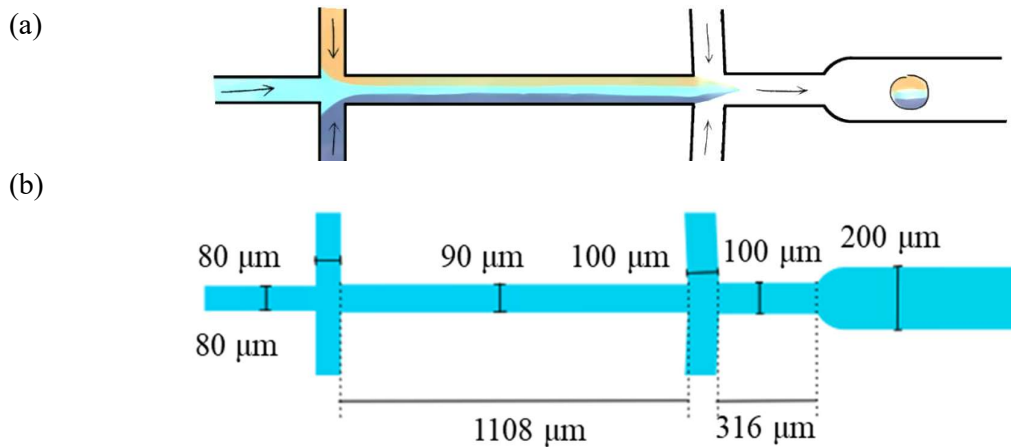


**Figure 2.11.** Functioning of nozzle of the first device based on the combination→ generation approach, here named *Blue Chip* (a). Blueprint of the nozzle of this device (b).

The *Blue Chip* has other features that differentiate it from our previous designs, as can be seen on its blueprint in figure 2.12. First, the channels that carry oil lack corners, which eases the removal of water, dust and other impurities that could reach it; second, reservoirs (that consist in a wide zig-zagged channel) are integrated between the nozzle and the filters in all the channels that transport water or solutions with reactants in order to delay the arrival of oil to the filters in case of backflow; and finally, the filters are improved (figure 2.13).

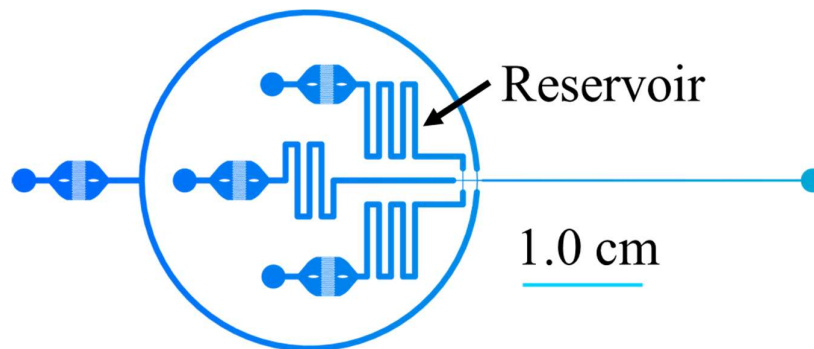


**Figure 2.12.** Blueprint of the first chip used in the combination→ generation approach (*Blue Chip*). The channel acting as a reservoir is marked as such.

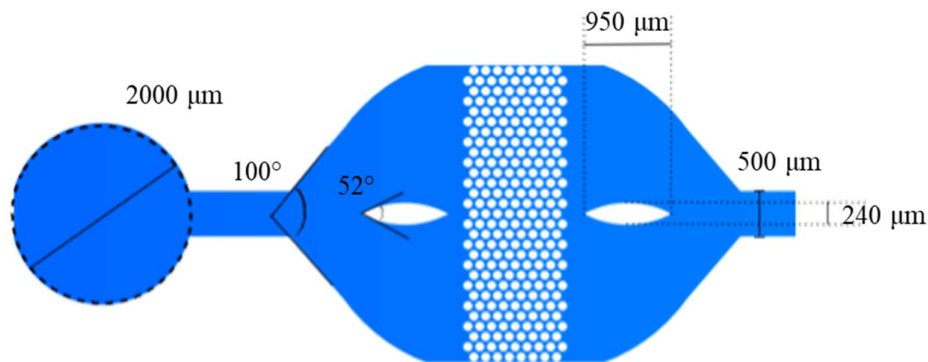


**Figure 2.13.** Improved filter of the Blue Chip, containing 246 columns. Compared with the previous filter, the new one is wider and shorter, which reduces the pressure drop generated by the filter.

Just as in the previous approach, we analyzed the performance of the *Blue Chip* by substituting the solutions of reactants by water and food colorant. In figures 2.14 and 2.15 the performance of this device is shown. It is easy to note that even if the three flows are contained in the same channel (blue, orange and colorless), they do not seem to mix by perpendicular or turbulent flows. This is because of the laminar character of the flows in this channel (as predicted by the low Reynolds number of the flows involved when they are contained inside such a narrow channel). The only mixing mechanism identified here is the diffusion of the colorant, observed as fuzzy boundaries between the colors of each flow that become more prominent as the flows advance. This device successfully generates streams of droplets as the ones shown in figures 2.14 and 2.15 under a wide range of flow rates.

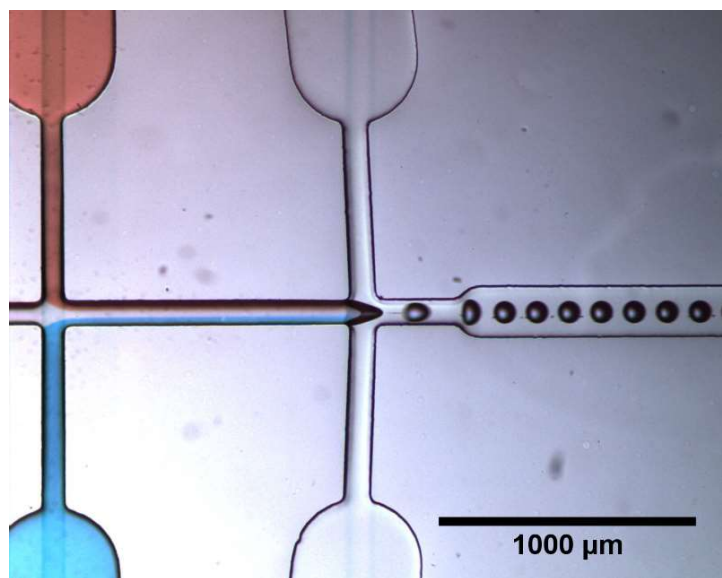


**Figure 2.14.** Microscopy images of the Blue Chip (first device based on the combination→ generation approach in operation): General view.

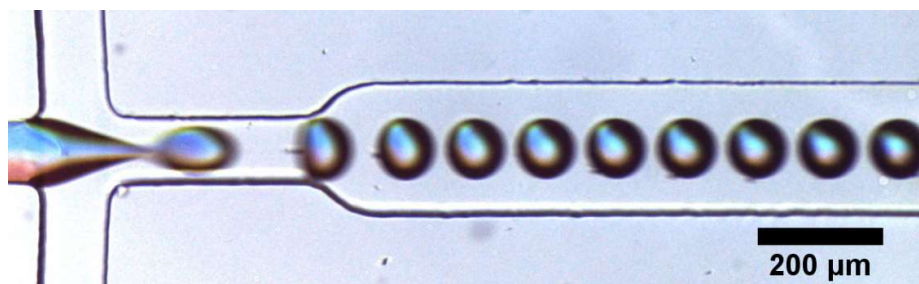


**Figure 2.15.** Microscopy images of the *Blue Chip* (first device based on the combination→ generation approach in operation): Stream of droplets analyzed under the microscope.

It is interesting that if scrutinized with enough care, the droplets generated in this experiment contain different colors (figure 2.15). The upper part of the droplets has a reddish color, just as the flow of water coming from the upper channel, while the lower part of them is blue, like the other flow of colored water. Note that, the colors do not leave its originating hemispheres instantly. This is an evidence of the prevalence of the *symmetry problem* in this device when it is used in this way. It is worth mentioning that there is a slight degree of diffusion of the colorants between the point where they are combined and the point where the droplets are formed. When only water with colorants is used, this diffusion does not seem to be too pronounced, and the buffer layer seems to separate both colors even after the droplet is formed.

Unfortunately, the *Blue Chip* led to the formation of solids inside of the channels when solutions with reactants were used (as explained in part 3). The origin of the formation of these solids is related with some degree of intermixing of the reactants caused by their lateral diffusion in the channel before the droplets are formed and will be described further in chapter 3.1. To circumvent the issues of this chip, and in particular to limit issues caused by diffusion, a new chip was developed (*Red Chip*), and it is shown in figures 2.16 and 2.17. Note that this new device does not have a reservoir between the nozzle and the filters. This is explained in chapter 3, and it is so because a proper starting sequence of flow rates allowed us to avoid backflow.

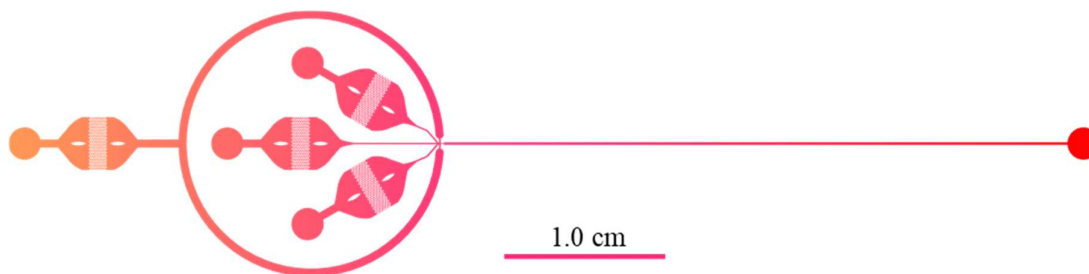


**Figure 2.16** Blueprint of the *Red Chip* (second device based on the combination→ generation approach). The filters have the same design as those in the *Blue Chip*.

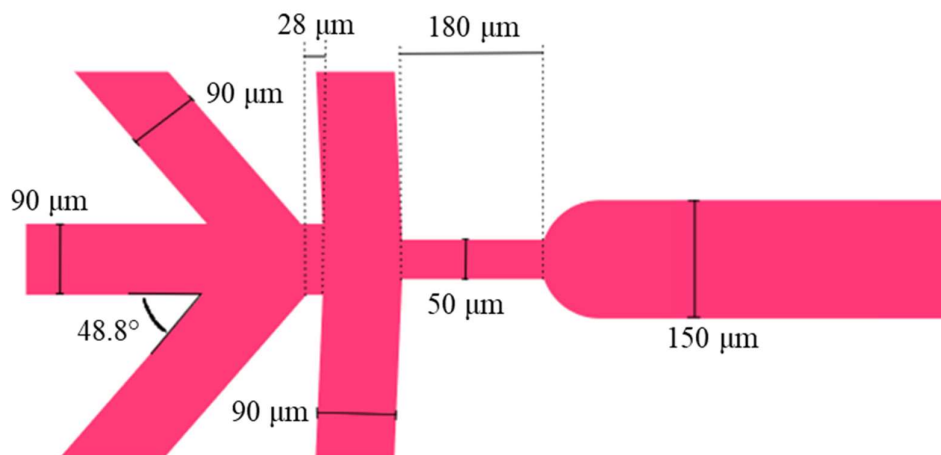


**Figure 2.17.** Blueprint of the nozzle of the Red Chip (second device based on the combination→ generation approach).

The *Red Chip* (the second based on the *combination*→ *generation* approach) is operated just as the *Blue Chip*. There is no difference in its behavior when operating without reactants. The only noticeable differences appear when solutions with reactants substitute the colored water, and this is discussed at length in chapter 3.1. Here it is only worth mentioning that, while the *Purple Chip* could work successfully for periods of 10 minutes (*generation*→ *combination*, see chapter 3.1) and the *Blue Chip* could work for around an hour before clogging, the *Red Chip* was the first one that allowed the synthesis of  $[\text{Fe}(\text{pz})\text{Pt}(\text{CN})_4]$  in a continuous way until the syringes with solutions of reactants were empty (after ~4.5 h). This does not mean that this device can work *ad infinitum*. It only means that it can work for more than 4 hours without clogging.

We designed a new chip, with small modifications, for which the performance was dramatically improved with respect to the *Red Chip*. The channels carrying oil to the nozzle were reduced, curves were incorporated in the exit nozzle (to eliminate the *symmetry problem*), and more importantly, the angle at which the reactants enter the nozzle was set to  $55^\circ$  (see chapter 3.2 for further details). This last chip is named *Green Chip* and is the most advanced device we have tested so far. Figures 2.18 and 2.19 show the blueprint of the *Green Chip*

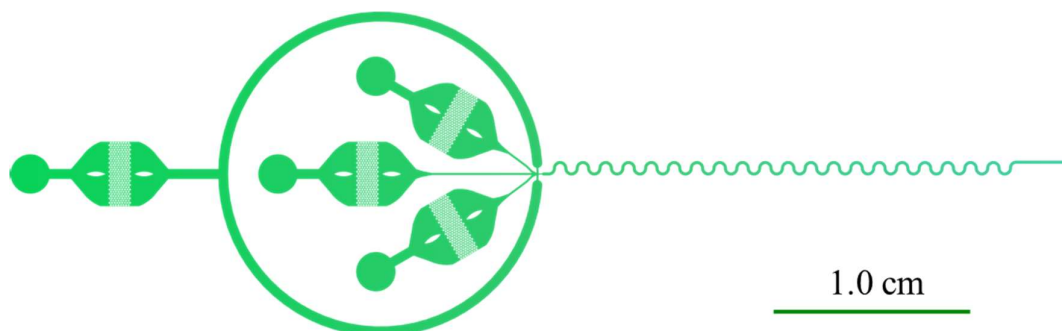


**Figure 2.18.** Blueprint of the Green Chip (third device based on the combination→ generation approach). The filters have the same design as those in the Blue Chip.

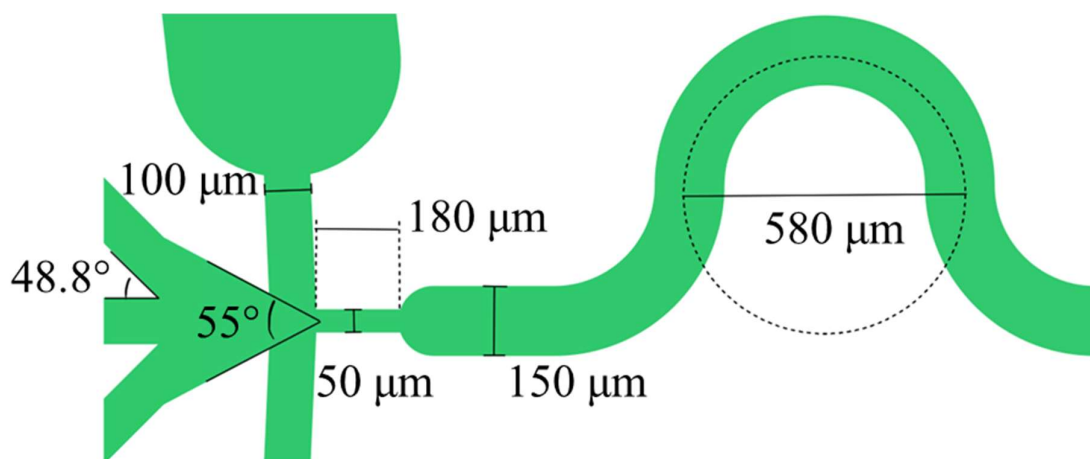


**Figure 2.19.** Blueprint of the nozzle of the Green Chip (third device based on the combination→ generation approach).

#### 2.2.4. Summary and conclusions to developed microfluidic devices for the synthesis of switchable materials.

The first part of this chapter dealt with the methods we developed to use chip-based droplet microfluidics for the synthesis of solid materials. There are two approaches to perform chemical synthesis in droplet-base microfluidics, here named *generation→ combination* and *combination→ generation*. We explore the use of both approaches but at this point, we only presented the behavior of these devices when solutions without reactants were pumped through them. All our devices can be successfully operated when water with food colorant substitutes the reactant solutions. In the chips based on the *generation→ combination* approach, this means that under the adequate conditions, the pairs of droplets are formed at the same time and that they merge at the end of the nozzle. The chips can be operated this way for extended periods of time.

In the chips based on the *combination→ generation* approach, we can see that the solutions with colorants are always separated by the water of the buffer layer. Even once the droplet is formed, we can see that the colorants stay at each hemisphere of the droplet and a layer of water divides them. In the *Blue Chip* (first device based on the *combination→ generation* approach), a slight diffusion of the food colorant can be seen between the point where the colorants are combined and the point where the droplets are produced.

All these devices have limitations as well. Due to the high flow rates needed for their operation, the pressure drop along the exit channel is very high, so this channel cannot be extended. This limits the residency time offered by these systems. Moreover, the mixing inside the droplets can be improved in the *Blue, Red and Green Chips* by the incorporation of chaotic mixers or curvatures in the nozzle or the exit channel.

At this point, the driving force of the evolution of the devices (*Purple, Blue, Red and Green*) is not very clear. Nevertheless, part 3 describes the performance of these devices when

they are operated using solutions with reactants, and the reader will become aware of the failures of each device that led us to the design of the next one. It is important to note that the experience acquired from these devices will lead to newer devices in the future. The device shown in the conclusions of this chapter (*Black Chip*) is an interesting candidate to replace the *Green Chip*, incorporating upgraded filters and mechanisms to reduce the hazards in the laboratory.

### *Chapter 2.3. In situ fine-tuning of microfluidic chips by swelling and its application to droplet microfluidics.*

For many applications of droplet microfluidics, the size of the droplet plays a major role in the performance of the chip. For example, in the crystallization of proteins using microfluidics, Zheng *et al.* argue that depending on the mechanism, the nucleation rate can depend either on the volume of the droplet (in the case of homogenous nucleation), or on the surface of the droplet (in the case of heterogenous nucleation).<sup>12</sup> This idea can also be extrapolated to the synthesis of other materials. For instance, Shi *et al.* found the coexistence of both mechanisms in the microfluidic synthesis of  $\text{KAl}(\text{SO}_4)_2$ ,<sup>13</sup> and it seems judicious to assume that the size of the droplets in microfluidics influences the chemical environment inside it. Unfortunately, although this idea makes sense from a theoretical point of view, only a few studies are focused on the effect of the droplet size because of the difficulties to control it accurately.

The growing interest to generate droplets with a controllable and narrow size distribution has led to many studies focused on predicting the size of droplets generated in microfluidic chips and, as explained in part 1.1, the related equations depend on the mechanism the droplet is generated through.<sup>6,14-16</sup> Generally, a model that allows the easy calculation of the droplet size with low accuracy, but at very accessible computational cost, is to assume that their diameter changes linearly with respect to the inverse of the capillary number (equation 1.9 from chapter 1.1).<sup>3</sup> With this in mind, a few experimental strategies can be easily deduced. The simplest one is to use a single chip and modulate its operating conditions, i.e. adjusting the flow rates,<sup>3,15</sup> adding a surfactant to the continuous phase<sup>17</sup> or changing the viscosity<sup>18</sup> as well as the temperature of the fluids.<sup>3</sup> The general set of tools to modulate the size of the droplets contains these techniques as well as some active methods, based on the use of an external energy input to manipulate the fluids (for example, through the use of electric fields,<sup>19,20</sup> channel deformations<sup>21,22</sup> or mechanical forces<sup>23-25</sup>).

Each one of these methods presents a set of advantages and disadvantages. For example, most active methods to control the size of droplets require additional sophisticated infrastructures, like voltage sources<sup>19,20</sup> or ultrasound generators.<sup>23-25</sup> Additionally, some approaches to the active control of the size of droplets involve the manufacture of multilayer chips, which requires the use of mask aligners.<sup>21,22</sup> The passive methods to control the droplet size have drawbacks as well: Changing the fundamental operating parameters of a microfluidic system (like the flow rates or the temperature), has a significant impact on the reaction conditions, which complicate the analysis of the effect of the droplet size on the reaction. For instance, Paseta *et al.* analyzed the effect of the residence time on the microfluidic synthesis of MOFs ( $\text{Fe-MIL-88B-NH}_2$ ) and found that longer reaction times were related with the production of larger particles.<sup>26</sup> Likewise, Faustini *et al.* report that longer residency times in the microfluidic synthesis of HKUST-1 lead to higher synthetic yields but with lower BET pore surface areas in the product.<sup>27</sup> Finally, a way to keep the operating conditions constant and to avoid the use of active methods to modulate the size of the droplets, is to change the geometry of the chip. A change in the geometry of the chip affects the linear flow speed of the

fluid and, therefore, the capillary number as well. To adjust the size of the droplets this way, it is necessary to test multiple geometries and fabricate a new chip *ab initio*, at each iteration. This makes this approach highly impractical and costly.

With this in mind, we developed a new method to change the size of some critical dimensions in microfluidic chips, which allows the modulation of the size of the droplets using a single PDMS chip. Our method does not require the use of additional infrastructure, of surfactants, or changes in the temperature and the flow rates used. Instead, the geometry of the chip is adjusted through the addition of a swelling agent that causes controlled deformations in the PDMS chip *in situ*.

The phenomenon of swelling is well known and has been studied for decades. Nevertheless, the literature about the possible applications of this phenomenon is scarce. A few recent studies focus on some critical aspects of the swelling of PDMS, like the study of Saunders *et al.* about the kinetics of swelling of PDMS when it is exposed to vapors of organic solvents,<sup>28</sup> or the article of Dangla *et al.* about the effect of swelling on the deformation of microchannels.<sup>29</sup> In general, swelling is considered as something to be avoided, and solvents that cause it are said to be “incompatible with PDMS”.<sup>30,31</sup> Despite the negative opinions about swelling, here we propose to use it to modify the geometry of a PDMS chip in a controlled way and exploit this feature for the modulation of the size of droplets.

### 2.3.1 General approach

The first step to make use of swelling for any application is to gain some understanding about how PDMS swells when it is exposed to a mixture of solvents: one of them that is known for causing PDMS to swell (or *swelling agent*) and another one, known to be inert towards PDMS. The idea is that when PDMS is exposed to mixtures of these solvents, the magnitude of the swelling will depend on the concentration of the swelling solvent: The higher this concentration the bigger the swelling. We could then be able to modulate the geometry of the PDMS chip, the size of the channels in which the droplets are formed and consequently the droplet size.

In a first step, we wanted to understand how the geometry of a wall made of PDMS changes when the concentration of the swelling agent is increased. To do so, we fabricated a chip containing a set of walls of different thicknesses and exposed them to different mixtures of toluene and mineral oil. Here, we chose toluene as the swelling agent because it is known to cause a significant swelling of PDMS (increasing its size in 31%).<sup>31</sup> PDMS is known to be inert towards mineral oil and, in fact, mineral oil is used very often as the continuous phase in droplet microfluidics. Section 2.3.2 describes our results in this set of experiments. The results of these experiments gave us the information required for the design of the next experiments, i.e. the knowledge that PDMS swells almost linearly with the increase of the concentration of toluene.

In a second step we analyzed the kinetics of swelling and de-swelling of PDMS. It is very difficult to measure small differences in the width of a microscopic feature, so instead of analyzing the kinetics of swelling directly, we measured it indirectly from the change of the diameter of the droplets produced by a swelled T-junction. It is easy to measure the diameter of hundreds of droplets produced this way because of two main reasons: First, free software to

analyze images, like Image-J, can be used to measure the dimensions of those droplets automatically; and second, having a large number of measured droplets increases the accuracy of the determination of the average diameter dramatically. For these reasons, we fabricated a PDMS chip containing a T-junction, where droplets were generated and measured during extended periods of time. We increased the concentration of the swelling agent in a single step and determined how the droplet size changed with time. Later, the concentration of the swelling agent was decreased, and the evolution of the diameter of the droplets was analyzed as well. In section 2.3.3, we present the results of the experiments regarding the kinetics of the swelling-induced change in the diameter of the droplets.

In a third step, we analyzed how the diameter of the droplets is influenced by the progressive increase of the concentration of a swelling agent. Once we knew how much time was needed to reach a practical equilibrium, after which the diameter of the droplets changed marginally, we used the same design of T-junction and increased the content of swelling agent in small steps to see how the diameter of the droplets was affected by the presence of the swelling agent. The results of these experiments can be found in section 2.3.4.

Finally, to claim that this procedure is compatible with other experiments, we tested this principle in different scenarios: Changing the swelling agent, using different flow rates, mixing the carrier fluid of mineral oil and toluene with surfactants, swelling and de-swelling a chip to identify whether it could preserve its integrity and behavior after many cycles, and repeating some experiments with chips with different heights. Section 2.3.5 describes these additional experiments as well as our results.

In part 3 we describe the use of this approach on a real scenario, synthesizing solid particles of the Prussian Blue Analog  $\text{Rb}_x\text{Mn}[\text{Fe}(\text{CN})_6]_{(x+2)/3}$ .

### *2.3.2 Swelling in PDMS walls*

Branched polymers can display swelling when they are immersed in a solvent with a high affinity to its building blocks. Clearly, crosslinked polymers with a high molecular weight cannot be dissolved easily, so when they are immersed in a solvent, instead of migrating into the solvent phase and dissolve, they tend to host solvent molecules between the polymer chains. Since the solvent molecules hosted between the polymer chains occupy some space, the polymer expands. The more molecules are hosted in the polymer matrix, the more the polymer expands. In fact, swelling is a story about a competition between two intermolecular forces: On one side the building blocks of the polymer are attracted to each other (which prevents swelling); and on the other side, such building blocks interact with the solvent molecules (which favors swelling). This simple model helps us to understand a trend in the swelling ratios of PDMS in terms of the balance of these forces (the swelling ratio is measured as the relative increase in size of PDMS when it is immersed in a solvent). Although with some exceptions, this model successfully predicts that solvents made of small molecules with low polarity tend to have a higher swelling ratio than large or polar molecules. For example, when PDMS is soaked in pentane or triethylamine (made of small molecules with low polarity), it increases it

size in 44% and 58%, respectively; and when it is immersed in water (which is polar) or in mineral oil (with large molecules), no swelling is observed.<sup>31</sup>

Since the expansion of a piece of PDMS soaked in a swelling agent is relative to its original size, the absolute increase in its dimensions is larger when the PDMS pieces are bigger. For instance, a very thin PDMS structure of around 10  $\mu\text{m}$  surrounded by two channels is practically a membrane. If it swells, its size might change greatly with respect to its original size but, being so thin, the absolute increase in its size is minimal. In contrast, a thicker structure with a size in the mm or cm range, even if it swelled with the same swelling ratio as the membrane, having a larger initial size, its absolute expansion would be dramatically larger. This poses a natural problem in the controlled swelling of PDMS chips: If the PDMS structures in the chip swell with the same ratio, does it mean that larger PDMS motifs have a higher absolute expansion than thinner ones? And in that case, to which extent is it possible to control the swelling in designs with motifs of different dimensions? To address this issue, we built a 75  $\mu\text{m}$  high chip containing a single channel (500  $\mu\text{m}$  wide) zigzagging around walls with different widths, varying gradually from 30 to 770  $\mu\text{m}$  (*Chip A*), as shown in figure 2.20.

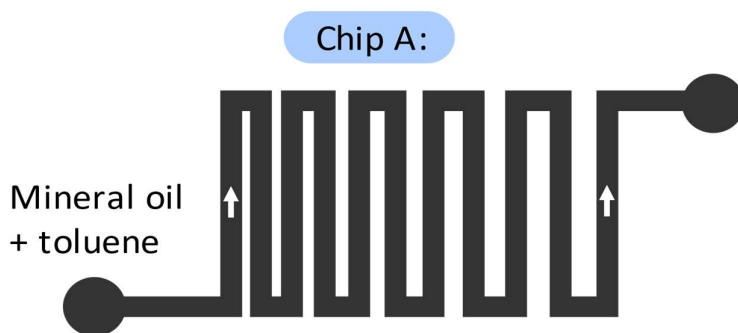


**Figure 2.20.** *Chip A, comprising a zigzagged channel running around PDMS walls with a different thickness. Here, only a simplification of the geometry of the chip is presented to help the reader to understand the main features of this chip. In the real one, the widths of the walls changed too dramatically to be easily seen in the same image.*

Through this channel, we pumped mixtures of mineral oil and toluene in different ratios, where the concentration of toluene (acting as a swelling agent) varied from 0 to 48% V/V. The concentration of toluene was increased in steps of 6%, waiting 40 minutes in each step. The total flow rate was set to:  $Q_o = Q_{Mineral\ oil} + Q_{Toluene} = 1500 \frac{\mu\text{L}}{\text{h}}$ . The concentration of toluene was modulated in situ by adjusting the relative flow rates of mineral oil ( $Q_{Mineral\ oil}$ ) and a 50% V/V solution of toluene in mineral oil ( $Q_{Toluene50\%}$ ). These two fluids were combined and mixed in-line using a metallic T-junction and a PEEK frit mounted on a low pressure ETFE union assembly as shown in figure 2.21.

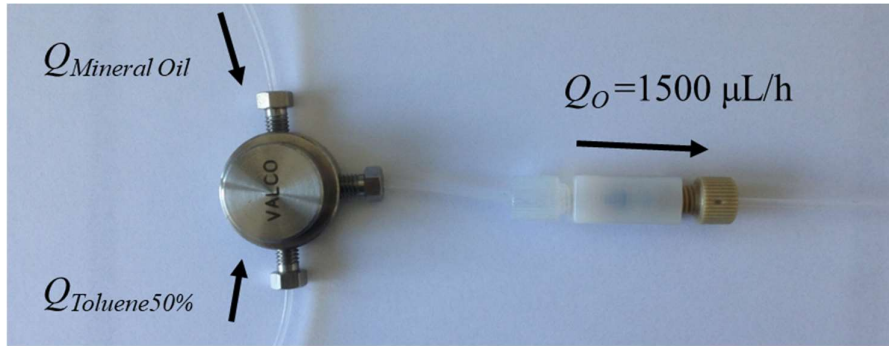


**Figure 2.21.** Mixing device where mineral oil and a mixture of toluene and mineral oil are combined in an external T-junction and mixed in a PEEK frit mounted on a low-pressure ETFE union assembly.

To quantify the effect of swelling, *chip A* was placed under the microscope, exposed to different concentrations of toluene and the deformation of each wall ( $\delta w$ ) was determined:

$$\delta w(C_T) = w(C_T) - w_0 \quad (2.11)$$

Here,  $\delta w(C_T)$  is the deformation at the toluene concentration  $C_T$ ,  $w(C_T)$  is the width of the wall when it is exposed to the mixture of mineral oil and toluene, and  $w_0$  is its original width. Measurements were performed 20, 30 and 40 minutes after increasing the concentration of toluene and we did not find any difference in the thickness of the walls between 30 and 40 minutes of exposure to the swelling agent.

Just as we expected, the effect of the swelling of PDMS depends on the original thickness of each wall ( $w_0$ ). In the thinnest wall ( $w_0 = 30 \mu m$ ), a clear damage to the material is seen, as shown in figure 2.22.

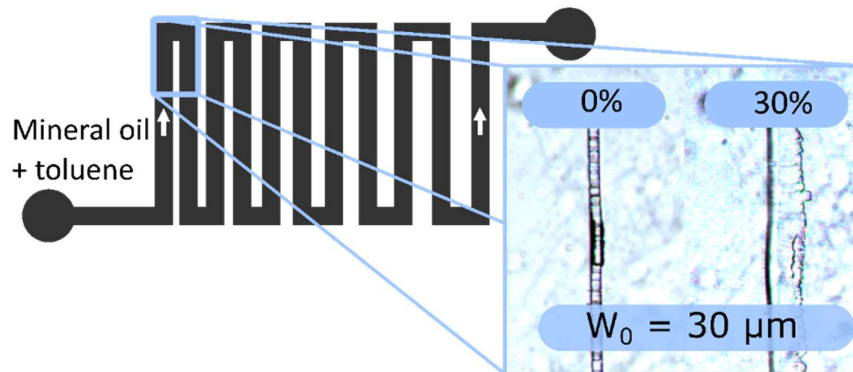


**Figure 2.22.** Damage of the  $30 \mu m$  PDMS wall after exposing it to a 30% V/V solution of toluene and mineral oil.

Figures 2.23 to 2.25 show the deformation of the walls from  $w_0 = 50 \mu\text{m}$ , to  $w_0 = 720$  as a function of the concentration of toluene, where the red line in each plot corresponds to the linear regression of the measurements.

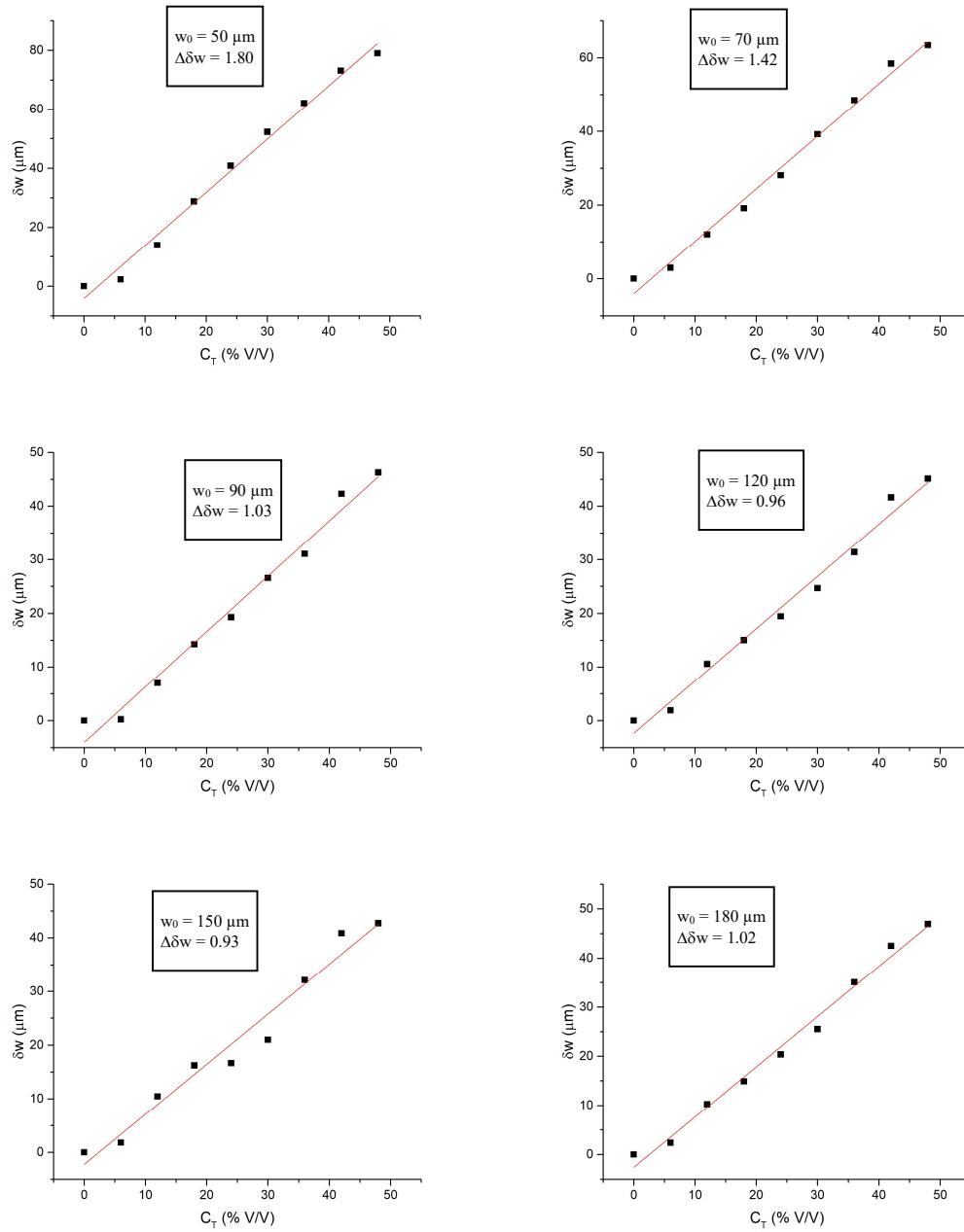


**Figure 2.23.** Deformation of the PDMS walls with a thickness  $w_0$  between 50 and 180  $\mu\text{m}$ .

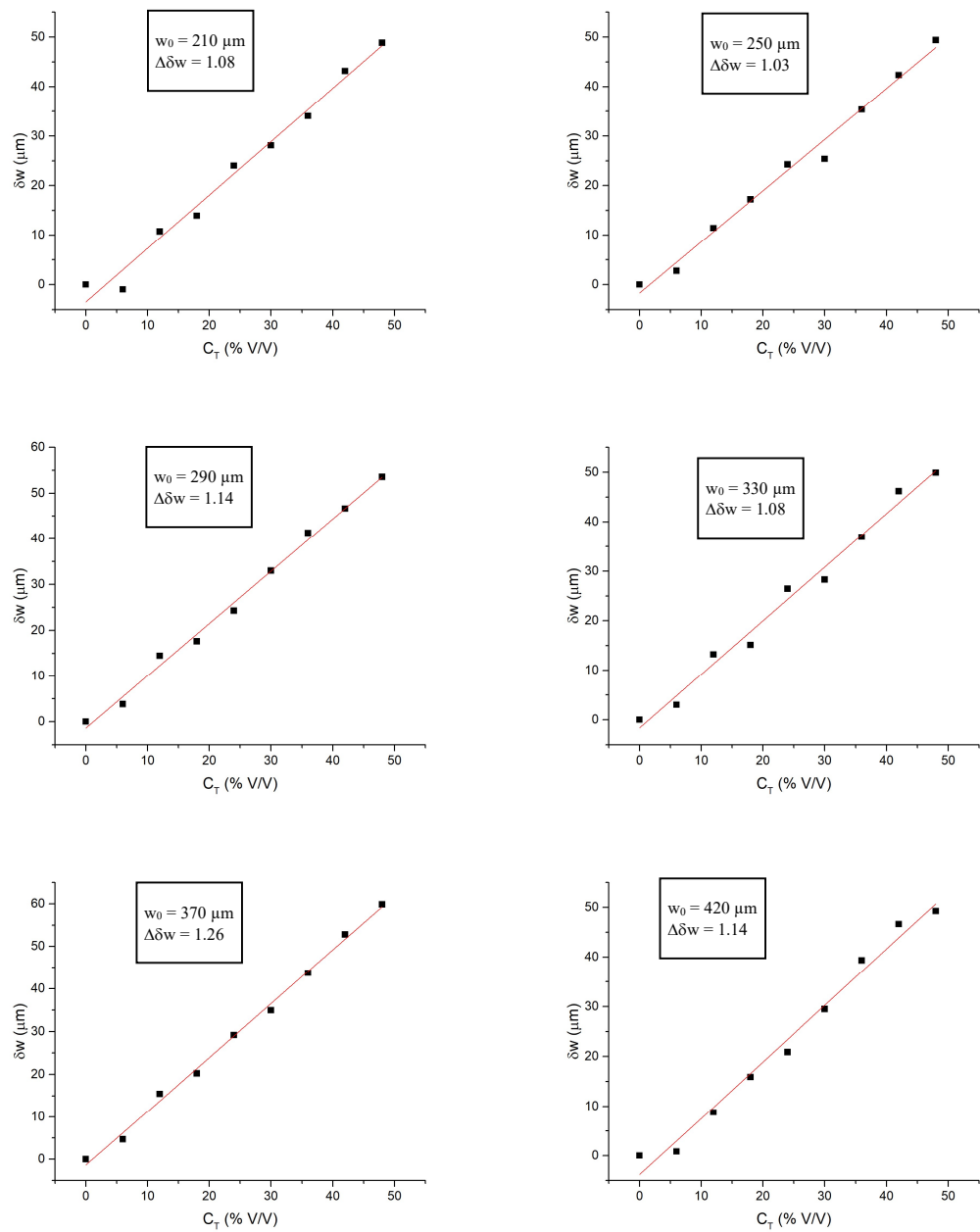


**Figure 2.24.** Deformation of the PDMS walls with a thickness  $w_0$  between 210 and 420  $\mu\text{m}$ .

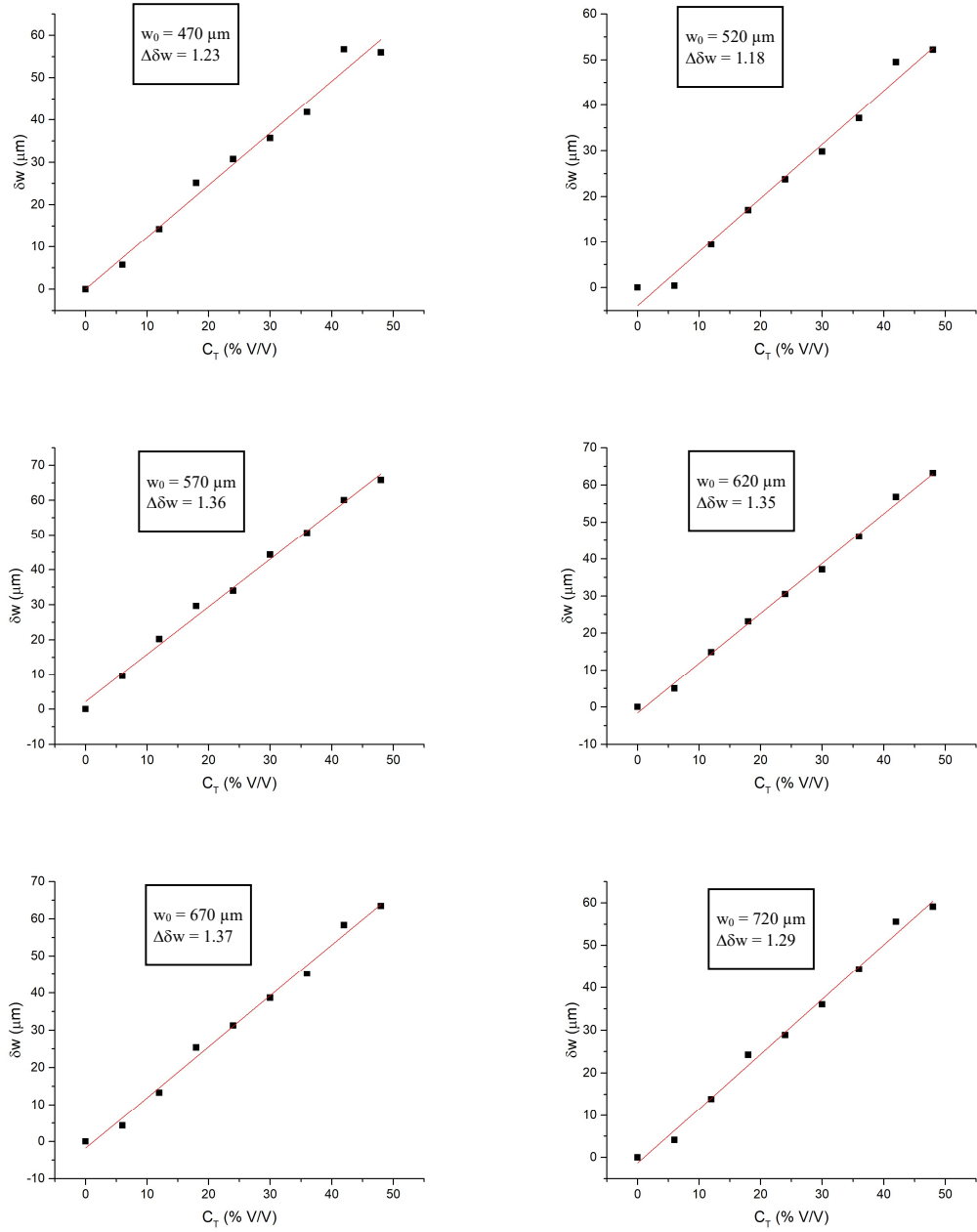


**Figure 2.25.** Deformation of the PDMS walls with a thickness  $w_0$  between 470 and 720  $\mu\text{m}$ .

It is very interesting that in all the walls, the deformation  $\delta w$  reach stable values that resemble a straight line. From these plots, we estimate the swelling response coefficient  $\Delta\delta w$ , which is equal to the slope of the linear regressions:

$$\Delta\delta w = \frac{d\delta w}{dC_T} \quad (2.12)$$

Except for the wall with 30  $\mu\text{m}$  of width, the walls swell linearly as the concentration of toluene increases. This linear response is present in all the walls, even if there is variation in the swelling response coefficient across different walls. It is very encouraging to find such a linear behavior in the response of PDMS to swelling. First, it makes very easy to predict the deformation of a given wall exposed to a determined concentration of a swelling agent. For this, it is enough to measure its deformation when it is exposed to two different concentrations of toluene, and the expected deformation can be inter- or extrapolated easily. Second, microfluidic devices have diverse motifs, and it is very useful to know that all of them swell linearly independently of their dimensions. The values of the swelling response coefficient as a function of the initial width of the wall are presented in figure 2.26 (the bars correspond to the 95% confidence interval).

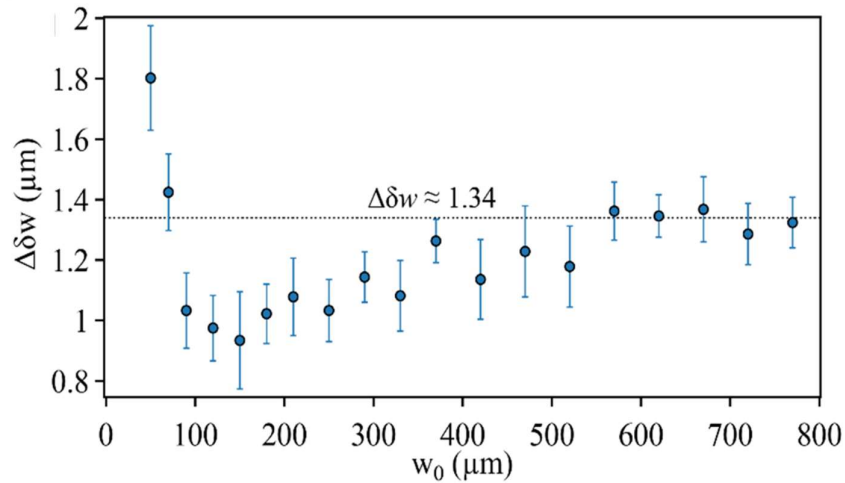


**Figure 2.26.** Swelling response coefficient in PDMS walls with different thicknesses. The bars correspond to the 95% confidence interval.

The swelling response coefficient is similar for all the walls, with an expansion ranging from 0.9 to 2  $\mu\text{m}$  per percent of toluene, and our results can be divided into 3 sections. The first one corresponds to the walls with an initial width below 70  $\mu\text{m}$ . In such cases (the first two points in figure 2.26 that correspond to the data sets  $w_0 = 50 \mu\text{m}$  and  $w_0 = 70 \mu\text{m}$ ), we observe an outstandingly large response of the material. The response reaches a minimum in the walls with an initial width  $w_0$  between 100 and 150  $\mu\text{m}$ , where the second regime starts. From this point on, the response coefficient increases asymptotically until it reaches a plateau at around  $w_0 = 570 \mu\text{m}$ . The third regime contains all the walls with  $w_0 \geq 570 \mu\text{m}$ , and their

swelling response coefficient remains around 1.34  $\mu\text{m}$  of expansion per percent of toluene. In this regime, the swelling response coefficient changes marginally.

The analysis of these results must answer three questions. First, we explain why the walls swell linearly with the concentration of toluene. Afterwards, we explain why the walls with different thicknesses have different swelling response coefficients. Finally, we give an explanation about why this response coefficient reaches a plateau in the thicker walls.

The linear response of the swelling of PDMS exposed to toluene is not completely surprising. We do not have an easy way to quantify the amount of toluene trapped in the PDMS matrix, but if we assume that it is proportional to its expansion (which is quite reasonable), we can say that PDMS obeys a Henry-like behavior. In nature, it is very common to see that the amount of matter adsorbed or absorbed by a matrix is proportional to the pressure or concentration of the sorbed species. For instance, at low pressures the solubility of gases in liquids is proportional to their partial pressure.<sup>32</sup> In more complex systems, for example where the sorption follows a Langmuir isotherm, the Henry-like behavior is preserved at low pressures or concentrations.<sup>32</sup>

The reasons why the walls with different thicknesses behave differently and why the behavior of the thicker walls loses this thickness-related response are less intuitive. When a piece of PDMS is immersed in toluene, it swells until increasing its linear size by about 31%.<sup>31</sup> This means that if PDMS can swell without any constraints, the final size is proportional to its original dimensions. In such cases, the equilibrium depends on the balance of the intermolecular forces (polymer-polymer and polymer-solvent). However, PDMS in a microfluidic chip is covalently bonded to a rigid glass substrate that hinders its free expansion. This means that the balance of forces that define how much solvent is hosted by the polymer matrix is now affected by mechanical forces opposing its expansion. On one side, as the PDMS walls are exposed to higher concentrations of toluene, more molecules are hosted in the polymer matrix and, on the other side, as the deformation increases, there is a stronger mechanical force opposing the insertion of more solvent molecules into the polymer matrix. To understand this, we shall make an analogy, where we see the PDMS as a sponge that can hold large amounts of liquids when it is not subjected to a mechanical force but when it is squeezed, it loses its capacity dramatically. The glass slide to which the PDMS chip is attached does not really contract the PDMS, but it limits its expansion. This means that, as PDMS swells, the glass slide generates some stress on the PDMS, that “squeezes” some molecules out of the PDMS. This stress can be propagated with a different degree of efficiency across the PDMS. Structures displaying a lower degree of ease to propagate this tension (like very thin walls), would behave more like a free sponge when compared with other motifs that propagate this stress more efficiently. Therefore, their response depends on their thickness (as it is the case of the walls where  $w_0$  is between 100 and 500  $\mu\text{m}$ ). In thicker walls, the mechanical hindrance caused by the rigidity of the glass seems to reach a balance with the forces that favor swelling, and although this balance is complex to describe, it is phenomenologically simplified as a constant response coefficient.

About the origin of the outstanding response in the thinnest walls (for  $w_0 = 50 \mu\text{m}$  and  $w_0 = 70 \mu\text{m}$ ), it is only possible to speculate. Intuitively, since in those cases the height of the

wall is larger than its width, swelling is stronger in the vertical than in the lateral direction, and buckling can easily occur. A curved structure would seem larger under the microscope than its actual size, so the real swelling response coefficient in thin walls is difficult to determine.

These observations are very important for using the controlled swelling to modulate the geometry of a chip, since they show the first limitation of this technology: The distance between motifs in a microfluidic chip can affect their swelling response coefficient; so, to achieve a uniform swelling in the chip, the motifs must be separated from each other by a critical distance. In the chip we analyzed, this distance is around 570  $\mu\text{m}$ .

Clearly, a straight microfluidic channel with no motifs around it can be conceived as a channel surrounded by two semi-infinite walls. Since those theoretical walls would have an initial width larger than 570  $\mu\text{m}$ , they would belong to the third category of our results, and their swelling response coefficient would remain close to 1.34  $\mu\text{m}$  of expansion per percent of toluene. Attention must be paid to the fact that such walls would be exposed to a swelling agent only on one of their sides (because the other one would remain infinitely far away), so their swelling response coefficient should be halved as 0.67  $\mu\text{m}$  of expansion per percent of toluene. Nevertheless, since the channel is constituted by two of these walls swelling at 0.67  $\mu\text{m}/\%$ , the channel shrinks of 1.34  $\mu\text{m}$  per percent of toluene (twice the expansion of each wall).

### 2.3.3 Kinetics.

It is very complicated to analyze the kinetics of PDMS swelling by the direct measurement of the deformation of the channels using a conventional microscope. This is because the expansion of PDMS due to swelling is very subtle, so many important changes occur at a scale below the maximum resolution allowed by the experimental setting. These limitations can, nevertheless, be overcome. For instance, Saunders *et al.* analyzed the kinetics of swelling of PDMS films exposed to vapors of swelling agents using an interferometric refractometer.<sup>28</sup> In our case, it was more appropriate to use a droplet generator and see how the droplet size evolves with time (analyzing the kinetics of PDMS swelling indirectly), than to measure the deformation of the channels directly.

In fact, with our current infrastructure we can capture and measure many different droplets automatically using IC Capture and Image-J. This way, we can extract statistical information about the diameter of the droplets and improve the accuracy of our measurements enormously. Moreover, it is convenient for us to measure the kinetics using a droplet generator because we consider that swelling can be a great tool to modulate the size of droplets in the synthesis of materials. For that reason, it is more important for us to understand the kinetics of effect of swelling on the size of droplets, than the kinetics of swelling itself.

For this purpose, we built a PDMS chip containing a T-junction with 50  $\mu\text{m}$  wide and 105  $\mu\text{m}$  high channels (*Chip B* in figure 2.27). In our experiments using this device, a flow of water following a straight path is intercepted laterally by a flow of mineral oil that breaks the flow of water down into a stream of droplets. Although most groups use T-junctions in the opposite configuration (where water intercepts the path of mineral oil laterally), we used the

same configuration as the one used by Frenz *et al.*<sup>9</sup> in their dual nozzle for droplet pair generation. Therefore, we analyzed the behavior of a T-junction in our configuration (where oil intercepts the path of water laterally), instead of using the configuration that most researchers use. In any case, there are not many reasons to believe that this principle would only work in one of those configurations and not work in the other. The procedure to fabricate this chip is explained in the appendix.

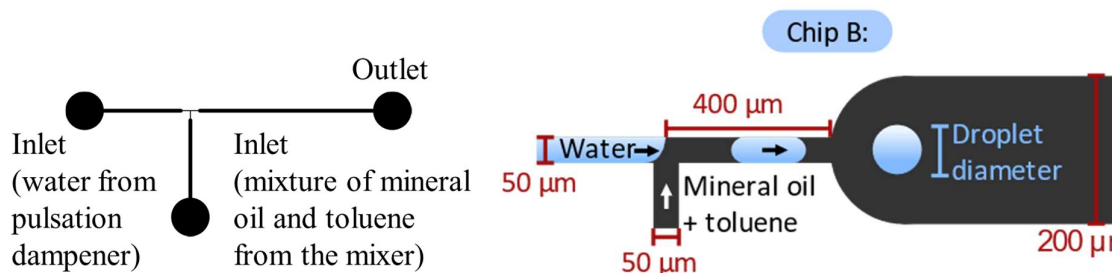


**Figure 2.27.** T-junction with 50 μm channels used to analyze the effect of swelling on the size of the produced droplets: overall aspect of the device (left) and geometry of the T-junction (right).

To measure the time required to produce droplets of a constant size, we followed the following procedure, as shown in figure 2.28 (the flow rate of water was set to 100 μL/h, and the flow of the solution of toluene in mineral oil, to 1800 μL/h):

- Initially, the concentration of toluene was set to  $C_T = 20\%$  V/V during 1h. The purpose of this stage was to ensure the contact between the piston of the syringe pumps and the plunger of the syringe.
- Afterwards, the concentration of toluene was changed in single steps from  $C_T = 20\%$  to  $C_T = 5\%$  V/V and *vice versa* repeatedly, letting the system reach equilibrium along 1.5h.

Instead of using a concentration of toluene of 0%, we used  $C_T = 5\%$  V/V because that ensured that the piston in the syringe pump always exerted some force on the plunger of the syringe, reducing the time lag between the moment the piston in the syringe starts moving and the moment when the liquid starts flowing through the tubing (the syringes have some flexible parts, which might need time to reach an equilibrium deformation). The high flow rate of mineral oil reduced the time required for the solution of toluene in mineral oil to reach the chip under the microscope. Additionally, keeping such high flow rates reduced the pulsations from the pump. In preliminary experiments, different flow rates were quickly scanned and these flow rates were selected because they allowed the formation of a single row of droplets at a concentration of toluene of 20%, and the size of the droplets at 5 and 20% of toluene seemed to change notoriously under these flow rates. Clearly, other flow rates could also be used with the same authority. A picture was programmed to be taken each second, leading to a total of 32269 pictures in this experiment, which contain more than 600 000 droplets.

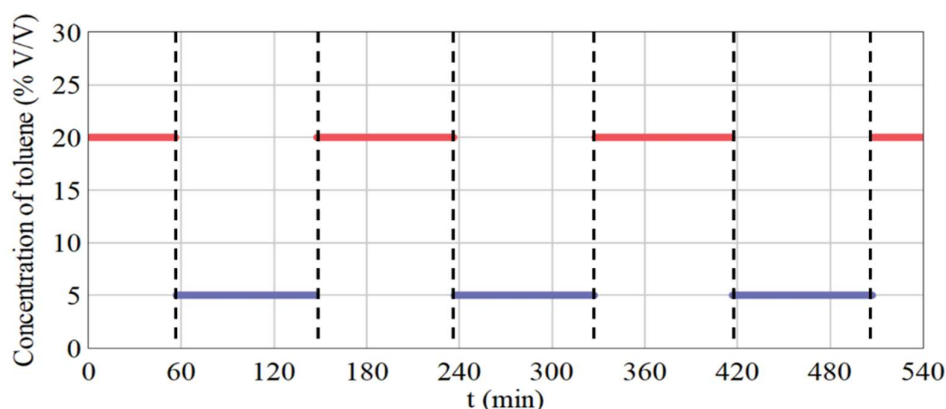


**Figure 2.28.** Program of the concentration of toluene used for the experiments.

To reduce the magnitude of the pressure oscillations in the flow of water, we built a PDMS chip (figure 2.29) designed to dampen high-frequency oscillations, and we connected it between the syringe with water (mounted on the pump) and the chip under the microscope. Since the swelling agent in these experiments is mixed with the mineral oil, it does not reach the pulsation dampener (which means that this ancillary damping device is not subject to swelling). The pulsation dampener is composed of three parts: a filter, 5 cm of a 1 mm wide channel (that due to the flexibility of PDMS, acts as a small capacitor) and 50 cm of a 90  $\mu\text{m}$  wide channel (acting as a flow resistor). According to the hydraulic analogy presented in chapter 1.1, the functioning of this device is analogous to the low pass filters used in electric guitars to reduce the treble. Without the use of such pulsation dampener it is still possible to perform these experiments; nevertheless, the dispersity index in the droplet size is dramatically affected because of noise pollution (independently of whether the chip is swollen or not).

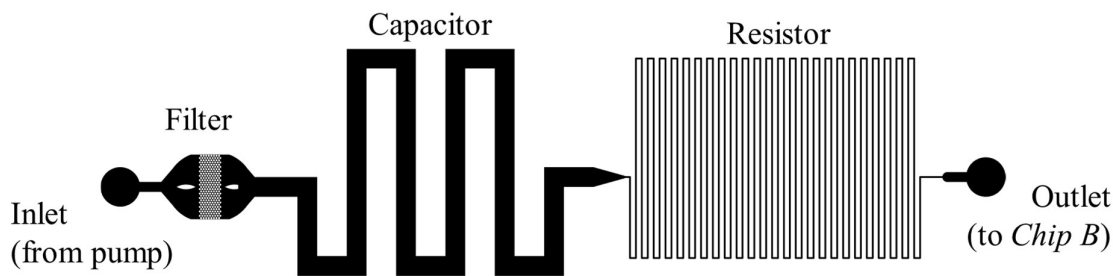


**Figure 2.29.** Pulsation dampener to eliminate the high frequency noise pollution. In the experimental setting, the pump carrying water is connected to the inlet, and the outlet is connected to chip B.

The geometry of the chip (shown in figure 2.27 and named “Chip B”), as well as the size of the droplets it produces are strongly affected by the swelling when the concentration of toluene is increased from 5 to 20% V/V, as is shown in figure 2.30. When the concentration of toluene was set to 5% V/V, the size of the droplets was 64  $\mu\text{m}$ . Once the concentration of toluene was raised to 20% V/V, the size of droplets reduced to 43  $\mu\text{m}$  after 90 minutes. All the

channels in the chip, including the ones comprised in the T-junction, reduced their size when the concentration of toluene was raised.

The geometrical change in the T-junction might be the most important factor affecting the size of the droplets, but it is not the only one. Toluene has a lower viscosity than mineral oil so, as stated in chapter 1.1, a change in the viscosity of the continuous phase implies a change in the size of droplets. Nevertheless, care must be taken in the direction of this effect: While a decrease in the dimensions of the channels leads to smaller droplets, a reduction in the viscosity (as happens when the concentration of toluene is increased) would lead to bigger droplets. This means that the shrinkage of the channels and the reduction in the viscosity (both caused by the presence of toluene), would have opposite effects on the droplets size.

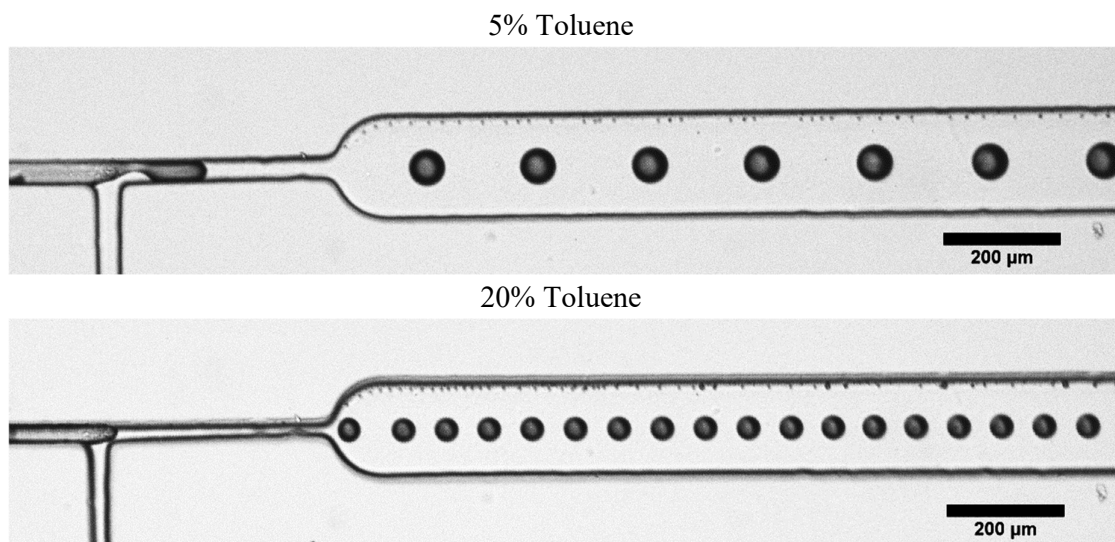


**Figure 2.30.** Comparison of the geometry of the chip and the droplet size when the concentration of toluene is 5% V/V (up) and 20% V/V (down).

When we analyzed the time evolution of the size of the droplets, as plotted in figure 2.31, we see gradual changes that are reversible in each cycle. To gather information about the kinetics of the swelling and de-swelling processes, we analyzed the sections of the curve highlighted in blue (de-swelling) and red (swelling). In these experiments, when all the droplets observed in the last minutes before changing the concentration of toluene were analyzed, the variation coefficient (also known as dispersity index) was between 0.7 and 1.1%, which is better than the values usually found in literature.

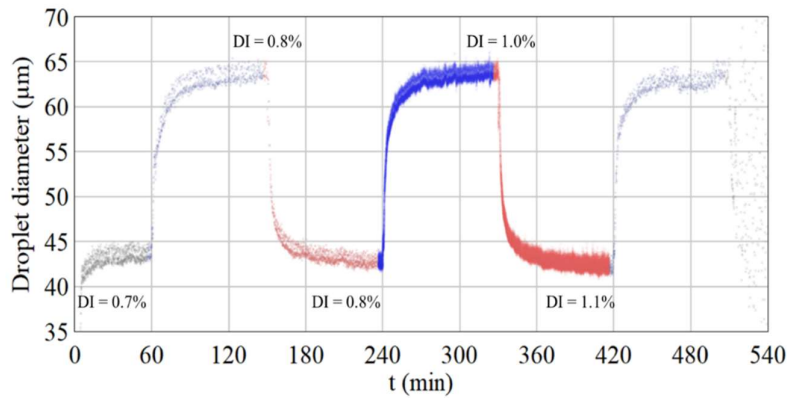


**Figure 2.31.** Evolution of the size of droplets across multiple cycles to establish the kinetics of their swelling-induced changes. The dispersity index (DI) was determined considering all the measured droplets of the last minute before each change in concentration. The cycle used for the analysis is highlighted. Only 1 in every 50 droplets of the curves corresponding to the other cycles are plotted to reduce the computational cost for the plot.

Figure 2.32 shows the average droplet size in each picture. The blue dots correspond to the measurements of the droplets in the de-swelling process, and the red ones, to the droplets in the swelling process.

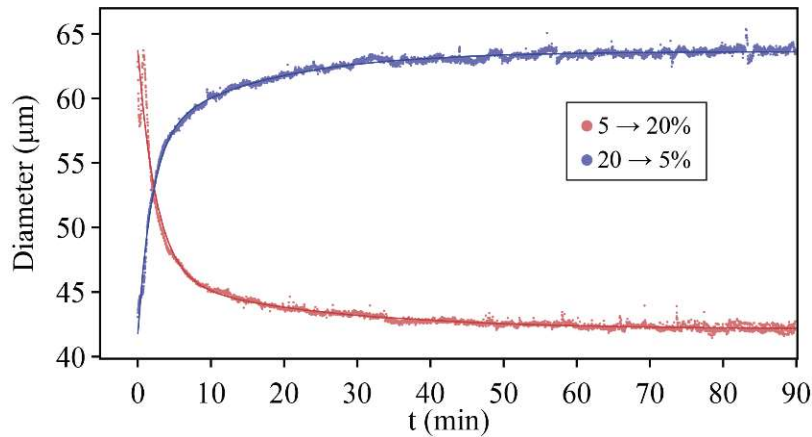


**Figure 2.32.** Time evolution of the size of droplets (averaged in each second) to determine the kinetics of swelling and de-swelling. The red dots correspond to the measured diameter of the droplets when the concentration of toluene was increased from 5 to 20% V/V; the blue dots correspond to the measurements when the concentration of toluene was decreased from 20 to 5%. The continuous lines correspond to the best fits to a bi-exponential model.

The change in the size of the droplets does not follow a single exponential process (as would be intuitively expected). Instead, it is very consistent with bi-exponential models. The lines in figure 2.32 show the best bi-exponential fit of the experimental results (equation 2.13).

$$Diameter = D_0 + \Delta D_1 e^{-\frac{t}{\tau_1}} + \Delta D_2 e^{-\frac{t}{\tau_2}} \quad (2.13)$$

According to our fit, at least two physical phenomena seem to coexist in the swelling and de-swelling processes (one of them, having a time constant around 2 minutes; and the other, in the order of 15 to 20 minutes). This observation agrees remarkably well with the results reported by Saunders *et al.*<sup>28</sup> who characterized the kinetics of PDMS swelling in thin films exposed to vapors or organic solvents as a double diffusion process. Remembering that the changes in viscosity and surface tension that result from the increase in the concentration of toluene should appear as soon as the solution with the new composition reaches the nozzle – and considering that the dead time in our device is of only a few seconds – the evolution of the droplet size (that occurs in the scale of tens of minutes) cannot be associated with the change in the composition of the carrier oil. In the entirety of our setup, the only parameter that has a characteristic evolution time in the range of tens of minutes is the swelling process. So, without a doubt, the kinetic experiments announce that the change in the size of the droplets is directly affected by the change in the geometry of the chip due to swelling. Table 2.2 shows the fitted parameters associated with the swelling and de-swelling processes.

Parameter	20 → 5% (V/V) (blue curve)	5 → 20% (V/V) (red curve)
$D_0$ ( $\mu\text{m}$ )	63.6	42.1
$\Delta D_1$ ( $\mu\text{m}$ )	-15.2	17.4
$\tau_1$ (min)	1.94	2.50
$\Delta D_2$ ( $\mu\text{m}$ )	-6.66	4.19
$\tau_2$ (min)	15.7	22.2
$\bar{R}^2$	0.973	0.990

**Table 2.2.** Fitting parameters resulting from the kinetic analysis of the swelling and de-swelling when the concentration of toluene in decreased from 20 to 5% and increased from 5 to 20% V/V.

From these values, we can deduce that the stabilization time for these experiments is about 30 minutes (95% of the change in the diameter of the droplets is achieved after this time). A time-lapse video showing the evolution of the size of the droplets in this experiment after a sudden change in the concentration of toluene from 0% to 20% V/V and from 20% to 0% V/V is available online:<sup>27</sup>

<https://onlinelibrary.wiley.com/action/downloadSupplement?doi=10.1002%2Fadmt.201900232&file=admt201900232-sup-0001-S1.mp4>

Nevertheless, we developed a method to accelerate the process. Since the kinetics of swelling are based on diffusion processes, they should depend on the concentration gradient of

the swelling agent at the interface between PDMS and the fluid. This means that it is possible to reduce the swelling time by exposing PDMS to a high concentration of toluene for a short period of time (so a high number of solvent molecules enter the polymer matrix). After this short exposure to high concentrations of toluene, this concentration is reduced to a value known to cause the desired magnitude of swelling, thus minimizing the concentration gradient. Since at this point the polymeric matrix already hosts many solvent molecules, the time required to absorb the equilibrium amount of solvent molecule is reduced. To show this principle, we flowed a solution with 50% of toluene in the mineral oil in a T-junction (*chip B*) for 3 minutes and later, we reduced this concentration to 30% in a single step. With this method, we reduced the equilibrium time to only c.a. 8 minutes ( $Q_O = 1000 \mu\text{l/h}$  and  $Q_w = 100 \mu\text{l/h}$ ), as shown in figure 2.33.

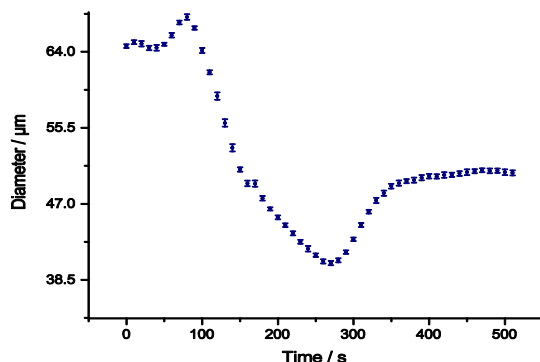


**Figure 2.33.** Accelerated swelling method. Here the diameter of the droplet reaches the equilibrium in 8 minutes instead of 30.

It is interesting to note that in the first moments after the content of toluene is increased, the diameter of the droplets increases somewhat (instead of decreasing). This is very interesting because it is likely the consequence of the change in the viscosity of the continuous phase that occurs in a stepwise fashion before the channel can even begin to deform. In other words, the PDMS takes minutes to swell, but the composition of the continuous phase changes instantly as the new solution of toluene in mineral oil reaches the chip (after a few seconds corresponding to the deadtime of the system).

### 2.3.4 Modulation of the droplet size.

To show how PDMS swelling can be used for the modulation of the size of droplets, we used the same T-junction (*chip B*) to produce a stream of droplets of water, while the continuous phase was composed by a mixture of toluene and mineral oil. The concentration of toluene was increased from 0 to 50% V/V in 20 steps, waiting 30 minutes to let the system reach equilibrium after each step. The flow rate of water in this experiment was set to  $30 \mu\text{L/h}$ , while the flow rate of the carrying oil was  $1800 \mu\text{L/h}$ . When the flow rate of water in this experiment is compared with the one used in the experiment carried out to analyze the kinetics, it is easy to note that they are not the same. The reason for this difference relies in the fact that, if droplets become smaller, the distance between them is reduced as well.

The experiments performed to study the kinetics only reached a 20% V/V concentration of toluene, but the concentration of toluene in this new experiment was as high as 50%. This means that the droplets in the new experiment are expected to be closer to each other than in the previous one. If the droplets are too close to each other, we cannot measure them easily and accurately (even if they do not merge). To ensure that the droplets would keep a safe distance between each other, the easiest way is to reduce the flow rate of water.

In this experiment, a picture was taken every second during more than 10 hours. This experiment resulted in more than 42 000 pictures containing more than a million droplets. Figure 2.34 shows the pictures of the system at selected concentrations of toluene. These pictures were taken just before increasing the concentration of toluene to the next step (i.e. after letting the system reach equilibrium for 30 minutes) and it can be seen that the droplets are separated from each other even when the concentration of toluene reaches 50% V/V. A time-lapse video showing the evolution of the size of the droplets as the concentration of toluene in the continuous phase is increased can be found online.<sup>27</sup>

<https://onlinelibrary.wiley.com/action/downloadSupplement?doi=10.1002%2Fadmt.201900232&file=admt201900232-sup-0002-S2.mp4>

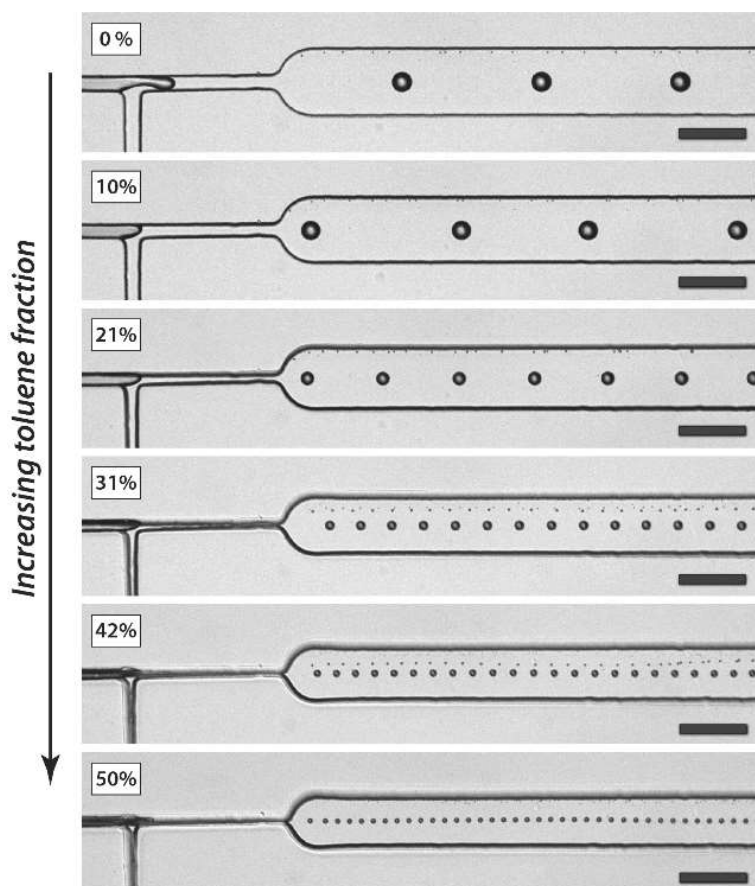


**Figure 2.34.** Geometry of the chip and droplet size when the PDMS chip is exposed to different concentrations of toluene. The scale bar corresponds to 200  $\mu\text{m}$ .

After letting the system reach equilibrium for 30 minutes, the size of the droplets was measured and averaged over one minute. With this methodology, we plotted the diameter of the droplets at different concentrations of toluene, as shown in figure 2.35 (the circle size is proportional to the droplet size).

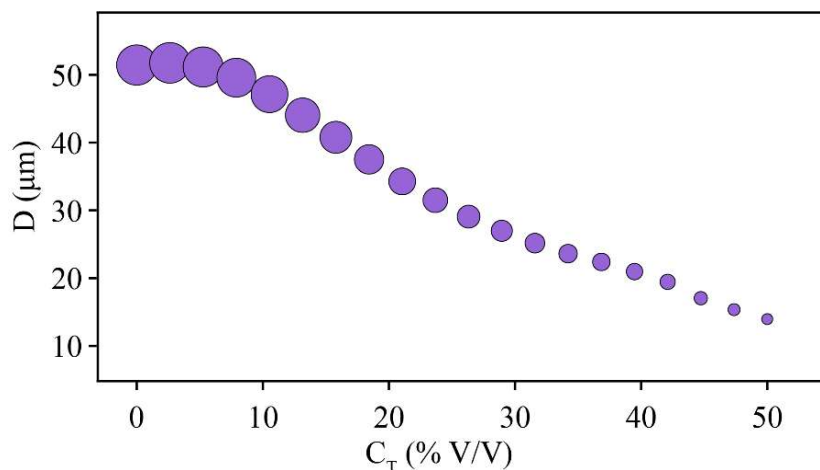


**Figure 2.35.** Evolution of the droplet size as the concentration of toluene increases.

At 0% concentration of toluene, the droplets have a diameter of 53  $\mu\text{m}$ , and as the concentration of toluene increases, they are progressively reduced until they reach a diameter of 14  $\mu\text{m}$  when the concentration of toluene is equal to 50%. The evolution of the droplet size is almost linear as the concentration of toluene increases, and before trying to analyze the factors that drive this behavior away from linearity, it should be noted that this behavior was not even expected to be linear. First, it must be considered that, there are different mechanisms for the generation of droplets, described in section 1.1.4. Which mechanism the droplets are formed through, depends on different parameters, but mainly from the capillary number. As the dimensions of the channels change, so does the capillary number as well. As a direct consequence of this, the mechanisms for the droplet generation might change too. Unfortunately, the time a droplet takes to be produced is too short, so we cannot easily differentiate droplets formed from the dripping or squeezing mechanisms. In case the mechanism does change, there would be a change in the response of the droplet size to modifications in the geometry of the channel. This means that, for instance, droplets formed with 0% toluene may not be generated via the same mechanism as the ones formed when the concentration of toluene is 50% leading to possible non-linear behavior. Second, based on the complexity of the models used to describe the size of droplets, even if the droplets were formed via the same mechanism, the droplet size is never supposed to change linearly with a reduction of the critical dimensions of the channels.

One of our main concerns when this method was proposed and developed was that swelling could change the flexibility of the chip. The ease to compress the PDMS in a chip could interfere with the pressure oscillations involved in the generation of droplets. In such a case, a chaotic interplay between the droplet generation and the instant deformation of the chip could lead to a large variation in the size of the droplets. For this reason, it was necessary to analyze whether swelling was related to an increased dispersity index (also named coefficient

of variation). Figure 2.36 shows the dispersity index measured over one minute after letting the system reach equilibrium for 30 minutes.

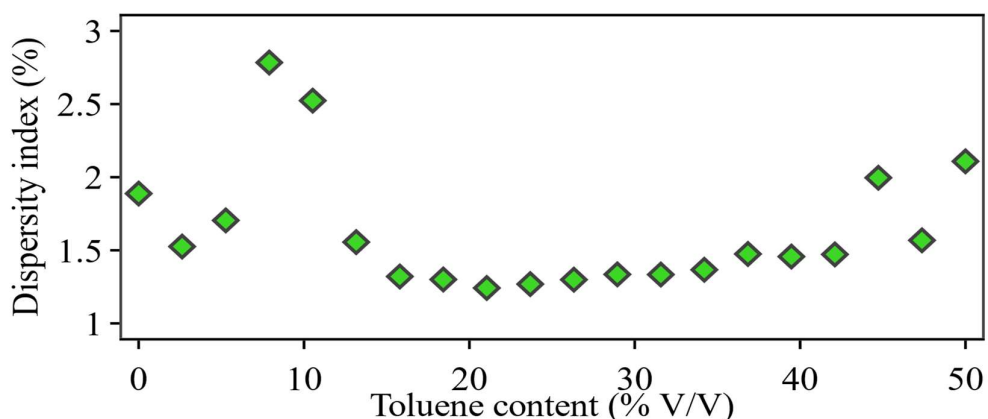


**Figure 2.36.** Dispersity index (also called coefficient of variation) in the droplets generated at each concentration of toluene.

Fortunately, as shown in figure 2.36, in all the concentrations we studied, the dispersity index is in the range of  $2 \pm 1\%$ , which is the range expected in droplet microfluidics (3% in co-flow<sup>33</sup> and 5% in flow-focusing<sup>34</sup>). This variation (from 1 to 3%) might appear drastic, but care should be taken in what these values really mean. If a droplet has a diameter of 50  $\mu\text{m}$ , as the ones measured at low concentrations of toluene, each percentage point represents 0.5  $\mu\text{m}$ . Since the pictures taken in this experiment have a resolution of 1.033  $\mu\text{m}/\text{pixel}$ , a change of 0.5  $\mu\text{m}$  is below the spatial resolution of data contained in the pictures. It means that, with the infrastructure we used, we cannot claim to determine the dispersity index with less than 1% of uncertainty. In any case, this experiment was performed during almost 12 hours at room temperature without acoustic isolation, so the variation in the dispersity index might well be originated by external factors. We must remember, nevertheless, that the reason we analyzed the dispersity index was to be sure that swelling did not worsen the droplet size distribution. In this sense, our solid answer is that the dispersity index is not dramatically affected by swelling.

### 2.3.5 Reliability- related experiments.

Before proposing this methodology for practical applications, there are a couple of aspects that must be analyzed. The first one relates with the question about whether the integrity of a PDMS chip, as well as its swelling responsiveness, can be preserved after many cycles of swelling and de-swelling, and after extreme deformations. To test this, we fabricated a T-junction (*chip B*) 105  $\mu\text{m}$  in height and operated it to generate droplets of water in an analogous way as in the previous experiments ( $Q_o = 1800 \mu\text{l/h}$  and  $Q_w = 100 \mu\text{l/h}$ ). In this experiment, we set the concentration of toluene to 20% and measured the diameter of the droplets. Afterwards, we stopped the flow of water and performed 10 cycles switching the concentration of toluene from 0 to 20% and back to 0%, waiting 30 minutes at each stage (which represents an hour per cycle). After those ten cycles, we set the concentration of toluene again to 20% and measured

the diameter. The size distribution of the droplets measured before and after cycling the chip are shown in figure 2.37.

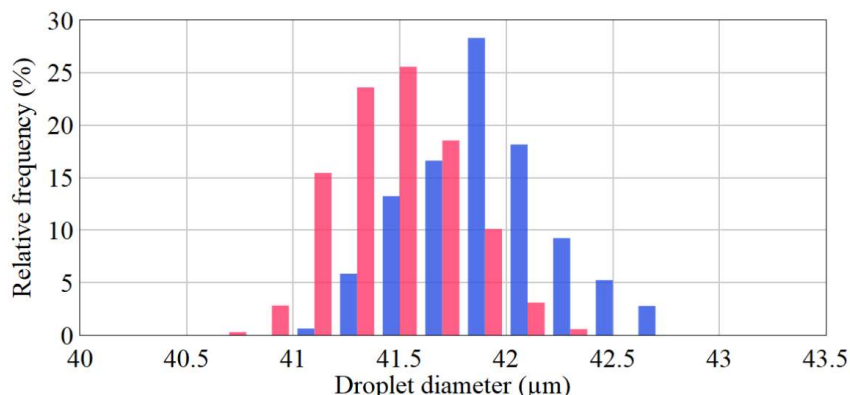


**Figure 2.37.** Size of droplets generated before (blue,  $n = 325$ ) and after (red,  $n = 356$ ) subjecting the PDMS chip to 20 cycles of swelling and de-swelling.

Table 2.3 summarizes the mean diameter, standard deviation and dispersity index of the droplets formed before and after the cycles. As can be seen in figure 2.37 and table 2.3, there is only a marginal change in the diameter of the droplets, standard deviation and dispersity index before and after cycling.

	Mean diameter (µm)	Standard deviation (µm)	DI (%)
Before cycling	41.9	0.33	0.8
After cycling	41.5	0.28	0.7

**Table 2.3.** Mean diameter, standard deviation and dispersity index of the droplets generated before and after cycling the concentration of toluene.

A time-lapse video showing the changes in the geometry of this PDMS device during the cycles in the concentration of toluene between 0 and 20% V/V can be found online:

<https://onlinelibrary.wiley.com/action/downloadSupplement?doi=10.1002%2Fadmt.201900232&file=admt201900232-sup-0003-S3.mp4>

Additionally, to evaluate whether the integrity and responsivity of the chip is preserved after a strong swelling, we subjected the same chip to a 50% mixture of toluene and mineral oil for 30 minutes. Under these conditions, the channel practically collapsed on itself. Once we reduced the concentration of toluene back to 0%, the channels recovered their initial geometries as shown in figure 2.38.

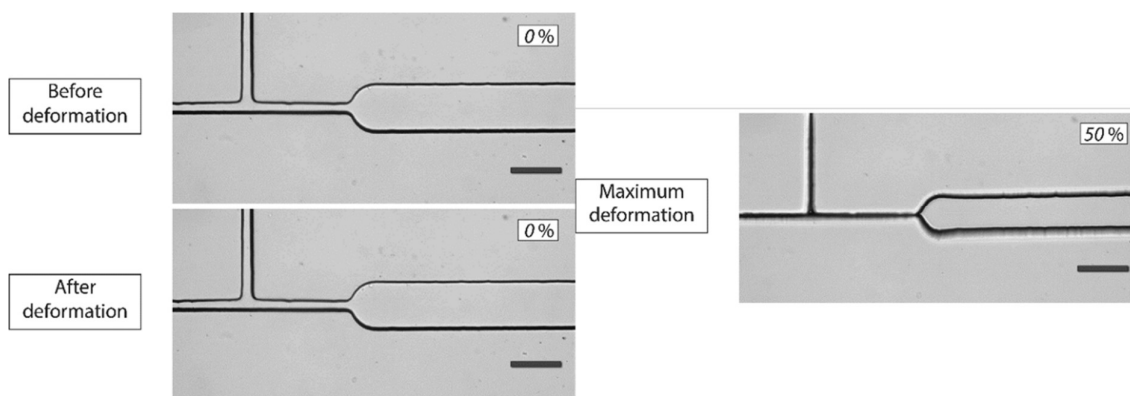


**Figure 2.38.** Geometry of a PDMS chip with  $105\ \mu\text{m}$  in height in the three conditions it was subjected to: Up left, at 0% toluene (before deformation); right, at 50% toluene (maximum deformation); and down left, at 0% toluene (after deformation). All experiments were performed with  $Q_{\text{oil}} = 500\ \mu\text{l/h}$ . The scale bars correspond to  $200\ \mu\text{m}$ .

A time-lapse video showing the change in the geometry of this chip when it is suddenly exposed to solutions of toluene in mineral oil at 50% and 0% V/V is available online:<sup>27</sup>

<https://onlinelibrary.wiley.com/action/downloadSupplement?doi=10.1002%2Fadmt.201900232&file=admt201900232-sup-0004-S4.mp4>

As already mentioned, the degree of swelling depends on the balance of different forces. On one side is the force that emerges from the intermolecular interactions between the solvent molecules and the polymer matrix, favoring swelling. On the other side are the intermolecular interactions between different chains in the polymer matrix, as well as the mechanical forces (rising from the fact that the PDMS is attached to a rigid glass slide), opposing the expansion of PDMS. Any factor influencing these forces could alter their balance. According to this reasoning, if the tension between the rigid glass slide and the expanding PDMS is propagated with more efficiency, the equilibrium point of swelling can be affected and reduced. According to this, the height of the chip can play a fundamental role in the swelling response coefficient (and in the responsiveness of the chip to swelling in general): Larger voids between the rigid glass and the flexible PDMS should reduce the propagation of the tension, favoring swelling. Originally, we believed that such contribution would be minimal. Nevertheless, we changed our minds after performing an experiment to analyze this effect.

To examine how the height of a chip influences the swelling process, we prepared 4 chips with a T-junction (*chip B*), having different heights: 33, 50, 67 and  $105\ \mu\text{m}$ . Each chip was subjected to the same procedure, consisting of flowing a solution of toluene in mineral oil with a concentration increasing from 0 to 40% in steps of 10%, and letting the system reach equilibrium for 30 minutes in each step ( $Q_{\text{oil}} = 1000\ \mu\text{L/h}$ ). We captured the geometry of the chips at each concentration and summarized those pictures in figure 2.39.

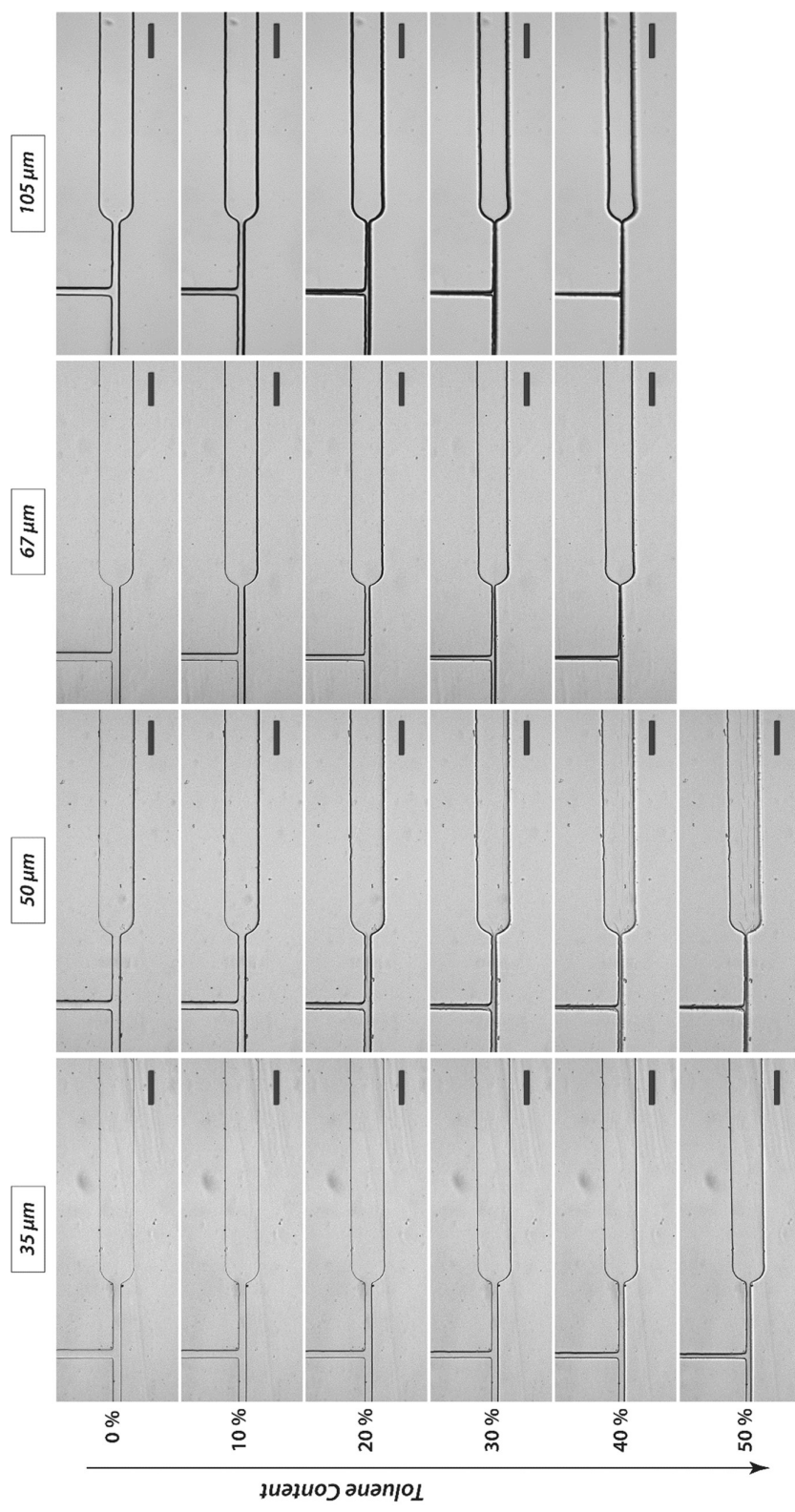


**Figure 2.39.** Effect of the height of the channels on the swelling behavior of the chip. The scale bar corresponds to 200  $\mu\text{m}$ .

In figure 2.39 it is qualitatively seen that chips with higher motifs are more responsive to swelling than those with lower ones. This is quite interesting because of the new possibilities and limitations it adds to the control of swelling in PDMS structures and deserves a proper analysis that goes beyond the reach of this project. From these pictures, we estimate the response coefficient for each device as shown in table 2.4

Height of the chip ( $\mu\text{m}$ )	Swelling response coefficient $\Delta\delta w$ ( $\mu\text{m}$ )
35	0.47
50	0.54
67	0.84
105	1.29

**Table 2.4.** Swelling response coefficients for chip B with different heights.

Due to the dimensions of these T-junctions and the high flow rates of the viscous oil solutions we pump across their channels, there should be a considerable pressure drop between the inlets and the outlet of this chip. For this reason, we can legitimately question to which extent, the high pressure in the channels can interfere with the swelling process. To analyze this effect, we pumped a solution of toluene in mineral oil through a channel with 105  $\mu\text{m}$  in height containing the T-junction of the previous experiments. This time, we made two sets of experiments. In the first one, we set the concentration of toluene to 0% (having only mineral oil) and increased the flow rate from 0 to 2000  $\mu\text{L/h}$  in different steps, waiting 30 minutes at each one. In the second set of experiment, we set the concentration of toluene to 20% and basically did the same program of flow rates as in the first set of experiments. The only difference is that we did not perform this experiment when the flow rate of the solution was set to 0  $\mu\text{L/h}$  because in such conditions, the toluene molecules leaving the solution to enter the polymer matrix could not be replenished since, of course, the solution is not moving.. From equation 1.7 (chapter 1.1), we can estimate the pressure on this chip at different flow rates when the concentration of toluene is equal to 0%, as presented in table 2.5.

Flow ( $\mu\text{L/h}$ )	250	500	1000	2000
Pressure (mbar)	19	38	76	152

**Table 2.5.** Expected pressures in chip B (105  $\mu\text{m}$  high) at different flow rates using light mineral oil.

The pictures of the geometry of the chip are shown in figure 2.40 and we do not observe any appreciable difference in the geometry of the chip when the values of the flow rates were modified.

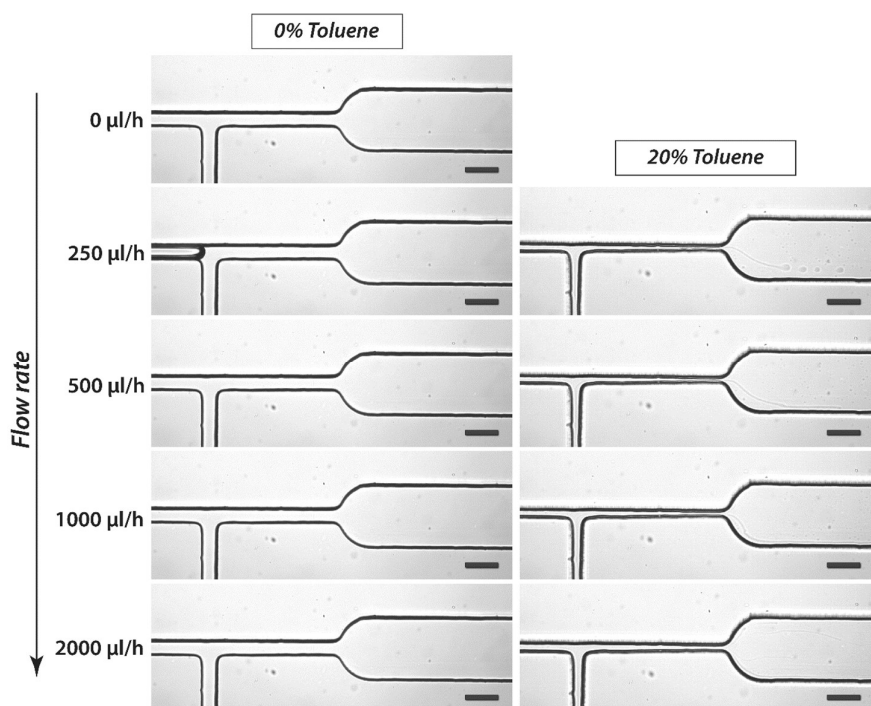


**Figure 2.40.** Effect of the flow rate of the fluids on the swelling behavior of the chip.

In the last set of experiments of this section, we verified if this approach is compatible with experiments using surfactants. One of the main goals of this project is to develop new methods to synthesize materials without using surfactants. In fact, without the restriction in their use, we could probably control the size of the droplets by simply modulating the amount of surfactant in the oil. The chemistry we propose here is free of surfactants (since they can be difficult to wash away in case a solid is synthesized using this technology). Just as we identified the potential use of swelling to control the size of droplets without the use of surfactants, someone else could find further applications for it in other areas of microfluidics that require the use of surfactants.

With this in mind, we used a chip with the same design of the previous experiments and 105  $\mu\text{m}$  in height and performed two sets of experiments. In the first one, a solution of toluene and mineral oil without surfactant was pumped through the chip ( $Q_{\text{oil}} = 1000 \mu\text{l/h}$ ). The concentration of toluene was increased from 0 to 40% V/V in steps of 10%, waiting 30 minutes to let the system reach equilibrium. In the second set of experiments, a solution of toluene in mineral oil with 2% of Span 80 was pumped through the same chip, and the concentration of toluene was increased from 0 to 40% in the same way as in the previous set of experiments. The difference between these sets is that the first one is performed without any surfactant, while the second was performed using span 80. The geometries of the chips for each condition are shown in figure 2.41.

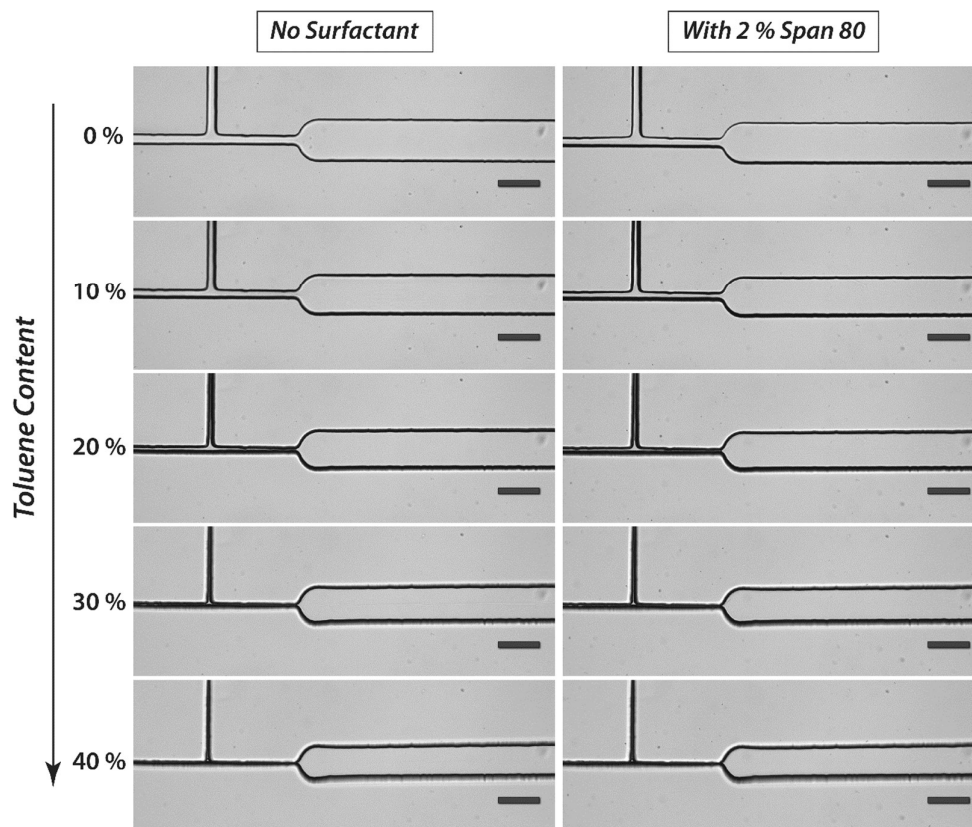


**Figure 2.41.** Effect of the surfactant on the swelling behavior of the PDMS chips.

The geometries of the chip shown in figure 2.41 change when the concentration of toluene flowing across them is increased. However, this deformation does not seem to change when Span 80 is added into the solution of toluene in mineral oil.

Once we established that the presence of surfactant does not affect the deformations caused by swelling notoriously, we checked whether the presence of surfactants affected the modulation of the generation of droplets itself in a swollen chip. To do this, we simply used the same chip as in the previous case (*chip B*) and pumped a solution of toluene in mineral oil with 2% Span 80 ( $Q_{\text{oil}} = 1000 \mu\text{l/h}$ ). At the same time, water was pumped into the chip with the same configuration as the one used in the study of the kinetics of swelling and the modulation of the size of droplets ( $Q_{\text{water}} = 100 \mu\text{l/h}$ ). The concentration of toluene was increased from 0 to 40% in steps of 10%, letting the system 30 minutes to reach equilibrium. The pictures of the system in each measurement are shown in figure 2.42.

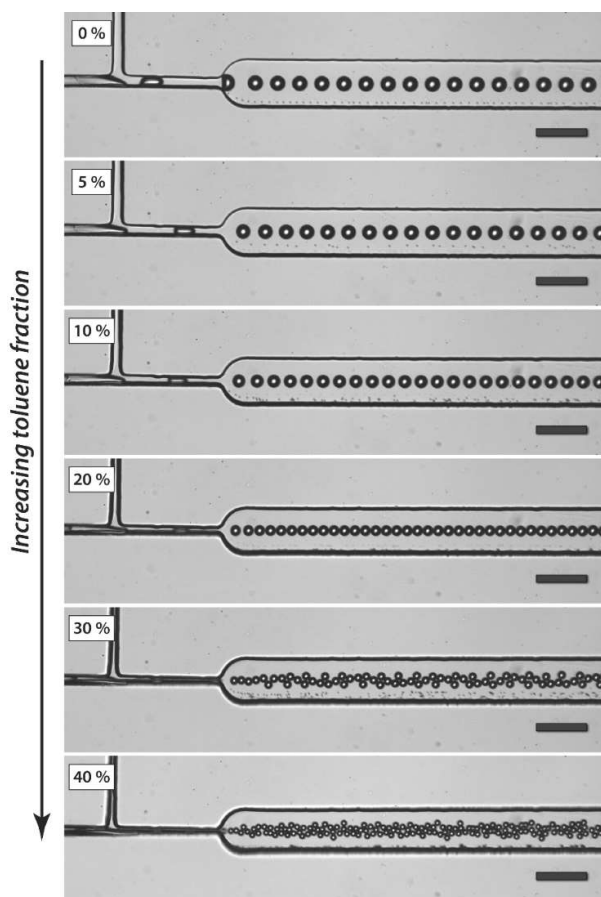


**Figure 2.42.** Swelling-based modulation of the droplet size when surfactants are added to the oil-toluene mixture.

The droplets produced in this experiment reduce their size as the concentration of toluene increases and the channels in the T-junction are deformed. Qualitatively, the presence of surfactants does not seem to affect the swelling response of the material or its use in the modulation of the size of droplets. Maybe the most remarkable observation in this set of experiments is the way the droplets are ordered in the channel. Up to a concentration of toluene of 20% V/V, there is a single column of droplets barely touching each other. At higher concentrations of toluene, the droplets cannot stay in a single column anymore and collide with each other. Without surfactant, these collisions would cause the droplets to merge; nevertheless, since in this set of experiments we used 2% Span 80 in the carrier oil, instead of merging, the traffic congestion of droplets in the channel leads to displacements of the droplets out of the center of the channel. This displacement leads to the formation of a pattern at a 30% concentration of toluene, and to a chaotic arrangement when the concentration is equal to 40%. A time-lapse video showing the change of the size of the droplets when the PDMS chip is exposed to a solution of toluene in mineral oil at different concentrations using surfactants is available online:

### *2.3.6 Summary and conclusions about the use of swelling to modulate the critical dimensions of PDMS chips and the size of droplets produced by them.*

In this chapter, we show the development of a new technique to modulate the size of droplets, based on the deformation of the motifs in a microfluidic chip through the swelling of PDMS. The possibilities, as well as the limitations of this method were presented.

First, we show that PDMS in a chip swells linearly when the concentration of the swelling agent (here toluene) is increased. The response coefficient of this process depends on the dimensions of the motifs. Here we show that it depends on the thickness of the PDMS wall. We identify that, in larger walls the swelling response coefficient increases until reaching a plateau in walls above 500  $\mu\text{m}$ .

Then, we analyzed the kinetics of this swelling process through the measurement of the droplets of water produced by a PDMS T-junction and carried by different mixtures of toluene and mineral oil prepared *in situ*. We identify that in the swelling and de-swelling processes, the time evolution of the diameter of the droplets can be fitted by a bi-exponential model. One of the time constant of this model is very short (around 2 minutes) and the other is longer (ranging 15 to 20 minutes).

Afterwards, we show that is possible to reduce the swelling time by increasing the content of the swelling agent beyond the expected operating conditions and reducing it later.

Later, we used this principle to modulate the diameter of the droplets produced by a T-junction in a PDMS chip. We managed to reduce the diameter of the produced droplets from 53  $\mu\text{m}$  (at 0% toluene) to 14  $\mu\text{m}$  (at 50% toluene). The reduction in the diameter of the droplets is almost linear with the concentration of toluene. It is important to note that this method does not increase the dispersity index in the diameter of the droplets: At all concentrations we worked, the DI remains below 3%, and in most cases, it stays below 2%.

After this experiment, we conducted a set of reliability-related experiments. There, we showed the following:

- After 10 cycles of swelling at de-swelling (changing the concentration of toluene from 0 to 20% in each cycle), the droplets produced by a PDMS T-junction have the same size.
- After a strong swelling and de-swelling (rising the concentration of toluene to 50% and reducing it back to 0%) no damage of the chip or changes in its geometry can be observed.
- After analyzing the swelling of PDMS chips with different heights, we see that PDMS devices with higher channels are more affected by swelling.
- Changing the flow rates of the mixtures of toluene and mineral oil did not influence the geometry or the swelling of the PDMS devices notoriously.

- The incorporation of surfactants into the solution of toluene in mineral oil does not affect the swelling of the PDMS chips.
- The size of the droplets produced in a PDMS chip can be modulated with this technique even when the mixture of toluene and mineral oil contains surfactants.

From these results we can conclude that, contrary to the common ideas, swelling can be a useful tool in microfluidics. Through it, we can reversibly tune the dimensions of PDMS motifs *in situ* and control the sizes of droplets produced either by a T-junction. Modulating the size of droplets in this way does not require the use of surfactants, which ensures their absence in the final product. Moreover, the additional infrastructure requirements to implement this technique is very low, since it only implies the use of an extra pump for the swelling agent (either pure or in a solution) and a mixer made by an external T-junction and a PEEK frit mounted on a low-pressure ETFE union assembly. Additionally, this method does not lead to an increased size dispersion of the produced droplets.

This method is compatible with other technologies as well. For example, a live image analysis feedback mechanism could adjust the size of the droplets in chips where the swelling response coefficient and its effect on the droplet size are either unidentified or vaguely known.

An additional potential use of this technology relates with the minimum size at which a microfluidic PDMS channel can be crafted using soft lithography. A device can be fabricated with channels as small as the infrastructure of the laboratory allows, and then shrunk further by the addition of a swelling agent.

This technology has drawbacks as well. First, the swelling agent we use (toluene) can be toxic to living organisms. This means that it cannot be used for many applications of microfluidics related with biology. In such cases, new swelling agents more compatible with life must be found (which does not seem an easy task, due to the low polarity they require). Moreover, some parts of the experimental settings used for microfluidics can interact with the swelling agent. For example, the pistons of plastic syringes can swell when they are exposed to toluene, therefore impoverishing their performance.

In part 3, we will describe how this technology performs in a real case scenario, when a PDMS chip is used for the synthesis of the Prussian Blue Analog  $\text{Rb}_x\text{Mn}[\text{Fe}(\text{CN})_6]_{(x+2)/3}$ . This material is very interesting for its switching properties, but also because in our experience, its fast precipitation leads to an easy clogging of our devices, making it a very challenging target for microfluidic synthesis.

## 2.4 Perspectives of Part 2.

In this part, we described our project from the perspective of microfluidics without the use of reactants. At the beginning, we describe the theoretical framework of the two approaches for the synthesis in chip-based droplet microfluidics. Afterwards, we describe the evolution of the devices we used, and finally, we describe a new method to modulate the size of the droplets produced by a PDMS chip exposed to a swelling agent. The results of this part are summarized in sections 2.2.4 and 2.3.6.

The evolution of the devices shown in chapter 2 (and represented in figure 2.43), leads to the natural question about what the future devices might look like. Before the end of this PhD we were working on a newer device based on the *Green Chip* with additional features.

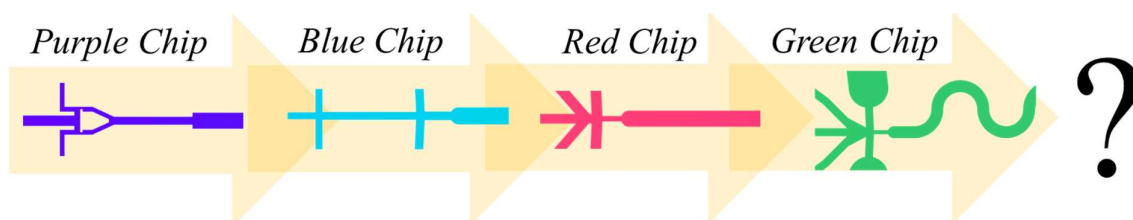


**Figure 2.43.** Evolution of the microfluidic devices presented in chapter 2.2.

The *Black Chip*, shown in figure 2.44 is a conception about how the future devices might look like. The first feature to mention is the addition of a channel that surrounds the critical parts of the chip and arrives to the pool cut at the end of exit channel (for more details about this pool, see part 3, section 3.1.5.c). In case of clogging while the chip is not being supervised, the pumps keep injecting fluids into the chip, until the pressure inside it eventually makes it detach from the glass slide it is pasted on. When this happens, reactants and products can be ejected outside of the chip contaminating the surroundings. In case of such event, the security channel of the *Black Chip* redirects the flow towards a pool preventing its ejection. Additionally, the *Black Chip* has an integrated ruler next to the exit channel, with marks every 2.5 mm (small lines), 5.0 mm (medium lines) and 10.0 mm (long lines). This ruler helps the operator to carve the pool to collect the product at a desired distance from the nozzle (shown in dotted blue lines in figure 2.44).

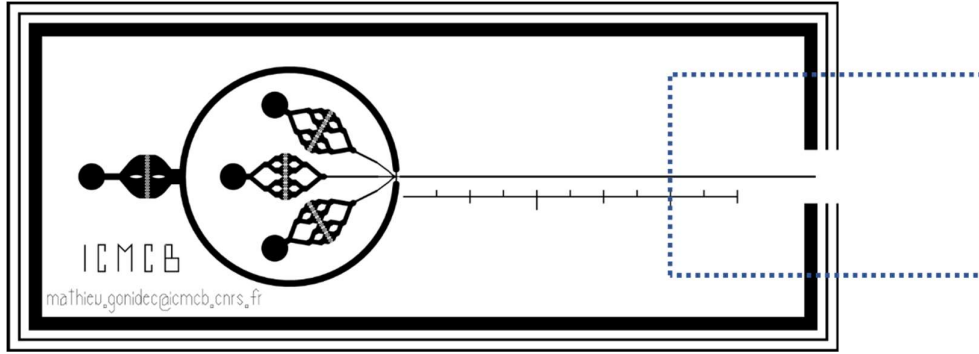


**Figure 2.44.** Blueprint of the Black Chip (the fourth device based on the combination→ generation approach).

While the *symmetry problem* in the *Green Chip* was solved by adding curves to the exit channel, the *Black Chip* incorporates a zig-zagged channel in the nozzle (figure 2.45). This way, the contents of the droplets are mixed as soon as the droplet is formed. The other dimensions of the nozzle are the same as in the *Green Chip*.

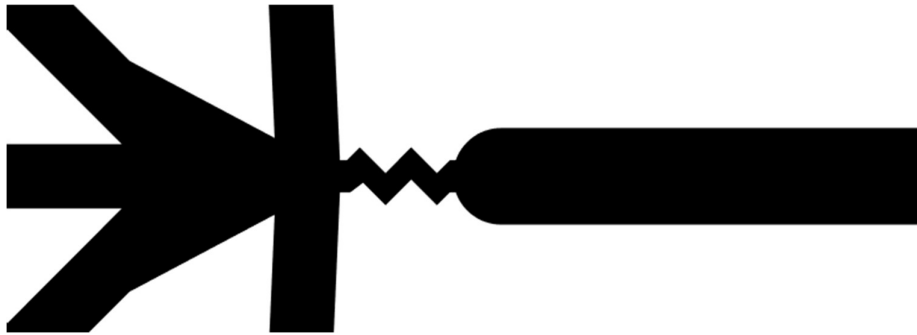


**Figure 2.45.** Nozzle of the Black Chip containing a zig-zagged channel.

To ease the elimination of the oil-bridges, the filters of the *Black Chip* were modified (figure 2.46). First, the fluids that arrive to them are distributed through branched channels to promote a homogenous arrival of fluids to it (therefore avoiding regions of lower flow speeds where oil would be difficult to be washed away). Moreover, the number of columns is reduced to avoid the accumulation of large volumes of oil on them. Each group of seven columns is separated by a wall to avoid the lateral migration of oil across the filter.

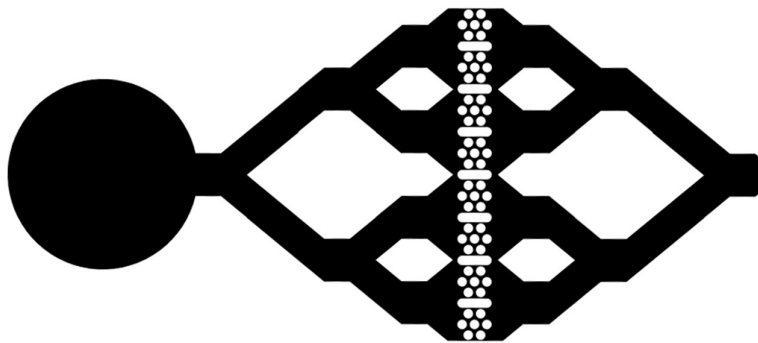


*Figure 2.46. Blueprint of the filter of the Black Chip.*

To ease the collaborations with other groups, it would be convenient to be able to share our devices with them, either by shipping our devices to other groups worldwide or by exchanging them personally in conferences. To ease the communication with whoever receives one of our devices, a contact email is printed on the lower part of the chip.

Very likely, the *Black Chip* is compatible with the droplet size modulation through swelling described in chapter 2.3. This should be tested, and in case it works, these two technologies together could allow us and other scientists worldwide to analyze which solids prepared using microfluidics are influenced by the size of the droplets they are synthesized in and which ones are not.

## References to part 2.

- 1 T. Forestier, S. Mornet, N. Daro, T. Nishihara, S. Mouri, K. Tanaka, O. Fouché, E. Freysz and J.-F. Létard, *Chem. Commun.*, 2008, **36**, 4327–4329.
- 2 L. Moulet, N. Daro, S. Mornet, N. Vilar-Vidal, G. Chastanet and P. Guionneau, *Chem. Commun.*, 2016, **52**, 13213–13216.
- 3 C. A. Stan, S. K. Y. Tang and G. M. Whitesides, *Anal. Chem.*, 2009, **81**, 2399–2402.
- 4 MATEST S.p.A., <http://www.matest.com/en/>.
- 5 L. Frenz, A. El Harrak, M. Pauly, S. Bégin-Colin, A. D. Griffiths and J.-C. Baret, *Angew. Chemie Int. Ed.*, 2008, **47**, 6817–6820.
- 6 P. Zhu and L. Wang, *Lab Chip*, 2017, **17**, 34–75.
- 7 D. R. Link, E. Grasland-Mongrain, A. Duri, F. Sarrazin, Z. Cheng, G. Cristobal, M. Marquez and D. A. Weitz, *Angew. Chemie - Int. Ed.*, 2006, **45**, 2556–2560.
- 8 L.-H. Hung, K. M. Choi, W.-Y. Tseng, Y.-C. Tan, K. J. Shea and A. P. Lee, *Lab Chip*, 2006, **6**, 174–178.
- 9 L. Frenz, J. Blouwolf, A. D. Griffiths and J. C. Baret, *Langmuir*, 2008, **24**, 12073–12076.
- 10 H. Song, J. D. Tice and R. F. Ismagilov, *Angew. Chemie Int. Ed.*, 2003, **42**, 768–772.
- 11 I. Shestopalov, J. D. Tice and R. F. Ismagilov, *Lab Chip*, 2004, **4**, 316–321.
- 12 B. Zheng, J. D. Tice, L. S. Roach and R. F. Ismagilov, *Angew. Chemie - Int. Ed.*, 2004, **43**, 2508–2511.
- 13 H. Shi, Y. Xiao, X. Huang, Y. Bao, C. Xie and H. Hao, *Ind. Eng. Chem. Res.*, 2018, **57**, 12784–12791.
- 14 V. van Steijn, C. R. Kleijn and M. T. Kreutzer, *Lab Chip*, 2010, **10**, 2513–2518.
- 15 P. Garstecki, M. J. Fuerstman, H. A. Stone and G. M. Whitesides, *Lab Chip*, 2006, **6**, 437–446.
- 16 X. Chen, T. Glawdel, N. Cui and C. L. Ren, *Microfluid. Nanofluidics*, 2015, **18**, 1341–1353.
- 17 S. L. Anna and H. C. Mayer, *Phys. Fluids*, 2006, **18**, 121512.
- 18 J. D. Tice, A. D. Lyon and R. F. Ismagilov, *Anal. Chim. Acta*, 2004, **507**, 73–77.
- 19 S. H. Tan, B. Semin and J.-C. Baret, *Lab Chip*, 2014, **14**, 1099–1106.
- 20 D. R. Link, E. Grasland-Mongrain, A. Duri, F. Sarrazin, Z. Cheng, G. Cristobal, M. Marquez and D. A. Weitz, *Angew. Chemie Int. Ed.*, 2006, **45**, 2556–2560.
- 21 Y. Zeng, M. Shin and T. Wang, *Lab Chip*, 2013, **13**, 267–273.
- 22 J.-H. Choi, S.-K. Lee, J.-M. Lim, S.-M. Yang and G.-R. Yi, *Lab Chip*, 2010, **10**, 456–461.
- 23 A. Bransky, N. Korin, M. Khoury and S. Levenberg, *Lab Chip*, 2009, **9**, 516–520.
- 24 H. Willaime, V. Barbier, L. Kloul, S. Maine and P. Tabeling, *Phys. Rev. Lett.*, 2006, **96**, 4–7.
- 25 J. Xu and D. Attinger, *J. Micromechanics Microengineering*, 2008, **18**, 65020.
- 26 L. Paseta, B. Seoane, D. Julve, V. Sebastián, C. Téllez and J. Coronas, *ACS Appl. Mater. Interfaces*, 2013, **5**, 9405–9410.
- 27 M. Faustini, J. Kim, G.-Y. Jeong, J. Y. Kim, H. R. Moon, W.-S. Ahn and D.-P. Kim, *J.*

- Am. Chem. Soc.*, 2013, **135**, 14619–14626.
- 28 J. E. Saunders, H. Chen, C. Brauer, M. Clayton and H. P. Loock, *Soft Matter*, 2018, **14**, 2206–2218.
- 29 R. Dangla, F. Gallaire and C. N. Baroud, *Lab Chip*, 2010, **10**, 2972–2978.
- 30 M. Kim, Y. Huang, K. Choi and C. H. Hidrovo, *Microelectron. Eng.*, 2014, **124**, 66–75.
- 31 J. N. Lee, C. Park and G. M. Whitesides, *Anal. Chem.*, 2003, **75**, 6544–6554.
- 32 P. Atkins, P. W. Atkins and J. de Paula, *Atkins' Physical Chemistry*, OUP Oxford, 2014.
- 33 P. B. Umbanhowar, V. Prasad and D. A. Weitz, *Langmuir*, 2000, **16**, 347–351.
- 34 S. Takeuchi, P. Garstecki, D. B. Weibel and G. M. Whitesides, *Adv. Mater.*, **17**, 1067–1072.



## Part 3. Microfluidics applied to the synthesis of switchable materials.

### *Introduction.*

In the general description of spin crossover (chapter 1.2) it has been mentioned that the switching behavior of these materials is very sensitive to many factors, especially to the particle size, morphology and crystallinity. Therefore, the procedures used to synthesize these materials play an important role in influencing those features and, consequently, the overall switching behavior of the material. Table 3.1 summarizes the most used synthetic approaches to obtain particles of spin crossover materials.

	<i>Layering</i>	<i>Bulk</i>	<i>Microemulsion</i>
<b>Crystal size</b>	<b>cm to mm-scale</b>	<b>mm to <math>\mu\text{m}</math>-scale</b>	<b>nm-scale</b>

**Table 3.1.** Comparison of synthetic methods of spin crossover materials and the obtained crystal sizes.

Generally, when these materials are synthesized by slow diffusion using a layering setup, crystals large enough to be analyzed by single crystal X-ray diffraction can be obtained. If the reactants are mixed in the conventional mix-and-stir procedure in a beaker (*in bulk*), micrometric particles are formed. Depending on the material and the concentration conditions, some nanoparticles can also be obtained. Finally, the most used method to synthesize nanoparticles of spin crossover materials is the reverse microemulsion technique,<sup>1-3</sup> which is of great value since there is great interest in using them as active components in micro- and nanodevices because of their bi-stable behavior.<sup>4-6</sup>

Reverse microemulsions act as a collection of confined nanoreactors which volume can be adjusted in order to control the particle sizes. In reverse microemulsion syntheses, two suspensions of aqueous solutions of reactants dispersed in a non-polar medium are prepared, forming micelles.<sup>7</sup> Afterwards, these suspensions are mixed, allowing the micelles with reactants to merge randomly. By doing so, the reactants mix and react inside those nanoreactors (Figure 3.1).

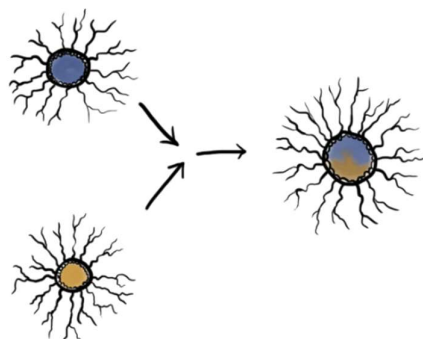


**Figure 3.1.** *Nanometric micelles merging in a reverse microemulsion synthesis.*

This methodology presents, nevertheless, some drawbacks. First, nothing forces the strict 1-to-1 coalescence of micelles containing each solution of reactants. This means that the stoichiometry of the actual reaction conditions remains uncontrolled and obeys a distribution that is purely statistical: Many micelles with the same solution can collide and merge before they encounter a micelle with the complementary reactants. Secondly, the big amounts of surfactants used in this technique lead to a strong presence of surfactants in the obtained nanoparticles that might affect their behavior (in chapter 1.2, it was stated that some surface phenomena can play a major role in finite spin crossover systems). Because of these reasons, there is a general interest to diversify the synthetic routes of these nanoparticles, and especially, to develop methods that do not require the use of surfactants.

Additionally, the fact that some features of these materials depend on the reaction conditions, blurs the systematic comparison of their properties and in some cases, it may be the reason why different research groups disagree about the behavior of some compounds. In fact, a precise comparison of their properties would require the development of reaction procedures capable to perform reactions with a high degree of control and reproducibility.

As already discussed in this manuscript, we propose the use of microfluidics as an alternative procedure to synthesize spin crossover materials. Flow chemistry, and especially chip-based microfluidics, has enabled the synthesis of micro- and nanocrystals with a high degree of control (particularly in syntheses involving reactions that present fast reaction kinetics, as described in chapter 1.1).<sup>8-17</sup> We chose droplet microfluidics to create microreactors in which the reactions can occur, because this approach allows a controlled, reproducible and efficient mixing of the contents of each droplet. Moreover, thinking about the long-term goals of this research, microfluidic synthesis can be a platform to perform more complex procedures (like quenching a reaction with a time accuracy in the ms scale, or a sequential addition of reactants to obtain core-shell particles).

In this part we will first describe the compound we selected to synthesize by microfluidics and then the different synthetic strategies we explored. Afterwards, improvements and perspectives will be proposed to extend this approach to other coordination compounds.

## Chapter 3.1. Synthesis of Hofmann $[\text{Fe}(\text{pz})\text{Pt}(\text{CN})_4]$ 3D network

### 3.1.1 What is known on the $[\text{Fe}(\text{pz})\text{Pt}(\text{CN})_4]$ compound.

Before describing the behavior of spin crossover materials, we must briefly explain how their switching behavior is analyzed. Remember that each state (HS or LS) has different properties (like density, color, magnetic susceptibility, etc.). This means that it is possible to follow the spin conversion in a material by analyzing any of these parameters under different conditions (for example, scanning different temperatures). For convenience, we follow this change by its molar  $\chi T$ -value. This value is the product of the molar magnetic susceptibility (or  $\chi$ ) and the temperature (T). To determine the value of  $\chi$ , VSM (vibrating-sample magnetometers) or SQUID (superconducting quantum interference device) magnetometers are used.<sup>18</sup> By doing so, we expect the Fe(II) ions in HS state to have a  $\chi T$ -value close to 3 emu K/mol, while LS Fe(II) ions should have a  $\chi T$ -value close to 0 emu K/mol.<sup>18</sup>

After a careful review of the existing spin crossover compounds, we chose  $[\text{Fe}(\text{pz})\text{Pt}(\text{CN})_4]$  as our target material because of many reasons. First,  $[\text{Fe}(\text{pz})\text{Pt}(\text{CN})_4]$  precipitates in a single, well-known structure<sup>19</sup> (Figure 3.2). No other phases have been reported so far which will strongly limit the possibility to obtain a different polymorph using microfluidics. The compound is a 3D network based on  $[\text{FePt}(\text{CN})_4]$  planes linked to each other by bridging pyrazine ligands. This leads to a porous structure hosting solvent molecules.

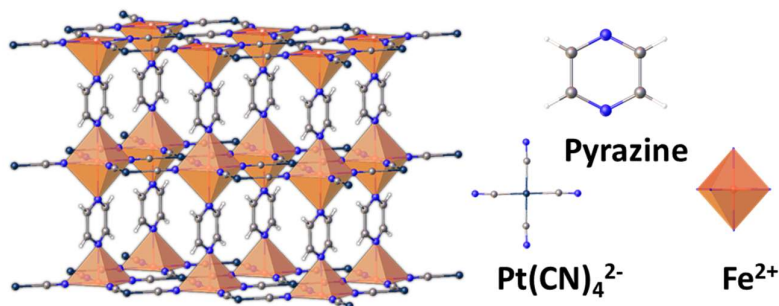


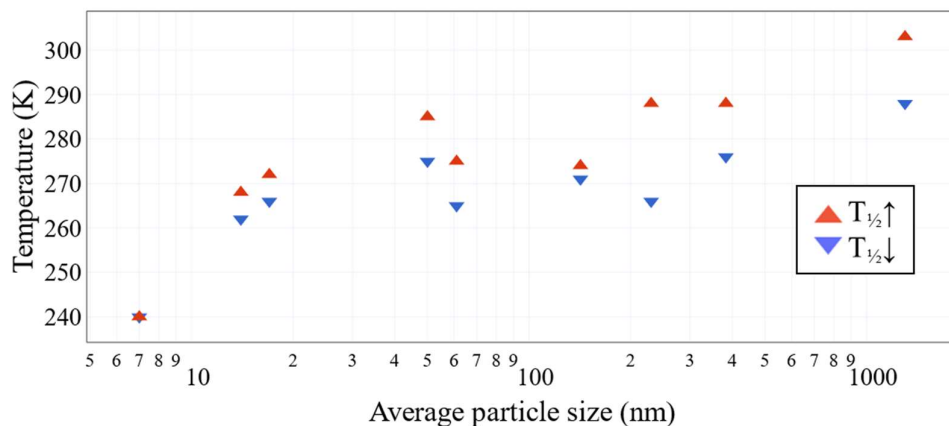
**Figure 3.2.**  $[\text{Fe}(\text{pz})\text{Pt}(\text{CN})_4]$  metal-organic framework. The structure of this compound is composed of inorganic sheets of Fe(II) and  $\text{Pt}(\text{CN})_4^{2-}$  that expand periodically in 2 dimensions and are connected vertically to other sheets by pyrazine molecules.

Second, when fully dehydrated, this material presents a wide thermal hysteresis centered at room temperature. Although spin crossover materials presenting no hysteresis could be useful for some purpose in the future, most potential applications of spin crossover are centered on hysteresis. Moreover, hysteresis is a size-dependent feature in spin crossover materials (see chapter 1.2), so the downsizing effect arising from the synthetic method used for their preparation might be reflected in differences in their switching behavior.

Third, for the sake of comparison, we need to start with a material that has already been studied at the nanoscale. The two spin crossover materials that have been widely studied at the nanoscale are  $[\text{M}(\text{pz})\text{Pt}(\text{CN})_4]$  (M(II) being a 3d metal ion) and the compounds of the “triazole” family. Both materials present hysteresis and have a well-know structure, so the preference of one above the other is, to some degree, arbitrary. Regarding  $[\text{Fe}(\text{pz})\text{Pt}(\text{CN})_4]$ , some groups have synthesized it using reverse microemulsion, and their results show the general trend seen upon size reduction: <sup>1-3</sup>

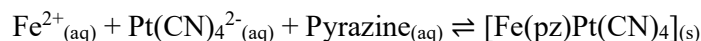
- Smaller hysteresis range.
- Smoother curves of their  $\chi T$ -plots.
- Increasing residual HS fraction at low temperatures.
- Lower transition temperatures ( $T_{1/2} \uparrow$  and  $T_{1/2} \downarrow$ ).

Figure 3.3 shows the comparison between the results obtained by these groups when analyzing the magnetic behavior of nanoparticles of  $[\text{Fe}(\text{pz})\text{Pt}(\text{CN})_4]$ .<sup>1-3</sup> This figure plots the evolution of the switching temperatures in warming and cooling modes,  $T_{1/2} \uparrow$  and  $T_{1/2} \downarrow$ . Although the results published by different groups follow a clear and consistent trend, the values of  $T_{1/2} \uparrow$  and  $T_{1/2} \downarrow$  differ between each other. The reason for these mismatches might originate from the sensibility of spin crossover towards defects and dopants in the crystals, the presence of surfactants below the detection limit, the aggregation of particles after the sample is synthesized or simply the physical method used to characterize their properties (like SQUID or VSM, under vacuum or not, temperature scan rate and so on).



**Figure 3.3.** Comparison of the switching temperatures observed in particles of  $[\text{Fe}(\text{pz})\text{Pt}(\text{CN})_4]$ .<sup>1-3</sup>

Fourth, the reaction that leads to the formation of the  $[\text{Fe}(\text{pz})\text{Pt}(\text{CN})_4]$  uses only two reactant solutions. This point is of importance as it allows the use of droplet microfluidics with only two solutions, either in the *generation*  $\rightarrow$  *combination* or the *combination*  $\rightarrow$  *generation* approaches.  $[\text{Fe}(\text{pz})\text{Pt}(\text{CN})_4]$  is synthesized according to the following scheme:



Three reactants are needed in the reaction mixture to synthesize this material:

1. A source of Fe(II) ions, like  $\text{Fe}(\text{BF}_4)_2$  or  $\text{Fe}(\text{OTf})_2$ .
2. A source of  $\text{Pt}(\text{CN})_4^{2-}$  ions, like  $\text{K}_2\text{Pt}(\text{CN})_4$  or  $(\text{NH}_4)_2\text{Pt}(\text{CN})_4$ .
3. A source of Pyrazine.

In fact, almost any salt of Fe(II) and  $\text{Pt}(\text{CN})_4^{2-}$  soluble in water can be used for this purpose as long as the side product formed by the corresponding counterions are soluble in water as well. Intuitively, this reaction can be performed by preparing three solutions of reactants. However, the synthesis of  $[\text{Fe}(\text{pz})\text{Pt}(\text{CN})_4]$  is generally simplified into the mixing of a solution of the  $\text{Pt}(\text{CN})_4^{2-}$  salt into a mixture of iron salt and pyrazine.<sup>19</sup> This simplification will allow the use of the microfluidic geometries developed in chapter 2.1.

### 3.1.2 Strategy followed.

In general, we propose to use microfluidics to generate a stream of droplets of water separated from each other and carried by a flow of oil, where each droplet contains all the reactants to synthesize  $[\text{Fe}(\text{pz})\text{Pt}(\text{CN})_4]$ , as shown in figure 3.4.

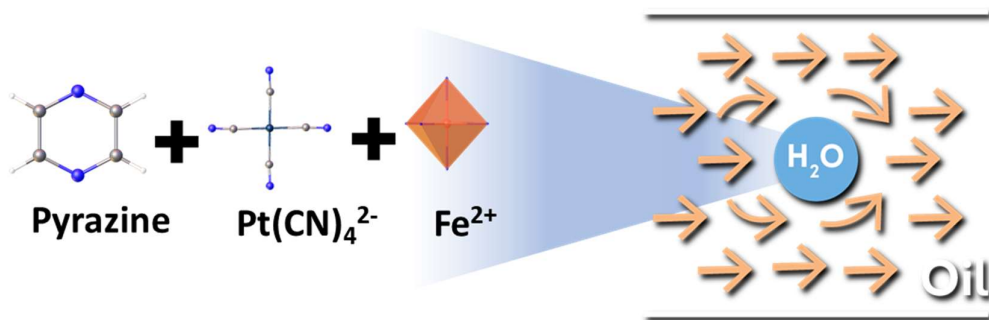


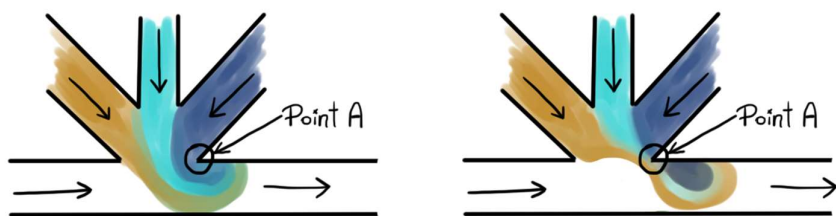
**Figure 3.4.** General strategy for the droplet-based microfluidic synthesis of  $[\text{Fe}(\text{pz})\text{Pt}(\text{CN})_4]$ .

The task of the microfluidic device consists then in fabricating these droplets, just as if the device were a miniaturized factory. Since our main goal is to apply microfluidics to the synthesis of coordination compounds, the obtained particles should be compared to references. This will be done first by comparing the resulting materials to reference samples obtained with different or similar conditions. In a second step, the information from the literature (figure 3.3) will put our syntheses into a wider perspective. Nevertheless, our global goal is to advance as far as possible in the development of techniques that allow the tunable, monitored and reproducible synthesis of switchable SCO materials in general. Ultimately, this goal is unreachable because there is always room for improvement in these aspects.

For the synthesis of reference compounds, we followed literature procedure performed in beakers.<sup>2,19</sup> It should be noted that, according to these previous reports, so far, no group has reported the spontaneous formation of nanoparticles this way, which gives the impression that this procedure does not lead to the formation of nanoparticles spontaneously. As we will describe later in this chapter, this could depend on the cleaning procedure used to wash and dry the samples.

The fact that  $[\text{Fe}(\text{pz})\text{Pt}(\text{CN})_4]$  precipitates as micrometric particles adds an additional degree of complexity to the use of microfluidics for the synthesis of this material, since it means that the chip can easily clog after the precipitation of  $[\text{Fe}(\text{pz})\text{Pt}(\text{CN})_4]$ . In general, when microfluidics is used to carry reactions that do not form nanoparticles spontaneously, clogging becomes a major issue. This is the case, for example of the synthesis of  $\text{BaSO}_4$ . This material does not form nanoparticles spontaneously when it is precipitated from aqueous solutions, and in the microfluidic synthesis of  $\text{BaSO}_4$ , Nirvik Sen *et al.* describe that clogging is a major concern that needs to be considered when the synthesis reactor is designed.<sup>20</sup> On the other side, quantum dots do precipitate spontaneously as nanoparticles, and in their microfluidic synthesis, clogging is either not mentioned,<sup>11,17</sup> or simply prevented by degassing the solutions of reactants.<sup>10</sup>

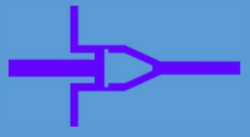
In our case, since  $[\text{Fe}(\text{pz})\text{Pt}(\text{CN})_4]$  – in the concentration conditions we used – could easily clog the device as it precipitates, it is mandatory to avoid the direct contact between the droplets and the walls of the channel. This makes it impossible to use some strategies that were successful in synthesizing other materials. For example, Song *et al.* and Shestopalov *et al.* used a perpendicular droplet generation strategy to improve the mixing efficiency of a microfluidic device for synthesis reactions (like the one presented in chapter 1.1 and shown in figure 3.5)<sup>21,22</sup>. Although this approach can easily solve the symmetry problem presented in chapter 1.1, the risk of clogging in this device is quite high, as shown in figure 3.5. Indeed, when the droplet starts to form, point A is surrounded by one of the solutions (here shown in blue). Nevertheless, in a later moment of the formation of the droplet, the same point is surrounded by the other solution (here shown in yellow). Since this point is in the proximity of the wall, the linear flow speed there is quite slow and very likely both reactants will encounter, leading to the formation of crystals. The low linear flow speed here means that such crystals are hardly going to be washed away, so their formation and growth will trigger a cascade of processes until the chip is clogged.



**Figure 3.5.** Risk of clogging in a device where reactants enter laterally into the exit channel, taken from the literature.<sup>21,22</sup> In this example, both solutions can be in direct contact with the walls at point A, increasing the risk of clogging.

For these reasons, our most complex challenge for the continuous and surfactant-free synthesis of  $[\text{Fe}(\text{pz})\text{Pt}(\text{CN})_4]$  using droplet microfluidics is the adequate choice (or design) of the chip geometry to perform the reaction. For that, we will use the devices we presented and discussed in chapter 2.1. Recapitulating them, our approaches can be divided into two

branches: *generation*→ *combination* (droplets are generated and then merged to combine the reactants) and *combination*→ *generation* (reactants are combined in a single channel that encounters a droplet generator, leading to a stream of droplets containing all of the reactants *ab initio*). The precise geometries of these devices can be found in chapter 2.1, and their overall aspect is shown in table 3.2

<i>Generation</i> → <i>combination</i>	<i>Combination</i> → <i>generation</i>		
			
<i>Purple Chip</i>	<i>Blue Chip</i>	<i>Red Chip</i>	<i>Green Chip</i>

**Table 3.2.** Overall aspects of the geometry of the nozzles in the devices described in part 2.

### 3.1.3 Preliminary tests.

The preliminary work based on the *generation*→ *combination* approach of droplet microfluidics, consisted in using the dual nozzle proposed by Frenz *et al.*<sup>23</sup> (*Purple Chip*, 65 μm in height, discussed in chapter 2) to generate a pair of droplets carried by mineral oil.<sup>1</sup>

Originally, the reactants consisted in an aqueous solution of  $K_2[Pt(CN)_4]$  (at 0.14 M) on one side, and of pyrazine (at 1.4 M) and  $Fe(BF_4)_2$  (at 0.14 M) in water on the other side. It was found that dissolving pyrazine in only one solution led to an asymmetric generation of droplets by the junctions, i.e. the size of the droplets generated on each junction, as well as the frequency of their generation, was not the same. This asymmetry impeded the correct operation of the device, as shown in figure 3.6.

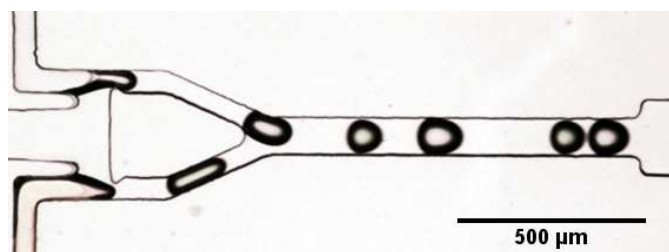


**Figure 3.6** Performance of the device when pyrazine is present in only one solution of reactants. Here the droplets are not generated in a synchronized manner.

<sup>1</sup> These tests have been performed during the internships of J. Touja and M. Buisson, directed by M. Gonidec in 2016.

To overcome this problem, they separated the total amount of pyrazine in both solutions, maintaining a similar density, viscosity and surface tension in both. This way, the first solution contained  $K_2[Pt(CN)_4]$  (0.14 M) and pyrazine (0.7 M), while the second one contained  $Fe(BF_4)_2$  (0.14 M) and pyrazine (0.7 M). Using this setting, at  $Q_{oil} = 2100 \mu L/h$  and  $Q_{H_2O} = 600 \mu L/h$ , droplets of the reactant solutions were easily prepared with the same frequency. In fact, these droplets were produced in pairs, which announced that the dual nozzle worked successfully.

J. Touja and M. Buisson reported the successful synthesis of  $[Fe(pz)Pt(CN)_4]$ ; nevertheless, due to yet unidentified reasons, we could not reproduce this process for extended periods of time (see below).

In our experiments, even if the concentrations of reactants were not identical to the ones used by J. Touja, M. Buisson and M. Gonidec, the symmetrical partitioning of pyrazine in the two reactant solutions (instead of only one) was kept.

### 3.1.4 The first approach for the synthesis of $[Fe(pz)Pt(CN)_4]$ : *Generation* → *combination*.

Our first attempts at the microfluidic synthesis of  $[Fe(pz)Pt(CN)_4]$  were based on the *generation* → *combination* approach. The geometry of the corresponding devices, as well as their behavior when they are operated with water and food colorant instead of reactants is described in chapter 2.1. The general geometry of these kind of devices (*Purple Chip*) is shown in figure 3.7.



**Figure 3.7.** Geometry of the nozzle and exit channel in the *Purple Chip A*.

When this chip was operated using reactant solutions, the droplet pair generation was successful, but when the droplets of each pair met at the end of the nozzle they did not always merge. During some periods of time, the droplets were formed in pairs and merged successfully. These periods were, however, preceded and followed by other periods in which the droplets either did not merge, or did so randomly. Figure 3.8 shows the device as it worked under these conditions.

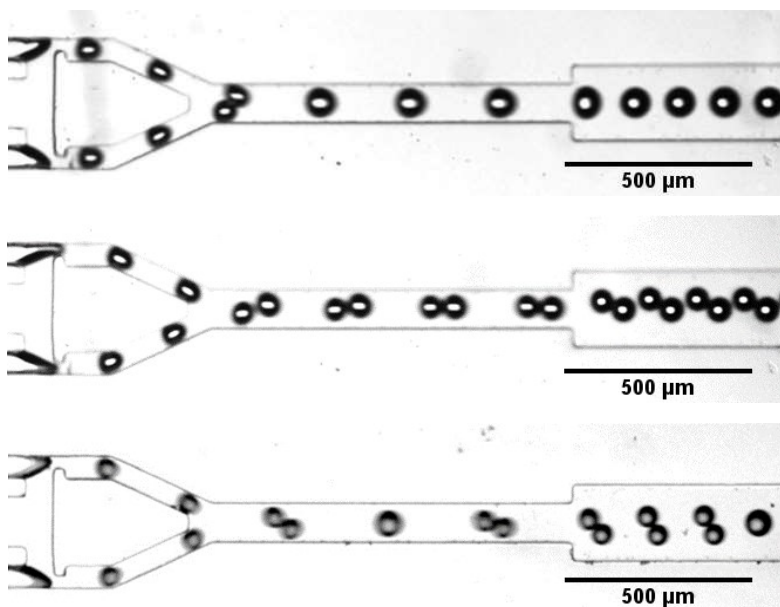


**Figure 3.8.** Performance of the Purple Chip A. The system fluctuated between three identifiable regimes: The droplets merged efficiently (up), the droplets were formed in pairs but did not merge (middle), or the pairs or droplets occasionally merged (down).

Contrary to the experiments performed without reactants, exploring the space of possible flow rates here did not result in the discovery of regimes of stable production and merging of droplets. This raises a question: Why would a system produce and merge droplets of water efficiently, but once the water is substituted for solutions with reactants, it fails to do so, even if the droplets are produced in pairs? It could be related to the differences in density, viscosity and surface tension between the pure water and the reactant solutions, but unfortunately, further analysis would be needed to completely elucidate the mechanisms underneath this result.

The proximity of the droplets generated by this device (even during the periods when the merging was inefficient) directed our interest towards methods to bring them closer once they leaved the nozzle. A sudden widening of the channel leads to gradients in the linear flow speed of the fluids, that can promote the collision and merging of droplets.<sup>17</sup> Based on this principle, we designed a set of devices that were meant to bring the droplet pairs closer and to promote their collision and merging. The first one of this kind (*Purple Chip B*) is presented in figure 3.9. Here, two rectangular sections widen the channel from 100 to 200 μm suddenly. Just as in the previous *Purple Chip A*, this geometry was efficient at generating and merging pairs of droplets of water with food colorant (figure 3.10) but failed in doing the same once these fluids were changed to solutions with reactants. This means that the incorporation of the rectangles in the exit channel did not play a significant role in promoting the merging of the droplets.

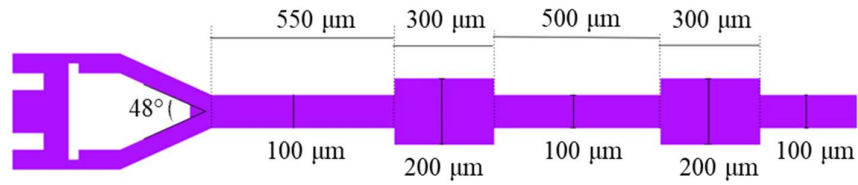


**Figure 3.9.** Blueprint of the Purple Chip B including sections designed to promote droplet merging.

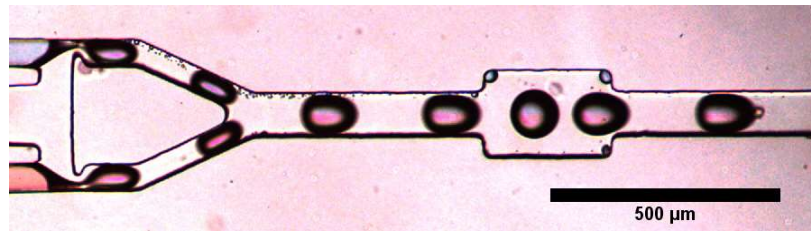


**Figure 3.10.** Performance of the chip presented in figure 3.9 at merging droplets of water with food colorant.

Here, it must be noted that the droplets do not merge in the rectangular sections designed for that purpose. Instead, they merge just after they leave the nozzle. This means that the droplets are formed almost exactly at the same time. This has the disadvantage that the liquids in the final droplets remain at their original hemispheres and the *symmetry problem* is not solved.

Because of the failure of the previous chip, other geometries were designed to promote the merging of the droplets. They can be divided into two groups (figures 3.11 and 3.12). They all contain a widening of the channel, as in the design that was just mentioned, but in the second family (figure 3.12) an additional feature is introduced: a pair of parallel permeable walls to hold the stream of droplets in the middle of the channel. These kind of walls were reported to help the merging of droplets.<sup>24</sup>

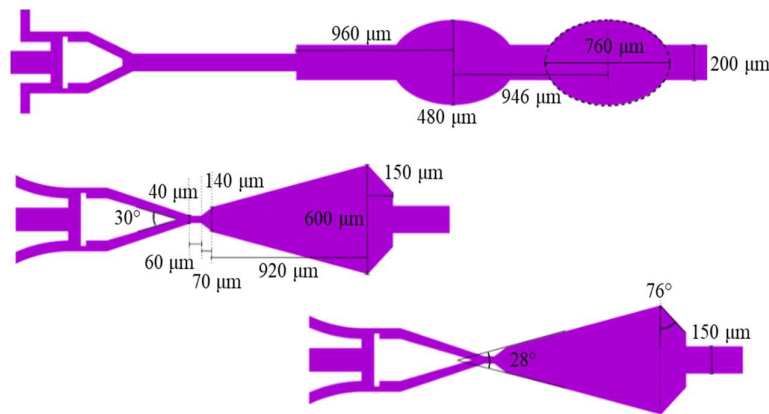


**Figure 3.11.** Blueprints of the additional geometries tested for Purple Chips, with widening of the channel.

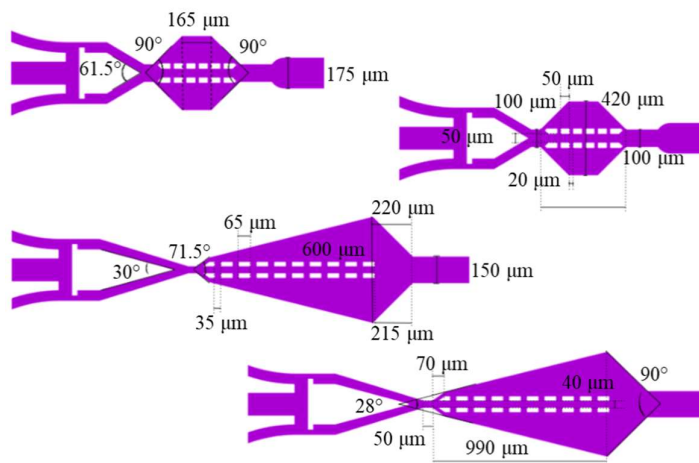


**Figure 3.12.** Blueprints of the Purple Chip geometries with walls to hold the stream of droplets in the middle of the channel.

Unfortunately, the performance of these devices (all of them) did not differ drastically from that of the first chip. This does not mean that bringing the droplets closer to each other is useless. It only means that the distance between the droplets in each pair was too long for these methods to have a significant advantage, or that origin of the problem was not strictly the distance between the droplets. In other words, these methods can bring droplets closer together, but the droplets only merge if they collide fast enough. In our case, either the original distance between the droplets was above that threshold and therefore none of these methods made a significant improvement, or the droplets did not collide with enough strength to merge. Using any of these devices led to an inefficient merging of droplets, and for this reason the first approach was dismissed.

Even, if no success was found with this approach, there is a qualitative lesson to be learnt from it, and that is worth mentioning. First, remember that, as described in figure 3.8, when solutions with reactants were used, the behavior of these systems switched between three identifiable regimes. In some occasions, chips designed by this approach kept working successfully for more than 10 minutes continuously; in other occasions, chips did not work at all. In the geometry shown in figure 3.9 (*Purple Chip B*), the chips that worked for relatively long periods of time and the chips that did not work at all were prepared from the same master. So, it seems that there are some parameters, beyond the geometry and the flow rates, that have an influence on how long the device can produce and merge droplets of solutions with reactants efficiently. In fact, the duration of these periods of successful performance could not be related with any variable and we did not find a methodology to prolongate them. Any explanation for this can only be speculative at this point.

### 3.1.5 The second approach for the synthesis of $[Fe(pz)Pt(CN)_4]$ : *Combination*→ *generation*.

The second approach we followed for the microfluidic synthesis of  $[Fe(pz)Pt(CN)_4]$  was based on combining the reactants in a single channel that reaches a flow-focusing junction where the flow is cut down into a stream of droplets containing all the reactants *ab initio*. The first geometry we used for his purpose is described in chapter 2.1 and briefly recalled in figure 3.13.

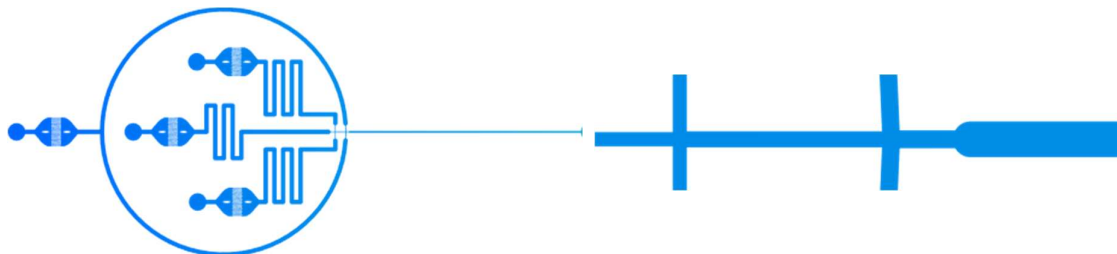


**Figure 3.13.** Geometry of the Blue Chip.

Chapter 2.1 describes the functioning of this chip using oil and water with food colorant. When the flows of colored water are substituted by solutions with reactants, new challenges arise. Remember that, as explained in chapter 2.1, the proper functioning of devices based on the *combination*→ *generation* approach depends on whether the buffer layer can stop the reactants from entering in contact. So, if for some reason there is a perturbation in the flows of solutions with reactants (for example, in the face of strong pressure oscillations), both solutions with reactants can enter in contact before the droplets are formed. When this happens, the reaction occurs in the interior of those channels (instead of the interior of the droplets). To which extent this event can irreversibly disturb the device, depends on the amount of product that precipitates and whether it is strongly attached to the walls of the chip. In most cases, even when not enough precipitate is formed to clog the channel, some particles strongly attached to the walls interfere with the flows, cascading all the mechanisms towards clogging. This means that pressure oscillations can negatively affect the behavior of this device very easily.

#### 3.1.5.a. The design of a starting sequence to avoid backflow and the formation of oil-bridges at the beginning of the operation of the chips.

The pressure oscillations can have different origins that range from acoustic pollution, to pulses in the pumps, so reducing them is a complex task. A source of pressure oscillations that should be strongly addressed is the formation of oil-bridges after the occurrence of a massive backflow (see chapter 2.2). Backflow appears when the force needed to overcome the fluidic resistance of the exit channel is comparable to the force needed to expand the other channels mechanically so, instead of flowing only through the exit channel, oil pushes the other fluids backwards. This device incorporates a wide channel between the nozzle and the filters that helps to prevent the arrival of oil to the filters, which was quite helpful, but did not completely solve the problem.

Surprisingly, the solution to the problems of backflow and formation of oil-bridges in the filters of the chip did not rely on changing the geometry of the chip, but in designing a

program of flow rates at the beginning of the experiment. Figure 3.14 shows an example of the starting sequence that can efficiently avoid backflow in these devices.

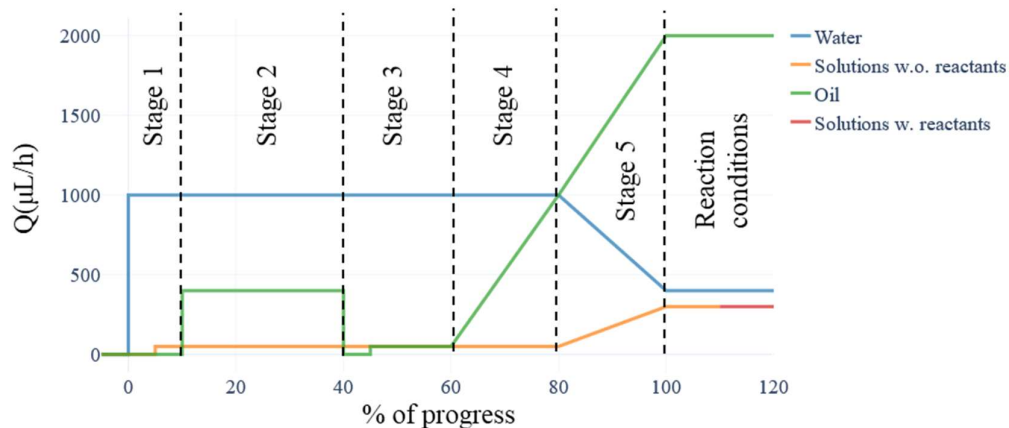


**Figure 3.14.** Program of flow rates to be performed at the beginning of the experiment to avoid backflow in the devices based on the combination  $\rightarrow$  generation approach (Blue, Red and Green Chips). The tubes connecting the syringes with solutions with reactants to the chip are initially full of water. Before this water is displaced by the solutions with reactants, this fluid is expressed here as “solutions w.o. reactants”.

This sequence is explained as follows:

- **Experimental setting.** All the tubes that will transport either water or solutions of reactants are filled with water. The flow of all the syringe pumps is set to zero. At this point, the only tube that is not full of water is the one transporting oil.
- **Stage 1.** The flow of water in the buffer layer is set to 1000  $\mu\text{L/h}$ . After  $\sim 5$  minutes, the flow rate of solutions with reactants is set to 50  $\mu\text{L/h}$ . Because the tubes transporting reactants are full of water, only water is pumped into the chip at this point.
- **Stage 2.** The flow of oil is increased to  $\sim 400$   $\mu\text{L/h}$ . This flow is kept constant until the oil reaches the chip. Once it enters the chip, the flow should be stopped suddenly.
- **Stage 3.** Around 30 seconds should be waited until the flow of oil stops. Afterwards, the flow of oil must be set to 50  $\mu\text{L/h}$  until it reaches the flow-focusing junction (at least on one of both sides; remember that in the nozzle, two flows of mineral oil intercept a flow of water in a perpendicular way at each side of it).
- **Stage 4.** The flow of oil is increased at a rate low enough to avoid backflow.
- **Stage 5.** When the flow rate of oil reaches around 50% of the expected reaction conditions, the flow of water in the buffer layer is slowly decreased, while the flow rates of solutions with reactants and oil are gradually raised until all flow rates reach the expected reaction conditions. After this point, the solutions with reactants should displace the water along the tubes and will slowly arrive to the chip.

If the starting sequence is performed correctly, the experiment begins by the arrival of reactants into the chip. In our case, the solution of Fe(II) and pyrazine has a characteristic yellow color, that is very helpful when trying to monitor the advance of the reactants across the tubes and in the chip. Unfortunately, the same cannot be said about the colorless solution with pyrazine and  $K_2[Pt(CN)_4]$ . In fact, the arrival of reactants into the nozzle is more easily seen by the emergence of an apparent interface that divides the flows of solutions with reactants from the buffer layer, as shown in figure 3.16b (see below). The origin of this line is related with the fact that the presence of solutes in the solutions with reactants causes a major difference in their refractive indices with respect to the pure water solution.

### 3.1.5.b. The performance of the Blue Chip.

Exploring different flow rates at which the *Blue chip* (1<sup>st</sup> device based on the *combination*→*generation* approach) could be operated efficiently, it was seen that, at the beginning of the experiments, the behavior of this device has a strong resemblance to the case when only water and food colorant were used (described in chapter 2.2); nevertheless, after around 15 minutes of functioning, a precipitate is formed in the channel that contains both solutions with reactants as shown in figure 3.15.

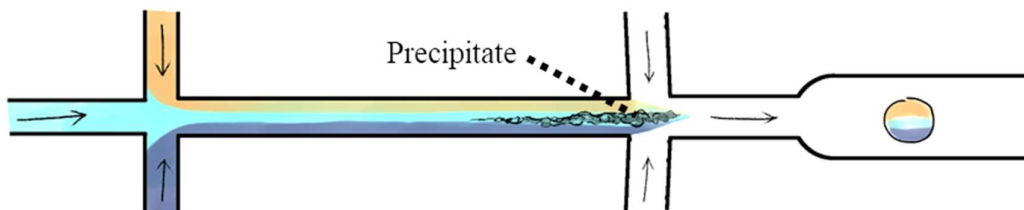


**Figure 3.15.** Formation of a precipitate in the nozzle of Blue Chip.

This precipitate appears initially next to the flow focusing junction and grows backwards forming a “needle” along the channel. Figure 3.16 shows a long exposure picture of this needle under the microscope using crossed polarizers. Crystals formed in this needle are large enough to twist the angle of light, so they appear to glow under the microscope.

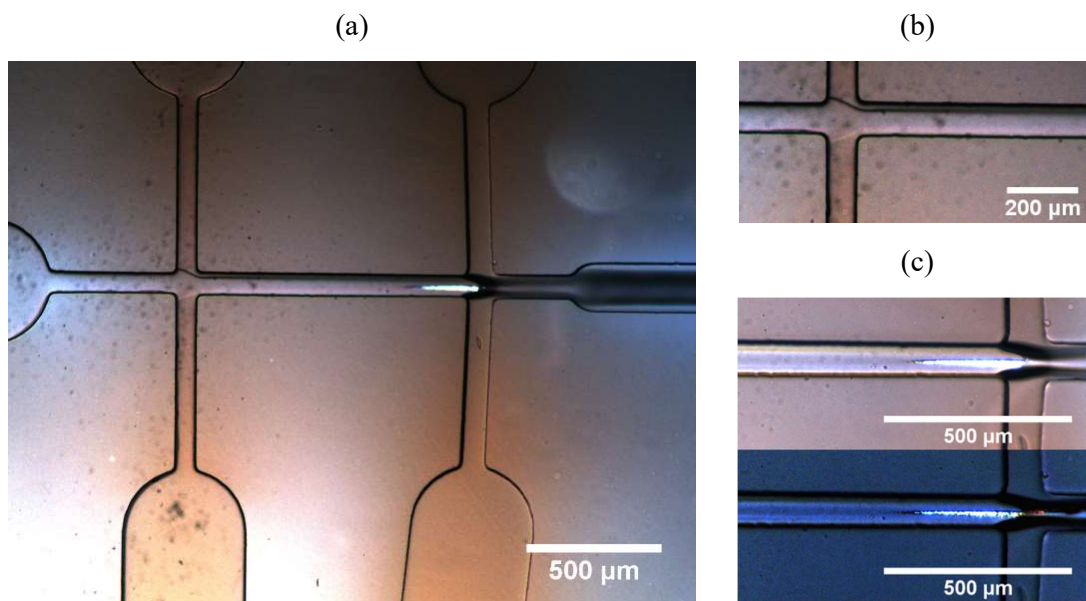


**Figure 3.16.** Long exposure pictures of the Blue Chip under crossed polarizers, when operating with solutions with reactants. General view (a), apparent interface where the solutions with reactants meet the buffer layer (b) and zoom-in to the needle with different intensities of light for a better view of the walls of the chip and the needle-like precipitate (c).

Moreover, the needle-like precipitate seems to grow in the direction of the flow as well, forming a solid structure in front of the nozzle. As soon as it reached a certain length, it was washed away by the drag force exerted by the fluids. Figure 3.17 shows the formation and removal of this structure. After this structure is washed away, another equivalent structure started forming again at the junction. This process occurred in a cyclical way in periods of ca. 70 to 90 seconds.

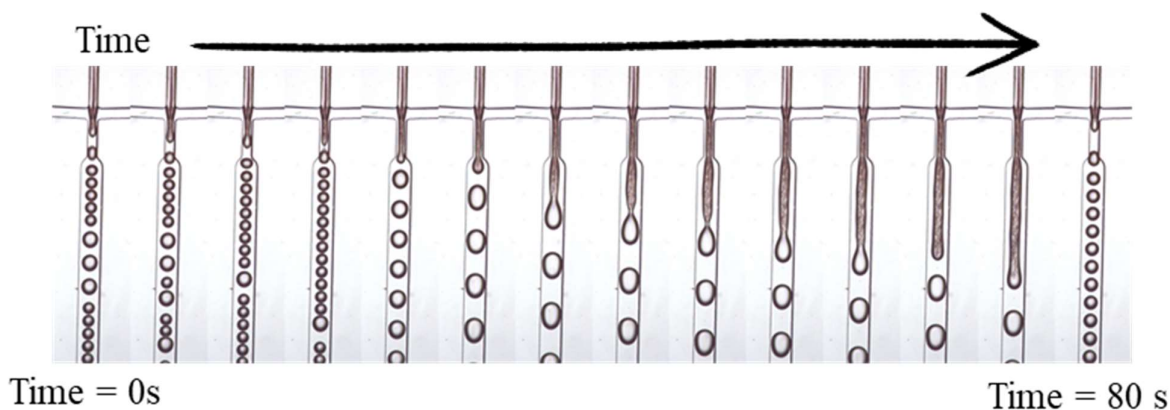


**Figure 3.17.** Formation and release of a solid structure made by  $[\text{Fe}(\text{pz})\text{Pt}(\text{CN})_4]$  in the microfluidic system. The orientation of the chips was rotated  $90^\circ$  clockwise to reduce the space of the figure.

To reduce the formation of this structure, we lowered the flow rates of solutions with reactants and increased the flow of the buffer layer. The flows were set to the following values:

Solution with reactants 1:  $[Fe(II)] = 0.16 M$ ;  $[pz] = 0.8 M$ ;  $Q = 600 \mu L/h$ .

Solution with reactants 2:  $[Pt(CN)_4^{2-}] = 0.16 M$ ;  $[pz] = 0.8 M$ ;  $Q = 600 \mu L/h$ .

Buffer layer:  $Q = 1200 \mu L/h$ .

Mineral Oil:  $Q = 2100 \mu L/h$ .

This way, the system could be operated successfully during 1.5 h until eventually, it clogged irreversibly because the needle showed in figure 3.17 grew until it occupied the whole cross section area of the channel. Unfortunately, most of the sample obtained this way was lost during the cleaning process and no magnetic measurements were performed, but enough product was obtained to perform TEM analysis (JEOL JEM-1400 Plus at an acceleration voltage of 60 kV). Figure 3.18 shows the TEM images that correspond to this sample.

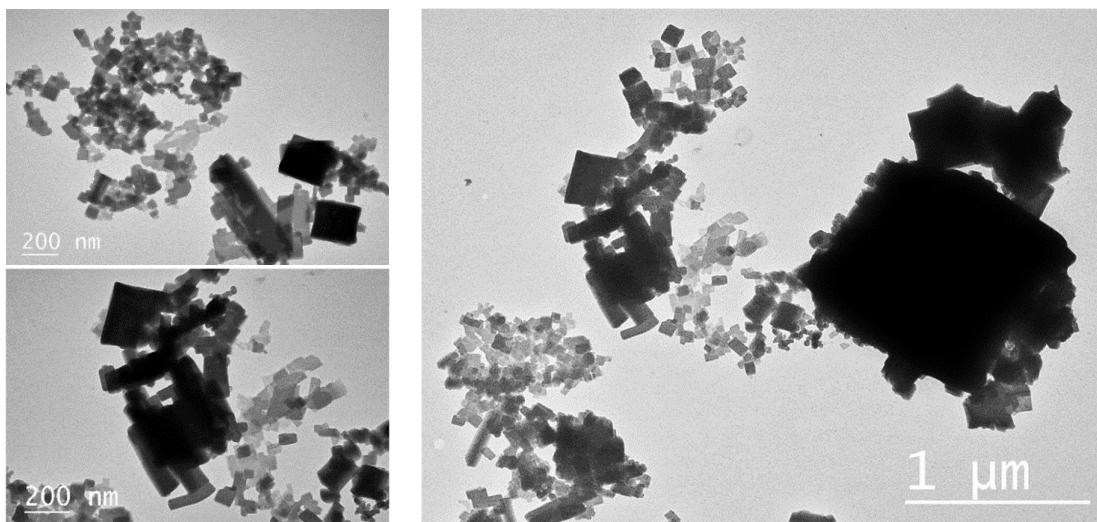


**Figure 3.18.** TEM pictures of the particles of  $[Fe(pz)Pt(CN)_4]$  obtained using the Blue Chip.

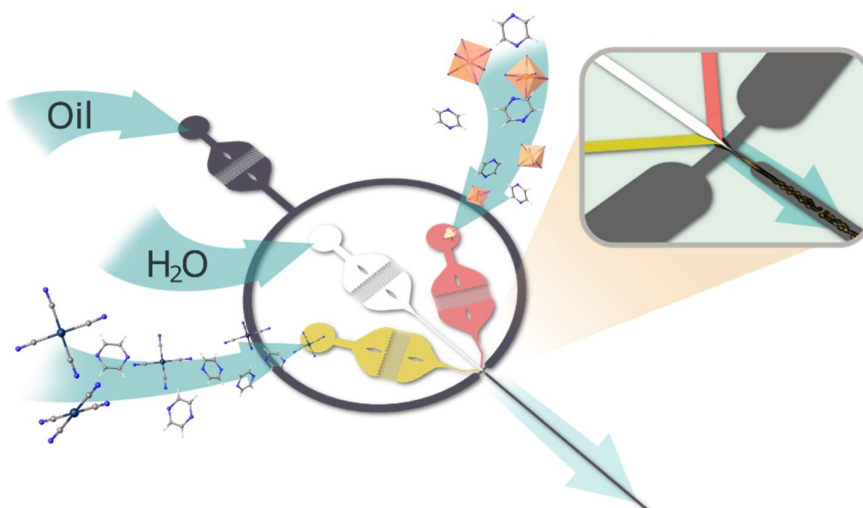
Even if this device could not work as expected because of clogging, it can certainly work successfully for longer periods than the devices based on the *generation*  $\rightarrow$  *combination* approach (*Purple Chips*). And even if it cannot generate a stream of droplet with a uniform size, the effect that microfluidic synthesis has on the features of the obtained particles is clear: In this sample, there is a staggering amount of small square-like particles below 100 nm in diameter. Unfortunately the particle size here cannot be related to the droplet size during the synthesis, first because the size of the droplets changed during the experiment (due to the formation of solids in the nozzle) and second, because some of the product was not synthesized inside a droplet, but in precipitated structures similar to the one presented in figure 3.17.

The period of successful work of this device could be extended by a proper selection of flow rates. Nevertheless, in this device there are 3 flow rates that can be modulated: The ones of the reactants, the one of the water between them and the one of the oil. For this reason, the

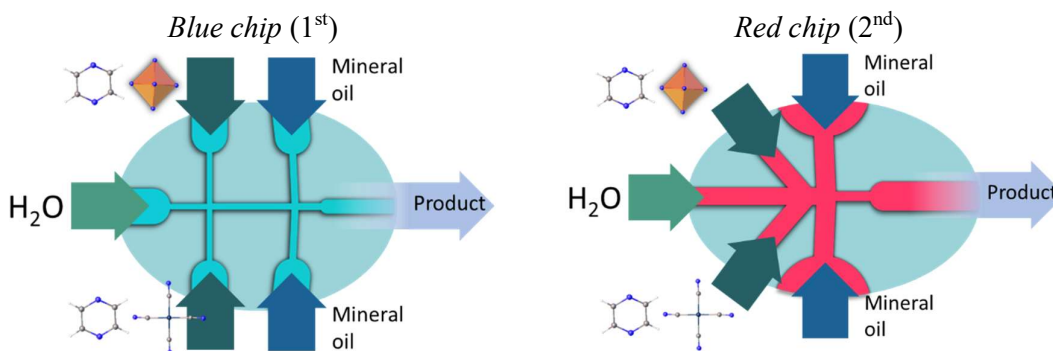
space of possible states of the system has 3 dimensions. We decided not to explore all the possibilities because there is a clear failure in the design of this device: The channel between the point where the solutions and water are combined is too long. For this reason, we designed a new device (*Red Chip*) where the distance between the combination of reactants and the droplet generation is shorter.

### 3.1.5.c. The performance of the Red Chip.

The geometry and the functioning of the *Red Chip* (the second chip based on the *combination*→*generation* approach) is discussed in chapter 2.1 and is summarized in figure 3.19. Of course, the main difference between this device and the previous one is the length of the channel that contains the solutions with reactants before they reach the nozzle (reduced from ~1.1 mm in the previous one, to ~30  $\mu\text{m}$  here, as compared in figure 3.20). Because of this change, the formation of the needle that clogged the channel in the previous device was hindered.



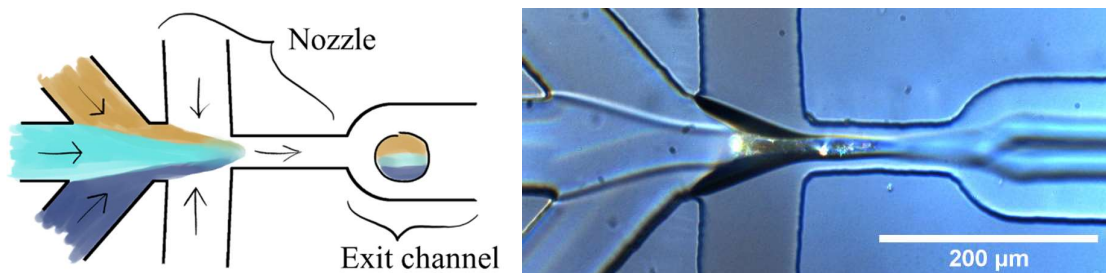
**Figure 3.19.** Geometry and functioning of the Red Chip.



**Figure 3.20.** Comparison of the geometry of the Blue and Red Chips.

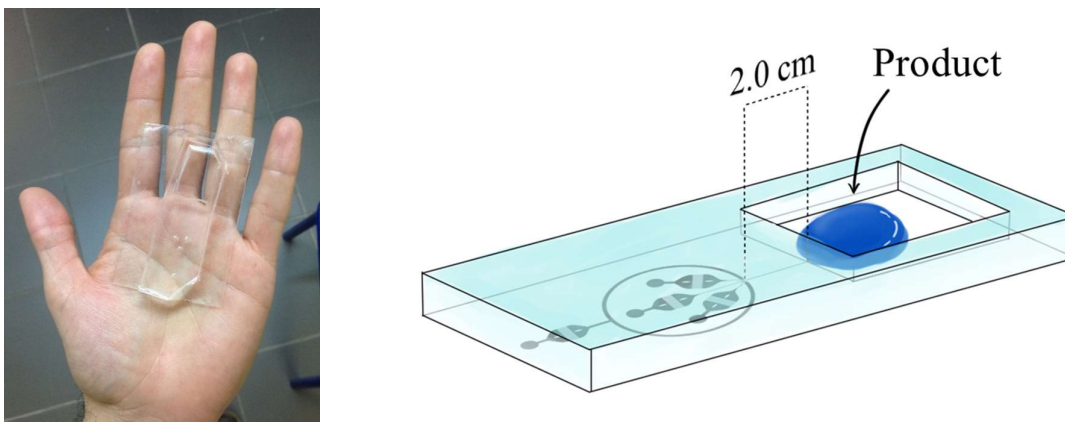
There are other differences worth mentioning in this device with respect to the previous one. First, note that in the *Red Chip*, the channels with reactants practically reach the nozzle. Since the channels carrying oil arrive to the nozzle as well, the vicinity around the nozzle is crowded with channels. This means that the channels with reactants cannot intercept the channel perpendicularly. Therefore, the solutions with reactants reach the nozzle from a diagonal direction. Second, to increase the distance between droplets, the width of the exit channel in the *Red Chip* device is only 150  $\mu\text{m}$  (smaller than the 200  $\mu\text{m}$  in the *Blue Chip*). Finally, since the starting sequence efficiently avoids backflow at the beginning of the experiment, the new device did not require an additional channel (a reservoir) to contain the volume of oil during the backflow.

Figure 3.21 (left) shows the ideal functioning of this device, which is the same as the one depicted in figure 3.20 (right). On the right side of figure 3.21, a long exposure picture of this device under crossed polarizers allows to easily see a solid tip formed in the nozzle. At optimal conditions the speed at which this tip grows is minimal and does not affect the performance of the chip. In non-optimal conditions, the device can still work successfully if the size of this tip reaches a plateau (when the rate at which crystals grow is the same as the speed at which they are torn away), which unfortunately would lead to the contamination of the product by large particles synthesized in the tip (and not inside the droplets).



**Figure 3.21.** Schematic functioning of the nozzle and the exit channel of *Red Chip* (left), and long exposure picture under crossed polarizers of the nozzle under a real scenario in the synthesis of  $[\text{Fe}(\text{pz})\text{Pt}(\text{CN})_4]$  (right). It should be noted that after some minutes a solid tip is formed. When using solutions with reactants in this device, it is interesting to note that the concentration of reactants is so high, that it affects its index of refraction. For this reason, under the microscope a thin interface is seen between the flow of solutions and the buffer layer.

Collecting the sample synthesized using this approach was first attempted by attaching a tube to the end of the exit channel. Nevertheless, sedimentation at the end of the exit channel led to clogging. To collect the product without risks of clogging, a hole was carved at the end of the exit channel 2.0 cm away from the nozzle. This hole, served as a reservoir at the end of the chip, where the product was easily collected from. A chip with these features is shown in figure 3.22 (left), while the hole is depicted in figure 3.22 (right).



**Figure 3.22.** Aspect of the Red Chip (left), and the hole cut from the chip to recover the product (right).

Such a device with 75  $\mu\text{m}$  in height was operated successfully until the syringes containing the solutions of reactants were empty (1.0 mL) using the following conditions:

Solution with reactants 1:  $|\text{Fe(II)}| = 0.16 \text{ M}$ ;  $|\text{pz}| = 0.8 \text{ M}$ ;  $Q = 225 \mu\text{L/h}$ .

Solution with reactants 2:  $|\text{Pt(CN)}_4^{2-}| = 0.16 \text{ M}$ ;  $|\text{pz}| = 0.8 \text{ M}$ ;  $Q = 225 \mu\text{L/h}$ .

Buffer layer:  $Q = 450 \mu\text{L/h}$ .

Mineral Oil:  $Q = 3500 \mu\text{L/h}$ .

A true improvement was made in terms of working period. We were able to use this device long enough to empty the syringes with reactants without clogging the chip, even if it does not necessarily mean that this device could operate indefinitely.

In our case, we identified through trial-and-error the operating conditions that lead to a successful performance of chips with this geometry. However, many chips broke or clogged irreversibly during our searching process. After a careful and systematic search, it is possible to operate this chip successfully up to 4 hours (long enough to perform a reaction). If the conditions are not optimal, randomness seems to play a role in the clogging of this device.

In this device, the diameter of the exit channel is larger than the nozzle. Because of this, there is a reduction in the linear flow speed of the droplets, which makes them collide and occasionally merge. Additionally, a kind of “traffic jam” distorts the path of the droplets, displacing them out of the center of the channel. As explained in chapter 1.1, the *symmetry problem* only arises when the droplets are positioned in the x-z plane of symmetry. This means that the “traffic jam” makes some droplets merge, but at the same time it solves the *symmetry problem*. Figure 3.23 shows the stream of droplets when this device is used with reactant solutions.

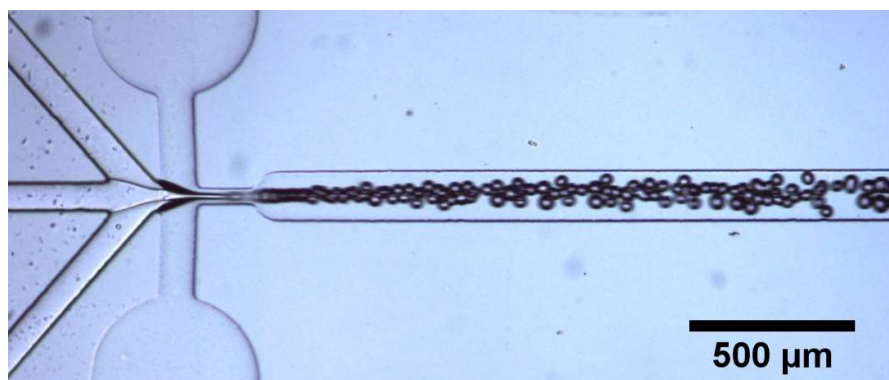


**Figure 3.23.** Stream of droplets formed in the Red Chip when solutions with reactants are used.

The size distribution of the droplets generated in this experiment are difficult to measure (the borders cannot be sharply identified, and the droplets cannot be identified automatically using ImageJ). Nevertheless, a histogram can be generated by measuring the droplet sizes manually on our pictures, as shown in figure 3.24. It must be noticed that even if the size distribution is quite broad (number  $n$  of droplets measured = 297, mean diameter = 32.5  $\mu\text{m}$ ,  $\text{sd} = 5.4 \mu\text{m}$ , dispersity index = 17%), the diameter of almost all of them (98%) lies below 50  $\mu\text{m}$ .

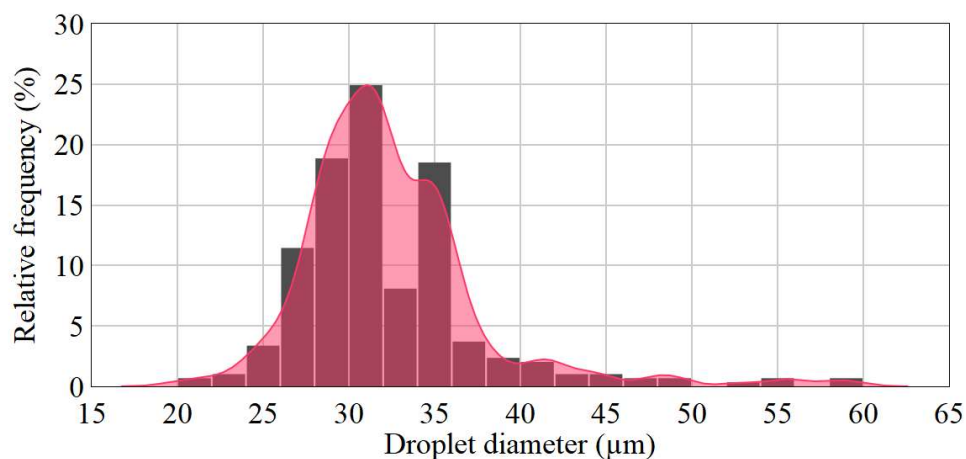


**Figure 3.24.** Histogram of the diameter of the droplets generated in the Red Chip.

*3.1.5.d. The design of a finishing sequence to avoid diffusion of reactants and the formation of precipitates in the chip at the end of its operation.*

The last aspect to mention about the behavior of this microfluidic system is that after finishing the reaction, when all the pumps are suddenly stopped, the reactants slowly mix inside the chip and form enough precipitate to clog it. A method to avoid this issue consists in designing a sequence of flow rates. This sequence is analogous to the starting sequence presented

previously in figure 3.14 but is designed to be performed at the end of the experiment. The finishing sequence is shown in figure 3.25.

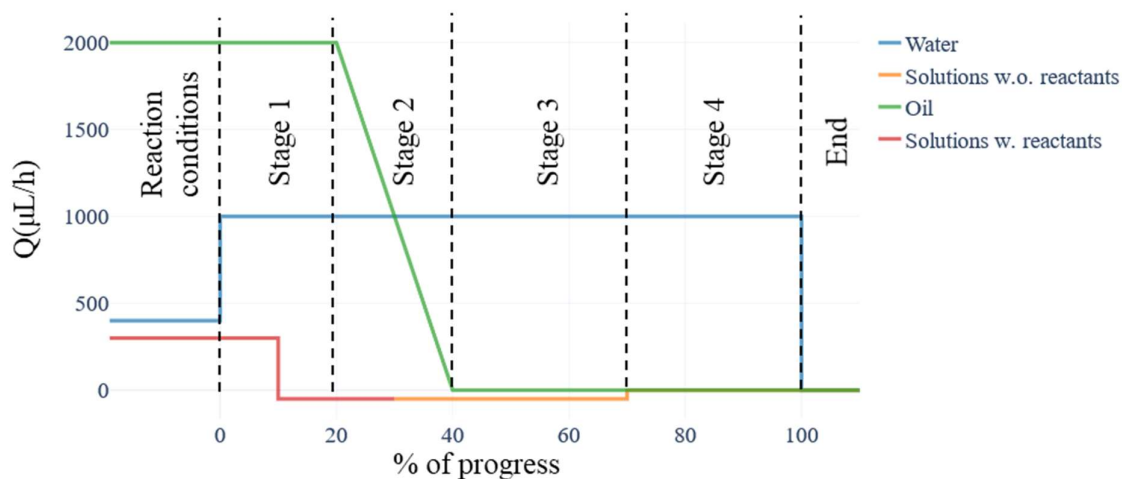


**Figure 3.25.** Program of flow rates to be performed at the end of the experiment to avoid mixing of the reactants in the devices based on the combination→ generation approach.

- **Experimental setting.** After the reaction occurs, two aspects should be considered. First, due to the flexibility of the system (PDMS, tubes and syringes), there is accumulated pressure in the system. If the flow rates were suddenly set to zero; oil, water and solutions with reactants would still flow across the chip until the pressure is stabilized again. Secondly, the only thing that stops the reactants from entering in contact is the buffer layer of water, which is thinner than a human hair.
- **Stage 1.** The flow of water is increased above 1000 μL/h. This helps to preserve the buffer layer. Additionally, it makes water flow back into the channels that carry the reactant solutions. Afterwards, the flow rate of reactants is set to -50 μL/h (the pumps are pulling solution instead of pushing it) to let the water enter those channels further. Solutions with reactants sporadically flow to the nozzle because of the pressure fluctuations caused by the changes of the flows rates. This stage is finished when the solutions with reactants are not seen in the nozzle anymore.
- **Stage 2.** The flow rate of oil is slowly reduced to zero. Caution must be taken in this step. If the flow of oil is reduced suddenly, the pressure loss can cause the reactants to flow again and reach the nozzle.
- **Step 3.** After the flow rate of oil reaches zero, the pumps corresponding to the reactants are kept at -50 μL/h for ~10 minutes, so water can displace the solutions with reactants in the tubes.
- **Step 4.** The flow rates of reactants are set to zero. The flow rate of the buffer layer is kept at 1000 μL/h to displace the oil in the exit channel for around 5 minutes. Afterwards it is set to zero and the experiment is over.

### *3.1.5.e. Cleaning the microfluidics-synthesized sample (first successful experiment).*

The precipitate obtained with this procedure was yellow (which is expected for  $[\text{Fe}(\text{pz})\text{Pt}(\text{CN})_4]$  in the high-spin state). The cleaning process aims first at removing oil impurities and secondly at replacing the solvent molecules inside the pores of the structure (mainly water) by acetone, which is easier to remove afterwards.

After the synthesis, the product mixture contains mineral oil, water, particles of  $[\text{Fe}(\text{pz})\text{Pt}(\text{CN})_4]$ , and  $\text{KBF}_4$  that was formed as a by-product. Most mineral oil was eliminated by carefully extracting the aqueous phase with a pipette and pouring it into a centrifugation tube made of PTFE. The aqueous phase was washed three times by the addition of 15 mL of ethanol to the aqueous phase and centrifuged at 15 000 RCF for 15 minutes (to eliminate  $\text{KBF}_4$ ); it was washed twice by the addition of 10 mL of n-heptane and centrifuged at 3 000 RCF for 5 minutes (to eliminate the residual mineral oil); and once, by the addition of 20 mL of acetone and centrifuged at 3000 RCF for 20 minutes (to carry away the traces of water and exchange the molecules of water inside of the pores of the structure). The acetone of the powder thus obtained was finally eliminated by drying the sample in vacuum at  $100^\circ\text{C}$  for 1 hour.

### *3.1.6. Properties of the synthesized compounds.*

As explained, the properties of  $[\text{Fe}(\text{pz})\text{Pt}(\text{CN})_4]$  can be influenced by the method of synthesis. To make a comparison between the features of  $[\text{Fe}(\text{pz})\text{Pt}(\text{CN})_4]$  synthesized according to our microfluidic procedure ( $\mathbf{1}_{\mu\text{F}}$ ), and the properties of the same material synthesized in the conventional method ( $\mathbf{1}_{\text{ref}}$ ), two batches of  $[\text{Fe}(\text{pz})\text{Pt}(\text{CN})_4]$  were prepared.

#### *3.1.6.a Synthesis of a bulk-synthesized reference sample (first reference material).*

The bulk reaction was performed by adding 1 mL of an aqueous solution of  $\text{K}_2[\text{Pt}(\text{CN})_4]$  at 0.26 M (0.26 mmol) into a vial containing 3.5 mL of a solution of  $\text{Fe}(\text{BF}_4)_2$  at 0.066 M (0.23 mmol) and pyrazine at 0.066 M (0.23 mmol) dropwise for one hour (Figure 3.26) without agitation. For this, the solution containing  $\text{K}_2[\text{Pt}(\text{CN})_4]$  was loaded into a syringe mounted on a syringe pump, which was programmed to pump the solution at  $300\ \mu\text{L}/\text{h}$ . The product was filtered using a  $0.25\ \mu\text{m}$  PTFE membrane and washed with water. Finally, it was dried for 2 hours at  $130^\circ\text{C}$ . The concentrations were chosen to fall in a range that leads to nanoparticles when microemulsion approach is used.<sup>4</sup>

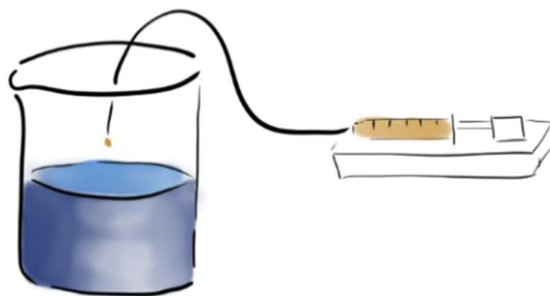


**Figure 3.26.** *Experimental setup for the bulk synthesis of  $[Fe(pz)Pt(CN)_4]$ .*

Although the concentrations here differ from the ones used in the microfluidic synthesis, they are typical of what a conventional reaction is. Of course, it is possible to question whether this procedure accurately represents the conventional methodology. Strictly, it does not. What has been expressed as *bulk* or *conventional methodology* is in fact a family of procedures, and the experimental setting presented in figure 3.26 correspond to only one possibility for synthesizing this material in bulk. In fact, the idea that all the syntheses performed in bulk happen in the same manner somehow ignores the potential effect of the stirring speed, the temperature, the dimensions and shape of the reactor and so on. Nevertheless, here we only need an archetypical sample prepared under one of the possible conditions under which this kind of compounds are generally synthesized. Another bulk sample was synthesized from solutions with the same concentrations and washed with the same procedure as the microfluidics-synthesize sample, and is discussed in section 3.1.7.

### *3.1.6.b. Characterization of the products.*

Samples  $1_{\mu F}$  and  $1_{ref}$  were characterized by Fourier Transform InfraRed (FTIR) spectroscopy and Powder X-Ray Diffraction (PXRD) to determine whether both samples were made of the same phase. FTIR was performed on a Nicolet 6700 FTIR spectrometer in Attenuated Total Reflectance mode. Sample  $1_{ref}$ , was analyzed using a PANalytical X'PERT MDP-PRO diffractometer (Cu-K $\alpha$  radiation), which was equipped with a graphite monochromator using the  $\theta$ - $\theta$  Bragg-Brentano geometry, while sample  $1_{\mu F}$  was analyzed using a PANalytical X'PERT MDP-PRO diffractometer (Cu-K $\alpha$  radiation) equipped with a Goebel mirror, using the transmission capillary geometry. For the transmission electron microscopy images (TEM) a JEOL JEM-1400 Plus operating at an acceleration voltage of 60 kV was used. Scanning Electron Microscopy images were recorded using a JEOL JSM-6400. The measurements of magnetic susceptibility were performed on a Microsense EZ7 Vibrating Sample Magnetometer with the 100-1000K EV1-LNA temperature control option, using a magnetic field of 15 kOe. For sample preparation, the materials were cold sealed in tin capsules and pasted with double-faced adhesive tape to a 3 mm quartz rod, which was later mounted on the VSM. The temperature was regulated by a flow of gaseous N $_2$  flowing at 12 standard cubic feet per hour. To subtract the background, the signal given by the bare 3 mm quartz rod and an empty capsule is subtracted from the signal obtained in the measurements.

The FTIR spectra, of both samples are presented in figure 3.27. Both spectra show the same bands, and the absence of absorption bands around  $1700\text{ cm}^{-1}$ , confirm that no acetone remains in the sample after the cleaning process.

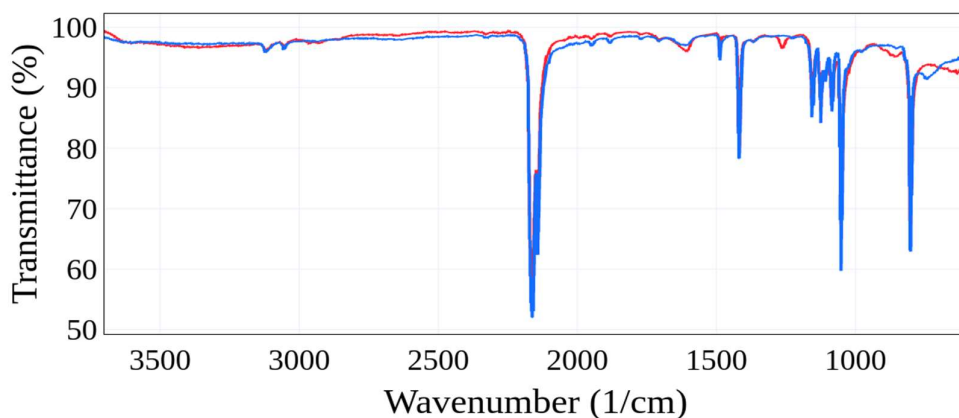


**Figure 3.27.** Comparison of the IR spectra of the bulk-synthesized (blue) and microfluidics-synthesized (red) samples.

The PXRD diffractograms, reported in figure 3.28, show similar patterns. We note that both samples are made of crystalline powders and display signals at the same angles. These angles match the ones calculated from the crystallographic structure reported by V. Niel *et al.*,<sup>19</sup> meaning that both are made of the same known phase reported in the literature. This is not surprising because there is only one reported phase of  $[\text{Fe}(\text{pz})\text{Pt}(\text{CN})_4]$  in the high-spin state (which corresponds to the one shown in figure 3.2).

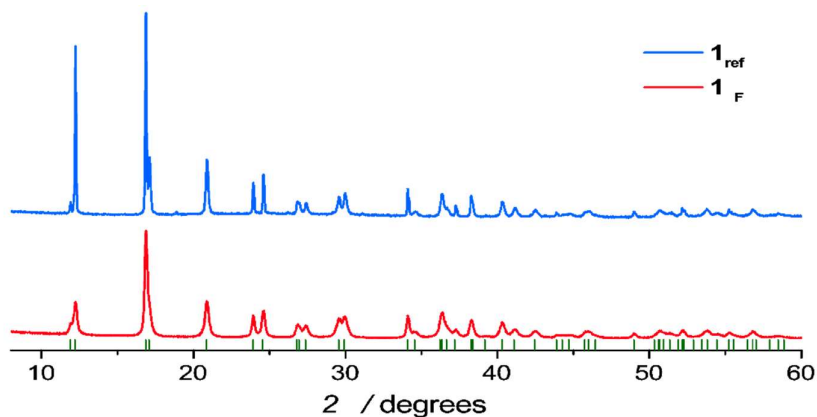


**Figure 3.28.** Comparison of the PXRD diffractograms of the bulk-synthesized (red) and microfluidics-synthesized (blue) samples.

The only remarkable difference between both diffractograms is the width of the peaks. This can be associated with a difference in the size of the coherent domain size of the samples. The smaller the coherent domain size, the wider the peaks are. Using profile matching, in a collaborative work with Dr. Mathieu Marchivie, we estimated the approximate size of the coherent domains of both samples to 176 nm in sample  $1_{\text{Ref}}$  and 34 nm in sample  $1_{\mu\text{F}}$ .

### 3.1.6.c. Magnetic characterization of the products.

The switching behavior of both samples was followed by measuring their magnetic susceptibility as a function of temperature, and in particular by following the evolution of the  $\chi T$  product with temperature. Before being weighed and prepared for measurement, the samples were dehydrated for 2 h at 400 K. Additionally, a dehydration step of 1h at 400 K was performed *in-situ* in the magnetometer just before the measurements. Figure 3.29 shows the  $\chi T$  plot of the sample synthesized in bulk measured in a VSM at 5 K/min.

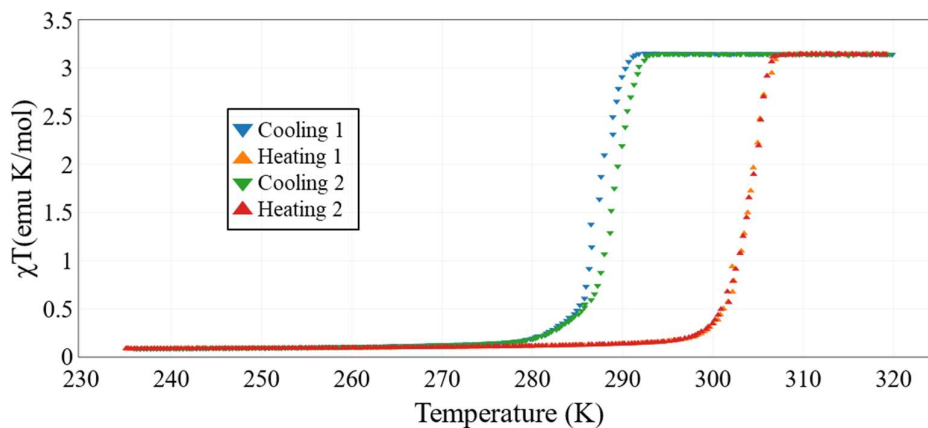


**Figure 3.29.**  $\chi T$  plot of the  $1_{ref}$  sample measured in a VSM @ 5 K/min.

The sample  $1_{ref}$  prepared using the bulk method displays abrupt changes between  $\chi T = 0.08$  emu K/mol at 250 K (a value expected for a LS Fe(II) metallic centers), and a value of  $\chi T = 3.14$  emu K/mol at 320 K (close to the expected value of 3 emu K/mol for the high-spin state, assuming  $S = 2$  and  $g = 2$ ). When the material is cooled down, this transition ( $T_{\frac{1}{2}\downarrow}$ ) occurs around 289 K. The values measured in both cycles are not equal, but differ in less than 2 K. Meanwhile, when the material is warmed up, the transition from low- to high-spin state ( $T_{\frac{1}{2}\uparrow}$ ) happens at 304 K. In both cycles,  $T_{\frac{1}{2}\uparrow}$  has the same value. The hysteresis range in this material measured at 5.0 K/min spans from 289 K to 304 K, which represent a 16 K-wide hysteresis loop. When this measurement is compared with the data reported in the literature regarding the transition temperature of bulk-synthesized samples, the  $\chi T$  values and the switching temperatures agree with the ones obtained by M. T. Delgado-Perez *et al.*<sup>2</sup> (from 288 to 303, measured at 1 K/min).

The sample prepared using microfluidics also displays spin crossover, and its corresponding  $\chi T$  plot is shown in figure 3.30.

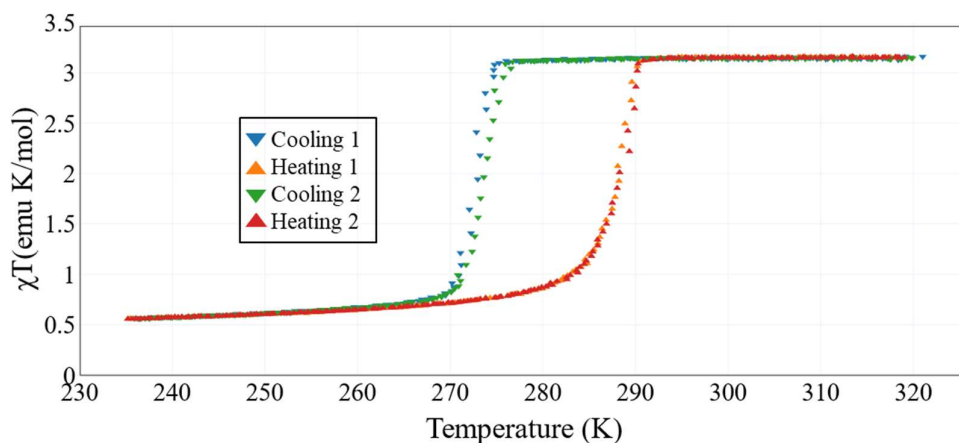


**Figure 3.30.**  $\chi T$  plot of  $I_{\mu F}$ . measured in a VSM @ 5K/min.

In this case, at high temperatures, the  $\chi T$  value also corresponds to Fe(II) ions in the HS state ( $\chi T = 3.14$  emu K/mol). When the sample is cooled down, the material displays a transition to LS at  $T_{\frac{1}{2}\downarrow} \approx 274$  K and asymptotically approaches a value of  $\chi T = 0.56$  emu K/mol, indicating the presence of a HS residue. When the sample is warmed up, the  $\chi T$  value rises at  $T_{\frac{1}{2}\uparrow} \approx 288$  K. Here as well, when the sample is cooled down, there is a marginal difference in the transition temperatures measured in the first and the second cycle, but both curves overlap when the sample is heated up. Figure 3.31 compares the behavior of both samples.

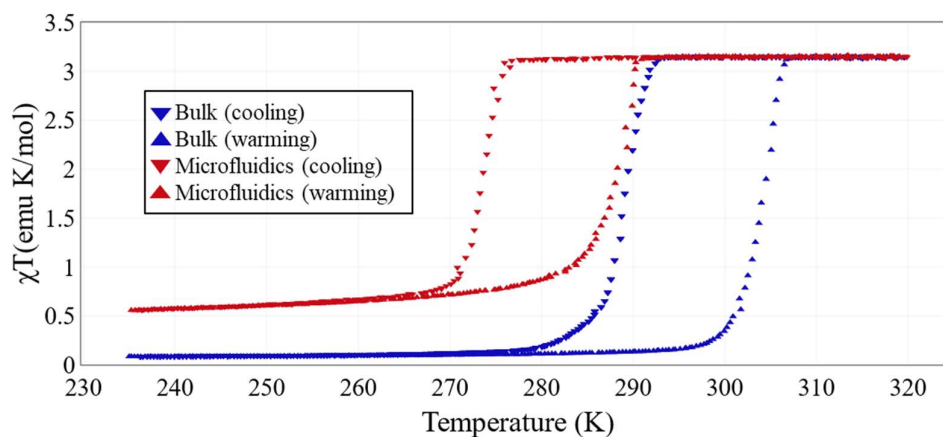


**Figure 3.31.** Comparison of the  $\chi T$  plots of  $I_{ref}$  (red) and  $I_{\mu F}$  (blue) samples.

As seen in figure 3.31, there is a clear difference in the hysteresis range of both samples. This difference in the switching behavior is very interesting from the point of view of spin crossover. Even if a change of the switching behavior of the  $[\text{Fe}(\text{pz})\text{Pt}(\text{CN})_4]$  particles synthesized in microfluidics was expected, the magnitude of this change was surprising (especially when considering that the hysteresis loops of both materials do not even overlap).

As explained in chapter 1.2, in the interacting model of spin crossover, the width of the hysteresis range is the consequence of the interaction constant  $\Gamma$ . It is quite intuitive that as a

spin crossover material loses cooperativity and the interaction constant decreases, the hysteresis loop becomes narrower until disappearing (when  $\Gamma < 2RT_{1/2}$ ). In our case, we identify a decrease in the width of hysteresis loop (measured as the difference in the values of  $T_{1/2}\uparrow$  and  $T_{1/2}\downarrow$ ) from 16 K in the bulk-synthesized material, to 14 K in the microfluidics-synthesized one (which may reflect a slight reduction in the cooperativity of the material). Nevertheless, the reduction of the interaction constant  $\Gamma$  cannot explain why the two curves do not overlap at any point.

In fact, the features of the  $\chi T$  curve of the microfluidics-synthesized sample correspond to the ones expected for nanoparticles: Reduction of the hysteresis width, lowering of the transition temperatures, smoother curves and a remaining HS fraction at low temperature. However, the syntheses of nanoparticles of this material normally require the use of nanometric-sized micelles. As stated before, there were no reports of  $[\text{Fe}(\text{pz})\text{Pt}(\text{CN})_4]$  precipitating spontaneously in form of nanoparticles. This logic leads to the formulation of two questions: The first one is whether microfluidic synthesis can reduce the size of particles of  $[\text{Fe}(\text{pz})\text{Pt}(\text{CN})_4]$  to the nanometric scale, and the second one, whether we can associate the switching behavior of the microfluidics-synthesized sample with the size of its particles. For this, we needed to determine the particle size and compare its switching temperatures with the ones reported in literature.

#### 3.1.6.d. Morphological characterization of the products (first successful experiment).

Electron microscopy on both samples was performed. Figure 3.32 displays the SEM pictures.

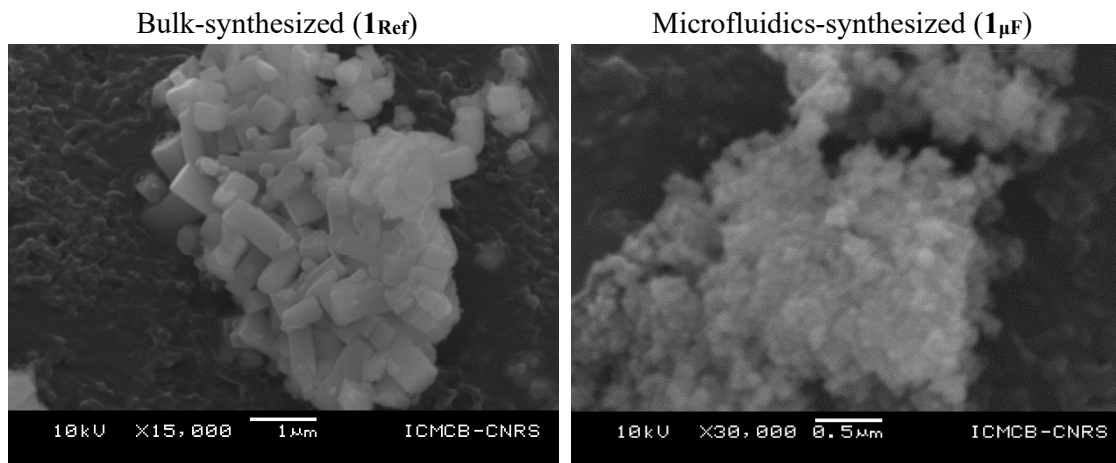


**Figure 3.32.** Comparison of the SEM imaged from the bulk-synthesized (left) and microfluidics-synthesized (right) samples.

Although the particles of the microfluidics-synthesized sample could not be resolved, from these pictures we observe that microfluidics had a strong impact on the morphology of the product. These samples were also analyzed using TEM, as shown in figure 3.33.

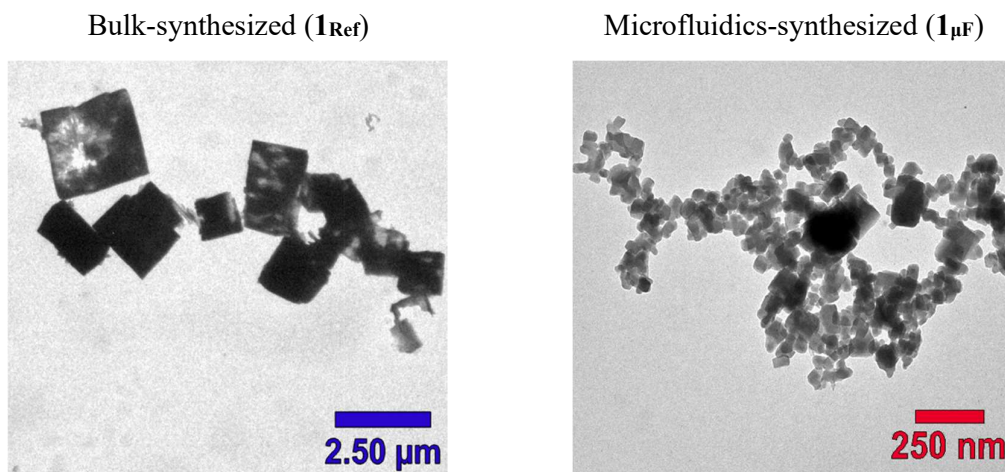


**Figure 3.33.** Comparison of the TEM images from the bulk-synthesized (left) and microfluidics-synthesized (right)  $[\text{Fe}(\text{pz})\text{Pt}(\text{CN})_4]$  samples.

We observe square-like particles in both samples with considerable differences in their size. When the particle size of these samples is determined from measuring many TEM pictures (figure 3.34), the sample synthesized using microfluidics clearly has smaller particles.

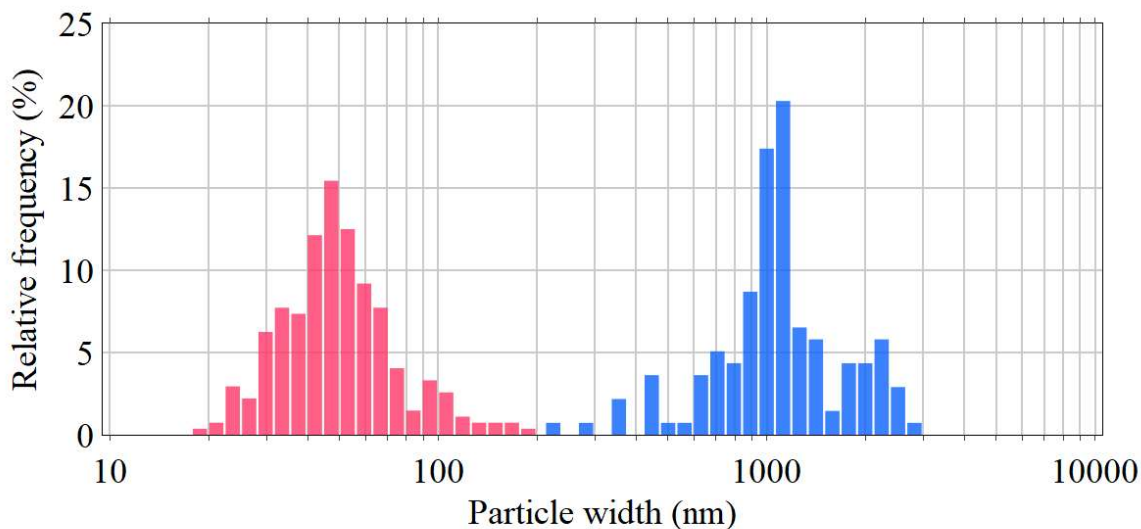


**Figure 3.34.** Particle size distribution of the bulk-synthesized (blue,  $n = 138$ ) and the microfluidics-synthesized (red,  $n = 122$ ) samples obtained from the TEM images.

Based on the particles measured using TEM (figure 3.34), the particles synthesized according to the conventional methodology have an average size of 1071 nm (log-cauchy distribution,  $\log d = 3.03 \pm 0.11$ ), while the particle size distribution of the microfluidics-synthesized sample is centered around 47 nm (log-normal distribution,  $\log d = 1.67 \pm 0.14$ ). This difference in size is consistent with the difference in the crystallographic coherent domain sizes observed from PXRD patterns.

Figure 3.35 displays an analysis that is complementary to the one in figure 3.34. Here, the goal is to express the percentage of the product volume that belongs to particles with a size below the one shown in the horizontal axis. For this analysis, the particles were first arranged by their size, and their volume was assumed to be proportional to  $V_{particle} \propto w^3$ , where  $w$  is the width of the particle visible from the TEM images. Afterwards, the volume of each particle was added sequentially. The resulting value is divided by the addition of the volume of all the particles. This analysis is performed to both samples (**1<sub>Ref</sub>** and **1<sub>μF</sub>**) for comparison. Here we can see that 50% of the product volume in the sample synthesized using microfluidics is contained inside of particles with a size below  $\sim 200$  nm, while the same value of the sample synthesized in bulk is  $\sim 2$   $\mu\text{m}$ .

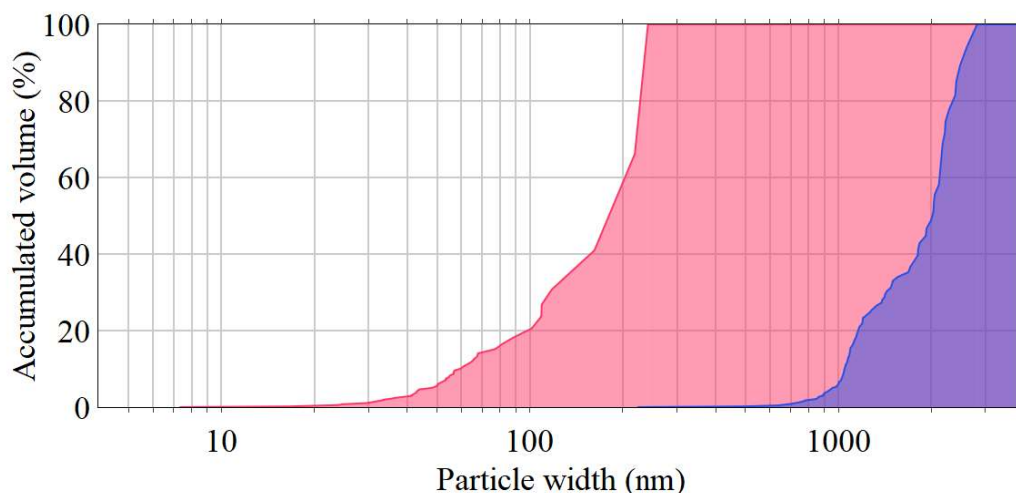


**Figure 3.35.** Percentage of the volume of the product that belongs to particles below a given width in the microfluidics-synthesized (red) and the bulk-synthesized (blue) samples.

#### 3.1.6.e. Comparison of results with the literature.

The particles we obtained can be compared with the results from the literature by their size and by their switching temperature. To make this comparison, the reported particle size and their transition temperatures are plotted in figure 3.36 together with the results we obtained. The grey triangles in this figure correspond to the switching temperatures of nanoparticles of  $[\text{Fe}(\text{pz})\text{Pt}(\text{CN})_4]$  reported in literature (synthesized using reverse microemulsion). Here the smaller particles tend to display lower transition temperatures and thinner hysteresis ranges than the bigger ones. However, there is a considerable dispersion in the data, and the shape of a curve that would connect the points in the plot of figure 3.36 is unclear. The green triangles in figure 3.36 correspond to our results. When we compare these, we can see that our results are quite close to what was reported previously, especially the results of M. T. Delgado-Perez *et al.*<sup>2</sup> Qualitatively, it seems like the transition temperatures we obtain (as well as the ones reported by M. T. Delgado-Perez *et al.*<sup>2</sup>) are higher than the general tendency reported by others. Unfortunately, the broad particle size distribution in our experiments, as well as the fact

that we used a different method to synthesize these particles blurs a more quantitative comparison with the literature.

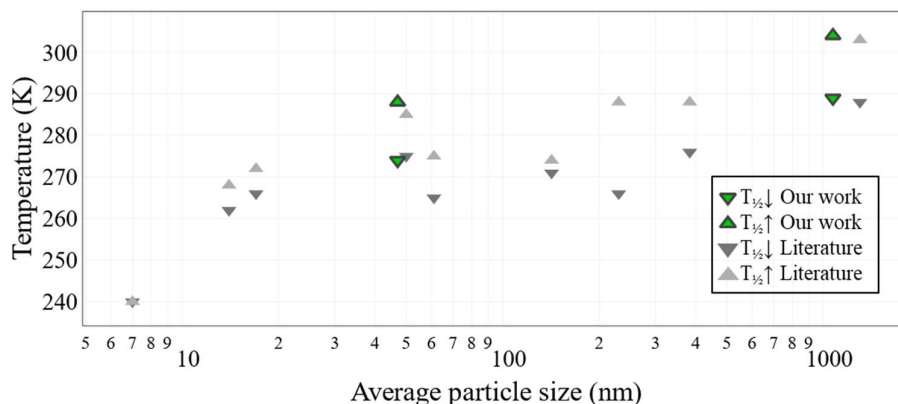


**Figure 3.36.** Comparison of the particle size and the transition temperatures of our samples and the ones found in the literature.

### 3.1.7. Reproducibility and performance.

From the previous analysis, it is tempting to conclude that the use of the *Red Chip* resulted in the synthesis of nanoparticle of  $[\text{Fe}(\text{pz})\text{Pt}(\text{CN})_4]$  with a particle size and a switching behavior similar to the ones synthesized using reverse microemulsion. To be able to claim that this compartmentalization of the reaction volume led to a downsizing effect of the particles, there are some aspects that must be addressed. First, the size of the droplets produced by the nozzle was established by only a couple of pictures, which is not a representative sample of all the droplets generated in the experiments, which represents a flaw in the sampling. Second, as explained before, the reference procedure was not performed with the same concentration of reactants as the microfluidics-synthesized sample. This means that the effect of concentration can be confused with the effect of the chemical environment in the microfluidic droplets. Third, the bulk-synthesized sample was filtered with a membrane, which means that particles smaller than the pore diameter might have been lost during the cleaning process.

Additionally, the particles synthesized using microfluidics were considerably aggregated, as can be seen in the pictures from TEM and SEM. Although these particles aggregate spontaneously (as can be seen directly from the changes in the appearance of the suspension), the high centrifugal force used in the separation process could contribute to the aggregation. This means that reducing the centrifugal force during the washing process could improve the quality in the measurements of the particle size.

To account for the previous remarks and the general observations in the operation of this chip mentioned in the previous section, we redesigned the process to synthesize  $[\text{Fe}(\text{pz})\text{Pt}(\text{CN})_4]$  in bulk and in microfluidics using the same chip (the *Red Chip*). Additionally, we changed the protocol to wash the product. Here are the differences with respect to the previous experiment (which are further described below):

- The pictures to measure the droplet size were equally distributed in time across the experiment.
- The reference sample was synthesized with the same concentrations as the microfluidics-synthesized sample.
- The bulk-synthesized sample was washed with the same protocol as the microfluidics-synthesized sample, so the nanoparticles that could be formed were not lost in the cleaning process.
- The flow rates of solutions with reactants were reduced and the flow rate of water in the buffer layer was increased to reduce the chances of forming solids in the nozzle.
- In the process of washing the products, the centrifugal force was reduced.
- The volumes of solvents used for the cleaning of the particles were reduced by a factor of 10.
- Before each centrifugation, the samples were let to rest for 5 minutes, so they could form aggregates which are easier to separate.

#### *3.1.7.a. Reaction conditions and performance.*

To carry this experiment, two solutions with reactants were prepared and pumped into the chip according to the following scheme:

Solution with reactants 1:  $|Fe(BF_4)_2| = 0.16 M$ ;  $|Pz| = 0.8 M$ ;  $Q = 175 \mu L/h$ .

Solution with reactants 2:  $|K_2Pt(CN)_4| = 0.16 M$ ;  $|Pz| = 0.8 M$ ;  $Q = 175 \mu L/h$ .

Buffer layer:  $Q = 700 \mu L/h$ .

Mineral Oil:  $Q = 3500 \mu L/h$ .

The microfluidic setup was operated under these conditions, to produce a stream of droplets until the syringes reached 50% of their capacity (2.5 hours). The 50 % remaining volume of solutions with reactants was kept for a batch in bulk for comparison, as described in section 3.1.6a.

To measure the droplet diameter, 18 pictures were selected. These pictures are homogenously distributed in time and have a separation of 8 minutes between each other. In total 477 droplets were measured. These droplets had an average diameter of  $57 \mu m$  (and  $\sigma = 14 \mu m$ , which implies a dispersity index of 25%) with the distribution shown in figure 3.37.

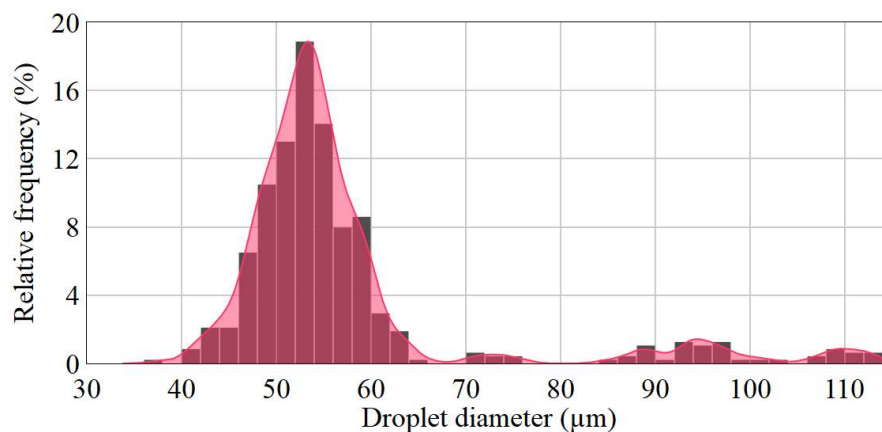


**Figure 3.37.** Droplet size distribution in the repetition experiment of the synthesis of  $[Fe(pz)Pt(CN)_4]$  using the Red Chip ( $n = 477$ ). The bars correspond to a conventional histogram, while the red area is the size distribution reconstructed by the KDE method.

The distribution shown in figure 3.37 corresponds to a Gaussian centered in 53  $\mu m$ . Intuitively, the difference in the diameter of the droplets with respect with the previous experiment can be explained by the difference in the flow rates used. Nevertheless, there is a considerable population of droplets with dimensions comparable to the channel that carried them. Figure 3.38 compares two archetypical cases of droplet production. The first one corresponds to the production of the droplets with the size distribution close to 50  $\mu m$  (figure 3.38, left). In the second case, we can see the formation of bigger droplets that have the same size as the channel (figure 3.38, right). This mechanism of droplet formation was not seen in the previous experiment. This means that the diameters of the droplets not only differ due to the difference in flow rates: they differ in the mechanism of droplet formation.

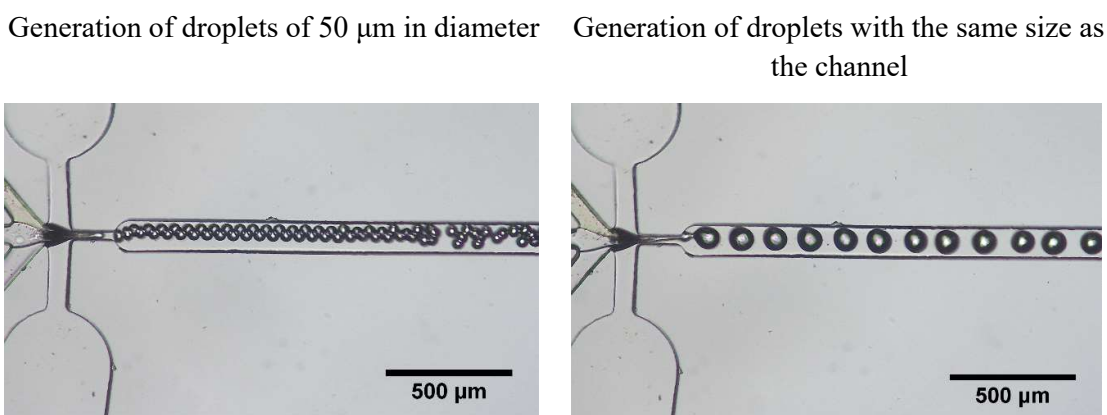


**Figure 3.38.** Comparison of the two droplet generation modes identified during the repetition experiment of the synthesis of  $[Fe(pz)Pt(CN)_4]$  using the Red Chip.

Additionally, it is possible to see the formation of solids in the nozzle shown in figure 3.38 (left), which might signal some degree of fouling of the chip. The appearance of the second droplet generation mechanism in this experiment might be related with some degree of fouling in critical areas of the chip, since the solids deposited on the walls can facilitate the aqueous effluents to wet them. Nevertheless, more information would be needed to clarify this.

At first glance, the droplet size distribution of figure 3.37 seems enough to describe the reactor size. Nevertheless, even if they are more reduced in number, bigger droplets contain more volume of the reaction mixture than the smaller ones. Because of this, to have an idea about how much of the reaction mixture was contained in droplets of each size, we need to calculate additional parameters beyond the simple relative frequency shown in figure 3.37.

We analyzed the droplet size distribution in the same way as we did with the particle size distribution in section 3.1.6.d. For this, we sorted the droplets by size and added their volumes consecutively. This way, we can tell how the droplets of each size contribute to the total volume of the reaction. The red line in figure 3.39 shows how each droplet contributes to the accumulated relative volume of the experiment. We can easily see that only 60% of the total reaction occurred inside of droplets below 70  $\mu\text{m}$ .

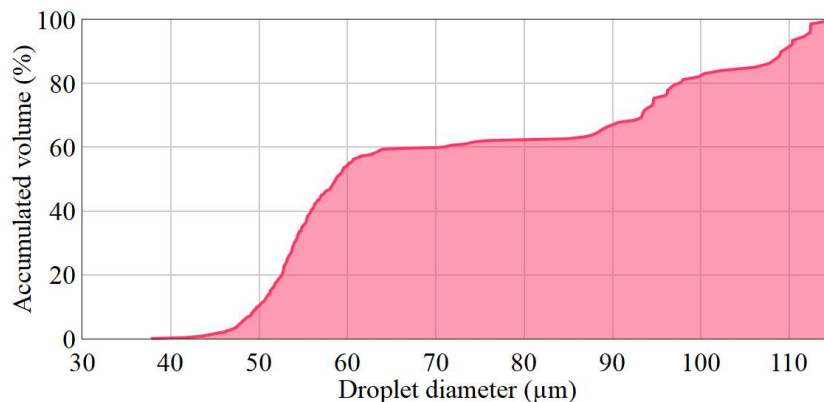


**Figure 3.39.** Percentage of the volume of the reaction mixture contained in droplets below a given diameter in the microfluidics-synthesized (red) and the bulk-synthesized (blue) samples.

### 3.1.7.b. Synthesis of a reference sample.

For comparison, the reaction to synthesize  $[\text{Fe}(\text{pz})\text{Pt}(\text{CN})_4]$  was performed in bulk,  $\mathbf{2}_{\text{ref}}$ , by the addition of 500  $\mu\text{L}$  of each of the same reactant solutions to a vial containing 2.0 mL of water under manual agitation. The addition time was of 10 seconds, which implies a flow of 50  $\mu\text{L}/\text{s}$  or 180 000  $\mu\text{L}/\text{h}$ . The final concentration in this experiment ( $|\text{Fe}^{2+}| = |\text{Pt}(\text{CN})_4| = 0.027 \text{ M}$ ;  $|\text{Pz}| = 0.27 \text{ M}$ ) is the same as the concentration used in the microfluidic synthesis.

### 3.1.7.c. Cleaning of the samples.

To avoid the elimination of the smaller particles during filtration and to ensure that the differences in particle size are only the consequence of the method of synthesis, both samples were washed using the same centrifugation protocol. First, the reaction mixtures were centrifuged at 1000 RCF for two minutes in 2 mL Eppendorf vials. Due to the presence of small amounts of mineral oil in the microfluidics-synthesized sample, a foam formed above the water level in the vial after centrifugation. To recover the solids dispersed in the foam, it was separated into another 2 mL Eppendorf vial and centrifuged again at 1000 RCF for two minutes before the liquid phases were eliminated and the solid was reinserted into the Eppendorf vial containing the remaining solids of the microfluidics-synthesized sample.

After the aqueous phases were eliminated, 1.5 mL of methanol was added to each vial (the one containing the bulk-synthesized sample and the one containing the microfluidics-synthesized sample). The vials were shaken manually to disperse the particles and, after 5 minutes of leaving them unperturbed, they were centrifuged at 1000 RCF for two minutes and the liquid phase was eliminated.

Afterwards, 1.5 mL of isopropanol was added to each vial and they were shaken manually to disperse the particles. Due to some properties of isopropanol (its viscosity, density and polarity), the particles of  $[\text{Fe}(\text{pz})\text{Pt}(\text{CN})_4]$  seem to stay in suspension for long periods of time. The aspect of both samples changed dramatically in this step: The particles from the microfluidics-synthesized batch,  $2_{\mu\text{F}}$ , were too small to be seen in suspension. Instead, the liquid phase seemed to have a yellow color while remaining translucent (figure 3.40, left). On the contrary, the particles from the bulk-synthesized batch gave the liquid phase a turbid aspect, as some of them could be seen with the naked eye (figure 3.40, right).

$2_{\mu\text{F}}$  Microfluidics-synthesized



$2_{\text{ref}}$  Bulk-synthesized

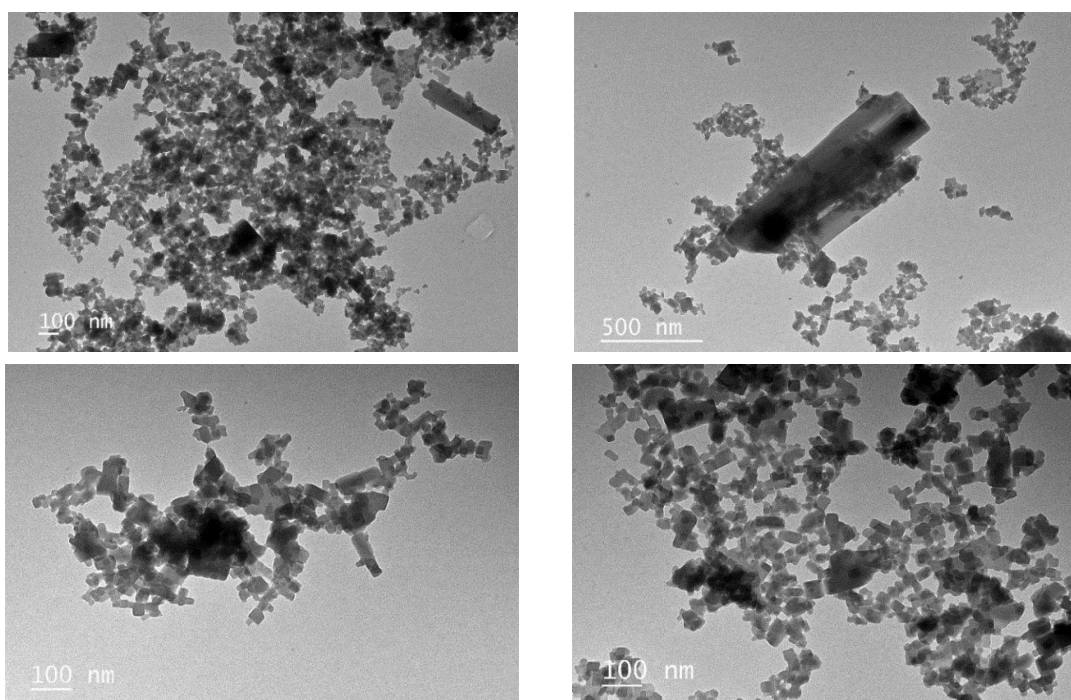


**Figure 3.40.** Aspect of the reaction product of both batches:  $2_{\mu\text{F}}$  (left) and  $2_{\text{ref}}$  (right) samples.

Samples were let to rest for 5 minutes and centrifuged at 700 RCF for 25 minutes before eliminating the liquid phase. Further on, 1.5 mL of toluene was added to the vials and they were centrifuged for five minutes. Finally, both samples were washed twice with acetone by eliminating the liquid phase, adding 1.5 mL of acetone and centrifuging at 700 RCF for two minutes.

*3.1.7.d. Morphological characterization of the products (second successful experiment).*

To characterize the morphology of the products, TEM images were taken with the same procedure used to characterize  $1_{\text{ref}}$  and  $1_{\mu\text{F}}$ . Figure 3.41 shows the TEM images of the sample synthesized using microfluidics,  $2_{\mu\text{F}}$ .



**Figures 3.41.** TEM images of  $2_{\mu\text{F}}$  in the repetition experiment.

These images show that the microfluidics-synthesized sample is made of square-like particles with an average diameter of 31.7 nm and a standard deviation of 31.4 nm (log-normal distribution,  $\log d = 1.42 \pm 0.20$ ). Figure 3.42 reports the histogram of the particle size. Compared to  $1_{\mu\text{F}}$ , the particles of the sample  $2_{\mu\text{F}}$  are smaller and have a slightly wider distribution.

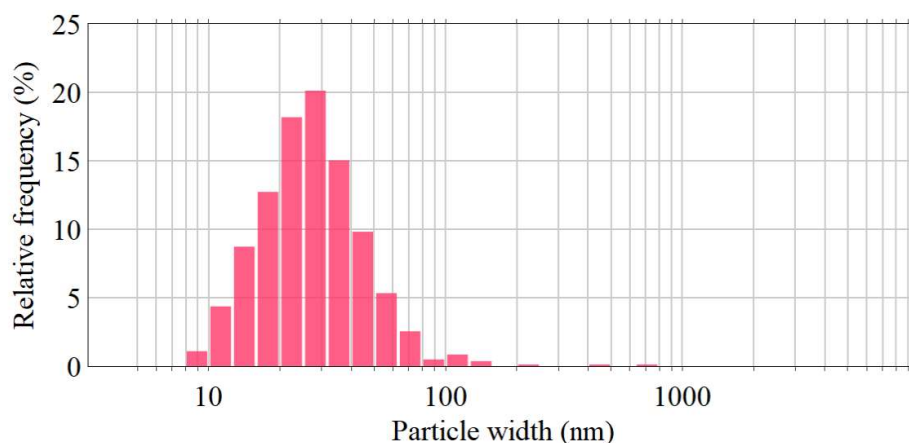


**Figure 3.42.** Particle size distribution of  $2_{\mu F}$  ( $n = 825$ ).

Although most particles in the microfluidics-synthesized sample have nanometric dimensions, there are some particles with a micrometric size. Even if they are quite reduced in number, their volume represents a considerable fraction of the total volume of the product (see the analysis at the end of this section).

The bulk-synthesized sample,  $2_{ref}$ , was also characterized by TEM and some images are reported on figure 3.43. An evident observation in this sample is the fact that, although micrometric particles can be seen, there is a significant population of smaller particles as well. Since this sample was not filtered, nanometric particles were not lost filtered out. These particles lower the average diameter to 224 nm with a standard deviation of 309 nm. The distribution in this case is not gaussian, the average  $\log(d) = 2.03$  with a standard deviation of 0.53. The histogram in figure 3.44 shows the particle size distribution obtained for this sample.

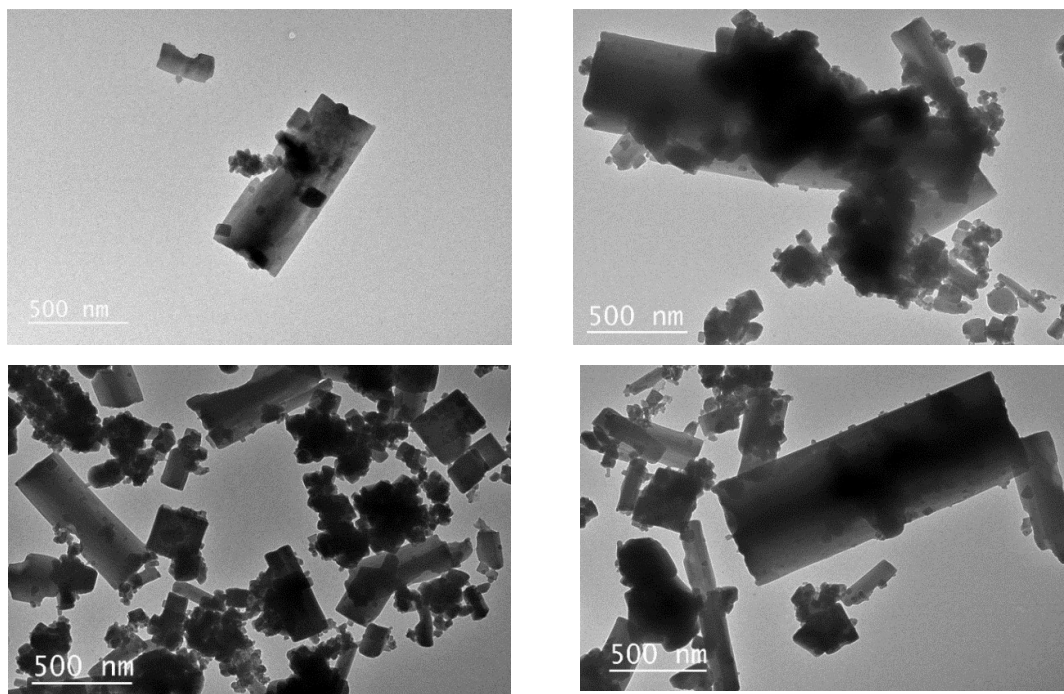


**Figure 3.43.** TEM images of the bulk-synthesized sample  $2_{ref}$ .

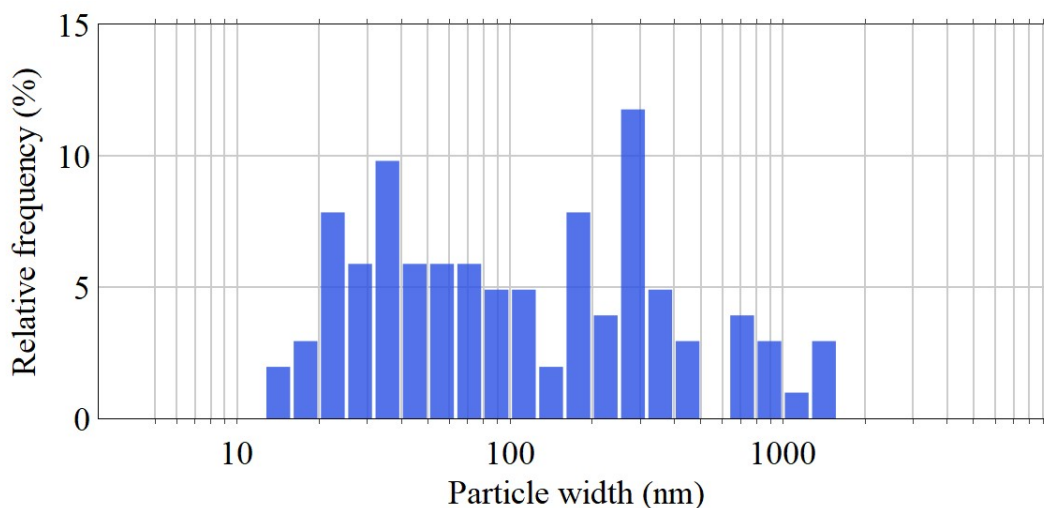


**Figure 3.44.** Particle size distribution of the bulk-synthesized sample,  $2_{ref}$ . ( $n = 102$ ).

The distribution in this histogram does not resemble a homogenous function and is astonishingly broad (since the particle diameter ranges from 15 nm to 1.6  $\mu\text{m}$ ).  $1_{ref}$  does not contain these small particles. Even if all the particles below 200 nm were washed away in the synthesis of  $1_{ref}$ ,  $2_{ref}$  seems to be composed of much smaller particles than in  $1_{ref}$ . This could follow from the differences in concentrations and addition times between  $1_{ref}$  and  $2_{ref}$ , but a definitive conclusion on the dilution effect would deserve a specific study. Nevertheless, even if there are many particles with a diameter below 100 nm in sample  $2_{ref}$ , they do not represent a big fraction of the volume of the product, as discussed below.

When the microfluidics-synthesized sample is compared with the bulk-synthesized one, two aspects are quite noticeable. First, there is a strong difference in the average particle size between samples  $2_{\mu F}$  and  $2_{ref}$  (31.7 nm and 224 nm correspondingly) which represents a seven-fold reduction in the average particle diameter and is an outstanding downsizing effect in comparison with other experiments of microfluidic synthesis.<sup>10,11,17,25–30</sup> Moreover, this result is consistent with the previous experiment involving  $1_{\mu F}$  and  $1_{ref}$  (see section 3.1.6).

The second notorious aspect from this comparison relates with the size distributions of both samples. Both distributions are broad but the standard deviation in the microfluidics-synthesized sample,  $2_{\mu F}$ , is smaller than the one of the reference material,  $2_{ref}$  (31.4 nm and 309 nm, correspondingly). Moreover, the dispersity indices of both samples are different as well: 99% for  $2_{\mu F}$ , and 137%, for  $2_{ref}$ . In other words, it seems that microfluidic synthesis additionally allows a better size distribution than the reference procedure.

The same analysis performed in section 3.1.6.d is done here to know the percentage of the volume of the product that belongs to particles below a given width. The result of this analysis is shown in figure 3.45.

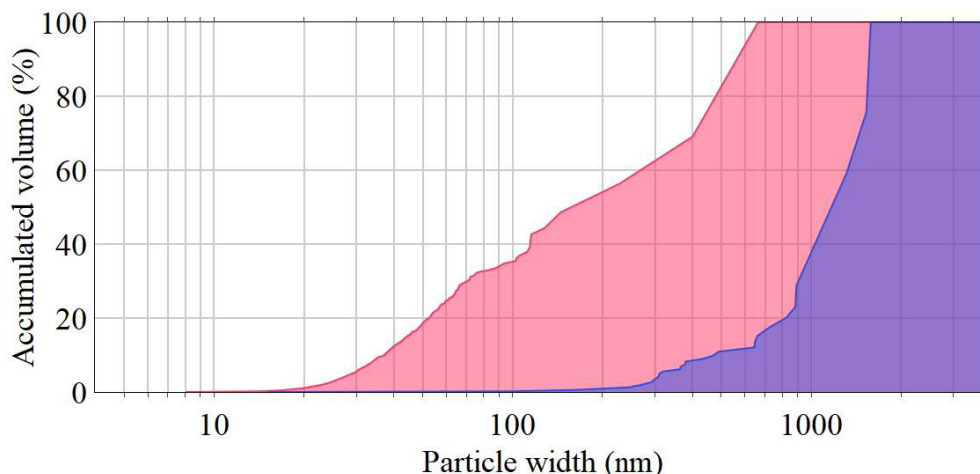


**Figure 3.45.** Percentage of the volume of the product that belongs to particles below a given width in the microfluidics-synthesized (red) and the bulk-synthesized (blue) samples.

When both samples are compared some aspects become very interesting. First, in the bulk-synthesized sample, only 2% of the product volume belongs to the particles with a diameter below 100 nm. The remaining 98% of the volume of the product belongs to bigger particles, and 50% of it belongs to particles with a diameter above 1  $\mu\text{m}$ . On the other side, the curve corresponding to the microfluidics-synthesized sample has ~40 % of the total product volume belonging to particles with a diameter below 100 nm and 50% below 200 nm.

These results can be compared with the ones found previously in the synthesis of  $1\mu\text{F}$ . It is interesting that in both experiments we observe a strong downsizing effects coming from the use of microfluidics to synthesize the material. In this first synthesis, almost all the droplets registered there have a diameter below 50  $\mu\text{m}$  and there are no particles with micrometric dimensions. In the second synthesis, 40% of the reaction volume was confined within droplets formed anomalously, and a big fraction of the reaction product belongs to particles above 200 nm in diameter (around 40%). This indicates that very likely, the size distribution of the particles depends on the formation of well-formed microscopic droplets.

### 3.1.8. Conclusions and discussion.

First of all, the *Red Chip* has clear advantages over the *Blue* one: while the latter clogged during the synthesis of  $[\text{Fe}(\text{pz})\text{Pt}(\text{CN})_4]$ , the *Red Chip* could work until the syringes were empty. Nevertheless, this device still presents failures in its design. During the operation of this device with reactants, some solid was formed in the nozzle. This solid seems to have affected the mechanism of generation of droplets in the second time we used it for the synthesis of  $[\text{Fe}(\text{pz})\text{Pt}(\text{CN})_4]$ . The droplet size distribution observed is very broad and the dispersity index of the droplets generated is very large.

With respect to the features of the product, the use of droplet microfluidic synthesis successfully leads to the desired phase of the selected  $[\text{Fe}(\text{pz})\text{Pt}(\text{CN})_4]$  compound with a noticeable size reduction compared to a conventional bulk synthesis (up to 20 times). The properties of the nanoparticles obtained using microfluidics agree with the ones reported on similar nanoparticles obtained using microemulsion techniques.

Despite these good results, we faced some reproducibility issues as just discussed. While in the first attempt it was possible to use the device to generate a homogenous stream of droplets, in the second one we observed a significant formation of solids in the nozzle even if the total concentration of reactants was lower than in the first case (due to the reduction in the flow rates of reactants). The fact that sometimes we see solids forming in the nozzle and sometimes we do not, implies that some additional unknown parameters can drastically affect the performance of the device. Moreover, the appearance of these solids in the nozzle might lead to the micrometric particles found in the second time the experiment was conducted.

It is not clear why the microfluidic-synthesized samples contain particles considerably smaller than the bulk-synthesized ones. Additionally, the homogeneity in the formation of droplets seems to be related with the particle size and particle size distribution. In the following, we propose some possible explanations.

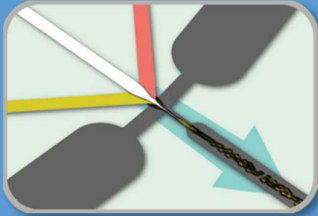
Intuitively, it is very easy to directly assume that a small reactor leads to the formation of small particles. The most straightforward mechanism of this principle is the steric restriction of growth of the particles through the spatial boundaries of the reactor. This strategy has been used for the synthesis of switchable nanoparticles inside micelles,<sup>1-3</sup> in block copolymers as proposed by B. Weber,<sup>31</sup> or within the pores of nanostructured silica matrices in the work of A. Bleuzen.<sup>32</sup> This is obviously not our case because the diameter of the droplets is in the range of 50  $\mu\text{m}$ , while the average nanoparticle obtained has a size of around 30-50 nm. To have an imaginary picture of this difference in size, consider that if this thesis was printed in A4 pages and all the pages were placed side by side, the arrangement of paper sheets would span along  $\sim 30$  m. Assuming it represents the diameter of the droplet, a microfluidics-synthesized nanoparticle of  $[\text{Fe}(\text{pz})\text{Pt}(\text{CN})_4]$  would have a diameter one thousand times smaller; i.e. a diameter of  $\sim 30$  mm (just as the black square in figure 3.46). It is a frequent misconception, a mistake that is very easy to commit, to believe that the microfluidic synthesis involves a kind of steric hindrance that limits the growth of particles. In fact, this idea would be comparable to believe that the dimensions of a beaker (in the range of centimeters) could limit the growth of a bulk synthesized particle (in the range of micrometers, 10 000 times smaller than the reactor where it was synthesized).



**Figure 3.46.** A square of 30 mm in length, representing the relative size of an average nanoparticle in the microfluidics-synthesized sample if the extension of this thesis (all the pages side by side) represented the diameter of the microfluidic droplet where it was synthesized.

Maybe the second most intuitive wrong impression about the microfluidic synthesis of nanomaterials is that the growth is limited by the amount of reactants contained in each droplet: Taking the density of  $[\text{Fe}(\text{pz})\text{Pt}(\text{CN})_4]$  from the crystallographic data ( $\sim 2.07 \text{ g/mL}$ ), its molar mass ( $435.09 \text{ g/mol}$ ) and final concentration of reactants used in an experiment ( $0.027\text{M}$ ), we can calculate that if the reaction yield is close to 100%, the volume of the product represents the 0.6% of the volume of the droplet. So, if we have a spherical droplet with  $50 \mu\text{m}$  in diameter ( $\sim 0.065 \text{ nL}$ ), it can be calculated that, depending on the operating flow rates in our experiments, each droplet has enough reactants to produce around  $371 \mu\text{m}^3$  of product (equivalent to a cube with a length of more than  $7 \mu\text{m}$ , if we assume the formation of one single particle). The average particle diameters we measure in microfluidics-synthesized samples are one or two hundred times shorter (millions of times smaller in volume).

Now that these two hypotheses are left behind, we must seek our answer deeper in the dynamics inside of the droplet (as explained in chapter 1.1). Table 3.3 highlights some differences of the reactor features between the bulk and the microfluidic syntheses.

	<i>Bulk</i>	<i>Droplet-based microfluidics</i>
		
<b>Mixing</b>	Chaotic and turbulent.	Led by internal fluxes in the droplet.
<b>Reactor size</b>	1-10 cm.	10-100 $\mu\text{m}$ .
<b>Interface</b>	Not moving, low surface area-to-volume ratio.	Moving, high surface area-to-volume ratio with the boundaries of the reactor, high interface area-to-volume ratio between the reactants.

**Table 3.3.** Comparison of the reaction environments in the bulk and droplet microfluidic syntheses.

In the classical nucleation theory, the growth of each embryo of particle is favored by the oversaturation (or the Gibbs free energy released per mole of product,  $\Delta\mu$ ), and is hindered by the interfacial tension between the particle and the liquid medium around it ( $\sigma$ ), as shown in figure 3.47 (left). When the particle is very small, the interfacial tension outmatches the oversaturation; nevertheless,  $\Delta\mu$  is proportional to the volume of the particle and  $\sigma$ , to its surface area. This means that if the particle grows,  $\Delta\mu$  increases faster than  $\sigma$ . When the particle reaches some critical dimensions, both contributions become equal and the particle has the same probabilities of re-dissolving or continuing its growth indefinitely. This idea is often described by plotting the value of  $\Delta G$  as a function of the radius of the particle (assuming it is spherical). When only the surface tension and the oversaturation contribute to  $\Delta G$ , this plot resembles the one shown in figure 3.47 (right).

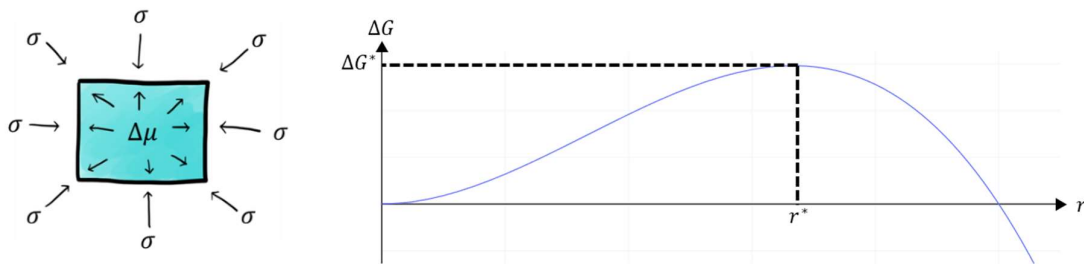


**Figure 3.47.** Left: Oversaturation ( $\Delta\mu$ ) promoting and interfacial tension ( $\sigma$ ) hindering the growth of an embryo in the classical nucleation theory; right: Free Gibbs energy ( $\Delta G$ ) of a growing particle as a function of its radius  $r$  (the critical nucleation radius is shown as  $r^*$ , and the energy barrier to reach such radius, as  $\Delta G^*$ ).

According to this model, the nucleation rate depends on the probability with which the embryos reach the critical dimensions required for further growth. In the slow diffusion techniques for the growth of single crystals, the low speed at which the reactants are mixed implies that the local oversaturation increases gradually. Therefore, only a few embryos reach their critical size and the total mass of product is contained in a few large crystals. In the case of microfluidics, if the mixing is very fast, the opposite effect is to be expected. As the local oversaturation suddenly increases, the nucleation rate rises as well. Because of this, instead of obtaining a few big particles, many small particles would be found.

Another possible contribution to the downsizing effect in these experiments is related with the high surface area-to-volume ratio of microscopic droplets. Some groups have reported that in droplet microfluidics, nucleation occurs in homogenous and heterogeneous ways.<sup>33,34</sup> Heterogeneous nucleation occurs when the boundaries of the reaction medium lower the energetic barrier that embryos must overcome in order to reach the critical nucleation radius. Here, when a particle is growing on the boundaries of the droplet, one of its sides is in contact with the aqueous phase, while another is in contact with oil. Therefore, the contribution of the surface of the particle to the energy barrier ( $\Delta G^*$ ) does not only depend on the interface tension between the particle and the reaction medium ( $\sigma$ ). Instead, it depends on the other interfaces

involved as well: Between water and oil ( $\sigma_i$ ) and between the particle and oil ( $\sigma_s$ ),<sup>35</sup> shown in figure 3.48 (left).<sup>2</sup>

In other words, the interface itself can serve as a catalyzer and acts as a nucleation site (figure 3.48, right). Considering this, the high surface area-to-volume ratio of micrometric droplets involves a high number of nucleation sites affecting the reaction conditions.

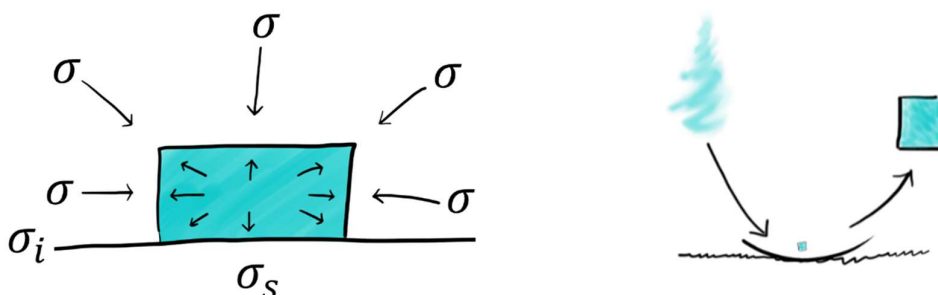


**Figure 3.48.** Left: interfacial tensions between the particle and two different media around it ( $\sigma$  represents the tension with water, and  $\sigma_s$ , with oil), and between water and oil  $\sigma_i$ ; right: A nucleation site conceived there as a region in the boundaries of the droplet where the particles can nucleate through a heterogeneous mechanism.

According to H. Shi *et al.*, the presence of nucleation sites can be analyzed by the incorporation of foreign particles into a reaction medium where a solid product is precipitating.<sup>36</sup> In the model they propose, the formation of nuclei in these sites involves two steps, as shown in figure 3.48 (right). In the first step, the reactants in solution form a particle at the interface (as just described), and in the second one, once the particle exceeds the critical dimension, it leaves the nucleation site (allowing the cycle to start again). In the context of microfluidics, this means that the fast fluxes inside the droplets might have an important contribution in making the heterogeneous nucleation process more effective. Although the interplay between the fast mixing and the heterogeneous nucleation might seem complex, remember that heterogeneous nucleation and fast stirring are used together to make small ice crystals in the preparation of ice cream.<sup>37</sup>

The strong currents inside the microfluidic droplets can, moreover, increase the nucleation rate in more complex ways. Secondary nucleation occurs when the particle surface participates actively in the nucleation process. For instance, the surface of a stable particle (with dimensions above the critical value) can act as an active set of nucleation sites. Before the new molecules become incorporated into the crystal, they might form some aggregates on the surface of the particle.<sup>38</sup> These aggregates can be washed away if the flow speed in the vicinity of the particle is strong enough to detach them from the surface before they become incorporated into the particle, as shown in figure 3.49. These aggregates can grow further after

<sup>2</sup> In chapter 2.2, the interface tension between oil and water is expressed as  $\gamma$ . Here, it is presented as  $\sigma_i$  to match the nomenclature in literature.<sup>35</sup>

they are sent back into the reaction medium. This would contribute to increasing the particle size distribution.

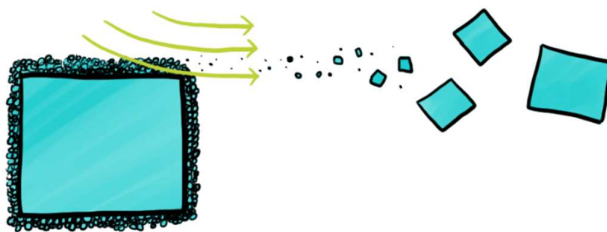


**Figure 3.49.** Secondary nucleation mechanism where a particle of the product itself triggers heterogeneous nucleation.

If the flow speed is fast enough, new mechanisms for nucleation can emerge. For example, the collision of particles can generate attrition fragments,<sup>38</sup> as shown in figure 3.50. Just as in the previous case, once these fragments are sent back into the reaction medium, they might grow further, and even recover the crystalline habit lost after the fragmentation.

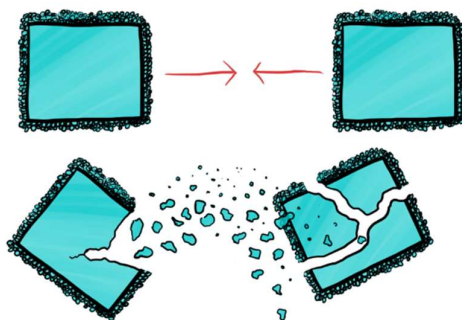


**Figure 3.50.** Two particles colliding to form attrition fragments.

The last hypothesis described here relates with the growth mechanism. In the classical nucleation mechanism, each particle continues its growth until the reaction medium lacks the reactants to continue its growth. In fact, the growth process can involve multiple steps, as shown in figure 3.51. First, many embryos below the critical nucleation size can aggregate and form a particle with dimension above the critical values. Second, many particles can form an aggregate, where the pieces are glued together by the reaction product as the reaction advances.



**Figure 3.51.** *Particles nucleating and growing through an aggregation mechanism.*

It is intuitive that the size reduction of the synthesized particles is related with a higher nucleation rate; nevertheless, the strong stirring inside microfluidic droplets might lead to smaller particles through hindering some crucial steps in the formation of bigger crystals. M. Rubio-Martinez *et al.* reported that continuous flow microfluidics can be used to control how crystals assemble to form more complex structures.<sup>39</sup> In our case, the particle formation in bulk might involve the aggregation of smaller particles as well. In that case, the downsizing effect we identify might be the consequence of the lack of aggregation due to the fast stirring during the reaction time.

It is very interesting how the microfluidic synthesis of solids can be enriched by the diversity of nucleation models, and how these two fields could give each other information about the mechanisms of nucleation and growth, as well as their applications. There are many models for the crystal nucleation and growth, and all the hypotheses presented here are based only on speculation. More research is needed before associating the downsizing effect to any of these models. In any case, these mechanisms are not mutually exclusive and the right answer in this matter could be a combination of many of them. Hopefully, in the future, microfluidics could be used to target specific aspects of the particle nucleation and growth. Nonetheless, the device just presented could be highly improved, as described in the next chapter.

## Chapter 3.2. Improvements of devices based on the combination→ generation approach

With the idea of improving the devices to promote a better reproducibility of the synthesis, several strategies can be explored. At the same time, we wanted to extend this approach to the synthesis of other coordination compounds. So, this chapter gathers experiments to be considered as perspectives to explore further in future works. We decided to work on the design of the exit channel, and to apply the swelling approach to the synthesis inside various droplet sizes. Several other coordination compounds were tested in the frame of several collaborations with David Harding, José Antonio Réal and Corine Mathonière. In the frame of these collaborations mononuclear or extended networks were explored, however, this chapter only reports some preliminary results obtained on a Prussian Blue Analogue synthesized in the group.

### 3.2.1. Improvement of the device.

We developed a last device for the synthesis of these materials. It is almost identical to the one shown in figure 3.19 but has a slightly different nozzle and a curvy exit channel (as shown in figure 2.18 of chapter 2.2) to eliminate the symmetry problem and promote mixing. The new device (*Green chip*: 3<sup>rd</sup> device based on the *Combination*→ *generation* mechanism) is shown in figure 3.52.

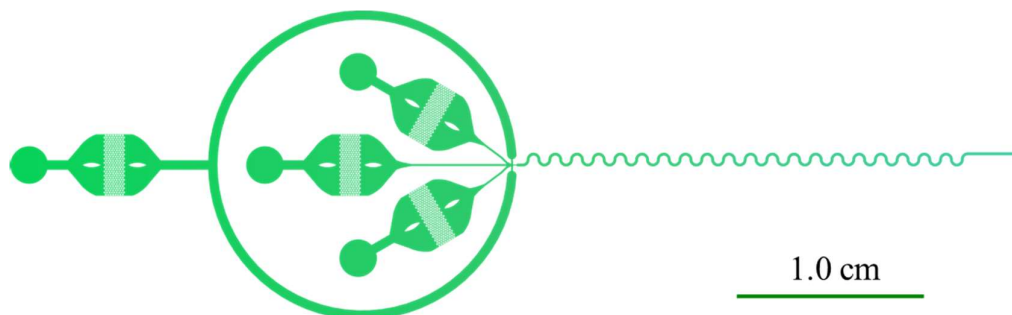


**Figure 3.52.** *The Green Chip.* The operation as well as most of its parts are the same as the *Red Chip* with only two modifications: The exit channel has a curvy shape, and the geometry of the nozzle is optimized.

After examining many pictures of the *Red Chip* under operating conditions (figure 3.53), the reactants enter the exit channel in an angle of  $\sim 55^\circ$ , as shown in figure 3.53. This angle is not a universal value. Instead, it is the consequence of the flow rates we used, the viscosities of our reagents, and some critical dimensions of the chip (like the width of the channels focusing oil in the junction). The curve that these reactants must make in the nozzle of the *Red Chip* may lead to some degree of premature mixing. With this in mind, we developed a new device (the 3<sup>rd</sup> one based on the *combination*→ *generation* approach, here named the

*Green Chip*) where the channels with reactants are modified to let the reactants arrive to the nozzle with an angle of  $\sim 55^\circ$  (figure 3.53; right).

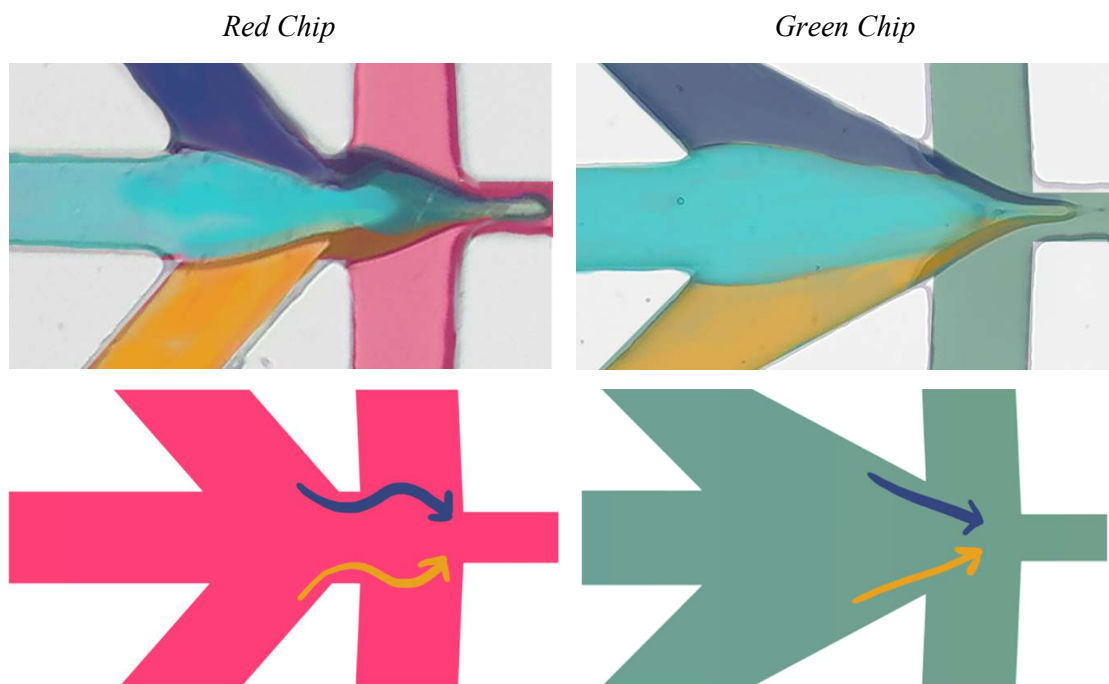
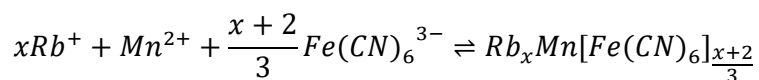


**Figure 3.53.** Comparison between the Red and the Green Chips in operation.

As mentioned in the introduction of this chapter, we also wanted to apply such an approach to other kinds of systems. We will present here some preliminary results obtained on Prussian Blue Analogs,  $Rb_xMn[Fe(CN)_6]_{(2+x)/3} \cdot zH_2O$  (hereafter named RbMnFe), synthesized in the frame of the PhD work of Thi Thiet Vu.<sup>40</sup> In general, Prussian Blue Analogues, or PBAs, are inorganic coordination polymers based on metal ions bridged by cyanido ligands. Many of these materials have switchable properties, which are the consequence of diverse mechanisms (like charge transfer or changes in the coordination sphere around the metallic centers). Their behaviors depend on some structural features (for example, the concentration of a doping agent,  $Rb^+$  in the present compound), as well as on their size which is well documented.<sup>41</sup> In this sense, they are very interesting materials to target using droplet microfluidics.

The first attempts to synthesize PBAs using the *Red Chip* (figure 3.19) led to the precipitation of the insoluble product in the nozzle, which in turn resulted in a permanent clogging of the device. It seems like PBAs are formed much faster and are less soluble than  $[Fe(pz)Pt(CN)_4]$  and Hofmann-type networks in general. Therefore, to test if the *Green Chip* outperforms the *Red* one, the synthesis of PBAs was a worthy goal. The reaction scheme to synthesize RbMnFe is the following:



To synthesize this material, we used the following conditions:

Solution with reactants 1:  $[MnCl_2] = 0.15\text{ M}$ ;  $[RbCl] = 0.75\text{ M}$ ;  $Q = 200\ \mu\text{L/h}$ .

Solution with reactants 2:  $[K_3Fe(CN)_6] = 0.15\text{ M}$ ;  $[RbCl] = 0.75\text{ M}$ ;  $Q = 200\ \mu\text{L/h}$ .

Buffer layer:  $Q = 700\ \mu\text{L/h}$ .

Mineral Oil:  $Q = 3500\ \mu\text{L/h}$ .

The reaction was performed for 2.5 hours, consuming 0.5 mL of each solution with reactants.

The droplets generated in this experiment are separated from each other by enough space to avoid their merging. Moreover, the fact that these droplets are not touching each other allows us to measure them automatically using macros in ImageJ. During the initial stage of the experiment, the instabilities in the flow related with the starting of the experiment led to a slight precipitation of product in the nozzle that did not affect the performance of the device. It is interesting to note that the reactants enter the droplets in such a harmonic way, that when the droplets exit the nozzle, each reactant can be seen as a hemisphere of the droplet, as highlighted in figure 3.55. The reactants seem to mix as the droplet advances along the exit channel. This means that regardless of the reaction kinetics or the solubility of the product, if this chip is operated in the adequate conditions, no product should precipitate in the nozzle and the device should not clog.

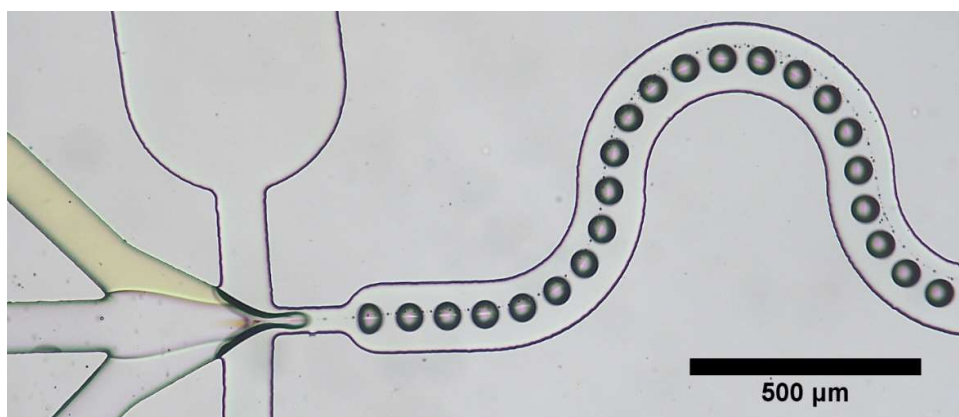


**Figure 3.54.** The Green Chip in operation during the synthesis of RbMnFe.

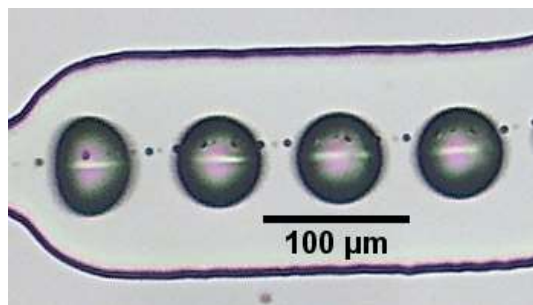


**Figure 3.55.** Zoom-in on the droplets recently generated in the Green Chip in operation during the synthesis of RbMnFe.

In this experiment, pictures of the operating device were taken each 5 seconds and a total of 44801 droplets were measured. The droplets had an average diameter of 53  $\mu\text{m}$  and a standard deviation of 1.8  $\mu\text{m}$ , which represents a dispersity index of 3.4%. Note that such a small dispersity index is below the reported value in flow-focusing configurations (5%),<sup>42</sup> which reflects the outstanding performance of this setting.

From the operating flow rates and the droplet size, the frequency of generation of droplets was calculated to be 14.1 million droplets per hour (or 3.9 kHz). During the experiment, around 35.3 million droplets were generated, and the measured droplets only represent 0.13% of all the droplets produced. It is interesting that as the droplets move at a constant speed, their position in the picture can be used to estimate the time elapsed since they left the nozzle. The 23 droplets present in the picture of figure 3.54 represent the time evolution of a typical droplet during the first 6 milliseconds after it leaves the nozzle. In this sense, we can estimate that the buffer layer separating the hemispheres of these droplets is still visible  $\sim 5$  milliseconds after they leave the nozzle. On one side, this is very favorable since we know that the reaction only happens once the droplet left the nozzle; but on the other side, it means that the time to reduce the symmetry problem could be drastically reduced by the asymmetrical incorporation of more obstacle shortly after the nozzle.

The high number of measured droplets allowed a fine determination of their size distribution, i.e. the histogram shown in figure 3.56.

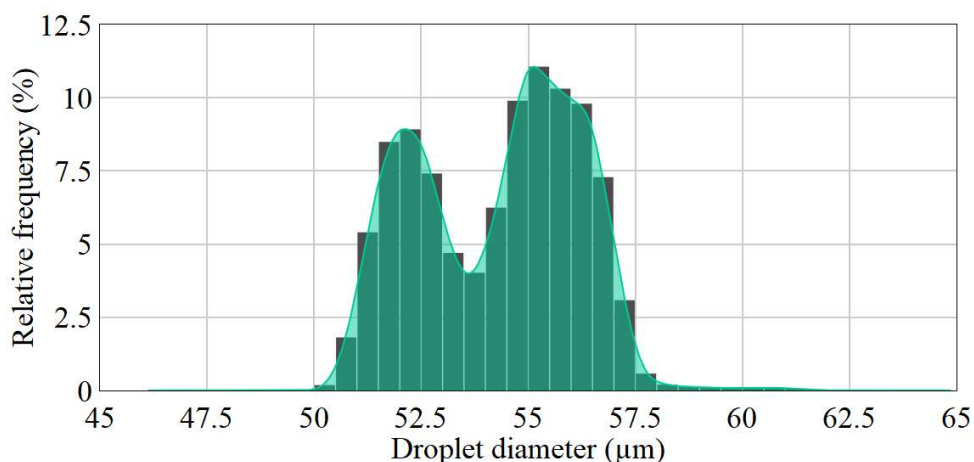


**Figure 3.56.** Droplet size distribution in the synthesis of  $\text{RbMnFe}$  using the Green Chip. The bars correspond to a conventional histogram, while the green area is the size distribution reconstructed by the KDE method ( $n = 44801$ ).

When this histogram is compared with the previous experiments, even if the reaction carried in this device is more challenging, its performance is clearly outstanding. Nevertheless, two distributions of droplet diameters can be identified in the histogram of figure 3.56: One of them having a peak around 52  $\mu\text{m}$ , and another around 56  $\mu\text{m}$ . This result is very unexpected,

so to understand this, the diameter of the droplets was plotted as a function of the time when they were detected as shown in figure 3.57.

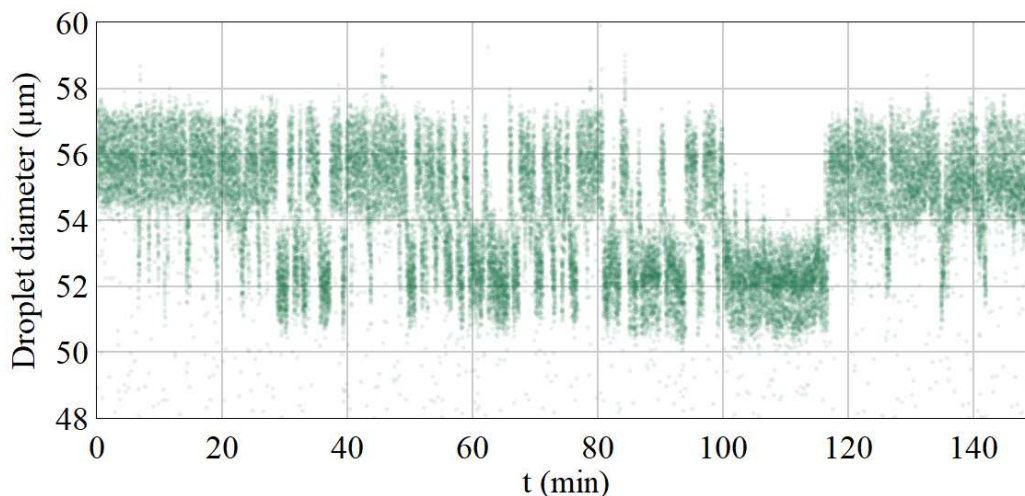


**Figure 3.57.** Diameter of measured droplets in the synthesis of RbMnFe using Green Chip.

The dots in figure 3.57 seem to form a set of clouds between 50 and 60  $\mu\text{m}$  during the 2.5 hours (or 150 minutes) of the productive operation of the device. These clouds can be easily divided into two categories: One of them corresponding to the diameters from 50 to 54  $\mu\text{m}$ , and another one, from 54 to 58  $\mu\text{m}$ . At any given time, the dots belong either to one or to the other category. Clearly, the cloud between 50 and 54  $\mu\text{m}$  is associated with the first peak in the histogram of figure 3.56 (centered around 51.5  $\mu\text{m}$ ). The other peak of the histogram belongs to the cloud between 54 and 58  $\mu\text{m}$  in the plot of figure 3.57. This leads to the idea that the system switches temporally between two states: one of them producing droplets of a diameter around 51  $\mu\text{m}$ , and another one producing droplets with a diameter around 55  $\mu\text{m}$ . The origin of the alternation of the system between these two states is still unknown and we can only speculate about its origin (performance of the pumps, presence of dust in the chip, noise pollution, etc.).

Although the production of droplets by the *Green Chip* using reactive flows alternates between two different states, the overall droplet size distribution is dramatically narrower than in the case of the *Red Chip*. Figure 3.58 compares the size distributions of the droplets with reacting solutions produced by these two chips.

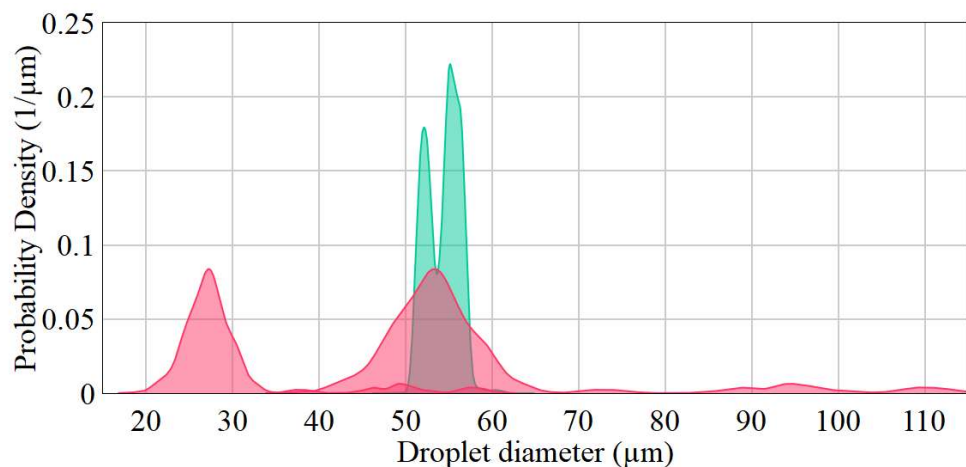


**Figure 3.58.** Droplet size distribution (from KDE) of the droplets with reacting solutions produced by the Chip Red (in red) and the Chip Green (in green). Note that the two red peaks belong to different experiments.

Finally, we can analyze the droplets measured in terms of the relative volume of the reaction medium contained in droplets of each diameter, just as we did with the previous experiments (figure 3.59). It is very interesting that in this experiment, 99% of the reaction occurred in droplets of a diameter between 50 and 57  $\mu\text{m}$ . This fact clearly means our *Green Chip*, clearly outperforms the previous one.

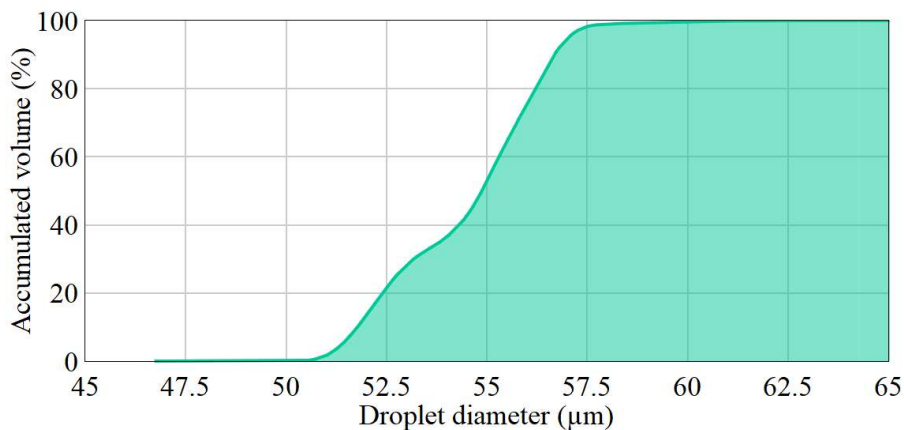


**Figure 3.59.** Relative volume of the reaction mixture contained in droplets of each diameter in the synthesis of RbMnFe using the Green Chip. The bars correspond to the histogram of the relative reaction volume; the line corresponds to the accumulated reaction volume in the individual droplets.

With respect to the product features, the analysis has not been done by our collaborators yet. It would be very interesting to determine how the microfluidic reaction environment affects the rubidium content in the product, its particle size, or its switching behavior. The last device

(*Green Chip*) can be improved in terms of the mixing time as well. There is still a long path to explore in this direction. Nevertheless, we preferred to make use of the limited PhD time that remained in addressing another pending issue regarding the potential use of swelling of PDMS to adjust the geometry of the chip *in situ*, as discussed in chapter 2.2.

### 3.2.2. The use of swelling to modulate the droplet diameter in an operating device.

In chapter 2.3, our approach to modulate some critical dimensions of PDMS chips through swelling is described. From our analysis, swelling can be used this way to modulate the size of droplets produced by devices with different geometries, with or without solvent, under different operating flow rates and pressures, etc. We demonstrate here that this technique can be applied to a real case scenario, where a chemical reaction (especially one where the product precipitates quickly) is carried out. For this task, we chose to use our best performing device (the *Green Chip*) and to try to induce swelling on it while it is performing the synthesis of a very complicated reaction (the synthesis of RbMnFe).

The procedure to test this is analogous to the one described in the microfluidic synthesis of PBAs with minor differences. Since the dimensions of the chip are reduced by the swelling, the internal pressure in the channels could increase above the tolerance of the chip. Because of this, the flow rates were lowered to ensure the physical integrity of the device. Therefore, the operation conditions were the following:

Solution with reactants 1:  $[MnCl_2] = 0.15 M$ ;  $[RbCl] = 0.75 M$ ;  $Q = 150 \mu L/h$ .

Solution with reactants 2:  $[K_3Fe(CN)_6] = 0.15 M$ ;  $[RbCl] = 0.75 M$ ;  $Q = 150 \mu L/h$ .

Buffer layer:  $Q = 200 \mu L/h$ .

Mineral Oil / Solution of toluene in mineral oil at 20%:  $Q = 2550 \mu L/h$ .

First, the chip was operated under these conditions using only mineral oil as the carrier phase, as shown in figure 3.60 (a). Enough sample was collected for further analysis and the content of toluene in the carrier phase was increased from 0 to 20% in a single step. After waiting 30 minutes to let the system stabilize, the device was kept working to collect a second sample. Figure 3.60 (b) shows the operating device under these conditions.

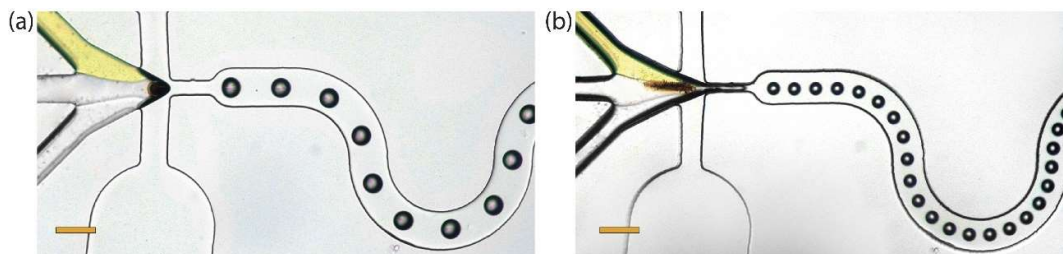


**Figure 3.60.** The *Green* in operation for the synthesis of RbMnFe in its pristine and swollen state (the scale bar corresponds to  $150 \mu m$ ).

In the first case, the diameter of the droplets was around  $78\ \mu\text{m}$ , while in the second, it was  $48\ \mu\text{m}$ . This means that the swollen chip produces droplets 77% smaller (in volume) than the pristine chip. In figure 3.60 (right) some degree of fouling can be seen in the nozzle; nevertheless, it did not affect the performance of the chip, and we continued the experiment without any additional intervention. Increasing the flow rate of the buffer layer between the solutions with reactants might have reduced the fouling of the nozzle. Nevertheless, the low degree of fouling here is quite impressive after considering the risk of clogging that comes from the fact that the solutions with reactants (that make a very insoluble solid) are flowing less than  $50\ \mu\text{m}$  away from each other in the nozzle, that the droplet volume was reduced more than 75% in only 30 minutes, and that the device produces thousands of droplets per second.

The particles of both samples were analyzed using TEM, resulting in the pictures shown in figure 3.61: Picture (a) corresponds to the sample synthesized using the pristine chip, and picture (b), to the sample synthesized in the swollen device. The particles measured in the TEM pictures of both samples, led to the histograms shown in figure 3.62.

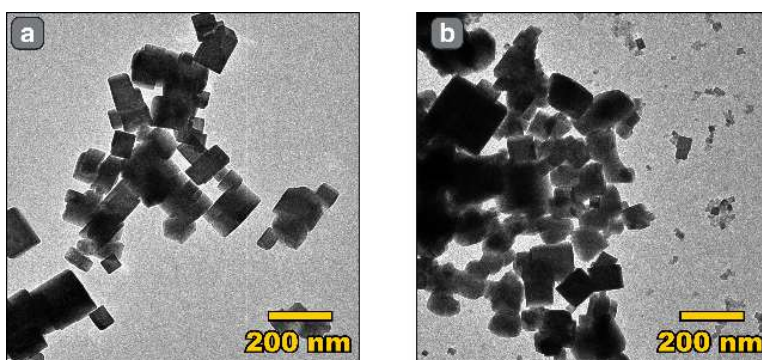


**Figure 3.61.** TEM images of the microfluidics-synthesized samples of  $\text{RbMnFe}$  using the Green Chip: (a) pristine device (b) swollen device.

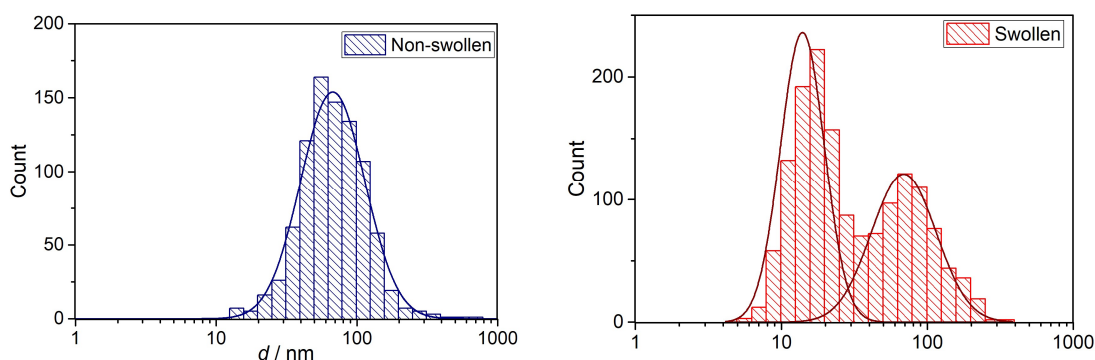


**Figure 3.62.** Particle size distribution of the microfluidics-synthesized samples of  $\text{RbMnFe}$  using the Green Chip. (left) pristine device (right) swollen device.

Both samples have a population of particles that resemble a log-normal distribution around 70 nm. The sample prepared in the swollen device has, nonetheless, an additional presence of smaller particles below 20 nm in diameter. It should be noticed that the sample obtained from the swollen device was collected after the stable regime was reached (see chapter 2.3). Therefore, the particles distributed around 70 nm do not come from the stabilization step that could provide a large range of particle size according to the reduction of the droplet diameter. Although the origin of the second mode in the sample synthesized in the swollen chip is still unknown, it might be related with some of the mechanisms previously described about the downsizing effect in droplet microfluidics. As already mentioned in the discussion of chapter 3.1, this is not related to any steric hindrance effect since there is still orders of magnitude between the droplet and nanoparticles sizes. However, all the possible explanations proposed for the size reduction could apply here since the reduction of the droplet size will strongly affect the mixing of the reactants.

The use of the swelling ability of PDMS, as investigated in chapter 2.2, applied to the synthesis of a coordination polymer, seems then to affect the size of the particles obtained. Even if still preliminary with plenty of space for improvement, this result is a promising milestone in the use of microfluidics in the synthesis of particles of controlled sizes.

Finally, it would be interesting to know if the Prussian Blue Analogues synthesized in the *Green Chip* have some differences with the ones from the bulk synthesis. At this point, only a qualitative result is available. When particles of RbMnFe are synthesized by mixing 5mL of a 0.1M of MnCl<sub>2</sub> and 5mL of a solution of Fe(II) at 0.1M and Rb at 1.0 M (concentrations similar to ours), the particles have a width around 2.2 μm as shown in the SEM image of figure 3.63. The difference in particle size between the samples of RbMnFe prepared in bulk and in microfluidics is comparable with the one found for [Fe(pz)Pt(CN)<sub>4</sub>]. These results are quite interesting because they suggest that droplet microfluidics might induce downsizing effect in the synthesis of many compounds.

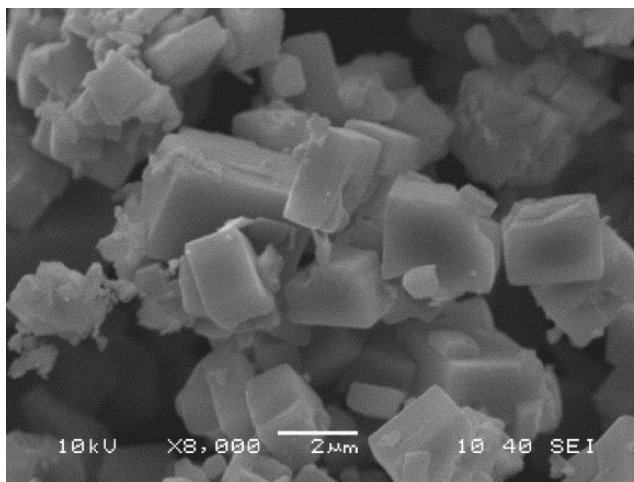


**Figure 3.63** SEM pictures of RbMnFe synthesized in bulk.

### 3.3 Conclusions to part 3

Along this chapter, the performances of different devices for the synthesis of solid switchable materials were described (especially for the synthesis of  $[\text{Fe}(\text{pz})\text{Pt}(\text{CN})_4]$ ). These devices started from the *generation*→ *combination* approach (where 2 droplets with complementary solutions with reactants are formed simultaneously and merge towards the end of the nozzle). Although these systems worked well when they were tested with water, they could not merge droplets with solutions with reactants efficiently.

In the second approach, *combination*→ *generation*, the reactants are combined in the same channel, which leads to a nozzle where a stream of droplets containing all the reactants *ab initio* is formed. Three devices based on this approach were used. The first one (the *Blue Chip*) could combine the reactants into the same droplet but was easily clogged by the product precipitating inside of the channels. The 2<sup>nd</sup> device (*the Red Chip*) was less easily clogged, allowing its operation for periods long enough to synthesize complete batches. Unfortunately, the size of the droplets produced by this device was highly polydisperse. Modifying some critical dimensions in the nozzle led to the design of a 3<sup>rd</sup> device (the *Green Chip*), which could produce highly monodisperse droplets with reactants.

When the achievements of these devices are compared, as in figure 3.64, a clear evolution of the capabilities of the devices can easily be seen.

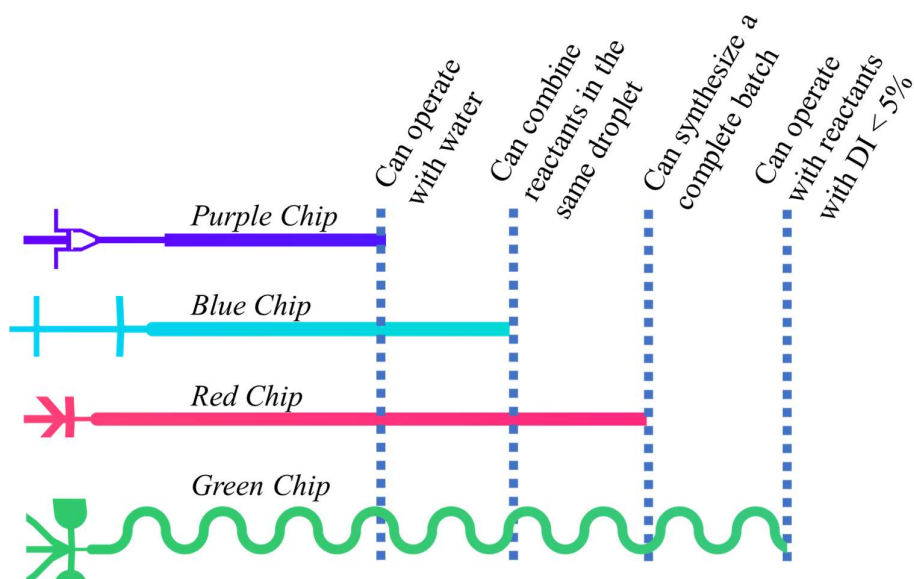


**Figure 3.64.** Comparison of the capabilities of the devices we designed.

The chemical environment inside the droplets has a clear effect on the particle size of  $[\text{Fe}(\text{pz})\text{Pt}(\text{CN})_4]$ . When this material is synthesized in droplet-based microfluidics, the particle size is significantly smaller than when it is synthesized in bulk. The reason of this downsizing effect is still unclear, but it is very likely related with the fast mixing occurring inside of

microfluidic droplets or with their high surface area-to-volume ratio. The switching behavior of these materials is very close to what was previously reported for particles of a similar size synthesized from reverse microemulsions.

Our main goal was to use chip-based droplet microfluidics to synthesize solid switchable materials in a reproducible and controlled way where the product displays reproducible and predictable properties. Unfortunately, we have not reached this goal. We have, nevertheless, achieved a great progress in the development of the systems and the technologies capable of such a complex task. We hope that this work will continue in the future until that goal is completed (and beyond).

## References to part 3

- 1 F. Volatron, L. Catala, E. Rivière, A. Gloter, O. Stéphan and T. Mallah, *Inorg. Chem.*, 2008, **47**, 6584–6586.
- 2 M. T. Delgado Perez, *Thesis: Structural investigation of the High-Spin→Low-Spin relaxation dynamics in spin crossover compounds*, Université de Genève, 2017.
- 3 I. Boldog, A. B. Gaspar, V. Martínez, P. Pardo-Ibañez, V. Ksenofontov, A. Bhattacharjee, P. Gütllich and J. A. Real, *Angew. Chemie - Int. Ed.*, 2008, **47**, 6433–6437.
- 4 A. Bousseksou, G. Molnár, L. Salmon and W. Nicolazzi, *Chem. Soc. Rev.*, 2011, **40**, 3313–3335.
- 5 K. Senthil Kumar and M. Ruben, *Coord. Chem. Rev.*, 2017, **346**, 176–205.
- 6 M. D. Manrique-Juárez, S. Rat, L. Salmon, G. Molnár, C. M. Quintero, L. Nicu, H. J. Shepherd and A. Bousseksou, *Coord. Chem. Rev.*, 2016, **308**, 395–408.
- 7 S. Slomkowski, J. V. Alemán, R. G. Gilbert, M. Hess, K. Horie, R. G. Jones, P. Kubisa, I. Meisel, W. Mormann, S. Penczek and R. F. T. Stepto, *Pure Appl. Chem.*, 2011, **83**, 2229–2259.
- 8 X. Z. Lin, A. D. Terepka and H. Yang, 2004, 1–6.
- 9 J. Wagner and J. M. Köhler, *Nano Lett.*, 2005, **5**, 685–691.
- 10 E. M. Chan, A. P. Alivisatos and R. A. Mathies, *J. Am. Chem. Soc.*, 2005, **127**, 13854–13861.
- 11 J. S. Owen, E. M. Chan, H. Liu and A. P. Alivisatos, *J. Am. Chem. Soc.*, 2010, **132**, 18206–18213.
- 12 L. H. Hung and A. P. Lee, *J. Med. Biol. Eng.*, 2007, **27**, 1–6.
- 13 K. I. Sotowa, K. Irie, T. Fukumori, K. Kusakabe and S. Sugiyama, in *Chemical Engineering and Technology*, 2007, vol. 30, pp. 383–388.
- 14 J. M. Köhler, J. Wagner and J. Albert, *J. Mater. Chem.*, 2005, **15**, 1924–1930.
- 15 J. M. Köhler, S. Li and A. Knauer, *Chem. Eng. Technol.*, 2013, **36**, 887–899.
- 16 J. Wagner, T. R. Tshikhudo and J. M. Köhler, *Chem. Eng. J.*, 2008, **135**, S104–S109.
- 17 L.-H. Hung, K. M. Choi, W.-Y. Tseng, Y.-C. Tan, K. J. Shea and A. P. Lee, *Lab Chip*, 2006, **6**, 174–178.
- 18 O. Kahn, *Molecular magnetism*, VCH, 1993.
- 19 V. Niel, J. M. Martinez-Agudo, M. C. Muñoz, A. B. Gaspar and J. A. Real, *Inorg. Chem.*, 2001, **40**, 3838–3839.
- 20 N. Sen, V. Koli, K. K. Singh, L. Panicker, R. Sirsam, S. Mukhopadhyay and K. T. Shenoy, *Chem. Eng. Process. - Process Intensif.*, 2018, **125**, 197–206.

- 21 H. Song, J. D. Tice and R. F. Ismagilov, *Angew. Chemie Int. Ed.*, 2003, **42**, 768–772.
- 22 I. Shestopalov, J. D. Tice and R. F. Ismagilov, *Lab Chip*, 2004, **4**, 316–321.
- 23 L. Frenz, J. Blouwolff, A. D. Griffiths and J. C. Baret, *Langmuir*, 2008, **24**, 12073–12076.
- 24 X. Niu, S. Gulati, J. B. Edel and A. J. deMello, *Lab Chip*, 2008, **8**, 1837–1841.
- 25 J. Wagner and J. M. Köhler, *Nano Lett.*, 2005, **5**, 685–691.
- 26 E. M. Chan, A. P. Alivisatos and R. A. Mathies, *J. Am. Chem. Soc.*, 2005, **127**, 13854–13861.
- 27 K.-I. Sotowa, K. Irie, T. Fukumori, K. Kusakabe and S. Sugiyama, *Chem. Eng. Technol.*, **30**, 383–388.
- 28 H. Nakamura, A. Tashiro, Y. Yamaguchi, M. Miyazaki, T. Watari, H. Shimizu and H. Maeda, *Lab Chip*, 2004, **4**, 237–240.
- 29 L. Malassis, R. Dreyfus, R. J. Murphy, L. A. Hough, B. Donnio and C. B. Murray, *RSC Adv.*, 2016, **6**, 33092–33100.
- 30 N. Qutub, B. M. Pirzada, K. Umar and S. Sabir, *J. Environ. Chem. Eng.*, 2016, **4**, 808–817.
- 31 O. Klimm, C. Göbel, S. Rosenfeldt, F. Puchtler, N. Miyajima, K. Marquardt, M. Drechsler, J. Breu, S. Förster and B. Weber, *Nanoscale*, 2016, **8**, 19058–19065.
- 32 G. Fornasieri, M. Aouadi, E. Delahaye, P. Beaunier, D. Durand, E. Rivière, P.-A. Albouy, F. Brisset and A. Bleuzen, *Materials (Basel)*, 2012, **5**, 385–403.
- 33 H. Shi, Y. Xiao, X. Huang, Y. Bao, C. Xie and H. Hao, *Ind. Eng. Chem. Res.*, 2018, **57**, 12784–12791.
- 34 M. Ildefonso, N. Candoni and S. Veessler, *Cryst. Growth Des.*, 2013, **13**, 2107–2110.
- 35 I. V Markov, *Crystal Growth for Beginners: Fundamentals of Nucleation, Crystal Growth and Epitaxy*, World Scientific, 2003.
- 36 W.-C. Chien, C.-C. Lee and C. Y. Tai, *Ind. Eng. Chem. Res.*, 2007, **46**, 6435–6441.
- 37 K. L. K. Cook and R. W. Hartel, *Compr. Rev. Food Sci. Food Saf.*, 2010, **9**, 213–222.
- 38 S. G. Agrawal and A. H. J. Paterson, *Chem. Eng. Commun.*, 2015, **202**, 698–706.
- 39 M. Rubio-Martinez, I. Imaz, N. Domingo, A. Abrishamkar, T. S. Mayor, R. M. Rossi, C. Carbonell, A. J. deMello, D. B. Amabilino, D. MasPOCH and J. Puigmartí-Luis, *Adv. Mater.*, 2016, **28**, 8150–8155.
- 40 J. H. González-Estefan, M. Gonidec, T. T. Vu, N. Daro and G. Chastanet, *Adv. Mater. Technol.*, 2019, **4**, 1900232.
- 41 L. Catala and T. Mallah, *Coord. Chem. Rev.*, 2017, **346**, 32–61.
- 42 S. Takeuchi, P. Garstecki, D. B. Weibel and G. M. Whitesides, *Adv. Mater.*, **17**, 1067–1072.



## General conclusions.

It is very unfortunate that spin crossover materials, having unique and engineerable switchable properties, lack a place in the contemporary industry. Yet, there are many challenges to address if we want to change this. Specially, we need to understand how the microscopic features of spin crossover materials affect how they behave, and in this context, we believe that microfluidics offers a solution: It provides chemical environments where the flows in the reactor are predictable and controllable in space and time to the scale of micrometers and milliseconds. Under such conditions, materials with reproducible and controllable features could be synthesized. Finally, from the systematic study of such materials we could unravel how their switching properties are influenced by their microscopic features.

In this thesis, we ambioned to use microfluidics to synthesize spin crossover materials, aiming at the production of particles with predictable and customized microscopic features, and we believe that such an achievement will very welcomed by the field of spin crossover. In this regard, ***we did not reach our goal***. We followed reasonable approaches to carry the microfluidic synthesis of  $[\text{Fe}(\text{pz})\text{Pt}(\text{CN})_4]$  and we identified that this compound is very challenging to synthesize this way.

Our efforts to synthesize this material in microfluidic systems are divided into two branches: the *generation*→*combination* approach (where two droplets with reactants are produced simultaneously and the reaction occurs after the two droplets merge) and the *combination*→*generation* approach (where two solutions of reactants are combined in a channel, which leads to a nozzle to produce a stream of droplets containing all the reactants *ab initio*). The main problem in the *generation*→*combination* approach is the difficulty to efficiently merge the droplets after they are formed. The main difficulty with the *combination*→*generation* approach is the sedimentation of product in the nozzle, eventually leading to the clogging of the device (since our product precipitates very quickly and can form particles, or aggregates of particles large enough to clog the device). Solving these issues required more time that what we expected; therefore, we did not reach our primary goal. Nevertheless, our venture was not in vain.

First, as we describe in chapters 2.2 and 3.1, we developed different devices based on designs available in literature. The failures in each device, led to the construction of the next one. This way, the geometries in our devices evolved in a logical way. Towards the end of this project, we developed a flow-focusing device capable of producing droplets with reactive flows with a dispersity index below 5%, surpassing the expected performance even if the reaction product precipitates very quickly.

In chapter 3.1, we describe the discovery that the droplet microfluidic synthesis of  $[\text{Fe}(\text{pz})\text{Pt}(\text{CN})_4]$  leads to particles much smaller than the ones obtained from conventional methods. This unprecedented downsizing effect is a surprising result because it represents a new method to obtain nanoparticulate materials without the use of surfactants. The mechanism underneath this effect is still unknown but it must be related with the reaction conditions inside the droplets.

Finally, in chapter 2.3 and 3.2 we developed a method to modulate the size of a stream of droplets *in situ*. This method is based on the controlled swelling of the PDMS chip and does not involve the use of surfactants or changes in the flow rates of the dispersed or continuous phases. Moreover, this method can be applied to an operating device carrying a reaction, where a solid precipitate very quickly.

The importance of this project does not rely on achieving the goal we had at the beginning of the thesis. Instead, it comes from the technological advances we developed in our struggle to achieve that goal. Our contributions to the human knowledge are the following three milestones:

- We designed a device capable of performing the synthesis of fast precipitating solid materials in droplet microfluidics, at relatively high solid fractions, with the droplets having a dispersity index below 5% (the *Green Chip*). The performance of this device is remarkable.
- We identified an unprecedented reduction in the size of particles of  $[\text{Fe}(\text{pz})\text{Pt}(\text{CN})_4]$  when they are produced in a microfluidic device, which represents a new method to obtain nanoparticles of this material.<sup>1</sup> This downsizing effect seems to hold true for the synthesis of PBAs as well.
- We developed a method based on PDMS swelling that allows the operator to control *in situ* the size of droplets of water carried by oil (without the need of surfactants or complex additional infrastructure).<sup>2</sup>

## *Perspectives.*

PhD students, postdocs and researchers can use our approaches and devices to synthesize materials that precipitate quickly (specially, the *Green Chip*) and future students could conclude this project and extend it to different materials. However, the design of devices (of any kind) is a never-ending process of evolution: identifying and correcting failures, upgrading, scaling up or down, automatizing, optimizing, etc. So, we cannot claim that we designed the perfect device. Future improvement is possible, as we show in the conclusion of part 2.

The surprising downsizing effect that we identify when  $[\text{Fe}(\text{pz})\text{Pt}(\text{CN})_4]$  is synthesized using droplet microfluidics deserves a deeper analysis. Specially, it would be interesting to determine if this reduction happens in other materials as well. If so, the *Green Chip* and its future variations could be used to elucidate the mechanisms of nucleation and growth in such materials. It would be also interesting to determine if this downsizing effect comes from the fast mixing occurring inside the droplets, from the high surface area-to-volume ratio of them, or from both. In this sense, to analyze the effect of the droplet size, the method we proposed based on PDMS swelling can be very helpful; and to analyze the effect of mixing, the *Black Chip* (or variations of it) can be used.

There are potential applications and areas of improvement in the method we developed to tune the dimensions of PDMS chips using swelling. It would be very interesting to use this

principle as a method to shrink channels below the resolution limit allowed by soft lithography, and to use such swollen devices to produce sub-micrometric droplets. Additionally, there might be ways to make this method compatible with biological samples (for example by using hydrogel-based devices).

These results were reported in the following publications:

- 1 J. H. González-Estefan, M. Gonidec, N. Daro, M. Marchivie and G. Chastanet, *Chem. Commun.*, 2018, **54**, 8040–8043.
- 2 J. H. González-Estefan, M. Gonidec, T. T. Vu, N. Daro and G. Chastanet, *Adv. Mater. Technol.*, 2019, **4**, 1900232.



## Appendix.

### Fabrication of the microfluidic devices and experimental setup.

#### *A.1 Fabrication method.*

The devices are fabricated through soft lithography. This technique consists in:

- Fabricating a master composed by a silicon wafer where a setoff with the desired geometry for the channels is printed using photolithography.
- Pouring a mixture of a low viscosity elastomer with a curing agent on the top of such master, and letting it harden to transfer the design on the master to the elastomer.

Particularly, our devices are designed using the Layout Editor Software. The resulting file is printed on a high-resolution mask by Selba S.A. and shipped to our laboratory. We use a SPIN-150 spin coater (SPS-Euroe) to coat the surface of a silicon wafer with a layer of SU-8 (Microchem) photoresist according to the specifications of the fabricant and the height we desire. Afterwards, we perform a pre-exposure bake to the wafer according to the specifications of the SU-8 photoresist fabricant. Later, we expose the coated surface of the silicon wafer to UV radiation using a UV-KUB 2 (KLOE) light source and apply a post-exposure bake. The unreacted SU-8 resin is washed using SU-8 revelator. Finally, the master is exposed to vapors of trichloro(1H,1H, 2H, 2H-perfluorooctyl)silane (Sigma-Aldrich) using a vacuum chamber. The height of the devices is determined using a mechanical profilometer (Dektak 6M, VEECO).

Once the master is ready, a mixture of SYLGARD 184 silicone elastomer base and curing agent in a 10:1 ratio is poured on the top of it (reaching a height of ~4 mm) and left in the vacuum chamber for ~30 minutes to eliminate any air bubbles. Later, PDMS is cured in the oven at 80 °C for 2 h. Afterwards, the chips are cut away from the master and protected with scotch tape on the side having the setoff of the channels, and the holes for the inlets and the outlet are drilled using a 1.2 mm Harris UNI-CORE punch.

A precleaned glass slide (CORNING, 75 mm × 50 mm) is coated with ~1.0 mL of a mixture of YLGARD 184 silicone elastomer base and curing agent in a 10:1 ratio using a spin coater at 2000 rpm for 1 minute and an acceleration of 500 rpm/s. This glass slide is partially cured in the oven at 80 °C for ~10 min until the surface is sticky enough for adhesion. The scotch tape on the PDMS chip is removed and it is placed carefully on the top of the coated glass-slide.

***For chips A and B (the ones to be exposed to a swelling agent described in chapter 2.3):***

A circle of aluminum foil is cut and placed in the bottom of a glass crystallizer. The PDSM device is placed on the top the circle of aluminum foil introduced in the oven at 80 °C for one hour. Before the experiment, PFA tubings with an internal diameter of 500 μm and external diameter of 1/16 in (IDEX Health & Science) are plugged in the inlets and outlet of the chip.

***For the pulsation dampener and the Purple, Blue, Red and Green Chips:***

The device is left to rest for one hour to eliminate potential bubbles of air trapped between the glass slide and the PDMS chip. Afterwards it is placed on a hot plate at 150 °C for ~3 minutes. Short sections of PFA tubings ~3 cm long with an internal diameter of 500 μm and external diameter of 1/16 in (IDEX Health & Science) are plugged in the inlets and outlet of the chip. Afterwards it is placed on the hot plate again for ~10 minutes. A circle of aluminum foil is cut and placed in the bottom of a glass crystallizer. The PDSM device is placed on the top the circle of aluminum foil introduced in the oven at 80 °C for one hour. Before the experiment, longer sections of tubing are connected to the ones already plugged in the chip, using a custom-made PDMS connection.

To fabricate the a custom-made PDMS connection, a 3 mL plastic Pasteur pipette is filled with a mixture of SYLGARD 184 silicone elastomer base and curing agent in a 10:1 ratio and kept in the oven at 80 °C for one hour. Later, the pipette is cut into sections, resulting in discs of PDMS with ~1.0 cm in height. A hole is drilled across the PDMS disc using a 1.2 mm Harris UNI-CORE punch. The two tubes to be connected this way are plugged on each side of the hole drilled across the PDMS disc. An example of a device before carrying an experiment is shown in figure A.1.



***Figure A.1.*** Two chips of a pulsation dampener on a glass slide. The tubing is already plugged into the chip and custom-made PDMS connection are placed on 3 of them. The tubing on the left side is left unconnected for clarity.

## A.2 Operation specifications.

Fluids are pumped into the device using syringes mounted on neMESYS 290N modules according to tables A1 (experiments described in chapter 2.3) and A2 (experiments described in chapter 2.2 and part 3).

Fluid	Syringe	Gearbox	Tubing from the syringe to the device
Water	2.5 mL ISL glass syringe	14:1	ID = 500 $\mu\text{m}$ , OD = 1/16 in
Mineral oil	10.0 mL ISL glass syringe	29:1	ID = 500 $\mu\text{m}$ , OD = 1/16 in
Solution of toluene in mineral oil at 50 % V/V	10.0 mL ISL glass syringe	29:1	ID = 500 $\mu\text{m}$ , OD = 1/16 in

**Table A1.** Details about the experimental setup in the experiments described in chapter 2.3.

Fluid	Syringe	Gearbox	Tubing from the syringe to the device
Water (buffer layer)	2.5 mL ISL glass syringe	29:1	ID = 250 $\mu\text{m}$ , OD = 1/16 in
Mineral oil	10.0 mL ISL glass syringe	29:1	ID = 500 $\mu\text{m}$ , OD = 1/16 in
Reactive flows	1.0 mL plastic syringe	14:1	ID = 250 $\mu\text{m}$ , OD = 1/16 in

**Table A2.** Details about the experimental setup in the experiments described in chapter 2.2 and part 3.